The neurophysiology of a mouse model of Timothy Syndrome

A thesis presented for the degree of

Doctor of Philosophy

By

Rosie Craddock

March 2024

Dedicated to my parents, Bridget, and Nick Craddock.

This would never have been possible without you… Nor, as you pointed out, would I exist.

Thank you.

Acknowledgements:

I was primarily based in the lab of the excellent Professor Frank Sengpiel throughout my PhD. I would not be the scientist I am today without him. He provided excellent academic and professional guidance throughout my studies. I am extremely grateful to have had him as my main supervisor.

To Fangli Chen, Dr Stephanie Bagstaff, Dr Bethany Frost, and Iustina Bouariu, I am lucky to have had you all as colleagues. Fangli has assisted with much of my research but has also taught me many practical skills. Stephanie has assisted with genotyping and with animal maintenance for my research. Beth assisted with my learning of animal handling and training techniques. To all of you, I am grateful for your friendship and for making these last few years so enjoyable.

Within my secondary lab, on the 3rd floor of the Hadyn Ellis Building, I also have many people to thank. Dr Cezar Tigaret provided me with training and access to equipment to complete my electrophysiology work. Professor Jeremy Hall provided advice which helped to shape the thesis. To all of those who I have worked with in the Hadyn Ellis Building over the course of my studies, I am grateful for your support, guidance, assistance, and friendship.

Thank you to Dr Adam Ranson, who provided an immense amount of help and advice, particularly when troubleshooting issues with the two-photon microscope, despite the fact he is now in Barcelona.

Outside of academia I would like to give a massive show of appreciation to my friends and family. Particularly my brothers Jos and Sandy, and my sisters-in-law Gwennan Clarissa. To my little niece, Lottie, the picture of you on my desk has made me smile every day during this write-up period. I know you are across the pond, cheering me on… or causing chaos for Sandy, which, to be honest, is just as good.

I will always be grateful to Ceferina and Alik, my closest friends, for their love and support. To my climbing guys, Chris, Luke, and Robbie, you all listened to me talk about brains far longer than you were socially obligated to. It did not go unnoticed. Also, thanks for teaching me how to up.

Finally, to my parents, Nick, and Bridget Craddock, to whom this PhD is dedicated, I am so grateful for your help over the course of my studies. I am especially grateful for everything you have done for me over the past year. Thank you.

Thank you to all those mentioned for your love, support, expertise, and advice.

Abstract:

Timothy syndrome (TS) is a multisystemic genetic disorder involving neuropsychiatric symptoms. TS is caused by heterozygous functional mutations in the neurophysiologically relevant *calcium voltage-gated channel subunit α1c* (*CACNA1C*) gene. Notable symptoms of TS are cardiac arrhythmia (long QT), syndactyly, hypoglycaemia, facial dysmorphisms, and neuropsychiatric phenotypes including autism spectrum disorder, epilepsy, and neurodevelopmental delay.

Three well characterised mutations in the *CACNA1C* gene, defined here as classical TS mutations, encode CaV1.2 channel α-1 subunits which lack voltage-dependent inactivation. On cell depolarisation, these channels allow a prolonged calcium influx into the cell. In cardiomyocytes this causes a prolonged action potential (AP), leading to long QT. TS mutations also impact cell development and migration around the body.

It is unknown how classical TS mutations impact neuronal function. In this thesis I investigate some of the neurophysiological changes resulting from the classical TS2 mutation. I explored how the TS2 mutation impacts basic visual processing, neuronal electrophysiology and parvalbumin inhibitory interneuron distribution across the brain using the TS2Neo mouse model of TS. I predict how the mutation will influence neural networks oscillations by use of computational modelling. Functional imaging demonstrated that TS2 alters a specific aspect of basic visual processing in mouse visual cortical cells, increasing contrast sensitivity to high spatial frequency visual stimuli. I provide the first electrophysiological evidence that classical TS mutations prolong the AP of mature pyramidal neurons within naturally developed, acute mouse brain tissue in the primary visual cortex, retrosplenial cortex and in CA1 of the hippocampus. I use immunofluorescent imaging to show that TS2 alters parvalbumin interneuron distribution across the mouse brain, with an increase in density in the visual cortex, and a decrease in density in the CA3 of the hippocampus. Computational modelling predicted that the mutation-related reduction in parvalbumin interneuron number reduces ɣ oscillatory power in the CA3.

Acronyms and definitions:

ACSF	Artificial cerebrospinal fluid
ADHD	Attention deficit hyperactivity disorder
AHP	After hyperpolarisation
ANOVA	Analysis of variance
AP	Action potential
ASD	Autism spectrum disorder
BK	Big potassium (channel)
BNC	Bayonet Neill–Concelman connector
C	Capacitance
CACNA1C	*Calcium voltage-gated channel subunit α1c (gene)*
CaV1.2	Calcium channel, voltage-dependent, L type, α 1C subunit (channel subunit)
CDI	Calcium-dependent inactivation
Classical TS	Timothy syndrome caused by G406R or G402S mutations in exons 8 or 8a of calcium voltage-gated channel subunit α1c causing CaV1.2 lacking voltage-dependent inactivation
Cntnap2	*Contactin-associated protein-like 2 (gene)*
CNV	Copy number variant
CSF	Contrast sensitivity function
CTIP	*CtBP-interacting protein* (*gene* and protein)
Daq	Data acquisition card
DF	Degrees of freedom
dF/F	Change in fluorescence relative to average fluorescence
dV/dt	Rate of change of voltage
ECU	Electronic control unit
EEG	Electroencephalogram
EGTA	Ethylene Glycol-bis(β-aminoethyl ether)-N,N,N',N'-Tetraacetic Acid)

En2	*Engrailed homeobox 2 (gene)*
HEPES	4-(2-hydroxyethyl)-1-piperazineethanesulfonic acid
FFT	Fast Fourier transform
FMR1	*Fragile X messenger ribonucleoprotein 1 (gene)*
g	Conductance
GABA	ɣ-aminobutyric acid
GAD67	Glutamate decarboxylase (molecular weight 67, enzyme)
GFP	Green fluorescent protein
GI	Gastrointestinal
HCN	Hyperpolarization-activated cyclic nucleotide–gated (channel)
HET	Heterozygous
I	Current
iPSC	Induced pluripotent stem cell
IQR	Interquartile range
xSy	Transmembrane domain x (numeric in roman numerals) of segment y (numeric in Arabic numerals)
KO	Knock out
KW	Kruskal-Wallis
LCD	Liquid-crystal display
LFP	Local field potential
Long QT	A prolonged interval between the Q and T waves of cardiac activity as measured by an electrocardiogram
Lx	Layer x
MeCP2	*Methyl CpG binding protein 2 (gene)*
MGN	Medial geniculate nucleus
N	Number of animals
n	Number of cells or measurements

NI	National Instruments
Nlgn4	*Neuroligin 4 (gene)*
NR	Non-responsive
OCD	Obsessive compulsive disorder
PBS	Phosphate-buffered saline
PFA	Paraformaldehyde
PFC	Prefrontal cortex
PMT	Photomultiplier tube
POMC+	Pro-opiomelanocortin expressing
Prop	Proportion
PSD	Power spectral density
PV	Parvalbumin
PV+	Parvalbumin expressing
RAM	Random access memory
ROI	Region of interest
RSC	Retrosplenial cortex
RT	Room temperature
R^2	Coefficient of determination
SATB2	*Special AT-rich sequence-binding protein 2 (gene* and protein*)*
SENP1	*Sentrin-specific protease 1 (gene)*
Shank1	*SH3 and multiple ankyrin repeat domains 1 (gene)*
Shank3	*SH3 and multiple ankyrin repeat domains 3 (gene)*
Sx	Segment x
Sf	Significant figures
SF	Spatial frequency
S1	Primary somatosensory cortex
τ	Time constant
TB SSD	Terabyte solid state drive
TS	Timothy syndrome

TSA	Atypical Timothy syndrome (any non-G406R *CACNA1C* mutation)
TS1	Timothy syndrome type 1 (G406R exon 8a)
TS2	Timothy syndrome type 2 (G406R exon 8)
UDP	User datagram protocol
V	Voltage
VDI	Voltage-dependent inactivation
VIP+	Vasoactive intestinal peptide expressing
VPA	Valproic acid
VRAM	Video random access memory
V1	Primary visual cortex
V1b	Binocular region of the primary visual cortex
WT	Wild type

Units:

A	Amperes
Cpd	Cycles per degree
°C	Degrees Celsius
F	Farads
Hz	Hertz
l	Litres
m	Metres
M	Molar
Osm	Osmoles
Ω	Ohm
s	Seconds
S	Siemens
V	Volts

Impact of the Covid-19 pandemic:

The research described in this PhD thesis was carried out between October 2019 and December 2023. The Covid-19 pandemic caused major disruption to the research described here. National lockdowns and University policies specific to the pandemic led to a change in my research plans. Between March 2020 and Summed 2021, I had limited access to the lab. My research was originally intended to be largely wet-lab based. The scope of my research was changed to include a computational element, such that I could make progress toward my PhD whilst working from home. I completed a computational project looking at how *CACNA1C* hemizygosity disrupts neural network oscillations in the CA3 of the hippocampus. This is described in Appendix 3. I adapted my PhD to complete a similar experiment exploring how classical TS mutations impact oscillations in the same network. This is described in chapter 4 of this thesis. This required that I complete immunofluorescence imaging study to explore how classical TS mutations impact parvalbumin interneuron cell number. This is described in chapter 3. The work described in chapters 3 and 4 were conducted to allow me to use my work which was completed at home to contribute toward the completion of my thesis. As such, I did not complete as much electrophysiological and/or in-vivo imaging research as was planned and warranted. This should be taken into account when considering the layout and completion of the work described in this thesis.

Contents

General introduction:

Timothy syndrome:

Disease overview:

Timothy Syndrome (TS) is a human, genetic, multisystemic disease that involves neurological phenotypes. It was first described in 2004 by Splawski *et al.* TS is rare, is typically fatal, and is caused by exonic mutations in the neurophysiologically-relevant calcium voltage-gated channel subunit α1c (*CACNA1C*) gene (Splawski *et al.*, 2004, 2005; Walsh *et al.*, 2018). The *CACNA1C* gene encodes the L-type voltage gated calcium channel α-1 subunit, CaV1.2.

Symptoms:

TS impacts many bodily systems. The symptoms of TS are specific but diverse. At the time of disease characterisation, the deadliest phenotype of TS involved a disruption in cardiac function (Splawski *et al.*, 2004). This was long-QT interval, which results in arrhythmia and in sudden cardiac arrest. Other symptoms noted were syndactyly, hypoglycaemia, immune deficiency, cognitive abnormalities, abnormal dentition, facial dysmorphisms including a pronounced overbite, seizures, and autism spectrum disorder (ASD, Splawski *et al.*, 2004). Further symptoms of TS which have been since been characterised include joint hypermobility (Splawski *et al.*, 2005). It should be noted that many TS patients have neurological abnormalities, and up to 80% of TS patients meet the diagnostic criteria for ASD (Splawski *et al.*, 2004).

Subtypes:

There are many subtypes of TS. The categorisation of these subtypes has recently been disputed, and is a topic of ongoing debate (Bauer, Timothy and Golden, 2021). For simplicity, I define TS subtypes based on specific *CACNA1C* mutations causative of the disease. TS mutations in the *CACNA1C* gene are always heterozygous. These genetic mutations are discussed in the "*CACNA1C* gene" subsection. TS type 1 (TS1) was the first characterised subtype of TS (Splawski *et al.*, 2004). Timothy Syndrome type 2 (TS2) was later described by the same research group (Splawski *et al.*, 2005). These mutations occur in alternatively spliced exons 8 and 8a of the *CACNA1C* gene. TS1 is defined here as being caused by a single point genetic mutation which results in a single amino acid substitution, G406R, in the transcript of exon 8a of the *CACNA1C* gene. TS2 is defined here as the disease caused by the single point genetic mutation which results in the G406R amino acid substitution in the transcript of exon 8 of the *CACNA1C* gene. Differences in exons 8 and 8a are described in the "*CACNA1C* gene" subsection. TS which is caused by any other mutation in the *CACNA1C* gene is defined here as atypical type TS (TSA). There have been multiple patients reported in the literature to possess a G402S mutation in exon 8 of the *CACNA1C* gene. The G402S mutation is classified as a TSA mutation here for simplicity. Although this is classified as TSA here, it should be noted that the G402S mutation alters CaV1.2 channel function in a similar way to the

TS1 and TS2 mutations, described in the "*CACNA1C* gene subsection below". All three of these mutations are referred to as "classical TS mutations" throughout this thesis to indicate the similarity in the impact of these mutations on CaV1.2 channel structure and function. A review of all TS patients with classical TS mutations (correct to a PubMed literature review undertaken March 2024) is given in subsection "TS patient case files and review". In this subsection, I outline the symptoms presented by each patient, provide a reference to the publication of the report, and state the reported causative mutation. Where the mutation was unclear in the report, this will be indicated. Typically the symptoms of TS2 patients are more severe than those seen in TS1 patients (Splawski *et al.*, 2005; Ergül *et al.*, 2015; Philipp and Rodriguez, 2016; Walsh *et al.*, 2018). TS2 patients typically have joint hypermobility, developmental delay, and prolonged QT interval. The impacts of these mutations on channel structure are detailed in the subsection "*CACNA1C* gene" below.

CACNA1C gene:

Overview of the CACNA1C gene and its functional relevance:

The *CACNA1C* gene encodes the L-type voltage-gated calcium channel pore-forming α-1 subunit, CaV1.2.

L-type voltage gated calcium channels contain up to 5 different subunits, the α-1, α-2, δ, β and ɣ subunits. The α-1 transmembrane subunit forms the pore of the channel. It is functional but has abnormal properties when expressed alone. The other 4 subunits are auxiliary and modify the functional properties of the α-1 subunit. A general overview of L-type voltage gated calcium channel subunit structure and function is provided in the subsection "L-type calcium channel and CaV1.2 α-1 channel subunit structure and function".

The *CACNA1C* gene is expressed in a huge number of tissues around the body (Uhlén *et al.*, 2015). The CaV1.2 channel subunit has many non-neuronal functions. The CaV1.2 channel subunit plays a role in the contraction of smooth and cardiac muscles. CaV1.2 also plays a role in hormone secretion from pancreatic β cells, including insulin secretion required for adequate glycaemic regulation. The CaV1.2 channel subunit is further known to hormone secretion from chromaffin cells of the adrenal medulla (Hofmann *et al.*, 2014). CaV1.2 function has also been shown to play a role in the development of both excitable and non-excitable cells around the body (Ramachandran *et al.*, 2013; Cheli *et al.*, 2016a). It should be noted that specific genetic mutations in the *CACNA1C* gene can result in Brugada syndrome, a long-QT syndrome which does not involve the extra-cardiac symptoms (such as the neurological symptoms) seen in TS (Hofmann *et al.*, 2014).

In the central nervous system, the *CACNA1C* gene is expressed in the cerebral cortex, in the cerebellum, and in the hippocampus (Uhlén *et al.*, 2015). The *CACNA1C* gene is specifically known to be expressed in glutamatergic neurons within the cortex of the mouse (Dedic *et al.*, 2018). CaV1.2 is predominantly localized to dendritic spines and shafts. CaV1.2 is found in the dendrites and somata of CA1 pyramidal cells and are found at higher levels in the smaller dendritic processes and spines (Leitch *et al.*, 2009). Within neurons, Cav1.2 is known to be involved in excitation-transcription coupling, and have been shown to be necessary for late-phase long-term synaptic plasticity in the CA1 of the hippocampus (Striessnig *et al.*, 2014).

The *CACNA1C* gene has also been shown to play a role in the development of specific neurons within the brain. This includes the development of parvalbumin (PV) expressing (PV+) inhibitory interneurons (Jiang and Swann, 2005). This is discussed in more detail in the subsection “Impacts of TS mutations on inhibitory neuron development and migration”. The *CACNA1C* gene has been found to play a role in radial migration and in neurite outgrowth during general neuronal development (Kamijo *et al.*, 2018). This is discussed in more detail in the subsection “Impacts of TS mutations on neuronal projections and migration”.

Of pathological relevance, the *CACNA1C* gene has been found by genome-wide association study to be implicated in schizophrenia, ASD, depression and bipolar disorder (Liu *et al.*, 2011; Lu *et al.*, 2012; Consortium, 2014; Li *et al.*, 2015; Yoshimizu *et al.*, 2015). As already indicated, specific genetic mutations in the *CACNA1C* gene result in TS, which typically involves neurological phenotypes. This indicates that the *CACNA1C* gene has neuropsychiatric functional importance.

A mouse model with homozygous knockout (KO) of the *CACNA1C* gene has been previously generated to explore the neurological function of the *CACNA1C* gene, however these animals were non-viable and died in-utero (Simms and Zamponi, 2014).

L-type calcium channel and CaV1.2 α-1 channel subunit structure and function:

CaV1.2 is an α-1 subunit. α-1 subunits are the pore-forming and mandatory element of the L-type voltage gated calcium channel. The CaV1.2 α-1 subunit has multiple important structural motifs. A voltage-sensor module is formed by segments 1 to 4 (S1-4) of each of the 4 homologous repeats (I-IV) of the transmembrane channel. The pore-forming region of the channel consists of S5 and S6 segments and the S6 linker region. The S6 linker region contributes toward the formation and function of the selectivity filter (Striessnig *et al.*, 2014). The S4 segment controls voltage activation of the channel (Simms and Zamponi, 2014). The loop between domains I and II, and the adjacent S6 segment of domain I (IS6) has been identified to be involved in voltage-dependent inactivation (VDI) of the CaV1.2 channel (Cens *et al.*, 2006). The C-terminal domain is involved in calcium-dependent inactivation (CDI) of the channel (Striessnig *et al.*, 2014). VDI, CDI and activation properties are determined by the structure of the α-1 subunit, but can be modified by the function of auxiliary subunits α-2, δ, β and ɣ (Catterall, 2011).

CDI involves the C-terminal domain as shown in Figure 1. Calmodulin typically binds to the C-terminal domain at 2 points. When the channel opens and calcium enters the cell, calcium binds this calmodulin and causes a conformational change in the C-terminal domain of the channel, inactivating the channel (Pitt *et al.*, 2001).

VDI involves the I/II linker region of the channel. Specifically, it involves the α-1 interaction domain of the region. This domain is negatively charged and is attracted to the positively charged amphiphilic helix N-terminal to IIS1, termed IIS0. On prolonged activation of the channel, the IS6-linked α-1 interaction domain becomes displaced toward the pore axis, resulting in the movement of the α-1 interaction domain toward the amphiphilic helix N-terminal to IIS1. IS6 is physically linked to the α-1 interaction domain and is forced into a conformational change from an open to a closed state (Korkosh *et al.*, 2019). Classical TS mutations are found in IS6 of CaV1.2 (Splawski *et al.*, 2004, 2005).

The structure of the α-1 L-type calcium channel subunit, CaV1.2, is shown in Figure 1.

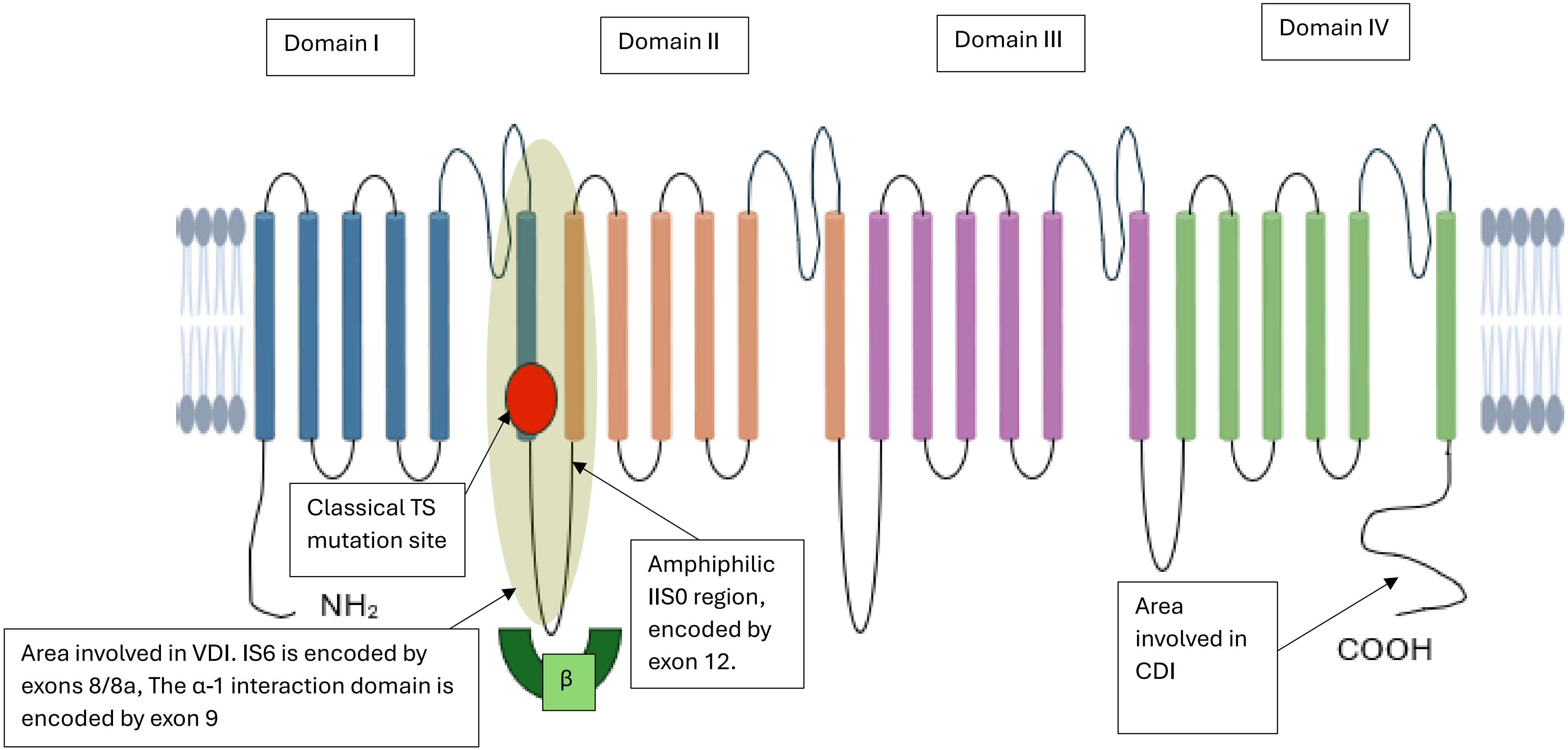

Classical TS mutation site

Area involved in VDI. IS6 is encoded by exons 8/8a, The α-1 interaction domain is encoded by exon 9

Amphiphilic IIS0 region, encoded by exon 12.

Area involved in CDI

Figure 1 Showing the structure of the CaV1.2 channel α-1 subunit. Each of the 4 domains are made of 6 transmembrane segments. The first 4 segments (where numbering starts from left to right) of each domain form the voltage sensor module. Segments 5-6 and the associated linker region form the pore of the channel. The S6 linker region (indicated) forms the selectivity filter of the ion channel. S4 of each domain controls activation of the channel. The C terminal domain is involved in CDI of the channel. The loop between domains I and II and DIS6 are involved in VDI of the channel. This is the region of the channel encoded by exons 8/8a of CACNA1C. This area is indicated in yellow. The point indicated in red shows the location affected by the classical TS mutations. A β subunit is also shown to indicate the interaction site between β and CaV1.2 subunits.

Evidence suggests that ɣ subunits are not involved in forming L-type channel complexes in the neuron (Catterall, 2011). The typical structure of an L-type calcium channel in a neuron is shown in Figure 2.

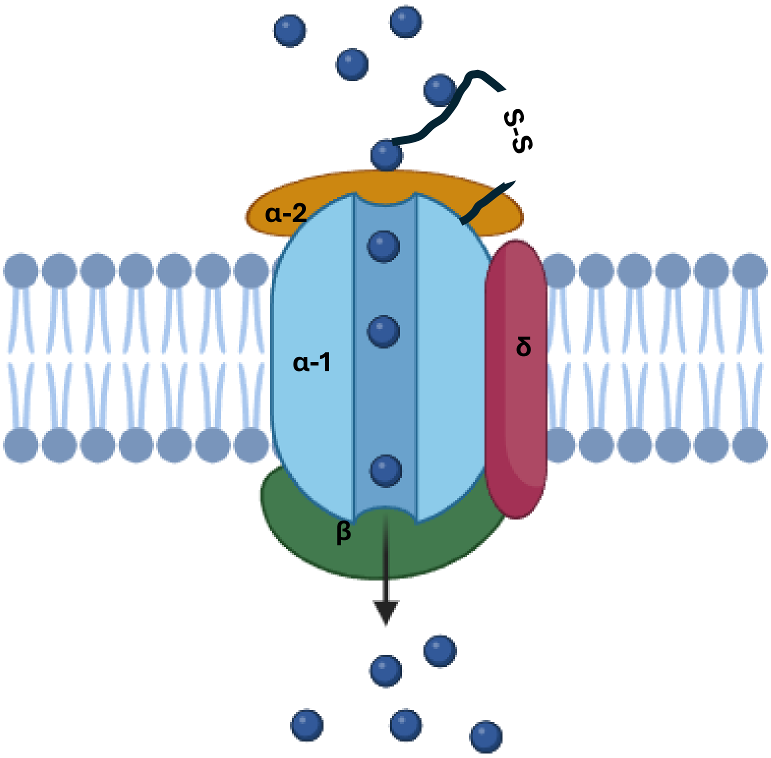

Figure 2 Showing the structure of a typical L-type calcium channel in the neuronal membrane. The α-1 subunit contains the voltage sensing and pore-forming structures of the channel. The auxiliary α-2 and δ subunits are bonded together by a disulfide bridge. These units interact with the α-1 subunit to change the channel's overall activation and inactivation properties. The α-2 subunit is extracellular but is associated with the membrane-bound δ subunit. The auxiliary β subunit is found intracellularly.

α-2 and δ subunits associate, and typically exist as a single α-2δ subunit complex due to intra-unit disulfide bonds (Dolphin, 2012). The interaction site between the α-2δ subunit complex and α-1 subunits is not yet clear. α-2δ subunits typically increase the maximum current density for α-1 subunits, like CaV1.2. α-2δ subunits increase the probability of L-type channel activation (Savalli *et al.*, 2016). α-2δ subunits can also increase the inactivation rate of α-1 subunits (Dolphin, 2012). Mutations in genes encoding α-2δ subunits have been found to be associated with various diseases including ASD, epilepsy, and Brugada syndrome, which typically involves a TS-like long QT interval (Dolphin, 2012).

β subunits are known to enhance the functional expression and alter the physical properties of CaV1.2. The β subunit interacts with the α-1 subunit through the α-1 interaction domain found between domains I and II of the α-1 subunit, which are encoded by exon 9 of *CACNA1C*. This interaction area is shown in Figure 1. Animal models with mutations in genes encoding β subunits have been found to have epilepsy and visual phenotypes (Dolphin, 2012).

Splice isoforms of the CACNA1C gene:

The *CACNA1C* gene has many splice isoforms. The CaV1.2 channel α-1 subunit produced from these isoforms can contain segments which are encoded by one of several alternatively spliced exons. There are 50 different exons of the human *CACNA1C* gene, and 49 of the mouse *CACNA1C* gene. 20 of these exons are known to undergo alternative splicing.

Alternative splicing sites encompass the N-terminus, the I-II linker region, the II-III linker region, IS5-S6. IVS2-S3 and the C-terminal domain. Alternatively spliced transcripts which lead to the expression of CaV1.2 channels containing short N-termini are found in the brain. The functional importance of this is not well understood. Alternative splicing between exons 31 and 33 which encode the IVS2-3 alters the activation potential of the resulting CaV1.2 channel. Alternative splicing between exons 41 and 42 which encode the C-terminal of the channel alters the inactivation kinetics, VDI and CDI of the channel (Hofmann *et al.*, 2014).

The two most common splice isoforms of *CACNA1C* in the brain contain exon 8. These isoforms are ENST00000399641 and *CACNA1C* n2199. ENST00000399641 and *CACNA1C* n2199 are expressed at similar levels in the cerebellum, while ENST00000399641 is by far the most highly expressed transcript throughout the rest of the brain (Clark *et al.*, 2019). There currently exists no information on which isoforms are found in specific cell-types or in specific subcellular locations.

Exons 8 and 8a of the CACNA1C gene:

Exons 8 and 8a are alternatively spliced in the CaV1.2 channel subunit. Exons 8 and 8a are very similar in terms of sequence and function. The exon 8 and 8a exons can each form the IS6 segment of the CaV1.2 channel subunit. Around 80% of CaV1.2 channel subunits in the heart and brain contain the IS6 segment encoded by exon 8, the remaining 20% contain the IS6 segment encoded by exon 8a. As 8a is expressed at a lower level in the heart and brain than exon 8, patients with TS1 tend to have less severe phenotypes as those with TS2 (Splawski *et al.*, 2004, 2005).

Changes in CaV1.2 channel structure and function resulting from the TS1 and TS2 mutations:

The TS1 and TS2 mutations occur in position G1216A of exon 8a and exon 8 of the *CACNA1C* gene, respectively (Splawski *et al.*, 2005). This results in the transcribed

Cav1.2 α-1 subunit having a glycine to arginine replacement at position 406 (G406R) of the respective exon of the channel. The G406R replacement occurs at the C-terminal end of IS6 of CaV1.2 channel α-1 subunit. This is the region of the ion channel which has been found to be involved in VDI (Cens *et al.*, 2006). The presence of glycine at position 406 of the CaV1.2 α-1 subunit is typically conserved between species, from humans through to the worm, indicating it's physiological importance in the function of the channel (Splawski *et al.*, 2004). The G406R substitution causes a change in the electrostatic properties of the channel as glycine is an unchanged amino acid and is replaced by arginine which has a positively charged guanidino group. The G406R replacement resulting from TS1 and TS2 mutations results in a CaV1.2 channel subunit that has a substantial reduction in VDI, with VDI occurring much slower in these TS mutant channels. Indeed, VDI in CaV1.2 has previously found to be almost completely abolished by the TS1 and TS2 mutations (Barrett and Tsien, 2008). The result of this reduced and almost absent VDI is that, on activation, when the cell in which the mutant channel is expressed is depolarised, the channel remains open for an extended period of time. When the cell containing the mutant channel becomes depolarised, the CaV1.2 channel activates, there is a prolonged depolarising current flowing through the mutant channel and an increase in calcium influx to the cell (Splawski *et al.*, 2004, 2005).

The TS G402S mutation causes a similar reduction and almost complete loss of VDI in the encoded CaV1.2 channel. The location of the mutation is also within the IS6 region of the α-1 subunit; the region involved in VDI. The G402S mutation in functionally very similar to the G406R mutations which cause TS1 and TS2 (Splawski *et al.*, 2005). As such, these 3 mutations are referred to as classical TS mutations here as they are functionally similar- all resulting in mutant channels which almost completely lack VDI.

Interestingly, classical TS mutations have also been found to impact CDI of the CaV1.2 channel subunit (Dick *et al.*, 2016). Classical TS mutations have all been found to reduce CDI of the CaV1.2 channel subunit. The effect of this change is to further prolong the depolarising current and calcium influx into cells containing the mutant channels on cell depolarisation.

For a more complete review of the changes in the CaV1.2 channel resulting from TS mutations, including those caused by TSA mutations not discussed in this thesis, please refer to Bauer, Timothy and Golden (2021).

Potential impacts of researching the neurophysiology of TS mutations in the CACNA1C gene:

A major deleterious and untreatable phenotype of TS at the present time is hypoglycaemia. Recent research has suggested that hypoglycaemia experienced by TS patients is at least partially a result of neurophysiological changes caused by TS mutations (Matsui *et al.*, 2023). Exploring the neurophysiological changes caused by TS mutations is clearly a useful endeavour for several reasons: a) This could help us to understand and identify potential therapies for the neurological symptoms of TS including hypoglycaemia; b) It will help us to identify and understand the neurological functions of the disease-relevant *CACNA1C* gene; c) It will help us to understand how changes in neurological function caused by TS mutations might result in ASD-type phenotypes, and thus, help us to better understand potential neuropathological mechanisms of ASD.

TS case files and review:

TS is a rare disease. Due to the deleterious effects of TS mutations, TS is typically not inherited, but is acquired as a de novo mutation. Typically, TS patients do not survive to reproductive age. As such, very few TS patients have been described to date. I have reviewed and completed a synthesis of genetic and symptomatic information provided in all case reports pertaining to individuals with classical TS mutations; TS1, TS2 and TSA caused by G402S mutation. A literature search of “Timothy Syndrome” on PubMed was used to find the published TS case files. This search was conducted on 09/03/2024. It is possible that there exist case reports of TS patients which were not identified by my search methods. Below is a table containing all information obtained from the reviewed patient case files.

Case reports of patients with classical TS:

Table 1 Case reports of patients with classical TS; Immunological indicates patients who have been reported to have episodes of either repeated or severe infections; Ophthalmic indicates that the patient has severe myopia, strabismus, abnormal eye movements, or blindness; GI symptoms indicates that the patient has been reported to have recurrent constipation, diarrhoea, or other digestive or gastro-intestinal issues, whether structural or functional; Exon= ? indicates patients where the exon in which the G406R mutation was present was not explicitly stated; OCD is Obsessive compulsive disorder

Reference	**Patient number (If relevant)**	**TS type**	**Mutation**	**Exon**	**Mosaic**	**Age on description**	**Sex**	**Alive/ deceased on description (A/D)**	**Cardiac**	**Immunological**	**Syndactyly**	**Facial dysmorphism**	**Any neuropsychiatric symptoms**	**Neurological injury**	**Other neurological**	**Developmental Delay**	**Intellectual disability**	**Language developmental delay**	**ASD**	**Other behavioural abnormalities, including attention deficit hyperactivity disorder (ADHD)**	**Epilepsy**	**Autism**	**Abnormal dentition**	**Baldness**	**Hypoglycaemia**	**Gastrointestinal (GI) symptoms**	**Hypotonia**	**Ophthalmic**	**Dysplasia and/or joint hypermobility**
(Corona-Rivera *et al.*, 2015)	NA	TS 1	G406R	8a	N	3 months	M	D	Y	Y	Y	NA	NA	NA	NA	NA	NA	NA	NA	NA	NA	NA	NA	NA	NA	Y	NA	NA	NA
(Dufendach *et al.*, 2013)	2 (mother)	TS 1	G406R	8a	Y	NA	F	A	N	NA	Y	NA	NA	NA	NA	NA	NA	NA	NA	NA	NA	NA	NA	NA	NA	NA	NA	NA	NA
(Dufendach et al., 2013)	1	TS 1	G406R	8a	N	1 year 5 months	M	A	Y	NA	Y	NA	NA	NA	NA	NA	NA	NA	NA	NA	NA	NA	NA	NA	NA	NA	NA	NA	NA
(Dufendach *et al.*, 2018)	3	TS 1	G406R	8a	NA	NA	NA	D	Y	Y	Y	Y	Y	NA	NA	Y	NA	NA	NA	NA	NA	NA	NA	NA	Y	NA	NA	NA	NA

(Dufendach et al., 2018)	4	TS1	G406R	8a	N	NA	NA	A	Y	N	Y	N	NA	NA	NA	NA	NA	NA	NA	NA	NA	NA	NA	N	Y	NA	NA	NA	NA
(Dufendach et al., 2018)	5	TS1	G406R	8a	N	NA	NA	D	Y	N	Y	N	Y	Y	NA	NA	NA	NA	NA	NA	NA	NA	NA	N	Y	NA	NA	NA	NA
(Dufendach et al., 2018)	6	TS1	G406R	8a	N	NA	NA	D	Y	Y	Y	Y	Y	Y	NA	Y	NA	NA	NA	NA	NA	NA	NA	Y	N	NA	NA	NA	NA
(Dufendach et al., 2018)	7	TS1	G406R	8a	N	NA	NA	A	Y	N	Y	Y	Y	NA	NA	Y	NA	NA	NA	NA	NA	NA	NA	Y	N	NA	NA	NA	NA
(Dufendach et al., 2018)	9	TS1	G406R	8a	N	NA	NA	A	Y	Y	Y	N	N	NA	NA	N	NA	NA	NA	NA	NA	NA	NA	Y	Y	NA	NA	NA	NA
(Dufendach et al., 2018)	10	TS1	G406R	8a	N	NA	NA	A	Y	Y	N	Y	Y	NA	NA	Y	NA	NA	NA	NA	NA	NA	NA	Y	Y	NA	NA	NA	NA
(Dufendach et al., 2018)	14	TS1	G406R	8a	Y	NA	NA	A	Y	N	Y	Y	Y	NA	NA	Y	NA	NA	NA	NA	NA	NA	NA	NA	Y	NA	NA	NA	NA
(Dufendach et al., 2018)	16	TS1	G406R	8a	N	NA	NA	D	Y	Y	Y	Y	Y	NA	NA	Y	NA	NA	NA	NA	Y	NA	NA	NA	Y	NA	NA	NA	NA
(Etheridge *et al.*, 2011)	1	TS1	G406R	8a	N	1 year	M	A	Y	NA	Y	Y	N	NA	N	N	N	N	NA	NA	N	NA	NA	NA	NA	NA	NA	NA	NA
(Etheridge et al., 2011)	2 (father)	TS1	G406R	8a	Y	NA	M	A	Y	NA	Y	N	N	NA	N	N	N	N	N	N	N	NA	NA	NA	NA	NA	NA	NA	NA
(Etheridge et al., 2011)	3 (index 2)	TS1	G406R	8a	N	14 years	F	A	Y	NA	Y	NA	Y	N	N	N	N	N	N	Y	N	N	NA	NA	NA	NA	N	NA	N

(Gao *et al.*, 2013)	2 (father)	TS1	G406R	8a	Y	NA	M	A	Y	NA	Y	NA	Y	NA	N	N	N	Y	NA	NA	NA	NA	NA	NA	NA	NA	NA	NA	NA
(Gao et al., 2013) also (Han *et al.*, 2020)	1	TS1	G406R	8a	N	2 years	F	A	Y	NA	Y	NA	Y	NA	N	N	N	Y	NA	NA	NA	NA	NA	NA	NA	NA	NA	NA	NA
(Krause *et al.*, 2011)	NA	TS1	G406R	8a	N	2 years	F	A	Y	NA	Y	Y	Y	NA	NA	Y	NA	Y	NA	NA	NA	NA	NA	Y	NA	NA	NA	NA	NA
(Sepp *et al.*, 2017)	NA	TS1	G406R	8a	Y	3 years	M	A	Y	N	N	N	Y	Y	N	N	N	N	N	N	Y	N	N	N	Y	NA	N	N	N
(Shu *et al.*, 2014)	NA	TS1	G406R	8a	N	5 years	F	A	Y	NA	Y	NA	NA	NA	NA	NA	NA	NA	NA	NA	NA	NA	NA	NA	NA	NA	NA	NA	NA
(Walsh *et al.*, 2018)	1	TS1	G406R	8a	N	1 year 7 months	F	A	Y	NA	Y	NA	Y	N	NA	NA	NA	NA	NA	NA	Y	NA	NA	NA	NA	NA	NA	NA	NA
(Walsh *et al.*, 2018)	2	TS1	G406R	8a	N	2 years	M	D	Y	NA	Y	NA	Y	N	NA	NA	NA	NA	NA	NA	Y	NA	NA	NA	NA	NA	NA	NA	NA
(Walsh *et al.*, 2018)	3	TS1	G406R	8a	N	24 years	F	A	Y	NA	Y	NA	Y	Y	Learning difficulties and weakness from neurological injury	NA	NA	NA	NA	NA	NA	NA	NA	NA	NA	NA	NA	NA	NA
(An *et al.*, 2013)	NA	TS1 or 2	G406R	?	N	16 years	M	A	Y	NA	Y	Y	Y	Y	NA	N	N	N	N	N	Y	N	Y	Y	Y	NA	NA	NA	NA
(Kallas *et al.*, 2018)	NA	TS1 or 2	G406R	?	N	2 days	F	A	Y	NA	N	Y	NA	NA	NA	NA	NA	NA	NA	NA	NA	NA	NA	NA	NA	NA	Y	NA	Y

(Kawaida *et al.*, 2016)	NA	TS 1 or 2	G 406R	?	N	45 days	F	D	Y	Y	Y	NA	NA	NA	NA	NA	NA	NA	NA	NA	NA	NA	Y	Y	Y	NA	NA	NA	NA
(Tunca Sahin and Ergul, 2018)	NA	TS 1 or 2	G 406R	?	N	4 years 6 months	F	A	Y	NA	Y	NA	Y	Y	NA	N	NA	NA	NA	NA	NA	NA	NA	NA	NA	NA	Y	NA	NA
(Zheng *et al.*, 2022)	1	TS 1 or 2	G 406R	?	N	1 year 2 months	M	NA	Y	NA	Y	NA	NA	NA	NA	NA	NA	NA	NA	NA	NA	NA	NA	NA	NA	NA	NA	NA	NA
(Zheng et al., 2022)	2	TS 1 or 2	G 406R	?	N	11 months	F	NA	Y	NA	Y	NA	NA	NA	NA	NA	NA	NA	NA	NA	NA	NA	NA	NA	NA	NA	NA	NA	NA
(Zheng et al., 2022)	3	TS 1 or 2	G 406R	?	N	8 years	M	NA	Y	NA	Y	NA	NA	NA	NA	NA	NA	NA	NA	NA	NA	NA	NA	NA	NA	NA	NA	NA	NA
(Zheng et al., 2022)	4	TS 1 or 2	G 406R	?	N	NA	M	NA	Y	NA	Y	NA	NA	NA	NA	NA	NA	NA	NA	NA	NA	NA	NA	NA	NA	NA	NA	NA	NA
(Zheng et al., 2022)	5	TS 1 or 2	G 406R	?	N	NA	F	NA	Y	NA	Y	NA	NA	NA	NA	NA	NA	NA	NA	NA	NA	NA	NA	NA	NA	NA	NA	NA	NA
(Zheng et al., 2022)	7	TS 1 or 2	G 406R	?	N	NA	M	NA	Y	NA	Y	NA	NA	NA	NA	NA	NA	NA	NA	NA	NA	NA	NA	NA	NA	NA	NA	NA	NA
(Diep and Seaver, 2015)	NA	TS 2	G 406R	8	N	3 years 6	F	A	Y	N	N	Y	Y	Y	NA	Y	NA	Y	NA	NA	Y	NA	NA	Y	Y	Y	Y	Y	NA

						months																							
(Philipp and Rodriguez, 2016)	NA	TS2	G406R	8	N	52 days	F	D	Y	NA	N	N	Y	Y	NA	NA	NA	NA	NA	NA	NA	NA	NA	NA	Y	NA	NA	NA	NA
(Splawski et al., 2005)	1	TS2	G406R	8	N	6 years	F	D	Y	NA	N	Y	Y	N	NA	Y	Y	Y	NA	NA	Y	NA	Y	NA	NA	NA	Y	NA	Y
(Walsh *et al.*, 2018)	5	TS2	G406R	8	Y	7 years	M	A	Y	NA	N	Y	Y	NA	NA	Y	Y	Y	NA	NA	NA	NA	NA	NA	NA	NA	NA	Y	NA
(Walsh *et al.*, 2018)	6	TS2	G406R	8	N	7 years	M	A	Y	Y	N	Y	Y	NA	NA	Y	Y	Y	NA	NA	NA	NA	NA	NA	NA	NA	NA	Y	Y
(Ergül *et al.*, 2015)	NA	TS2	G406R	8	N	2 years 6 months	F	A	Y	NA	Y	Y	Y	NA	NA	Y	NA	NA	NA	NA	NA	NA	NA	NA	NA	NA	NA	NA	NA
(Fröhler *et al.*, 2014)	1	TSA	G402S	NA	N	6 years	M	A	Y	N	Y	N	N	N	N	N	N	N	NA	NA	N	NA	NA	NA	NA	NA	NA	NA	NA
(Fröhler et al., 2014)	2	TSA	G402S	NA	N	8 years	F	A	Y	N	Y	N	Y	Y	NA	Y	Y	Y	NA	NA	Y	NA	NA	NA	NA	NA	NA	NA	NA
(Fröhler et al., 2014)	3 (father)	TSA	G402S	NA	Y	NA	M	A	N	N	Y	N	NA	NA	NA	NA	NA	NA	NA	NA	NA	NA	NA	NA	NA	NA	NA	NA	NA
(Delinière *et al.*, 2023)	1	TSA	G402S	NA	N	NA	NA	NA	Y	Y	N	N	Y	NA	NA	NA	NA	NA	Y	NA	NA	Y	N	N	N	N	NA	NA	NA
(Dufendach et al., 2018)	2	TSA	G402S	NA	N	NA	NA	A	Y	Y	Y	N	NA	NA	NA	NA	NA	NA	NA	NA	NA	NA	NA	N	N	NA	NA	NA	NA

(Delinière et al., 2023)	2	TSA	G402S	NA	N	NA	NA	NA	Y	N	N	Y	Y	NA	NA	Y	NA	NA	N	NA	NA	N	Y	N	N	N	NA	NA	NA
(Delinière et al., 2023)	3	TSA	G402S	NA	N	NA	NA	NA	Y	N	N	N	NA	NA	NA	NA	NA	NA	N	NA	NA	N	N	N	N	N	NA	NA	NA
(Delinière et al., 2023)	4	TSA	G402S	NA	N	NA	NA	NA	Y	Y	Y	N	Y	NA	NA	Y	NA	Y	N	NA	NA	N	N	N	N	N	NA	NA	NA
(Dufendach et al., 2018)	12	TSA	G402S	NA	N	NA	NA	A	Y	N	Y	N	Y	NA	NA	Y	NA	NA	NA	NA	NA	NA	NA	N	N	NA	NA	NA	NA
(Hermida *et al.*, 2021)	NA	TSA	G402S	NA	N	12 years	M	A	Y	NA	N	N	Y	N	N	Y	NA	NA	NA	NA	NA	NA	Y	NA	NA	NA	NA	NA	NA
(Hermida *et al.*, 2022)	NA	TSA	G402S	NA	N	14 years	M	A	Y	NA	NA	NA	NA	NA	NA	NA	NA	NA	NA	NA	NA	NA	NA	NA	NA	NA	NA	NA	NA
(Hiippala *et al.*, 2015)	NA	TSA	G402S	NA	N	13 years	F	A	Y	N	N	N	N	N	N	N	N	N	N	N	N	N	N	N	N	N	N	N	N
(Jacobs *et al.*, 2006)	NA	TSA	G402S	NA	N	21 years	M	A	Y	NA	N	Y	Y	Y	NA	Y	Y	Y	NA	Y (psychotic episodes and night terrors)	N	NA	NA	NA	NA	NA	NA	NA	NA
(Shah *et al.*, 2012)	NA	TSA	G402S	NA	N	26 years	M	A	Y	NA	N	NA	Y	NA	Y (unspecified)	NA	NA	NA	NA	NA	NA	NA	NA	NA	NA	NA	NA	NA	NA
(Splawski et al., 2005)	2	TSA	G402S	8	Y	11 years	M	A	Y	NA	N	N	Y	Y	Brain damage from heart attack induced coma	N	N	N	NA	Y (Signs of depression and OCD)	N	N	NA	NA	NA	NA	NA	NA	NA
(Zheng et al., 2022)	6	TSA	G402S	NA	N	NA	M	NA	Y	NA	Y	NA	NA	NA	NA	NA	NA	NA	NA	NA	NA	NA	NA	NA	NA	NA	NA	NA	NA
(Gershon *et al.*, 2014)	NA	TSA	G402S	NA	Y	28 years	M	A	Y	NA	NA	NA	Y	Y	Anoxic brain injury following cardiac arrest	NA	Y	NA	NA	Y (bipolar disorder, psychosis)	N	NA	NA	NA	NA	NA	N	N	NA

Review of classical TS patient case reports:

5/6 TS2 patients reported in the literature were explicitly stated to have some neurological abnormality. The 6th patient was aged just 52 days at time of death, and, as such, neurological abnormalities could not be tested for. All 5 of the patients who survived past early infancy had neurodevelopmental delay, 3 were reported to have intellectual disability, 4 were reported to have language delay, and 2 were reported to experience seizures. 4 were reported to have either hypotonia or joint laxity, and 3 of the 5 were reported to have ophthalmic issues. As the sixth patient could not be studied for neurological abnormality before death, it can be assumed that all TS2 patients have neurological abnormality.

Of the TS1 patients reported in the literature, 15/18 (83%) patients for which neuropsychiatric status was detailed were reported to have some form of neuropsychiatric abnormality. 5 TS1 patients were detailed in case reports not specifying neuropsychiatric status. 5/23 patients were reported to have seizures. 6/23 patients were reported to have generalised neurodevelopmental delay, 3/23 were reported to have a delay in language development. None of the TS1 patients were reported to have ASD or autism-type symptoms. However, results from ASD and/or presence of ASD/autism symptoms were only mentioned in the case reports of 3/23 of the TS1 patients.

It should be noted that 80% of the TS1 patients described in the initial characterisation of TS who were able to be assessed for ASD met the diagnostic criteria for ASD (Splawski *et al.*, 2004). These patients were not included in this review of patient case files as symptoms were not reported per individual patient. For a full idea of symptoms experienced by TS1 patients, it is advised that the information provided in the table above be considered alongside the information provided in Splawski *et al.* (2004).

10 case reports detailed patients with G406R mutations on an unspecified exon. Only 2 of these reports detailed the patient's neuropsychiatric symptoms, both showed that the patients had neuropsychiatric phenotypes.

17 case reports detailed patients with G402S mutations. These patients are categorized as having TSA but also as having a classical TS mutation. 10/17 of these patients were reported to have some neuropsychiatric abnormality. Neuropsychiatric status was detailed in only 12 of the reports, with 83% of those patients having a neuropsychiatric abnormality. 6/17 patients were reported to have neurodevelopmental delay. 3/17 were reported to have language delay. ASD was reported in 1/5 patients who were explicitly stated to have been ASD-tested. 2/5 of the patients for which ictal history was reported were stated to have a history of seizure. Interestingly, psychiatric symptoms were reported in 3/17 patients, 2 patients presented with psychosis, 1 with night terrors, 1 with bipolar disorder, and 1 presented with depression and obsessive-compulsive symptoms.

Unfortunately, some of the case reports used in this review detailed only the patient symptoms which were relevant to the physician's area of expertise. For example, cardiac symptoms and the presence/absence of syndactyly were the only two TS-related phenotypes reported for patients described in the case series written by Zheng *et al.* (2022). The authors of this reported case series were either plastic surgeons or cardiologists. Critical information regarding the neuropsychiatric and other extra-cardiac symptoms experienced by these patients cannot be obtained from these reports. As such, a large multi-centre study which could provide a general description of patient symptoms across all body systems affected by TS would be useful in providing a more comprehensive review of the symptoms and genetic mutations in documented TS patients. From this, we may be able to obtain more information as to which specific mutations are associated with specific functional changes in the *CACNA1C* gene.

Notes on interesting case reports of TSA and 12p13.33 patients:

Case reports from patients with non G402S TSA mutations are not reported here. A large proportion of these mutations have unknown functional impacts on the *CACNA1C* gene and the transcribed CaV1.2 channel α-1 subunit. However, it should be noted that many TSA patients are reported to have neuropsychiatric symptoms, including epilepsy, language deficits, ASD and neurodevelopmental delay (Gillis *et al.*, 2012; Gershon *et al.*, 2014; Hennessey *et al.*, 2014; Bozarth *et al.*, 2018; Kosaki *et al.*, 2018; Ozawa *et al.*, 2018, 2022; Po' *et al.*, 2019; Rodan *et al.*, 2021; Wang *et al.*, 2024). Interestingly, some TSA patients have been reported to have predominantly, or even exclusively, neuropsychiatric symptoms (Rodan *et al.*, 2021).

Interestingly, a patient who was found to have a microdeletion which disrupts the *CACNA1C* gene has been reported to have phenotypes like those seen in TS patients. The patient presented with language impairment, neurodevelopmental delay, hypotonia and joint laxity. The patient had facial dysmorphisms and behavioural abnormalities related to ADHD (Mio *et al.*, 2020). Patients with 12p.13.33 copy number variants (CNVs) have been found to have similar phenotypes (Thevenon *et al.*, 2013; Costain *et al.*, 2016). The 12p.13.33 chromosomal location includes the start of the *CACNA1C* gene. It is possible CNVs in this area may lead to TS-type neurological symptoms due to disruption of the *CACNA1C* gene and impact on CaV1.2 channel function in the brain. Understanding how changes in the *CACNA1C* gene impact neurological function could therefore enable us to better understand the neurological changes resulting from 12p.13.33 CNVs.

Current understanding of non-neuronal pathophysiological mechanisms of TS:

Cardiac phenotypes:

Currents flowing through L-type calcium channels such as those involving the CaV1.2 subunit underpin the action potential (AP) in the cardiac myocyte, and control the contraction and pacemaker function of these cells (Striessnig *et al.*, 2014). The presence of classical TS mutant CaV1.2 subunits in the cardiac myocyte causes a prolonged influx of positively charged calcium ions into the cell when the channel becomes activated, when the cell becomes depolarised. This directly causes a prolonged AP in these cells (Splawski *et al.*, 2004, 2005; Drum *et al.*, 2014; Dick *et al.*, 2016). The prolonged cardiac AP seen in TS is thought to disrupt the normal rhythmic contractions of the heart, directly leading to long QT which can then cause cardiac arrest (Splawski *et al.*, 2004, 2005). Non-G402S TSA mutations can cause a prolonged cardiac AP by other mechanisms, such as by reducing the threshold at which CaV1.2 channels activate (Bauer, Timothy and Golden, 2021).

Structural phenotypes:

Structural phenotypes of TS include syndactyly, abnormal dentition, joint laxity, and facial dysmorphisms. The facial dysmorphisms reported in children with TS often include an overbite, where the mandible (lower jaw) extends anterior the maxilla (upper jaw; Splawski *et al.*, 2004). Expression of a TS1-type *CACNA1C* rabbit homolog in the developing mouse results in the mandible reaching or surpassing the maxilla anteriorly as compared to mice expressing the wild-type (WT) homolog (Ramachandran *et al.*, 2013). In other words, classical TS mutations have been found to cause an overbite in both mice and in humans. This suggests that the TS1 *CACNA1C* gene enhances mandible development similarly in both the mouse and the human.

Ramachandran *et al.* (2013) sought to investigate the role of CaV1.2 in mandible development by manipulation of the *CACNA1C* homolog in zebrafish. Knockdown of the zebrafish *CACAN1C* homolog resulted in a reduction in mandible size, confirming the role of the *CACNA1C* gene in zebrafish mandible development. Injection of copy ribonucleic acid which encoded either the WT or the TS1 type rabbit *CACNA1C* homolog into these knock-down *CACNA1C* zebrafish rescued mandible size in each case. There was no difference in mandible size between fish expressing the WT or TS1 mutant *CACNA1C* rabbit homologous gene. However, the authors did find that expression of the TS1 mutant *CACNA1C* rabbit gene in zebrafish did increase chondrocyte size and number within the developing mandible as compared to knock-in of the WT rabbit homologous gene. This suggests that the CaV1.2 channel regulates mandible development through controlling chondrocyte development. Finally, the authors investigated the role of the CaV1.2 channel in the migration of cranial neural crest cells which form the facial structures during development. They found no evidence that the CaV1.2 channel had any involvement in neural crest cell migration.

Baldness:

Yucel *et al.* (2013) conducted a study where a TS1 mutant *CACNA1C* gene was conditionally expressed in stem cells which generate hair in the mouse. They found that expression of the TS1 mutant channel in the mouse disrupted the normal hair cycle of the mouse without affecting epidermal differentiation. The mutant channel inhibited hair production. Expression of the TS1 mutant channel caused the stem cells to remain quiescent and not produce hair. This led to baldness in the mouse. The authors found that expression of the TS1 mutant channel in these stem cells had the same effect on hair development as a heterozygous loss-of-function *CACNA1C* mutation. This suggests that the TS1 mutation causes a loss-of-function change in CaV1.2’s role in hair development and growth. This loss-of-function can be rescued by use of calcium channel blockers. Expression of the TS1 mutant channel did not appear to alter calcium currents in the stem cells.

The study indicated that the TS1 mutation causes a loss-of-function change in the CaV1.2 channel function within stem cells which control hair development. The change in function appears to be independent of the prolonged calcium currents flowing through the mutant CaV1.2 channels. This suggests that the CaV1.2 channel has some conductance-independent role within specific stem cells which regulate hair development, and that function is disrupted by classical TS mutations.

Non-neuronal mechanisms underpinning hypoglycaemia:

A large proportion of TS patients experience life-threatening hypoglycaemic episodes (Dufendach *et al.*, 2018). The pathological mechanisms by which TS mutations result in hypoglycaemia are not completely understood. A modelling study by Kummer *et al.* (2022) suggested that mutations in the *CACNA1C* gene can impact insulin secretion from pancreatic β cells. Inclusion of a TS-type channel in a pancreatic β cell computational model resulted in abnormal β cell membrane oscillations. Pancreatic β cell membrane oscillations are essential for insulin secretion. The research described by Kummer *et al.* (2022) predicted that expression of TS mutant CaV1.2 channels in pancreatic β cells could increase secretion from those cells. This would cause hyperinsulinemia, which typically results in hypoglycaemia. The authors suggested that the abnormal function of the channel in pancreatic β cells might lead to hyperinsulinemia, which results in the life-threatening hypoglycaemia seen in TS patients.

However, a recent study by Matsui *et al.* (2023) provided evidence that TS-related hypoglycaemia does not involve hyperinsulinemia. The authors found that a mouse model of TS2 had lower blood glucose levels as compared to WT mice, indicating that the mutation causes hypoglycaemia in the mouse as well as the human. However, the hypoglycaemia was not found to result from hyperinsulinemia. The authors found a **reduced** secretion of insulin, or **hypoinsulinemia**, in the TS2 mice as compared to WT. TS2 mice were noted to have glycosuria (glucose in the urine) which is typically seen to result from renal dysfunction. Glycosuria could potentially contribute to the hypoglycaemia in the TS2 mouse. The way in which the TS2 mutation could result in glycosuria is unknown and was not explored in the study. The researchers believed that glycosuria alone would not cause the hypoglycaemia seen in the mouse. The researchers found that glucagon secretion from pancreatic α cells and α cell size were also reduced in the TS2 mouse as compared to WT. This suggests that deficiencies in pancreatic α cells may result from the TS2 mutation. This is a further mechanism by which the TS2 mutation could cause the hypoglycaemia seen in the TS2 mouse. Interestingly, researchers also identified neuronal changes in the TS2 mouse which could cause hypoglycaemia. The changes are discussed in detail in the subsection "Neuronal mechanisms of hypoglycaemia".

Current understanding of the neurophysiology of TS:

Neuronal mechanisms of hypoglycaemia in TS:

Matsui *et al.* (2023) suspected that the TS2 mutation-related hypoglycaemia may be caused by neurological changes resulting from the TS2 mutation. Matsui *et al.* (2023) investigated whether the ability of the nervous system to sense glucose levels (glucose sensing) was disrupted by the TS2 mutation in the TS2 mouse. Abnormalities in glucose sensing can cause hypoglycaemia. Pro-opiomelanocortin expressing (POMC+) neurons within the arcuate nucleus of the hypothalamus are involved in glucose sensing which is critical to the control of blood glucose levels (Parton *et al.*, 2007). Matsui *et al.* (2023) found that expression of the TS2 mutant CaV1.2 channel subunit in POMC+ cells **alone** resulted in hypoglycaemia in the mouse. The authors proposed that expression of the TS2 mutant channel in POMC+ neurons of the hypothalamus disrupts glucose sensing in the brain which then leads to hypoglycaemia in the TS2 mouse. The expression of the TS2 allele in POMC+ cells of the hypothalamus was found to be sufficient to cause hypoglycaemia in the TS2 mouse. The mechanism by which the TS2 mutation impacts POMC+ cell function was not addressed in the study. This provides evidence that neurological changes resulting from the TS2 mutation can lead to hypoglycaemia.

Impacts of TS mutations on gene transcription in the neuron:

Transcriptional changes have been found in induced pluripotent stem cell derived neurons (iPSC-derived neurons) generated from a TS patient as compared to those generated from control subjects (Tian *et al.*, 2014). The transcriptional changes identified were predicted to be controlled by calcium-dependent transcription regulators. Interestingly, some of the gene modules which were seen to be dysregulated in the TS cell line are also known to be associated with ASD. This provides evidence that TS mutations impact transcription within the neuron in a potentially ASD-relevant way (Tian *et al.*, 2014). At least some of the transcriptional changes appear to result from abnormal calcium signalling through the mutant CaV1.2 channel subunit (Tian *et al.*, 2014).

Two potential mechanisms by which TS mutations could impact gene transcription have since been identified by a study which involved measuring the levels of transcripts in human embryonic kidney cells expressing G406R TS mutant CaV1.2 channels as compared to those expressing WT CaV1.2 channels (Servili *et al.*, 2020). TS mutant cells were found to have an increased depolarisation-evoked activation of the immediate early genes *Methyl CpG Binding Protein 2* gene (*MeCP2*) and *c-Fos* as compared to control. This effect involved the Ras/ERK/CREB signalling pathway. The increase in activity-related transcription was dependent on calcium influx through the TS1 mutant CaV1.2 channel subunit. A second mechanism by which the TS1 mutation was found to impact transcription in this model system was by an increase in basal transcription levels. This effect was calcium influx independent and required expression of an L-type calcium channel β auxiliary subunit. The auxiliary β subunit is known to be involved in gene transcription (Buraei and Yang, 2010). The presence of TS-type CaV1.2 channel subunits within human embryonic kidney cells was found to impact both basal and activity-related gene transcription. It should be noted that these results were not found within the neuron, but were believed by the authors to be neuronally relevant (Servili *et al.*, 2020).

TS has been found to alter the transcription of developmentally important genes, *special AT-rich sequence-binding protein 2* (*SATB2*) and *CtBP-interacting protein* (*CTIP2*; Panagiotakos *et al.*, 2019). These genes have important functions in the development of projection neurons which form important structures within the brain. This is discussed in more detail in subsection "Impacts of TS mutations on the development and migration of projection neurons".

A further study has found that the typical 5:1 exon8:8a expression ratio for the CaV1.2 channel is reduced in neural progenitor cell lines generated from stem cells of TS1 patients as compared to control lines (Panagiotakos *et al.*, 2019). This indicates that the TS1 G406R mutation in exon 8a of the *CACNA1C* gene may increase the level of expression of channel isoforms containing the mutant exon 8a as compared to the typical level of expression of the isoform containing the non-mutant 8a exon, and decrease the expression of channel isoforms containing exon 8. The mechanism by which this happens is not currently understood.

To summarise, classical TS mutations have been found to alter neuronal gene transcription in a potentially ASD-relevant way. Excitation-related transcription appears to be impacted by abnormalities in calcium influx into the cell through TS-mutant CaV1.2 channel subunits. Basal transcriptional changes have been found to result from a change in the ability of TS-mutant CaV1.2 α-1 subunits to activate the transcription-related β subunit of the L-type channel. The TS1-type mutation in the *CACNA1C* gene has been found to disrupt alternative splicing, such that CaV1.2 channels containing mutant exon are detected at a higher level than is usually expected.

Impacts of TS mutations on general neuronal development and structure:

TS mutations have been shown to alter the development and migration of several types of neuron (Krey *et al.*, 2013; Birey *et al.*, 2017, 2022; Panagiotakos *et al.*, 2019; Horigane *et al.*, 2020). TS mutations have also been found to impact single neuron structure (Krey *et al.*, 2013; Buddell *et al.*, 2019). Further evidence suggests that TS mutations can disrupt the composition of, as well as electrical and chemical signalling within, specific neuronal structures (Ehlinger and Commons, 2017; Rendall *et al.*, 2017; Birey *et al.*, 2022).

Impacts of TS mutations on inhibitory interneuron development and migration:

Neuronal culture experiments have used the study of forebrain spheroids generated from iPSC-derived neurons of TS1 and control subjects to explore the impacts of the mutation on neuronal migration and development. Forebrain spheroids are three-dimensional, laminated, cerebral-cortex-like structures which are formed from pluripotent stem cells. Spheroids specifically contain neurons from both deep and superficial cortical layers which are surrounded by astrocytes. Neurons in forebrain spheroids have transcriptional profiles which correctly map in-vivo foetal development

(Pasca *et al.*, 2015). Neurons migrate throughout the spheroids with a saltatory type movement, similar to natural neuronal migration throughout the developing brain in-vivo (Birey *et al.*, 2017). Immature inhibitory neurons in spheroids derived from TS1 iPSCs demonstrated abnormal migration as compared to those in control spheroids. Specifically, TS1 patient iPSC-derived neurons were found to migrate using more numerous, but shorter saltatory steps than did control subject iPSC-derived neurons (Birey *et al.*, 2017, 2022). The TS1 spheroids also had higher levels of synchronous activity than the control spheroids (Birey *et al.*, 2022). This suggests that the classical TS1 mutation disrupts interneuron migration and function within neural circuits of the brain, resulting in abnormal neural circuit synchronous activity. Interneuron migration has also been found to be disrupted in the cortex of a mouse model of TS (Horigane *et al.*, 2020). The study found that more immature interneurons reached the neocortex in the TS mouse model as compared to in WT mice. Interestingly, L-type calcium channels, such as CaV1.2 are known to be involved in the development of PV+ interneurons (Jiang and Swann, 2005). It is likely that TS mutations impact the development and migration of PV+ interneurons specifically, although this has not been directly explored previously. The literature to date suggests that classical TS mutations impact the development and migration of inhibitory interneurons, which then disrupts synchronous neural network activity within the brain.

Impacts of TS mutations on single neuron migration and structure:

TS mutations have been found to impact the development and structure of both dendrites and axons of the single neuron (Krey *et al.*, 2013; Kamijo *et al.*, 2018; Buddell *et al.*, 2019). The growth of neurites during development has been demonstrated to involve CaV1.2 function (Kamijo *et al.*, 2018). A study by Kamijo *et al.* (2018) demonstrated that classical TS mutations impact radial migration of cortical neurons, impairing the radial migration of layer 2/3 (L2/3) excitatory neurons in the brain. Studies involving the culture of iPSC-derived neurons, and culture of rat neurons with-and-without the TS1 mutation have demonstrated that the TS1 mutation increases the rate of activity-dependent dendrite retraction in the neuron. This dendritic retraction was found to be independent of the increased influx of calcium through TS-mutant CaV1.2 channel subunits (Krey *et al.*, 2013). An abnormally low number of dendritic branches were found on L2/3 cortical neurons in brains of TS model mice as compared to WT (Krey *et al.*, 2013). Basal dendrites play a key role in neural circuit formation and function (Spruston, 2008). The TS mutation has therefore been demonstrated to alter single cell migration and structure in a functionally relevant way. A further study of a classical TS-type mutation in the nematode worm has demonstrated that classical TS mutations can impact axonal development, negatively regulating axon termination (Buddell *et al.*, 2019). The current evidence suggests that TS mutations alter neurite projection and formation which then causes abnormal single-neuron structure in the adult brain. These changes may be functionally relevant to the aetiology of TS.

Impacts of TS mutations on the development and migration of projection neurons:

A study by Panagiotakos *et al.* (2019) found evidence that the TS1 mutation alters the expression of two developmentally important genes during the development of neural progenitor cells in culture. The mutation was found to increase expression of the *special AT-rich sequence-binding protein 2* (*SATB2*) gene but decrease the expression of the *CtBP-interacting protein* (*CTIP2*) gene in the neural progenitor cell. Similar findings were reported from the study of gene expression in iPSC-derived neurons from TS1 patients and control subjects, and from the study of gene expression in developing neurons within a mouse model of classical TS (Paşca *et al.*, 2011). Expression of the *SATB2* gene is required for the proper establishment of connections within the corpus callosum. Expression of the *CTIP2* gene is required for the specification of sub-cerebral projection neurons. Interestingly the authors found a reduced number of callosal projection neurons, and an increase in the number of sub-cerebral projection neurons in a TS mouse model as compared to WT (Panagiotakos *et al.*, 2019). This suggests that TS mutations can disrupt the development and migration of projection neurons within the brain. The mechanism by which TS mutations cause abnormal projection neuron migration appears to involve mutation-related changes in transcription within developing projection neurons of the brain.

Impacts of TS mutations on neuronal structures and on signalling pathways in the brain:

Mice with a TS2-type genetic mutation have been found to have abnormally small medial geniculate nuclei (MGN; Rendall *et al.*, 2017). This provides evidence that TS mutations can impact functional multi-cellular neuronal structures within the brain.

Ehlinger and Commons (2017) found evidence of abnormal serotonin content and turnover in several areas of a TS model mouse brain. Specifically, they found that the TS mouse model had a higher serotonin tissue content and axonal innervation in the dorsal striatum, and decreased serotonin turnover in the amygdala as compared to WT. Abnormalities in serotonergic signalling have previously been proposed to be involved in the aetiology of ASD (Muller, Anacker and Veenstra-VanderWeele, 2016). The changes in serotonin content found across the TS mouse brain may be related to ASD-relevant disruptions in neurological function in these mice. Paşca *et al.* (2011) found evidence that tyrosine hydroxylase was upregulated in iPSC-derived neurons from TS patients as compared to those from control subjects. Tyrosine hydroxylase is involved in the synthesis of catecholamine neurotransmitters: dopamine, norepinephrine, and epinephrine. They similarly found that iPSC-derived neurons from TS patients secreted more norepinephrine and more dopamine than did those from control subjects. TS mutations have therefore been evidenced to impact neuronal structure composition as well as catecholamine and serotonergic signalling within the brain.

Impacts of TS mutations on neuronal electrophysiology:

Interestingly, the classical TS1 mutation has been found to cause prolonged AP in iPSC-derived neurons in culture, similar to the effect of the mutation in the cardiac myocyte (Paşca *et al.*, 2011). Paşca *et al.* (2011) found that iPSC-derived neurons from TS1 patients had a prolonged increase in intracellular calcium concentration following cell depolarisation as compared to those from control subjects. This suggested that the mutant CaV1.2 channel, with much-reduced VDI was expressed within these neurons and contributed substantially toward the depolarisation-related calcium current in these cells. Interestingly, and unexpectedly, the AP widths of TS1 neurons were significantly wider than those measured from controls. The AP width was around 37% wider for TS neurons as compared to controls. Not addressed in this study was how the TS1 mutation prolonged the AP width within these cells. The neuronal AP waveform and width are not thought to be significantly impacted by depolarising currents flowing through L-type calcium channels, such as those flowing through the CaV1.2 channel α-1 subunit which is mutated in TS (Bean, 2007). However, findings described by Storm (1987) evidence that blocking calcium channel can impact the neuronal AP duration. The mechanism by which classical TS mutations, such as the TS1 mutation, could impact the AP duration in the neuron is therefore unclear. No study in the literature to date has explored whether classical TS mutations increase the neuronal AP width within mature and naturally developed neurons within functional brain tissue. A possibility is that the finding of Paşca *et al.* (2011) that the TS1 mutation prolongs the neuronal AP may be restricted to iPSC-derived neurons generated in culture. iPSC-derived neurons could potentially be physiologically dissimilar to naturally formed neurons in the brain in an unknown way.

Overall:

TS mutations impact neuronal structure and function at many levels. TS patients are known to have various neuropsychiatric phenotypes including ASD, epilepsy and neurodevelopmental delay. The neuronal expression of classical TS mutant CaV1.2 channel subunits is proposed to cause mechanistic changes which result in the neuropsychiatric symptoms seen in TS patients (Bader *et al.*, 2011; Krey *et al.*, 2013; Ehlinger and Commons, 2017). It has recently been found that expression of the TS2 *CACNA1C* allele in specific neurons of the hypothalamus is sufficient to cause disruption in blood glucose levels, which could result in the life-threatening hypoglycaemia seen in TS patients. Changes in neuronal function caused by TS mutations may therefore result in the neuropsychiatric abnormalities and life-threatening hypoglycaemia seen in TS patients.

Current evidence suggests that TS mutations impact the physiology of single neurons, functional neural circuits, and neuronal structures. TS mutations have been found to impact transcription in, and the development of, single neurons. TS mutations have further been evidenced to cause abnormalities in single neuron structure and electrophysiological properties. Inter-neuronal signalling and neural structures have also been found to be impacted by TS mutations. Of specific interest, classical TS mutations have been found to prolong the AP of iPSC-derived neurons by an unknown mechanism. Classical TS mutations have also been found to impact the development and migration of inhibitory interneurons in a way which may disrupt synchronous neural activity in the brain.

TS2Neo mouse model:

Development and genetics of the TS2Neo mouse model:

The TS2Neo mouse model was originally developed as a mouse model of ASD as many TS patients present with ASD (Bader *et al.*, 2011). On model characterisation, TS2Neo mice were reported as having ASD-type phenotypes such as altered social behaviour, vocalisations, repetitive and self-injurious behaviours (Bader *et al.*, 2011; Bett *et al.*, 2012). As such, it has been suggested that the TS2Neo mouse be used to study TS2-related neurophysiological changes which could lead to the ASD-type phenotypes which were described in the mouse (Bader *et al.*, 2011; Bett *et al.*, 2012).

The TS2Neo mouse model of TS is heterozygous for a mutant *CACNA1C* allele which has been genetically modified to contain the TS2-type G406R mutation in exon 8 of the *CACNA1C* gene as well as an inverted neomycin cassette. When the Rasmusson group developed the mouse model, mice heterozygous for the TS2 mutation without the neomycin cassette were found not to be viable (Bader *et al.*, 2011). The neomycin cassette is believed to reduce the expression of the deleterious TS2 mutant channel to a level at which the mouse survives (Bader *et al.*, 2011; Bett *et al.*, 2012). Indeed, TS2Neo mouse adrenal chromaffin cells are found to have an increase in the proportion of alternatively spliced CaV1.2 channels containing the non-mutant exon 8a with respect to exon 8, as compared with that ratio in WT mouse chromaffin cells (Calorio *et al.*, 2019). Adrenal chromaffin cells have an exon 8:8a expression ratio of around 5:1, similar to the ratio found in brain and heart cells. TS2Neo mice were found to have an exon 8:8a ratio within chromaffin cells of around 1:1 (Calorio *et al.*, 2019). Therefore, it is assumed that the TS2Neo mouse expresses a low level of the TS2 mutant channel containing the G406R mutation in cells around the body as a result of the neomycin cassette included in the genetic insert.

Alternative mouse models of TS:

In 2019, when I began my PhD, the only mouse models of TS which had been described in the literature were the TS2Neo mouse (Bader *et al.*, 2011; Bett *et al.*, 2012; Cheli *et al.*, 2016a; Ehlinger and Commons, 2017; Rendall *et al.*, 2017; Kamijo *et al.*, 2018; Calorio *et al.*, 2019), and mice which conditionally expressed a TS mutation within specific cell types (Paşca *et al.*, 2011; Ramachandran *et al.*, 2013; Yucel *et al.*, 2013; Drum *et al.*, 2014; Kamijo *et al.*, 2018; Panagiotakos *et al.*, 2019). The most studied and only readily available mouse model of TS was the TS2Neo mouse (available for purchase from Jax labs). As such, I used the TS2Neo mouse model to explore the effects of the TS2-type mutation on the neurophysiology of the mouse.

An alternative mouse model of TS has since been produced. This is known as the TS2 mouse model. The TS2 mouse model is heterozygous for a variant of the *CACNA1C* gene which is mutated exactly as is causative of TS2 in humans, and does not include the additional neomycin cassette found in the TS2Neo mouse. The TS2 mouse model was generated using newly available clustered regularly interspaced palindromic repeats technology. The generation of the TS2 mouse model, and exploration of hypoglycaemic symptoms and disease mechanisms in the mouse model are described by Matsui *et al.* (2023).

Key findings from research involving the TS2Neo mouse model:

The TS2Neo mouse model has been characterised in multiple ways to test its suitability in modelling the behavioural and neurological changes resulting from classical TS mutations in human TS patients (Bader *et al.*, 2011; Bett *et al.*, 2012) Further studies involved using the TS2Neo mouse model to explore neurophysiological changes which result from TS-type mutations in the mouse (Ehlinger and Commons, 2017; Rendall *et al.*, 2017; Horigane *et al.*, 2020), the aim being to identify mechanisms by which TS mutations can result in the neuropsychiatric and neurological changes seen in TS patients. Further studies involving the TS2Neo mouse have been conducted with the aim of studying the physiology of non-neurological elements of TS such as adrenal abnormalities (Calorio *et al.*, 2019).

Bader *et al.* (2011) described the TS2Neo mouse as having grossly normal health and diurnal rhythm. However, the authors found evidence that the TS2Neo mouse showed repetitive behaviours, altered social behaviours in a classic three-chamber test, abnormal ultrasonic vocalisations and increased persistence of contextual fear learning. These were considered to be ASD-related phenotypes. Bett *et al.* (2012) later described the TS2Neo mouse as displaying a maladaptive and injury-causing scratching pattern, which was considered as an ASD-relevant self-injurious behaviour. Other researchers have characterised the TS2Neo mouse as having increased social competitive dominance (Rendall *et al.*, 2017; Horigane *et al.*, 2020), impaired sensorimotor function, and reduced male-female vocalisations (Rendall *et al.*, 2017).

Interestingly, TS2Neo mice have also been found to have enhanced auditory processing capability for short-duration gaps and embedded tones within a stable auditory stimulus. In other words, the TS2Neo mice were more able to detect either a short break, or short duration change in tone occurring in a single auditory tone stimulus as compared to WT mice (Rendall *et al.*, 2017). This provided the first evidence that TS2Neo mice had a basic sensory processing abnormality as compared to WT. Sensory abnormalities are a core phenotype of ASD, a TS-related disorder (American Psychiatric Association, 2013). Basic sensory processing abnormalities have previously been demonstrated in ASD patients (Coulter, 2009; Marco *et al.*, 2011). Sensory processing is a basic neurological function which is key to survival for many species. The neural circuitry involved in sensory processing is similar in mice and humans (Schaffler, Middleton and Abdus-Saboor, 2019), and changes in basic sensory processing are relatively easily testable in both mice and in humans. Any changes in sensory processing resulting from TS mutations in mice are likely to be applicable to, and easily testable in patients with TS and ASD. Indeed, ASD patients have previously been reported to have auditory processing enhancements which are similar to those reported in the TS2Neo mouse (Bertone *et al.*, 2005; Mottron *et al.*, 2006; Rendall *et al.*, 2017). It is possible that the auditory processing enhancements seen in TS2Neo mice are caused by the same neurophysiological changes which result in ASD-type symptoms in patients with TS. When Rendall *et al.* (2017) described the TS2Neo mouse as having auditory processing enhancements as compared to WT mice, they also found that the TS2Neo mice had smaller MGN than did WT mice. The MGN is a subcortical neural structure involved in basic auditory processing. The change in MGN structure could potentially be related to the sensory processing abnormality found in the TS2Neo mice. This demonstrates that TS2Neo mouse can be used to suggest neurophysiological underpinnings of mutation-related changes in behaviour and neurological function.

TS2Neo mice have been demonstrated to have abnormalities in serotonergic signalling and serotonin levels within various areas of the brain (Ehlinger and Commons, 2017). These changes are described in a previous subsection “Impacts of TS mutations on neuronal structures and on signalling pathways in the brain”. A study by Krey *et al.* (2013) found that the TS2Neo mouse had abnormally short basal dendrites in L2/3 pyramidal cells of the frontal cortex. These changes are described in the previous subsection “Impacts of TS mutations on single neuron migration and structure”.

TS2Neo mice have been found to have enhanced myelination within various areas of the brain (Cheli *et al.*, 2018). Abnormalities in myelination and oligodendrocyte maturation have been proposed to be related to the aetiology of ASD (Galvez-Contreras *et al.*, 2020). It has previously been found that calcium influx through the CaV1.2 channel is required for the proper development and maturation of oligodendrocytes (Cheli *et al.*, 2016a). It therefore seems likely that abnormalities in calcium influx through the mutant TS-type channel in TS2Neo mouse oligodendrocytes leads to a disruption in their maturation and the resultant increase in myelination within the TS2Neo mouse brain. Although this is not a neuronal change, it is neurologically relevant, and could be involved in the aetiology of the neurological aspects of TS.

Abnormalities in the migration of inhibitory interneurons during brain development have been demonstrated in the TS2Neo as compared to the WT mouse (Horigane *et al.*, 2020). This reflects findings that TS mutations disturb inhibitory neuron migration in cultured human neurons from TS patients as compared to controls (Birey *et al.*, 2017, 2022; see subsection "Impacts of TS mutations on neuronal development and structure"). This is potentially ASD-relevant and demonstrates that changes in neurophysiology caused by classical TS mutations can be seen in the mouse as well as in the human. A leading theory on the pathophysiology of ASD suggests that the development of the disorder involves abnormalities in inhibition-excitation balance, and in inhibitory cell function within the brain (Contractor, Ethell and Portera-Cailliau, 2021). This work has led to a proposal that the TS2 mutation could disrupt the excitation-inhibition balance in the brain and/or alter inhibitory interneuron function in a way which may result in ASD-type functional abnormalities.

A study by Calorio *et al.* (2019) used the TS2Neo mouse model to explore the impact of the TS2 mutation on adrenal gland structure and function following the description of a TS patient with adrenal gland dystrophy (Kawaida *et al.*, 2016). WT mice typically express alternatively spliced CaV1.2 channels in a 5:1 ratio for exon 8:8a splice forms. In TS2Neo mice, this ratio was reduced to 1:1, providing evidence that the neomycin cassette reduces the expression of the mutant channel, in turn improving viability as was originally proposed by Bader *et al.* (2011). Electrophysiological study of adrenal chromaffin cells in the TS2Neo and WT mice found that the TS2Neo mutation resulted in calcium channel currents which showed reduced and delayed inactivation, suggesting that a TS-type channel was functionally expressed and contributing to the overall calcium current in these cells. Calorio *et al.* (2019) found that chromaffin cells from TS2Neo mice exhibited enhanced burst firing activity as compared to those from WT. Interestingly, the AP in the chromaffin cells from the TS2Neo mice were also longer in duration as compared to WT cells. The AP of chromaffin cells is underpinned by sodium, potassium and calcium channels currents (Hollins and Ikeda, 1996; Marcantoni *et al.*, 2008; Lingle *et al.*, 2018; Calorio *et al.*, 2019). TS2Neo chromaffin cells were found to have a reduced AP rate of rise suggesting mutation-related reduction in sodium channel density or conductance as compared to WT. TS2Neo chromaffin cells also had reduced after-hyperpolarisations, suggesting reduced potassium channel function as compared to WT. Calorio *et al.* (2019) found that sodium channel density was reduced in TS2Neo chromaffin cells as compared to WT which explains reduced rate of rise of the AP waveform. This reduction in sodium channel density could result in the increased AP duration seen in the chromaffin cells. They found no evidence that calcium-dependent big potassium (BK) channel currents were altered by the TS2Neo mutation. This provided key information regarding the aetiology of the adrenal changes seen in TS.

Summary of the TS2Neo mouse model and research completed to date:

The TS2Neo mouse model has been developed to explore the physiology of TS, specifically related to the neuropsychiatric phenotypes of the disease. The TS2Neo mouse has been behaviourally characterised, has been found to have a specific enhancement in auditory sensory processing, and has physiological changes which have also been demonstrated in iPSC-derived neuronal cell culture experiments. Current evidence supports the TS2Neo mouse as being a useful model to study the neurophysiological changes caused by classical TS mutations.

Research aims:

The overall aim of my PhD was to better understand the neurophysiology of TS. To achieve this aim, I studied the neurophysiology of the TS2Neo mouse model of TS and predicted the impacts of the TS2 mutation on neural network activity by computational modelling study. I also provide evidence that the TS2-type mutation alters basic sensory processing within the visual domain in the TS2Neo mouse.

To achieve my overall research goal, I developed 4 separate research aims all related to better understanding the neurophysiology of TS. These 4 separate aims are addressed in the 4 data chapters of this thesis.

My first aim was to provide evidence as to whether the classical TS2-type mutation in TS2Neo mice impacts basic sensory processing in the visual domain. This was based on the previous finding that the TS2-type mutation enhances a specific aspect of auditory processing in the TS2Neo mouse (Rendall *et al.*, 2017). To address this aim, I used functional two-photon calcium imaging alongside visual stimulation paradigms to measure the abilities of TS2Neo and WT mice to neurally process specific visual stimuli at the cortical level. I found evidence of a specific visual processing abnormality in the TS2Neo mouse as compared to WT. This is described in detail in data chapter 1.

My second aim was to provide evidence as to whether the classical TS-type mutation results in a prolonged AP in naturally developed neurons within functional brain tissue of the TS2Neo mouse as compared to WT. To achieve this aim, I used patch clamp electrophysiology in acute brain slices to measure the AP duration for pyramidal cells from three separate cortices of the TS2Neo and WT mouse brain. The APs of pyramidal cells from the primary visual cortex (V1), the retrosplenial cortex (RSC) and the CA1 of the hippocampus were prolonged in the TS2Neo mouse as compared to WT. I also completed exploratory data analyses to determine whether the classical TS mutation impacted various other electrophysiological properties in these cells. The experiment pertaining to this aim is described in data chapter 2.

My third aim was to determine whether the TS-type mutation impacts PV+ cell number in various areas of the adult TS2Neo mouse brain. This was based on the knowledge that the classical TS mutations disrupt inhibitory interneuron development and migration (Birey *et al.*, 2017, 2022; Horigane *et al.*, 2020), as well as the CaV1.2 channel— which is implicated in TS— being involved in PV+ cell development (Jiang and Swann, 2005). To achieve this aim, I used immunofluorescence and imaging techniques to label, image, and count PV+ cells within four areas of the TS2Neo mouse brain: the V1, RSC, the CA1 and CA3 of the hippocampus. I found an increased number of PV+ cells in V1, and a reduced number of PV+ cells in the CA3 region of the hippocampus in TS2Neo mice as compared to WT. This experiment is described in detail in data chapter 3.

My fourth aim was to model how the classical TS2 mutation and the TS2-related reduction in PV+ cell number, could alter functionally important ɣ oscillatory network activity within a well-defined neural circuit of the CA3 region of the hippocampus. Specifically, I explored how the presence of the classical-TS2 type CaV1.2 channel within pyramidal cells, and the TS-related reduction in PV+ cells could impact ɣ oscillations in the Betterton *et al.* (2017) pyramidal-PV+ cell neural network model of the CA3 by in-silico computational modelling study. I found that the TS-type modelled network had reduced ɣ oscillatory power as well as abnormalities in the power spectral density (PSD) of the oscillations. These changes were largely attributed to the TS-related reduction in PV+ cell number within the network model. This work is described in data chapter 4.

Data chapter 1 references a prior unsuccessful pilot study which preceded the experiment described in data chapter 1 and was not completed due to equipment malfunction. The details of this pilot study, the equipment malfunctions, the overhaul required to overcome the malfunctions, and details of the setup involved in the experiment described in data chapter 1 are provided in Appendix 1.

Modelling work described in chapter 4 uses mathematical equations and model parameters which are described in Appendix 2.

A further modelling experiment which explores how *CACNA1C* hemizygosity impacts ɣ oscillations in the CA3 is described in Appendix 3. This work was completed instead of wet-lab work due to a lack of laboratory access caused by the Covid-19 pandemic.

Data Chapter 1: Specific visual processing abnormality in TS2Neo mouse evidenced by in-vivo two-photon calcium imaging:

Introduction:

Multiple TS patients have been reported to have abnormalities in visual perception and in vision-related behaviours. The mechanism by TS mutations could impact visual perception has not been explored. Two TSA patients have been reported to have abnormalities in visual perception with comorbid developmental disorder (Gillis *et al.*, 2012; Bozarth *et al.*, 2018). One TSA patient described by Gillis *et al.* (2012) was found to be cortically blind with severe developmental delay. A further TSA patient described by Bozarth *et al.* (2018) was unable to visually or fixate at the age of 18 months. The patient described by Gillis *et al.* (2012) also had developmental delay, failing to meet appropriate developmental milestones.

TS2 patients have also been reported to have abnormalities in eye movement and function alongside neurological issues (Splawski *et al.*, 2005; Walsh *et al.*, 2018). Furthermore 80% of TS patients are found to meet the diagnostic criteria for ASD, a disorder in which sensory abnormalities are a key and debilitating symptom (Splawski *et al.*, 2004; Marco *et al.*, 2011; American Psychiatric Association, 2013).

The physiological mechanisms of sensory processing abnormalities in ASD patients are not well understood (Marco *et al.*, 2011), and those in TS patients have not been explored. It has been hypothesised that sensory processing abnormalities in patients with ASD may be causative of some of the more complex issues experienced by those with the disorder (Coulter, 2009; Marco *et al.*, 2011; Chokron *et al.*, 2020; Zhou *et al.*, 2023). Understanding the mechanisms of sensory processing abnormalities seen in ASD and in ASD-related disorders may provide a better understanding of the pathophysiology of ASD.

ASD patients frequently exhibit abnormal behavioural responses to specific visual stimuli. Examples include limited interest in images of faces, abnormal visual fixation on non-socially important visual stimuli, and gaze aversion (Dalton *et al.*, 2005; Coulter, 2009; Zhou *et al.*, 2023). Both gaze aversion and the limited interest in faces displayed by ASD patients have been attributed to abnormal processing of facial visual stimuli (Dalton *et al.*, 2005; Coulter, 2009; Zhou *et al.*, 2023). Over a third of ASD patients have been found to meet the diagnostic criteria for prosopagnosia. Prosopagnosia is a disorder defined by a reduced ability to recognize faces, which is thought to be due to abnormalities in facial information processing (Minio-Paluello *et al.*, 2020). It has been proposed that the lack of visual attention to facial stimuli, and reduced ability to perceive and recognise faces in ASD patients occurs as a result of differences in basic visual processing in the ASD brain (Coulter, 2009; Vlamings *et al.*, 2010; Zhou *et al.*, 2023). The notion that abnormalities in basic visual processing ability could result in ASD phenotypes is supported by the finding that up to 50% of individuals with cortical visual impairment present with ASD-type symptoms (Chokron *et al.*, 2020).

ASD patients have been found to have abnormalities in basic visual processing. Specifically, ASD patients have been found to be superior in processing high spatial frequency (SF) visual stimuli as compared to neurotypicals (Vlamings *et al.*, 2010; Kéïta *et al.*, 2014). In everyday life this can be observed as ASD patients having an enhanced ability to see the fine detail in visual images, and a reduced ability to see the big picture (Shah and Frith, 1983; Robertson and Baron-Cohen, 2017; Zhou *et al.*, 2023). Kéïta *et al.* (2014) found that ASD patients have an enhanced contrast sensitivity for simple visual gratings stimuli of high SF as compared to neurotypicals. Contrast sensitivity is a measure of the minimum contrast at which an individual can detect a visual stimulus of a given nature. It is typically taken as:

$$Contrast\ Sensitivity = \log 2\left(\frac{1}{Minimum\ Contrast\ Required\ For\ Perception}\right)$$

Kéïta *et al.* (2014) also found that ASD patients had a significantly different contrast sensitivity function (CSF) as compared to neurotypicals. A CSF is a measure of how an individual's contrast sensitivity for a visual stimulus varies with the stimulus SF. CSF is typically measured by showing an individual black-and-white gratings stimuli of differing SFs- of differing distance between bars. The SFs used span the perceptual range, with each SF being shown at varying contrasts. From this, the minimum contrast at which an individual can see the stimulus when shown at specific SFs across the visual range can be measured. The mathematical description of how the contrast sensitivity changes with SF is the CSF. For illustration purposes, I have included in Figure 3 an image showing a continuous gratings stimulus, where SF increases to the right, and contrast decreases to the top of the image. This can be used to measure CSF. My CSF is shown in red.

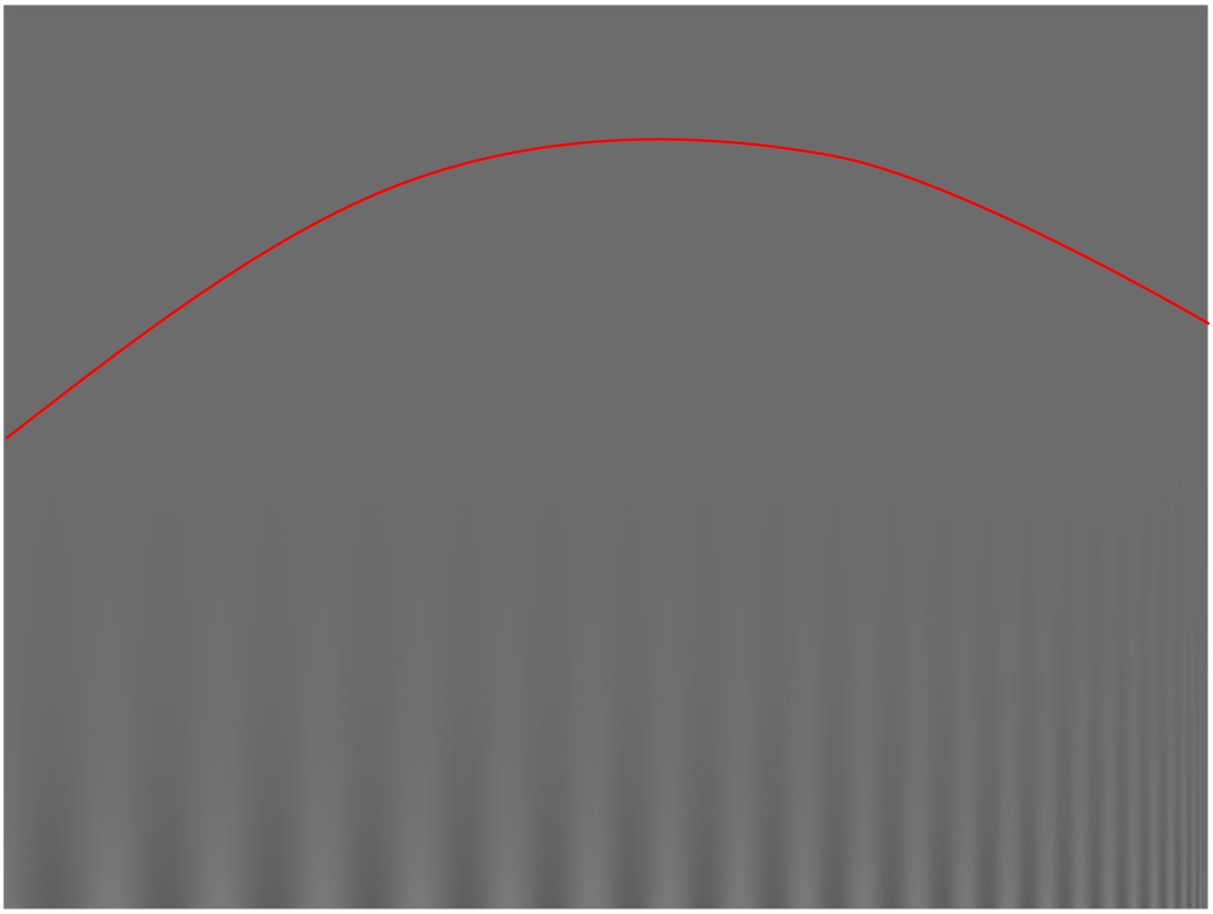

Figure 3 Example image used to measure CSF. The red line indicates the contrast at which I can detect the stimulus. This would be my CSF.

Kéïta *et al.* (2014) showed ASD patients and neurotypical subjects discrete grating stimuli of five different SFs spanning the human visual range. Stimuli of each SF were shown at 100% contrast, before being reduced to find the minimum contrast at which each subject could perceive the gratings. Individual participants indicated whether they could see the gratings by pressing a button on a keyboard. The contrast sensitivity and CSF from ASD and neurotypical participants was measured. From this experiment, it was found that ASD patients have a higher contrast sensitivity to high SF stimuli, and an abnormal CSF as compared to neurotypical control subjects.

A similar visual perceptual difference has also been reported in the inbred BTBR idiopathic ASD mouse model. Cheng *et al.* (2020) showed BTBR and WT mice gratings stimuli of varying SFs and contrasts, while measuring involuntary optokinetic reflex responses of the mice to each stimulus. A CSF from each mouse was obtained, as was a measure of contrast sensitivity for stimuli of each SF tested. The CSF and individual contrast sensitivities to stimuli of each SF were compared between BTBR and WT mice. BTBR mice were not found to have significantly different CSF as compared to WT mice but were found to have increased contrast sensitivity for stimuli shown at mid-high SFs. It should be noted that this enhanced perceptual ability was measured from reflex responses. These do not involve conscious visual perception and depends solely on processing involving sub-cortical structures (Distler and Hoffmann, 2011). The method used by Kéïta *et al.* (2014) to explore CSF and contrast sensitivity differences in ASD patients as compared to neurotypicals involved measuring voluntary responses from subjects. Conscious perception of a visual stimulus is required for an individual to provide such a response. Conscious visual perception relies on cortical processing involving V1 (Leopold, 2012). The method used to measure CSF and contrast sensitivity in the BTBR mouse involved measuring reflex responses which do not involve cortical processing of the visual stimuli. Involuntary reflex responses do not indicate conscious visual perception of the stimulus. ASD patients and BTBR mice were both found to have an abnormally enhanced contrast sensitivity to high SF stimuli, although the methods used to obtain these results differed.

Similar abnormalities in contrast sensitivity and CSF which appear to be related to ASD have not been tested for in the TS2Neo model mouse of TS. Preliminary sensory tests revealed no gross perceptual disturbances in the TS2Neo mouse (Bett *et al.*, 2012). However Rendall *et al.* (2017) found that TS2Neo mice had a superior ability to perceive complex auditory stimuli as compared to WTs. Specifically, TS2Neo mice were superior at detecting an embedded tone and silent gap of short duration within an acoustic stimulus as compared to WTs. This auditory processing enhancement reported in the TS2Neo mouse model is consistent with those reported in ASD patients (Bertone *et al.*, 2005; Mottron *et al.*, 2006). This suggests that classical TS mutations may result in abnormalities in basic auditory sensory processing, which resembled those found in ASD patients. Given that 80% of TS patients meet diagnostic criteria for ASD, this seems logical (Splawski *et al.*, 2004).

I hypothesised that the TS2Neo mouse would have abnormalities in processing visual stimuli as compared to WT in an ASD-related way. I specifically hypothesised that TS2Neo mice would have an abnormal CSF and increased contrast sensitivity to mid-high SF visual stimuli as compared to WT. I wished to test this hypothesis using methodology that is dependent on cortical processing of visual stimuli which is involved in conscious visual perception. I aimed to measure CSFs and contrast sensitivities to stimuli of specific SFs from TS2Neo and WT mice by showing them drifting black-and-white gratings stimuli of several discrete SFs spanning the mouse visual range at full-low contrast (100-3.2%), while recording responses of the mouse to stimuli of each SF at each contrast level. In a failed pilot study, I attempted to measure contrast sensitivity and CSF from TS2Neo and WT mice by use of both behavioural and neuronal methods. I aimed to record conscious behavioural responses from mice indicating their conscious detection of visual stimuli of each SF, at varying contrasts. I aimed to simultaneously measure the responses of neurons of L2/3 of the primary visual cortex binocular region (V1b) of TS2Neo and WT using two-photon calcium imaging, to measure visual detection at the cortical level. Mice were to be trained to consciously respond to visual stimuli of each SF used in the experiment, where stimuli were shown at maximum contrast. Training involved methods similar to those described by Burgess *et al.* (2017). I assumed that mice would generalise this associative learning, such that they would respond to the stimulus when shown at lower contrasts. Training of mice to respond to visual stimuli requires extensive training and typically involves high failure rates.

Functional imaging of V1b neurons was to be used to measure cortical processing of visual stimuli as required for conscious perception, for stimuli of differing SF and contrast. We were to use somatic calcium imaging in these neurons. Previous work has demonstrated that calcium signalling in pyramidal cortical cells accurately predicts conscious sensory perception in the mouse, at least in the dendrites (Takahashi *et al.*, 2016). The use of both methods was thought to be sufficient to measure CSFs and contrast sensitivities based on conscious visual perception, without relying on mouse learning and the assumption that mice can generalise learned responses to stimuli of reduced contrast. The methods used for neuronal functional imaging of V1b neurons were based on those previously used by our lab (Powell *et al.*, 2020; Craddock *et al.*, 2023). Imaging equipment malfunctioned during the training period of the pilot experiment and no data was acquired. Equipment overhaul was required for the microscopy equipment to resume functionality. This was a time-consuming process. As such, it was decided that the final experiment, reported in this chapter, would not involve behavioural training of, or recording of behavioural responses in mice. Details of the original experiment are provided in Appendix 1 alongside details of the original equipment setup, equipment malfunctions that resulted in the failure of the pilot experiment. Also detailed in Appendix 1 is the overhaul process, a detailed description of the equipment setup required to run the experiment described in this chapter, as well as the instructions and resources required to run the experiment reported here.

The experiment detailed here aimed to measure CSF and specific contrast sensitivity differences to visual stimuli of various SFs from TS2Neo and WT mice. My hypothesis was that TS2Neo mice would have increased contrast sensitivity to visual stimuli of mid and high SF as compared to WT mice. This was tested by measuring responses of V1b neurons from TS2Neo and WT mice to visual stimuli of specified SFs spanning the visual range of the mouse, each shown at contrast levels from 100-6.3%. The neuronal responses were measured by functional calcium imaging using a two-photon microscope system focused through a cranial window onto GCaMP6f-labelled neurons in L2/3 of V1b of the mouse brain. Details of the setup used in this experiment, as well as detailed instructions and resources required to run this experiment are provided in Appendix 1.

Methods:

Animals:

7 TS2Neo heterozygous (HET) mice, 1 WT sibling (Jax labs strain #019547, B6.Cg-Cacna1ctm2Itl/J), and 4 C57BL/6J mice (Jax labs; stock number 000664) were used in this study. Mice were not selected based on sex. The WT sibling and 4 C57BL/6J mice were grouped into a single WT control group, which will be referred to as WTs. This gave a TS2Neo HET group of 7 mice, and a WT group of 5 mice. Non-sibling C57BL/6J mice were required due to a lack of age-appropriate sibling mice at the time of study. Sample sizes were designed to be balanced, with a 6:6 ratio of HET:WT. A genotyping error led to an unbalanced 7:5 sample size. One WT mouse was euthanised before the end of the

experiment for humane reasons. This animal was excluded from the study. The animal was the single sibling WT mouse. Data could not be recorded from two mice from the TS2Neo group. The cranial window over V1b in these mice became occluded by bone regrowth before imaging. As such, 5 TS2Neo and 4 age-matched C57BL/6J mice were used to obtain the data reported in this study. The WT group contained 2 male and 2 female mice. The TS2Neo group consisted of 3 females and 2 males.

All experimental procedures on the mice were carried out in accordance with the UK Animals (Scientific Procedures) Act 1986, and the European Commission Directive 2010/63/EU. Housing and husbandry were provided by Cardiff University Biological Services. Mice were given regulation food and water ad-libitum and were subject to a normal light/dark cycle (12hours light, 12hrs dark). Mice were group housed and kept in enriched housing when not participating in experimental procedures. All individuals involved in the experiment and myself were blinded to mouse genotype throughout the study. Genotype was revealed only after data collection and processing, immediately before final analysis of the data.

Surgery:

Surgical procedures were performed under aseptic conditions. All mice underwent surgery at 10-12 weeks of age.

Prior to surgery, mice were given antibiotics and anti-inflammatories to reduce the risk of infection and to enhance post-surgical recovery. The antibiotic Enrofloxacin (5 mg/kg) was administered by sub-cutaneous injection. The anti-inflammatory drug Carprofen (5 mg/kg) was administered by sub-cutaneous injection. The glucocorticoid, Dexamethasone (0.15 mg/Kg), was given by intra-muscular injection.

Mice were anaesthetised using isoflurane vapour in oxygen. Anaesthesia was induced using 4% isoflurane. Anaesthesia was maintained using 1.5-2% isoflurane for the duration of the surgery. Anaesthetised animals were secured in a stereotaxic frame (David Kopf Instruments, Tujunga, CA, USA), the scalp and periosteum were removed from the dorsal surface of the skull. A custom head plate was attached to the cranium using dental cement (Super Bond, C&B). The aperture of the headplate was centred over the right hemisphere V1. This was 2.3mm lateral and 3.1mm posterior from bregma. A 3mm circular craniotomy was made in the described position.

Mice were injected in V1b at 3.1mm lateral, and 3.1mm posterior to bregma, with 150µl of AAV1.Syn.GCaMP6f WPRE.SV40 viral vector (CS2358, 1:10 dilution of 3.45x10^{13}gc/ml). This ensured that the fluorescent calcium indicator, GCaMP6f, would be expressed by neurons within the injected V1b area of these mice.

Following injection, the craniotomy was closed using circular glass inserts of 3 and 5mm, bonded together with optical adhesive (Norland Products; catalogue no. 7106). Two 3mm glass inserts sat within the headplate (Biochrom Ltd., product code 640720(CS-3R)), and one 5mm insert sat on top of the headplate (Biochrom Ltd., product code 640700). These inserts formed the cranial window through which

GCaMP6f-labelled cells in V1b were imaged. The window was sealed with dental cement (Super Bond, C&B). The mice were then left to recover under surveillance until the anaesthetic had worn off. Mice were then returned to their home cage with siblings and were left to recover for 3 days with daily post-operative checkups. During this 3-day period, mice were administered post-operative Enrofloxacin (37.8μg/ml) and Carprofen (333 μg/ml) dissolved in drinking water. After the recovery period, mice were allowed to rest for a further 4 days before they were habituated to handling and head-fixation to the two-photon microscope.

Two-photon imaging and visual stimulus presentation:

Mice were habituated to handling and head-fixation over a period of 1 week, using methods similar to those described by Aguillon-Rodriguez *et al.* (2021). Mice were placed on top of a custom designed cylindrical treadmill and were head-fixed to the two-photon microscope using the head plate described in the "Surgery" subsection. Mice were faced toward a calibrated PC screen positioned in the mouse's binocular field of view, 20cm away from the mouse. The PC screen was used to present visual stimuli to the animal during the experiment. For more details regarding the setup, please refer to Appendix 1.

I measured responses of neurons in V1b of TS2Neo and WT mice to visual gratings stimuli of varying SFs and contrasts. Two-photon calcium imaging of GCaMP6f-expressing neurons in in L2/3 of V1b of the mouse brain was used to measure neuronal responses to the presentation of visual stimuli to each mouse. L2/3 was targeted by using a focus depth of 150-250μm from the cortical surface. 42 different gratings stimuli were shown to each mouse. Gratings were displayed at seven different SFs across the mouse's visual range. The SFs used in this experiment were measured in cycles per degree (cpd), and were: 0.014, 0.031, 0.64, 0.128, 0.236 and 0.383. The specific SFs used in this experiment were based on those used by Umino, Pasquale and Solessio (2018) to measure CSF in mice by behavioural means. The SFs used were also within similar ranges of those used in other murine CSF experiments (Prusky and Douglas, 2004; Prusky *et al.*, 2004; Cheng *et al.*, 2020). Gratings of each SF were shown at six different discrete contrast levels, these were: 100%, 50%, 25%, 12.5%, 6.7% and 3.4%. As 7 different SFs were shown, each at 6 contrasts, a total of 42 different types of visual stimuli were shown to the animal. Further details of the visual stimuli which were shown to each animal in the experiment are provided in the subsection "Visual stimulation".

I processed two-photon imaging data with visual stimulus meta-data collected during the study such that I was able to identify neurons in V1b which were significantly visually responsive to stimuli of at least 1 SF when shown at 100% or 50% contrast. Cells which were visually responsive were tested to find which SFs they could respond to and to find the minimum contrast at which a response was elicited (the contrast sensitivity for that SF). From this, I obtained contrast sensitivities to each SF, and CSFs as neuronally measured from mice of each genotype. Details of the imaging methods used to record neuronal responses to visual stimuli are given in the subsection "Two-photon imaging".

More details of visual stimuli and imaging methods used in this experiment are given in the subsections below. Comprehensive details of the experiment setup, methods used, and instructions for replication of the experiment using similar equipment are provided in Appendix 1.

Visual stimulation:

42 different visual stimuli were presented to mice during this experiment. Visual stimuli consisted of simple black-and-white, vertical, drifting grating of a sinusoidal waveform. The nature of this stimulus is consistent with those used by Cheng *et al.* (2020). Stimuli were displayed across the full screen of a liquid-crystal display (LCD) PC monitor (Iiyama, B2080HS; width × height 26 × 47 cm^2). Full-screen presentation was used after empirical testing which found that full-screen stimulation evoked responses from a greater proportion of cells than did stimulus presentation within a gaussian window (data not shown). Stimuli were generated by a PC connected to the LCD monitor, using the psychophysics toolbox-3 package running on MATLAB 2022a (Kleiner *et al.*, 2007). The grating bars drifted unidirectionally to the right (from the perspective of the mouse) with a temporal frequency of 1.5Hz. Stimuli were displayed to the mouse for 3 seconds. This was followed by the presentation of a grey screen for 3 seconds. Neuronal activity was measured in V1b cells during the grey screen presentation to provide a background reading of each cell's baseline neuronal activity. The grey screen shown during this background 3 second period was of equivalent luminescence to the overall screen luminescence resulting from stimulus presentation.

The 42 different visual stimuli were shown in a pseudo-random order. This was repeated 5 times within a single experimental recording. A single recording session lasted 43 minutes. A single presentation of one of the 42 stimuli is referred to here as an experimental trial. From each mouse, 3 experimental recordings were collected. Up to 2 recordings were taken from each mouse on a single day. Each recording from a single mouse was taken from a different area of V1b, such that no cell was recorded from twice, and cells were sampled along different positions on the anteroposterior axis of V1b.

Two-photon imaging:

GCaMP6f was excited using 920nm pulses from a two-photon Ti:sapphire laser (Chameleon, Coherent). Laser pulses were regulated to a measured power of 50mW at the point of tissue excitation by use of a Pockel's cell (Conoptics, 350-380) and associated control unit (Conoptics, 302-RM). Emissions from two-photon excited GCaMP6f cells were recorded using a resonant scanning microscope (Thorlabs, B-Scope) equipped with a 16x0.8 water-immersion objective (Nikon, LWD 16x0.8W, DIC N2). The microscope was controlled by a PC running ThorImage software (v4.1.2021.9131), via a National Instruments data acquisition (DAQ) card (NI PCIe-6232, National Instruments). Data were acquired at a raw frame rate of 56Hz and were averaged using ThorImage software to give a final frame rate of 9.6Hz. Timestamps of two-photon imaging frames were collected using both the data acquisition toolkit in MATLAB 2022a and ThorSync software (v4.1.2020.1131), via PC-related DAQ cards.

Recordings were made from a 1250µmx1250µm (256x256 pixel) field of view, at a depth of 150-250µm from the pial surface, corresponding to cortical L2/3 of V1b.

Control of visual stimulus presentation and two-photon imaging equipment:

Control of the visual stimulus presentation and time-synced two-photon image acquisition was achieved by use of custom-made codes written in C# and in MATLAB, alongside the use of ThorImage and ThorSync software. All custom-made codes required to run this experiment are available on GitHub, while ThorImage and ThorSync software are open-source, and are available on request from ThorLabs. Instructions for how to set up the experiment, including instructions on software installation, and how to setup and use custom made codes are provided in Appendix 1.

Data processing:

Data obtained from each experiment were processed to extract a fluorescence trace from each cell imaged. This was a measure of the cell's fluorescence over the course of the experiment. This involved image registration and cell detection which were performed using Suite2P software (Pachitariu *et al.*, 2016). Cell fluorescence traces were smoothed using a 100-point moving window, and then down sampled 5 times for ease of analysis. These partially processed full-experiment cell fluorescence traces were further processed with respect to known stimulus timings, so that I could measure any changes in cell fluorescence resulting from the presentation of visual stimuli of each SF at each contrast shown. The mean cell fluorescence for the baseline period (grey screen period preceding stimulus presentation) was compared to that for the period where that specific stimulus was shown for each trial. Cells were deemed to be responsive to a stimulus if the mean stimulus presentation fluorescence of the cell was significantly, and, on average 30% higher than the mean fluorescence values for the corresponding baseline periods for all 5 trials of a given stimulus type (of specified SF and contrast). Significance testing for responsiveness involved Wilcoxon signed rank methods, where the threshold value was set to 0.01.

All cells which were found to be visually responsive were further tested to find the SFs to which they responded, and the minimum contrast at which they could respond to stimuli of SF to which they were responsive. Responsiveness was again defined as a significant increase in cell fluorescence during the stimulus presentation as compared to the baseline period (by Wilcoxon signed rank testing, threshold=0.01) with the presentation period average fluorescence being at least 30% greater than that for the baseline period. This processing produced the final dataset for this experiment. The final dataset contained data from all cells of all animals, and detailed the minimum contrast that each cell could respond to for stimuli of each of the 7 SF used in the study. All data processing stages after fluorescence extraction were performed using custom made codes written in MATLAB 2022a. The processing procedure described here is described in further detail in Appendix 1. Codes required to run the processing pipeline are available on GitHub. Instructions on how to set up and run the data processing pipeline can be found in Appendix 1.

Data analyses:

All data were analysed using R. I tested whether the proportion of all cells detected from 2-photon imaging recordings which were found to be visually responsive differed by genotype. This involved the use of Wilson's test of equal proportions using the stats package in R (Wilson, 1927).

Following this, genotype impacts on neuronal CSF were tested for, while controlling for between-animal variance. This was achieved using cumulative link mixed model regression. The details of this regression analysis are described in subsection "Modelling analysis". For simplicity in demonstrating genotype impacts on contrast sensitivity for stimuli of high as compared to low SF, a graph showing the percentage of neurons from animals of each genotype which were found to be responsive to either a high SF (0.128cpd) or low SF (0.014cpd) stimuli is also presented in the results section of this chapter. These data are presented for illustrative purposes only. No formal analysis of this data was completed.

Modelling analysis:

The final dataset described the minimum contrast to which each cell from each animal could respond to stimuli of each of the 7 SFs tested. Contrast sensitivity was taken as

$$Contrast\ Sensitivity = \log 2\left(\frac{1}{Minimum\ Contrast\ Required\ For\ Perception}\right)$$

for visual stimuli of each SF tested. As gratings of each SF were shown at six discrete contrast levels, which can be ordered from 100% to 3.4%, the minimum contrast to which the cell could respond was an ordinal measured variable. Contrast sensitivity then also fell in one of six levels. A seventh level was added to describe cells which did not respond to visual stimuli of the specific SF tested. This level was termed "NR" for non-responsive. Contrast sensitivity, the independent variable, could fall within one of seven discrete but ordered categories, making this measure an ordinal variable. The ordinal package in R was used to produce a cumulative link mixed model of how neuronal contrast sensitivity varies with SF, and how this differs by the genotype of the animal from which the cell was recorded. Between-animal variance in contrast sensitivity was also accounted for in this model. The assumptions of the cumulative link mixed model were tested graphically by plotting measured data against predicted model outcomes. The goodness of fit of the model was tested using Cox and Snell method included in the nagelkerke function of the rcompanion package (Mangiafico, 2023). The impact of genotype, SF, and genotype interacting with SF (difference in CSF by genotype) on contrast sensitivity was tested by use of the Anova.clmm function in the RVAideMemoire package (Herve, 2023). The significance of genotype, SF, and genotype-by-SF on contrast sensitivity was therefore tested. Significance of SF indicates that contrast sensitivity varies with stimulus SF, as it should for a mouse CSF. Significance of genotype indicates that contrast sensitivity for stimuli of any/all SF differs by genotypes, which, based on my hypothesis, I did not expect to be the case. This would indicate that cells have a higher general contrast sensitivity to visual stimuli of all SFs. Significance of the genotype-by-SF interaction term indicates that genotype impacts CSF- the test of my experiment hypothesis. The impact of genotype on contrast sensitivity for stimuli of specific SFs was tested after confirming that genotype impacted CSF. This was also part of my primary hypothesis. This post-hoc testing of genotype effects on contrast sensitivity for stimuli of specific SFs was completed by use of emmeans and multcomp packages in R (Hothorn *et al.*, 2023; Searle, Speed and Milliken, 2024). Post-hoc results were adjusted for multiple comparison using the Holm-Bonferroni correction method.

Results:

Neuronal CSFs obtained from mice by two-photon calcium imaging with visual stimulus paradigm:

Fluorescence traces from GCaMP6f-labelled neurons in V1b of mice were obtained. These were used as a proxy for measuring cell activity changes in response to visual stimulation. An example of traces obtained from a single cell recorded during an experiment is shown in Figure 4.

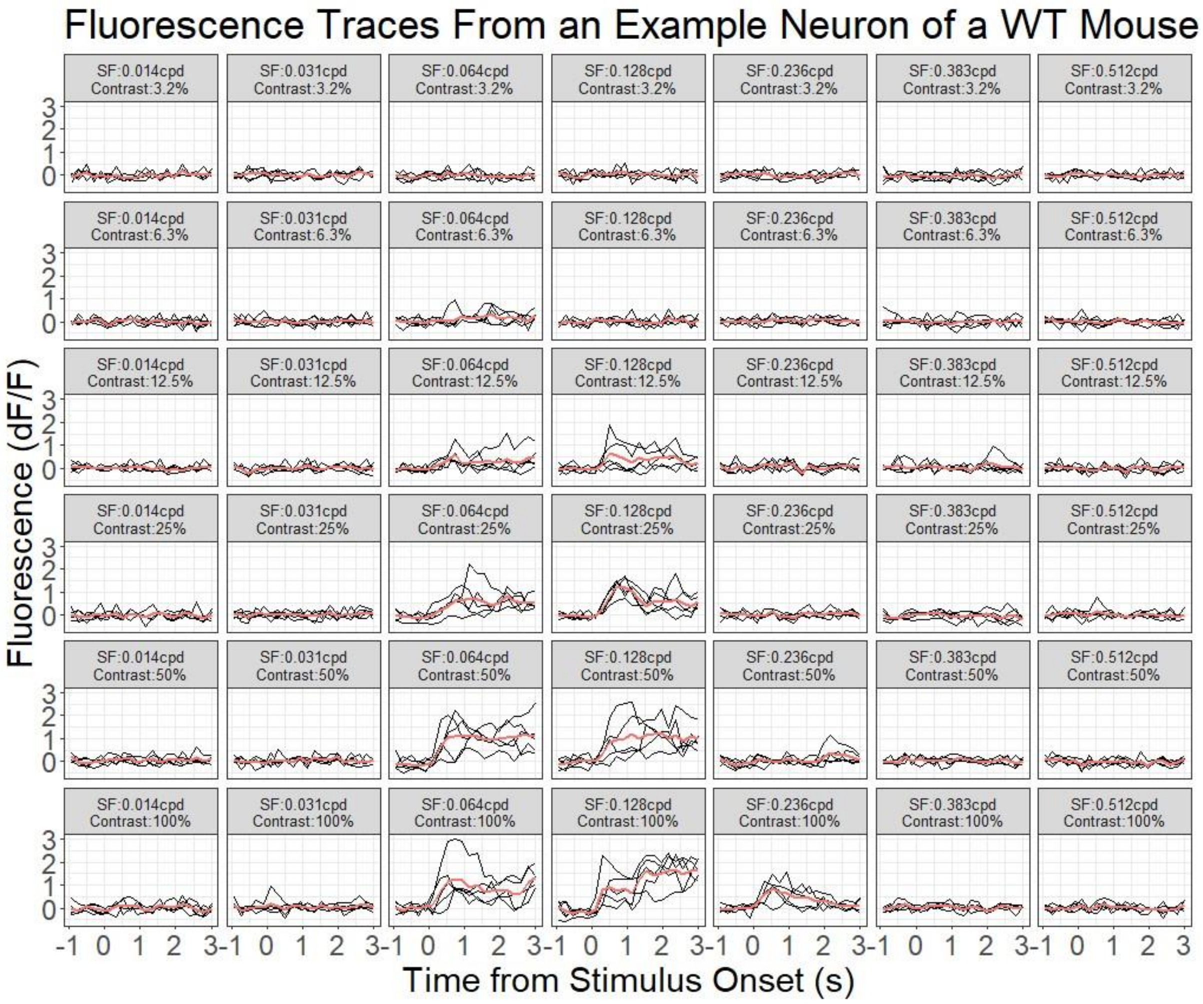

Figure 4 Example fluorescence traces of a GCaMP6f-labelled neuron from V1b of a WT mouse. This cell was responsive to stimuli of mid-high SF (0.064-0.128cpd). Fluorescence was measured as the change in

cell fluorescence over time relative to the average fluorescence of that cell (dF/F). Left-most plots show the cell fluorescence traces in response to stimuli of the lowest SF, with SF increasing with each plot to the right. The plots at the bottom of the image show the cell's fluorescence trace in response to stimuli at maximum contrast (100%). Plots higher up correspond to stimuli shown at lower contrasts. The SF and contrast to which each trace corresponds is shown in the title of each subplot. Black lines show the cell's fluorescence trace from a single trial (a single presentation of one of the 42 stimuli). Red traces show the average fluorescence trace of the cell to visual stimuli of that type. Time, expressed on the x axis, is relative to stimulus onset in seconds. The portion of the trace which is at time -1 to 0s corresponds to part of the baseline period, where a grey screen is shown before the stimulus is presented on screen. The portion of each trace from 0-3s corresponds to the 3 second period during which the stimulus was presented to the mouse.

For this specific cell, the CSF looks as shown in Figure 5.

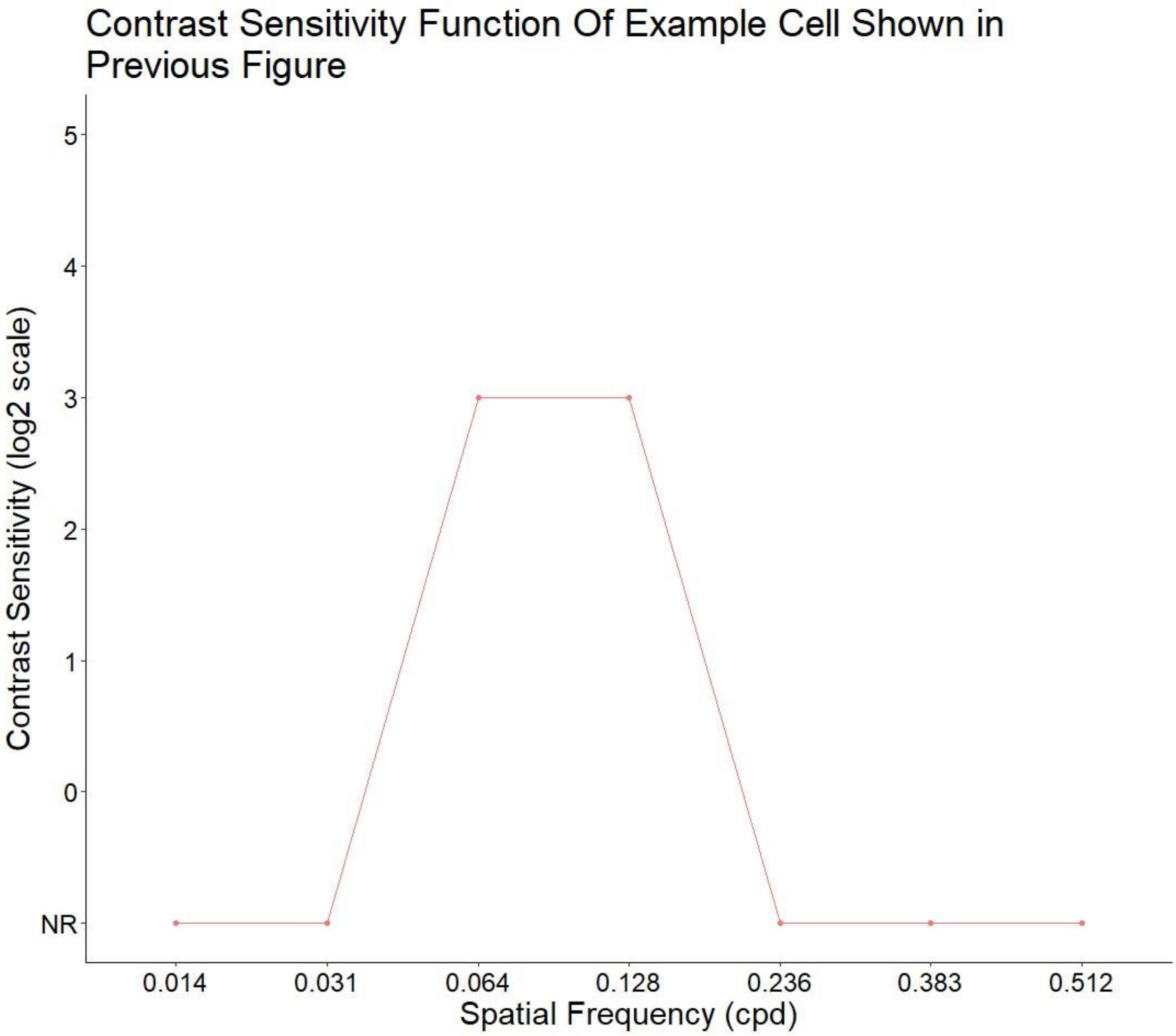

Figure 5 CSF of cell from which fluorescence traces are shown in Figure 4. The cell was found to be significantly visually responsive to stimuli of SFs 0.064 and 0.128cpd only, at contrast levels down to 12.5% in both cases. The cell is not responsive to stimuli at any other SF, as shown in this trace. Note that the points represent the processed data from each trace shown in Figure 4. Contrast sensitivity is measured as $log2(\frac{1}{Minimum\ Contrast\ For\ Response})$*.The minimum contrast for response value corresponds to the lowest contrast at which the stimulus was shown for the given SF, at which the cell gave a significant response. Thus, contrast sensitivity is measured on an ordinal 7-point scale. A contrast sensitivity of NR indicates that the cell was not responsive to stimuli of the given SF. SF is given in cpd.*

Figure 6 shows the average neuronal CSF from all visually responsive V1b neurons of a single WT animal imaged in this experiment. Figure 7 shows the average neuronal CSF from all visually responsive V1b neurons of a TS2Neo HET animal imaged in this experiment.

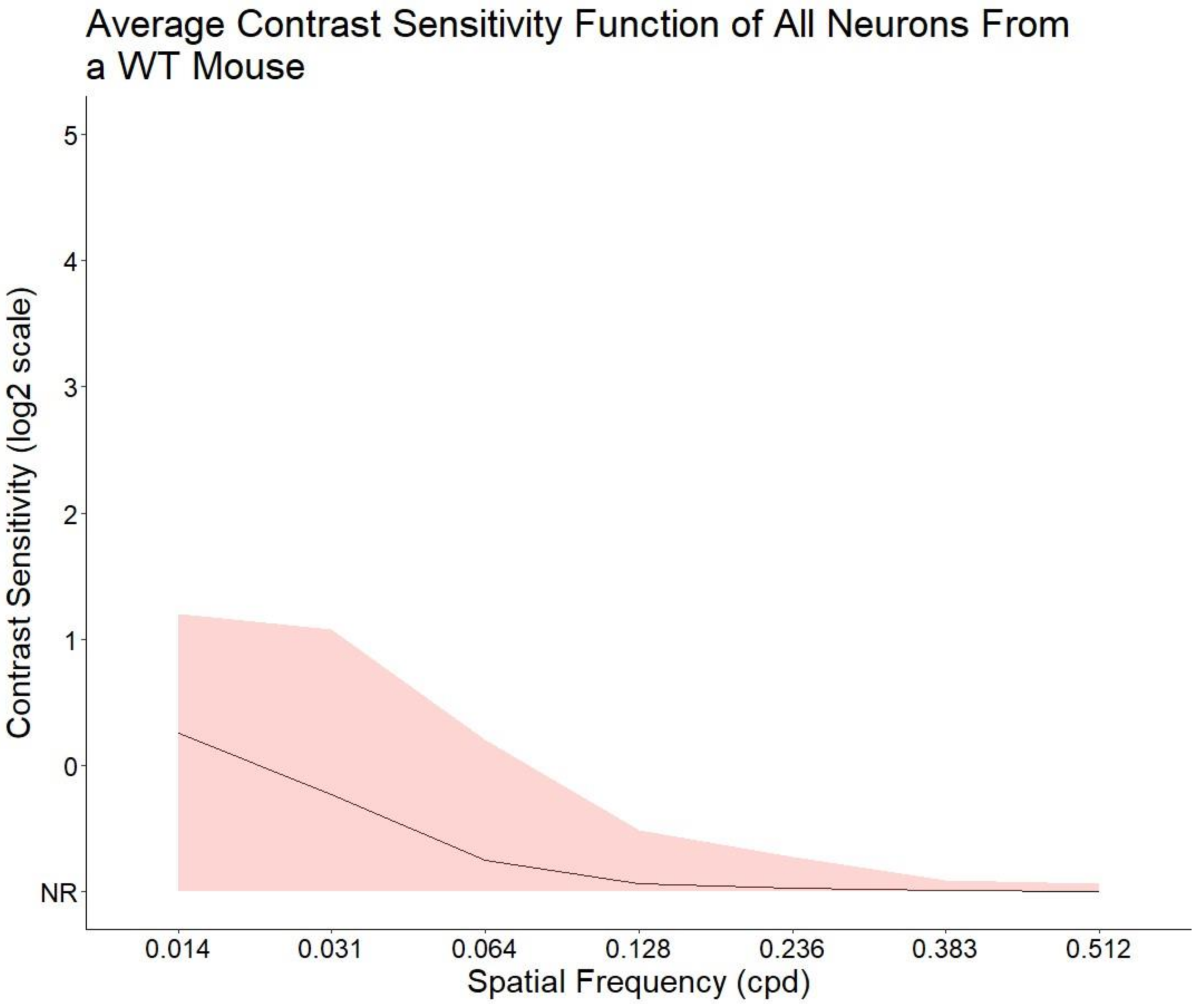

Figure 6 The average CSF from all visually responsive neurons imaged in a single WT mouse used in this experiment. Note how the contrast sensitivity is higher for lower-mid SF stimuli as compared to higher SF stimuli. The black line shows the mean contrast sensitivity, while the pink ribbon shows the variance in contrast sensitivity measured from cells in the experiment. Variance here is mean± standard deviation (lower boundary of variance being capped at NR). Contrast sensitivity is measured as $log2(\frac{1}{Minimum\ Contrast\ For\ Response})$. *Cells with contrast sensitivity of NR were not responsive to stimuli of the given SF. SF is given in cpd. This data was obtained from all 265 visually responsive V1b neurons recorded from a single WT animal.*

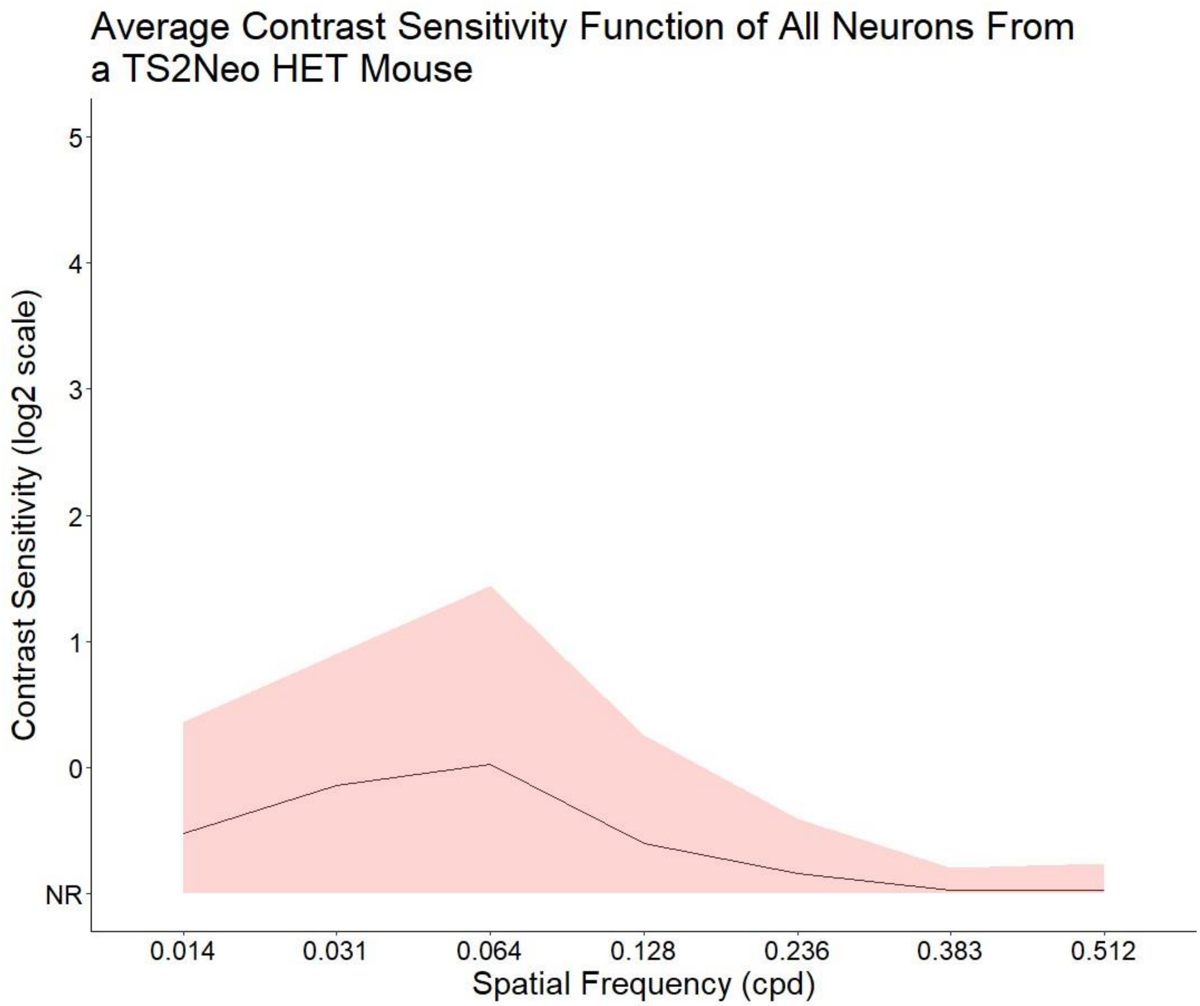

Figure 7 The average CSF from all visually responsive neurons imaged in a single TS2Neo HET mouse used in this experiment. Note how the contrast sensitivity is higher for mid-SF stimuli in this animal as compared to in the WT animal. The black line shows the mean contrast sensitivity, while the pink ribbon shows the variance in contrast sensitivity measured from cells in the experiment. Variance here is mean± standard deviation (with minimum contrast sensitivity being capped at NR). Contrast sensitivity is measured as $log2(\frac{1}{Minimum\ Contrast\ For\ Response})$. *Cells with contrast sensitivity of NR were not responsive to stimuli of the given SF. SF is given in cpd. This data was obtained from all 161 visually responsive V1b neurons recorded from a single TS2Neo HET animal.*

The total number of cells recorded from V1b of each animal was noted during data processing, and the proportion of these cells which were found to be significantly visually responsive was measured. A significantly lower proportion of all cells measured from TS2Neo mice were found to be visually responsive as compared to those from WT mice (Wilson test for equality of proportions: $P=2.1x10^{-6}$, $\chi^2=22.3$). 6.78% of all cells imaged in WT animals were found to be significantly visually responsive, while 5.09% of all cells from TS2Neo animals were visually responsive. For TS2Neo HET animals, the proportion of visually responsive cells varied between 2.10% and 8.15%. For WT animals, the proportion of visually responsive cells varied between 1.78% and 14.3%. This difference in data sampling is addressed in the “Limitations” subsection of the discussion.

Neuronal CSFs differ between TS2Neo and WT mice:

A cumulative link mixed model was generated to describe how contrast sensitivity differed by stimulus SF, by genotype and by SF-genotype interactions while accounting for between-animal variation. Variation in contrast sensitivity by SF is a CSF, a significant difference in contrast sensitivity by SF was expected. Variation in contrast sensitivity by genotype would suggest that genotype impacts contrast sensitivity for all visual stimuli, which was not an expected effect. Significant variance in contrast sensitivity resulting from the genotype-SF interaction would suggest that TS2Neo genotype impacts the CSF in the mouse. The proportional odds assumption of the model was tested graphically as described in the Methods section. The model was found to adequately meet this assumption.

The goodness of fit of the model to the data was assessed as described. The model was found to explain 17% of variances in contrast sensitivity measured for all cells (Cox and Snell (ML): pseudo R^2=0.170). Although this is low, this is to be expected as V1b cells tend to respond to stimuli of differing SFs. The SF to which a V1b neuron responds varies based on the cell's location, so different positions of cells within V1b could explain some of the variability not controlled for in the model (Zhang *et al.*, 2015).

SF of a visual stimulus significantly impacted neuronally measured contrast sensitivity to that stimulus ($P= 2.2x10^{-16}$, χ^2=1286, SF=6). This was expected, as contrast sensitivity to visual stimuli varies with the SF of that stimulus within CSFs. This positive result confirmed that the model appropriately described CSF data.

Contrast sensitivity was not found to vary with genotype (P=0.87, χ^2=0.03, degrees of freedom [DF]=1). This indicates that genotype does not impact contrast sensitivity in general. In other words, TS2Neo mice were not better or worse at seeing **all** types of visual stimuli as compared to WT mice. This was an expected finding. I did not anticipate a general difference in contrast sensitivity to visual stimuli across the board of SFs tested for TS2Neo as compared to WT mice.

The genotype-SF-interaction term included in the model was found to significantly impact contrast sensitivity ($P=4.1x10^{-16}$, χ^2=84.55, SF=6). This indicates that genotype impacts the CSF of mice. In other words, TS2Neo mice were found to have a significantly different neuronally measured CSF as compared to WT mice, providing evidence to support my hypothesis. The impact of genotype on CSF is shown in Figure 8.

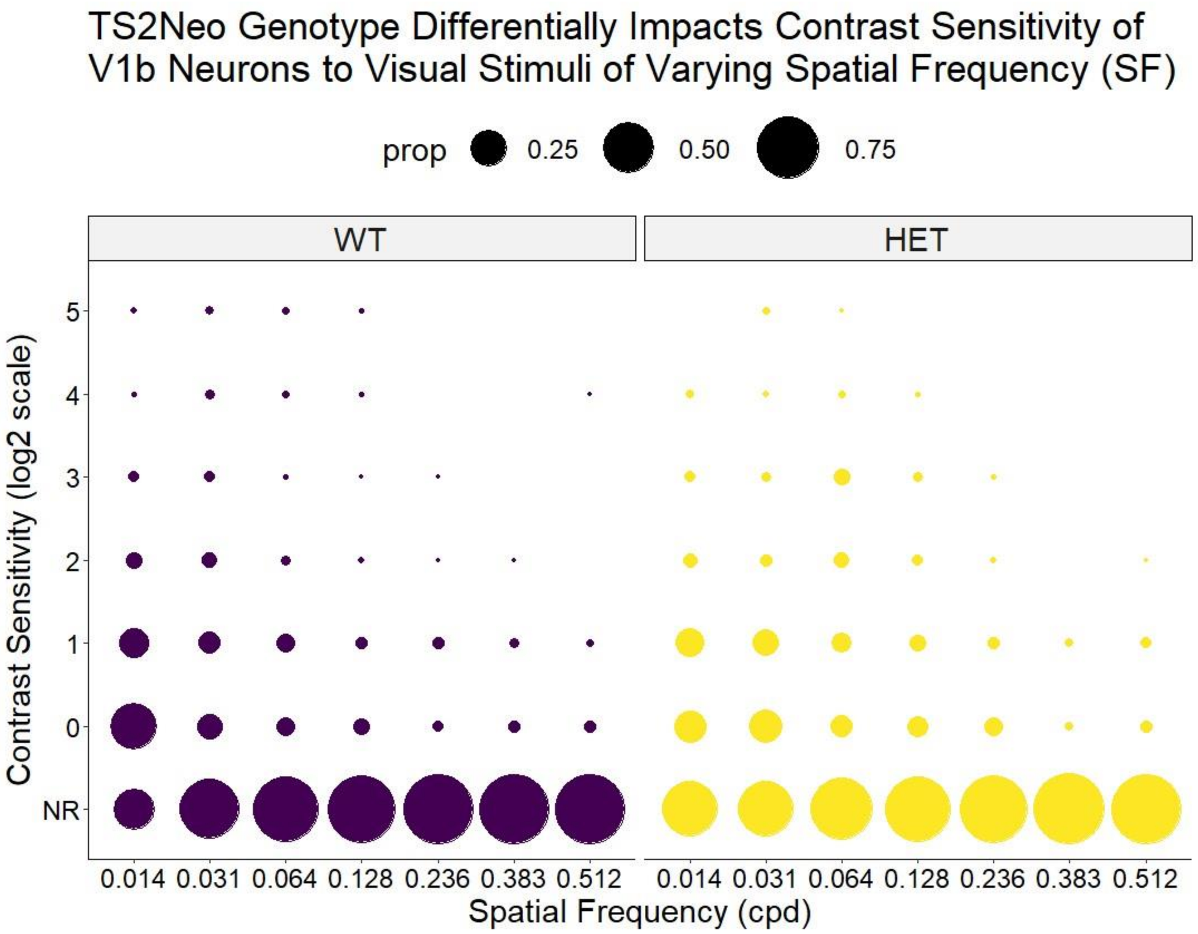

Figure 8 Plot showing how the contrast sensitivity of all cells differs by SF and genotype. HET subplot shows cells from TS2Neo HET mice, while the WT subplot shows cells from WT mice. Contrast sensitivity is measured as $log2(\frac{1}{Minimum\ Contrast\ For\ Response})$ *and NR means indicates cells that were not responsive to stimuli of the given SF. Contrast sensitivity of 0 indicates that cells responded to the stimuli at the given SF at 100% contrast only. Contrast sensitivity of 1 indicates that cells responded to the stimuli of the given SF at down to 50% contrast. SF is given in cpd. The size of the dots corresponds to the proportion of all visually responsive cells from animals of the specified genotype which fall within the contrast sensitivity category indicated on the y axis, for stimuli of SF shown on the x axis. The legend showing "prop" indicates the proportion of cells which corresponds to the given dot sizes, where prop is given in x/1. Note the difference in distribution of cells across the contrast sensitivity groups for stimuli of each SF by genotype. Specifically, cells from TS2Neo HET mice tend to fall within higher contrast sensitivity categories for stimuli of mid-high SF as compared to cells from WT mice, specifically for 0.064 and 0.128cpd stimuli. WT data was taken from 3360 cells across 4 animals (N=4, n=3360) HET (TS2Neo Heterozygous animal) data was taken from 3990 cells across 5 animals (N=5, n=3990).*

Figure 8 shows a plot with dots of various sizes on specific positions corresponding to the axes shown in the plot. SF is given on the x axis, while contrast sensitivity is given on the y axis. SF is in cpd, there is one column for stimuli of each SF tested. Contrast sensitivity is in log2(1/maximum contrast responsive to), where non-responsive cells fall within the category "NR". The size of the dots in each position displays the proportion of all visually responsive cells which fell into each contrast sensitivity category (indicated on the y axis) for visual stimuli of the SF specified (indicated on the x axis). The distribution of cells across the graph represents all neuronal CSFs from neurons of all animals from each genotype. Note how cells from TS2Neo mice tend to have higher contrast sensitivity to stimuli of mid-high range SFs (0.064cpd and 0.128cpd) as compared to WT mice, but have a lower contrast sensitivity to stimuli of low SF (0.014cpd) as compared to WT.

For completeness, similar plots for individual animals from each genotype are shown in Figure 9. This shows the between-animal variance in CSF-type distribution. This variance was accounted for in the cumulative link model regression used to analyse the dataset.

Between-Animal Variance in Contrast Sensitivitiy of V1b Neurons to Visual Stimuli of Various Spatial Frequencies (SF)

Figure 9 Plot showing contrast sensitivity of all neurons from each animal to visual stimuli of each of the specified SFs. Cells from WT animals are shown in purple. Cells from TS2Neo HET animals are shown in yellow. One subplot exists from each animal, the animal's identifier is indicated in the subplot title. Contrast sensitivity is measured as $log2(\frac{1}{Minimum\ Contrast\ For\ Response})$ *and NR means indicates cells that were not responsive to stimuli of the given SF at any contrast shown. SF is given in cycles cpd. The size of the dots corresponds to the proportion of all visually responsive cells from the specified animal which fall within the contrast sensitivity category indicated on the y axis, for stimuli of SF shown on the x axis. The legend showing "prop" indicates the proportion of cells which corresponds to the given dot sizes, where prop is given in x/1. The between-animal variance indicated in this plot was accounted for in the regression analysis method used. The number of visually responsive cells recorded from each animal is as listed (WT: CFRC038: n=532, CFRC039: n=1855, CFRC040: n=217, CFRC041: n=756; TS2Neo HET: CFRC032:n=714, CFRC033: n=1127, CFRC034: n=686, CFRC035: n= 1197, CFRC037: n=266).*

Cumulative link mixed model regression analysis indicated that CSF and contrast sensitivity measures for both WT and TS2Neo mice could be obtained from V1b neuronal imaging data. TS2Neo mice did not have any abnormalities in general contrast sensitivity, as expected. TS2Neo mice had abnormal CSF as compared to WT mice; they were found to have SF-specific abnormalities in contrast sensitivity as compared to WT mice.

TS2Neo genotype differentially changes contrast sensitivity to visual stimuli of high and low SFs:

Post-hoc testing was used to determine how the TS2Neo genotype impacted contrast sensitivity to visual stimuli of each of the 7 SFs tested. This involved comparison of the estimated marginal means predicted by model for cells of each genotype. The results are shown in Table 2 below:

Table 2 Results from post-hoc testing of cumulative link model to show the genotype impact on contrast sensitivity for each SF tested; sf means significant figures

SF (cpd)	**Z ratio (3sf)**	**P (3sf)**	**Adjusted P (Holm-Bonferroni; 3sf)**
0.014	-4.24	0.000100	0.000700
0.031	1.17	0.245	0.487
0.064	2.72	0.00650	0.0378
0.128	2.73	0.00630	0.0378
0.236	2.40	0.0166	0.0664
0.383	-1.65	0.0997	0.299
0.512	0.329	0.742	0.742

Cells from TS2Neo mice were found to have a significantly lower contrast sensitivity to visual stimuli of the lowest SF tested (0.014cpd) but were found to have a significantly higher contrast sensitivity to visual stimuli of mid-range SFs (0.064cpd and 0.128cpd).

No genotype differences in contrast sensitivity to stimuli of any other SF were detected (0.031cpd, 0.236cpd, 0.383cpd, 0.512cpd).

Based on the model, cells from TS2Neo mice were less likely to be responsive to stimuli of the lowest SF as compared to those WT (SF 0.014cpd: WT=59%, TS2Neo=40%), and were less likely to be responsive for all contrasts except the lowest tested as compared to those from WT (50% contrast: WT=35%, HET=20%; 25% contrast: WT=17%, HET=9%; 12.5% contrast: WT=7%, HET=3%; 6.3% contrast: WT=3%, HET=1%; 3.2% contrast: WT=1%, HET=1%).

Based on the model, cells from TS2Neo mice were more likely to be responsive to visual stimuli of mid-high range SFs as compared to those from WT (**SF 0.064cpd**: WT=17%, HET=27%; **SF 0.128cpd**: WT=10%, HET=17%). Cells from TS2Neo mice were found to be more likely to have higher contrast sensitivities to stimuli of mid-range SFs also (**SF 0.064cpd**: 50% contrast: WT=7%, HET=12%, 25% contrast: WT=3%, HET=5%, 12.5% contrast: WT=1%, HET=2%, 6.3% contrast: WT=0%, HET=1%, 3.2% contrast: WT=0%, HET= 0%; **SF 0.128cpd**: 50% contrast: WT=4%, HET=7%, 25% contrast: WT=2%, HET=3%, 12.5% contrast: WT=1%, HET=1%, 6.3% contrast: WT=0%, HET=0%, 3.1% contrast: WT=0%, HET=0%).

Cells from TS2Neo mice were also predicted to be more likely to be visually responsive to stimuli of mid-high range SF (0.064cpd and 0.128cpd) but less likely to be visually responsive to stimuli of low SF (0.014cpd) as compared to cells from WT mice. This difference is shown from the raw data in Figure 10.

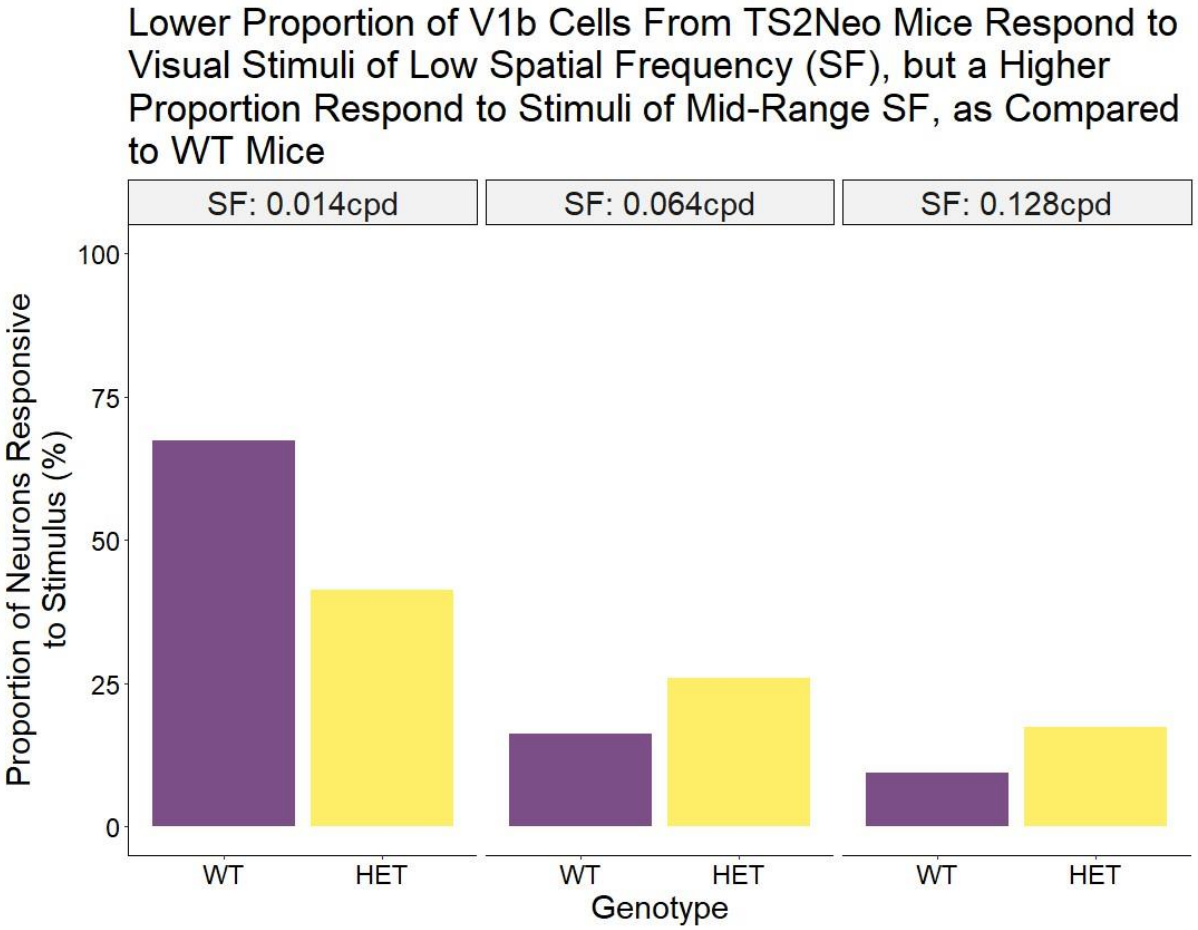

Figure 10 Figure showing the proportion of all V1b cells recorded from WT and TS2Neo mice which were found to respond to visual stimuli of one low SF stimulus (0.014cpd), and two mid-high range SF stimuli (0.064cpd and 0.128cpd) in this experiment. Responsive cell numbers are pooled across animals of each genotype. Note how the percent of cells which respond to visual stimuli of low SF is lower in TS2Neo as

compared to WT mice, but the percentage of cells which respond to visual stimuli of mid-high range SFs is higher in TS2Neo mice as compared to WTs.

In all, cells from TS2Neo mice were less likely to respond to stimuli of low SF (0.014cpd) but were more likely to respond to stimuli of mid-high SF (0.064cpd and 0.128cpd) as compared to cells from WT mice. Cells from TS2Neo mice also tended to have lower contrast sensitivity to stimuli of low SF and higher contrast sensitivity to stimuli of mid-high SF as compared to cells from WT mice.

Discussion:

Contrast sensitivity abnormalities in TS2Neo as compared to WT mice:

In this study, TS2Neo mice were found to have significant differences in a specific visual function as compared to WT mice based on the responses of GCaMP6f-labelled neurons recorded from V1b of mice from each genotype. TS2Neo mice were found to have significantly different neuronally measured CSFs. TS2Neo mice had a higher contrast sensitivity to mid-high SF visual stimuli (0.064cpd and 0.128cpd) as compared to WT mice, but had a significantly lower contrast sensitivity to visual stimuli of low SF (0.014cpd) as compared to WT. Neurons from TS2Neo mice were less likely to respond to visual stimuli of low SF, but more likely to respond to visual stimuli of mid-high range SF as compared to those from WTs. This study provides the first evidence of a visual processing abnormality in the TS2Neo mouse.

Contrast sensitivity abnormalities in TS2Neo mice as compared to visual abnormalities in TS patients:

The results of this study point to a basic visual processing abnormality in TS2Neo as compared to WT mice. This finding suggests that classical TS mutations may result in abnormal visual processing at the cortical level. The TS2Neo mice used in this experiment were designed to be heterozygous for a modified version of the TS2 mutant *CACNA1C* gene (Bader *et al.*, 2011; Bett *et al.*, 2012).

TS patients have previously been reported to have disturbed visual and neurological function (Splawski *et al.*, 2005; Gillis *et al.*, 2012; Bozarth *et al.*, 2018; Walsh *et al.*, 2018). Three TS2 patients reported in the literature have been found to have abnormalities in eye movement and function, with comorbid neurological disorder (Splawski *et al.*, 2005; Walsh *et al.*, 2018). The first TS2 patient described in Splawski *et al. (*2005) was reported to have abnormal eye movements, differing pupil sizes and developmental delay. Both TS2 patients reported by had eye abnormalities and developmental delay. Two TS2 patients were described by Walsh *et al.* (2018). One patient had abnormal eye movements, the other had strabismus, and both exhibited developmental delay. This suggests that the TS2 mutation disrupts both visual and neurological function.

My finding of abnormal visual function in the TS2Neo mouse suggests that the TS2 mutation may be associated with abnormalities in visual perception and processing.

Evidence to support this theory is provided by case reports from TSA patients, also described in the introduction of this chapter. Two TSA patients with TSA mutations exhibited visual perceptual dysfunctions (Gillis *et al.*, 2012; Bozarth *et al.*, 2018). Gillis *et al.* (2012) described a TSA patient who was unable to visually track or fixate at the age of 18 months. This indicates a lack of conscious visual perception by the patient (Overbeek *et al.*, 2018; Chokron, Kovarski and Dutton, 2021). The mutation found in this visually disrupted TSA patient causes an amino acid change, V1363A, which is predicted to alter the function of the CaV1.2 channel in a similar way to the G406R amino acid change which results from the TS2 mutation. Specifically, the V1363A change is predicted to disrupt gating of the CaV1.2 channel (Gillis *et al.*, 2012). Disruptions in CaV1.2 channel gating, specifically voltage inactivation, result from the TS2-related G406R change (Splawski *et al.*, 2005; Walsh *et al.*, 2018). Another TSA patient described by Bozarth *et al.* (2018) was found to be cortically blind, completely lacking conscious visual perception, also exhibiting abnormal gaze and having severe neurodevelopmental delay. The mutation which caused TS in this individual results in an amino acid change, A1473G, within the CaV1.2 channel. Again, this mutation is predicted to cause functional changes in the CaV1.2 like those resulting from the TS2 mutation. The amino acid substitution occurs in a similar position to that resulting from the TS2 mutation, but on domain IV instead of I (for TS1 and TS2 mutations). The effects of the G406R and A1473G amino acid substitutions resulting from TS2 and this specific TSA mutation are therefore predicted to cause similar impacts on channel function as caused by the TS2 mutation (Bozarth *et al.*, 2018). Case reports indicate that functional changes in the CaV1.2 channel which result in abnormalities in gating properties of the channel, such as those caused by the classical TS2 mutation, result in combined visual and neurological abnormalities in TS patients.

Findings from this study when considered alongside the reported phenotypes of TS patients suggest that TS mutations which reduce VDI of the CaV1.2 channel can result in disturbances in visual processing and function in the human and in the mouse.

Sensory processing abnormalities in TS and in TS2Neo mice:

It is possible that TS mutations may result in generalised abnormalities in sensory perception. In this study, I found a basic visual functional difference in TS2Neo mice as compared to WTs. TS2Neo mice were found to be better able to respond to visual stimuli of mid-range SFs, but were less able to respond to stimuli of low SF as compared to WT. A previous study by Rendall *et al.* (2017) found that TS2Neo mice had a superior ability to respond to short-duration disruptions within auditory stimuli as compared to WT mice. Perceptual abnormalities have now been reported in two sensory domains of the TS2Neo mouse. Differences in low level sensory function found in the TS2Neo mouse have yet to be tested for in TS patients, however, it seems that classical TS mutations may result in differences in generalised sensory processing and function across multiple sensory modalities. In support of this theory, it should be noted that TS is associated with ASD (Splawski *et al.*, 2004), which often presents with abnormal sensory processing symptoms across multiple sensory modalities (Marco *et al.*, 2011). Specifically, basic visual and auditory perceptual abnormalities have been reported in ASD patients (Marco *et al.*, 2011; Robertson and Baron-Cohen, 2017), as have now been found in the TS2Neo mouse both here and by Rendall *et al.* (2017). The superior auditory processing ability in TS2Neo mice found by Rendall *et al.* (2017) is similar to those previously reported in ASD patients (Bertone *et al.*, 2005; Mottron *et al.*, 2006). However, reports of ASD-type differences in auditory processing abilities are often conflicting (Kwakye *et al.*, 2011). The superior visual processing ability in TS2Neo mice found in this study is similar to those found in ASD patients in several reported studies. These are discussed in subsection “Comparison of contrast sensitivity abnormalities found in the TS2Neo mouse, in ASD patients and in mouse models of ASD”.

Overall, there is some evidence to suggest that TS mutations cause general abnormalities in sensory processing. The abnormalities in visual processing found in the TS2Neo mouse model of TS somewhat reflect those found in ASD patients.

Comparison of contrast sensitivity abnormalities found in TS2Neo mouse, in ASD patients and in mouse models of ASD:

As discussed in the introduction, Cheng *et al.* (2020) found that the inbred BTBR mouse model of idiopathic ASD had higher contrast sensitivity to mid-high SF visual stimuli as compared to WT mice. Kéïta *et al.* (2014) found that ASD patients had abnormal CSF, having higher contrast sensitivity to high SF stimuli as compared to controls.

In this study, I found that TS2Neo mice had an increased contrast sensitivity to mid-high SF visual stimuli as compared to WT. These findings are similar to those reported in ASD patients and in the BTBR mouse model of idiopathic ASD. This suggests that the TS2 mutation may cause changes in contrast sensitivity and CSF which are ASD-relevant.

It should be noted that the TS2Neo mouse model did not have increased contrast sensitivity to visual stimuli of the highest SF tested (0.512cpd) as compared to WT. This differs from the reported findings in ASD patients and in the BTBR idiopathic ASD mouse model (Kéïta *et al.*, 2014; Cheng *et al.*, 2020).

The lack of increased contrast sensitivity to visual stimuli of the highest SFs in the TS2Neo mouse model as compared to that seen in the BTBR mouse model of idiopathic ASD could have multiple explanations. Classical TS mutations may cause TS-specific abnormalities in CSF and contrast sensitivities which are different to those typically seen in patients with ASD. The difference in finding may also be due to this study measuring CSF and contrast sensitivity to visual stimuli of specific SFs by functional imaging of neurons in V1b; where the study of Cheng *et al.* (2020) used behavioural measures of contrast sensitivity.

It should be noted that the literature contains conflicting reports of measured contrast sensitivity and CSF abnormalities in ASD patients (Davis *et al.*, 2006; McCleery *et al.*, 2007; Koh, Milne and Dobkins, 2010; Milne and Buckley, 2010; Guy *et al.*, 2016). ASD is also frequently associated with comorbid neuropsychiatric disorders which are individually associated with changes in contrast sensitivity and CSF (Fam *et al.*, 2013; Dönmez *et al.*, 2020; Al-Beltagi, 2021). Differential inclusion of patients with such comorbidities, and variance in the age of patients included in the studies exploring contrast sensitivity in ASD could explain the heterogenous findings.

Overall, my finding that TS2Neo mice had abnormal CSF and increased contrast sensitivity to mid-high SF stimuli was similar to that found in ASD patients by Kéïta *et al.* (2014) and in the BTBR mouse by Cheng *et al.* (2020). However the increased contrast sensitivity to highest SF stimuli found in the BTBR mouse model of ASD mouse model reported by Cheng *et al.* (2020) was not found in the TS2Neo mouse model, although this could be due to methodological differences. Overall, my findings are similar to those reported in ASD patients and in the BTBR mouse model of ASD. This suggests that the TS2Neo mouse model has basic visual processing abnormalities which resemble those seen in ASD.

TS2Neo and ASD-related contrast sensitivity abnormalities and potential impact on complex issues experienced by ASD patients:

ASD related changes in basic visual perception have been proposed to result in some of the complex issues experienced by ASD patients (Behrmann, Thomas and Humphreys, 2006; McCleery *et al.*, 2007; Coulter, 2009; Vlamings *et al.*, 2010; Marco *et al.*, 2011). TS2Neo mice were found in this study to have differences in basic visual perception which resemble those found in ASD. It is possible that changes in visual perception caused by the ASD-related classical TS2 mutation could impact visual processing in an ASD-relevant way.

Complex perceptual abnormalities in ASD:

ASD patients are known to have abnormalities in the recognition and processing of faces (Pelphrey *et al.*, 2002; Dalton *et al.*, 2005; Coulter, 2009; Minio-Paluello *et al.*, 2020; Chokron, Kovarski and Dutton, 2021; Stantić *et al.*, 2022; Zhou *et al.*, 2023). Abnormalities in visual processing of faces has repeatedly been proposed to result from basic perceptual abnormalities in ASD patients (Vlamings *et al.*, 2010; Chokron, Kovarski and Dutton, 2021; Zhou *et al.*, 2023).

Vlamings *et al.* (2010) found that patients with ASD processed facial expression from images of faces using high SF in preference to low SF elements of facial the stimuli, while the opposite was true for neurotypicals. This same preferential responsiveness to high vs low SF stimuli was seen on presenting ASD patients with grating stimuli also, while again, the opposite was true for neurotypical subjects. This suggests that: a) ASD patients preferentially respond to high SF, as compared to low SF visual stimuli, while the opposite is true for neurotypical individuals; and b) ASD patients use high SF elements of facial stimuli in perception of faces, with the opposite being true for neurotypicals. In this study, I found V1b neurons of the TS2Neo mouse had higher contrast sensitivity to visual stimuli of high-mid SF as compared to WT. Indeed, the CSF was shifted more toward the higher SF stimuli for TS2Neo mice as compared to WTs, suggesting a preferential ability to respond to stimuli of higher SFs as compared to WT mice. This ASD-related mutation may lead to changes in basic visual processing which are also seen in idiopathic ASD. These changes in basic visual perception could lead to the development of abnormalities in facial processing seen in ASD.

Other theories suggest that mechanisms unrelated to basic perceptual abnormalities result in abnormal facial processing and recognition in ASD patients. Abnormalities in the function of the fusiform gyrus, which is involved in the processing of faces, has been suggested to result in ASD-type changes (Dalton *et al.*, 2005). A further theory suggests that impaired facial processing results from ASD individuals being unable to assign appropriate reward to social stimuli, including faces (Behrmann, Thomas and Humphreys, 2006).

Overall, it is thought that the deficits in perception of faces in patients with ASD result from either a) abnormalities in basic visual processing—such as the abnormal contrast sensitivities reported in the ASD-related TS2Neo mouse, in ASD patients and in the BTBR ASD model mouse—causing abnormal processing of complex stimuli; b) abnormalities in visual information processing of complex stimuli in higher visual areas; or c) abnormalities in assigning importance to socially relevant information. ASD patients typically have abnormalities in processing of faces.

I have demonstrated in this study that the ASD-related TS-type mutation causes basic visual processing abnormalities in the mouse. Based on this finding, and on findings of other studies in the literature, I propose that changes in basic visual processing may at least partially be responsible for the abnormal perception of faces reported in ASD patients.

Functional imaging of neurons in V1of awake behaving mice can be used to obtain contrast sensitivity and CSF measurements from disease model mice without the need for behavioural training of, or dependence on reflex response measurements from mice:

Contrast sensitivity and CSF are implicated in many neuropsychiatric as well as non-neuropsychiatric disorders (Kogan *et al.*, 2004; Skottun and Skoyles, 2007; Fam *et al.*, 2013; Niemeyer and Paradiso, 2017; Dönmez *et al.*, 2020; Perche *et al.*, 2021; Kadivar *et al.*, 2023). Mouse models are used in the study of many such disorders. Phenotypical abnormalities seen in mouse models of disease are often difficult to relate to those seen in the human condition. This is especially true for mouse models of neuropsychiatric disorder. Measuring changes in basic perceptual ability in a mouse disease model could provide a way in which one could detect phenotypical changes in the model which are also seen in the human condition.

Contrast sensitivity and CSF have both been used as a way of measuring phenotypical changes in mouse disease models previously (Feng *et al.*, 2013; Xiao *et al.*, 2019; Cheng *et al.*, 2020). Human experiments measuring CSF and contrast sensitivity in disease patient cohorts often involve measuring conscious responses to visual stimuli (Kogan *et al.*, 2004; McKendrick *et al.*, 2007; Kéïta *et al.*, 2014; Dönmez *et al.*, 2020). Conscious responses to visual stimuli require the involvement of cortical visual areas, such as V1 (Leopold, 2012). Experiments which involve measuring CSF and/or contrast sensitivity in mouse disease models based on behavioural responses of the animal to visual stimuli of varying SF and contrast. These behavioural responses are typically reflexive in nature. Reflexive responses to visual stimuli depend on lower visual areas which are not sufficient for conscious visual perception (Distler and Hoffmann, 2011). One cannot rely on measurement of reflexive responses of disease model animals to detect abnormalities in contrast sensitivity at the level of conscious visual perception in disease model animals. Measuring learned behavioural responses of disease model animals to visual stimuli of varying SF and contrast could be an alternative method to detect abnormalities contrast sensitivity and CSF in these animals. This method would involve training the animals to behaviourally respond to stimuli of each SF when shown at 100% contrast. The stimuli would then be shown at reduced contrast levels, and the behavioural responses of the animal to each stimulus shown at each contrast level would be measured. Using the behavioural responses of the animals as a measure of what the animal can see assumes that the animal can generalise the associate-learned response to a visual stimulus of each SF, at 100% to visual stimulus of that SF at lower contrasts. This method also requires extensive animal training, such that it can respond to visual stimuli of each SF with a high success rate. This method would be the most comparable to those used to measure contrast sensitivity and CSF in patient cohorts. However, the method would be time-consuming, potentially stressful for the animal, and would rely on the animal to be able to perceptually generalise stimuli of varying contrasts, such that they understand to respond to a stimulus of a given SF with a learned response, regardless of the contrast at which the stimulus is shown.

In this experiment, I measured the activities of GCaMP6f-labelled neurons in V1b of the mouse visual cortex in response to visual stimuli of varying SF and contrast, to obtain CSF and contrast sensitivity measures from mice. In this way, I was able to detect visual stimuli that the mouse could perceive at the cortical level without relying on detection of learned behavioural responses. The experiment involved a single 2-hour surgery, 1 week of handling and habituation, and just three 43-minute experimental recording sessions per animal.

The method described in this chapter, using the setup described in Appendix 1 could be used to detect contrast sensitivity and CSF functional changes in mouse models of specific diseases. This method does not rely on non-conscious reflexive responses and does not rely on the assumptions that learned behavioural responses to stimuli will be generalised for stimuli shown at reduced contrast levels.

This method could be adapted as described in Appendix 1 to allow for the measurement of conscious behavioural responses of mice to visual stimuli of each SF, shown at each contrast level alongside neuronal response measurement. Details of the experimental setup involved, and instructions for setup, installation and use of equipment and software, as well as the codes required to run the experiment are provided in Appendix 1. The imaging modality can easily be switched out with any other single-neuron functional imaging method which involves the use of NI DAQ sampling hardware which can be read into MATLAB. Adaptation of this experiment to use Python would be advantageous in the future, to avoid licence requirements and to avoid MATLAB-specific issues with DAQ hardware sampling (described in Appendix 1).

Limitations:

In this study, I reported TS2Neo related differences in contrast sensitivity and CSF based on measuring V1b neuronal activity as a proxy for conscious visual perception. Human experiments which involve measuring disease-related changes in CSF and/or contrast sensitivity often involve recording conscious behavioural responses to visual stimuli, such as yes/no answers (Kogan *et al.*, 2004; McKendrick *et al.*, 2007; Kéïta *et al.*, 2014; Dönmez *et al.*, 2020). I did not measure conscious behavioural responses to visual stimuli in this experiment, making the methods described here less comparable to those used in human experiments. For any single experiment I sampled hundreds to thousands of neurons within the field-of-view selected within a random dorsolateral and anteroposterior position in V1b from a single mouse. The ability of neurons to respond to stimuli of high SF is known to vary across the anteroposterior axis of V1 in the mouse (Zhang *et al.*, 2015). However, I sampled 3 separate regions along the anteroposterior axis of V1b from each animal to avoid this issue. I made every effort to ensure that areas sampled were similar across animals.

A potential limitation of this study is that I measured fluorescence emitted by the GCaMP6f calcium indicator as a proxy for measuring neuronal activity in V1b neurons. An increase in GCaMP6f-expressing cell fluorescence results from an increase in intracellular calcium concentration. An increase in intracellular calcium concentration, in turn, is assumed to result from an increase in cell activity. This is why changes in fluorescence of GCaMP6f-expressing neurons are often used as a proxy for measuring changes in neuronal activity (Chen *et al.*, 2013). The TS2 mutant CaV1.2 channel expressed by the TS2Neo mouse GCaMP6f-labelled neurons, almost completely lack VDI. These mutant channels remain open for an extended time period when activated, when the cell is depolarised (Splawski *et al.*, 2004; Bett *et al.*, 2012). This results in an abnormally prolonged influx of calcium into those cells (Splawski *et al.*, 2004). One would expect that a GCaMP6f-expressing neuron in the TS2Neo mouse would have a greater fluorescence increase on cell activity, as compared to a similar cell from a WT mouse. This could impact the proportion of cells found to be responsive to each visual stimulus in TS2Neo mice. This would impact my results. If this were the case, one would expect that a higher proportion of neurons recorded from TS2Neo mice would be found to be visually responsive as compared to WT. I tested whether the proportion of all cells found to be visually responsive recorded from TS2Neo and WT mice differed by genotype. A genotype difference was found, however, the proportion of neurons recorded from TS2Neo mice which were found to be visually responsive was lower than for WT mice. This was the opposite effect to what one would expect with the potential GCaMP6f-related methodological issue described. The genotype difference found could be due to variability in expression of GCaMP6f, in cranial window clarity and quality, or simply due to between-animal differences. These are all methodological variables which cannot be controlled for. A final limitation is that this study involved small sample sizes, with only 5 TS2Neo and 4 WT mice being used. Low sample sizes reduce the power of experiments, but also increase the risk of sample-dependent findings (Serdar *et al.*, 2021). However, it should be noted that the difference in CSF found between mice of each genotype was extremely statistically significant. Low statistical power did not appear to be an issue in this study.

Future experiments:

Repetition of this study, using larger sample sizes should be conducted. Any genotype difference in the proportion of all cells found to be visually responsive should be measured. Genotype differences in the proportion of cells found to be visually responsive could indicate that measuring changes in GCaMP6f-expressing neuron fluorescence as an indicator of cell activity is inappropriate in this instance. Should this be the case, repetition of this experiment using a virally transfected voltage indicator expressed in neurons such as that described by Liu *et al.* (2022) would be recommended.

Repetition of this experiment in TS2Neo and WT mice, or use of this method to test CSF and contrast sensitivity to visual stimuli of specific SF in any animal disease model could involve simultaneous recording of conscious, learned behavioural responses to visual stimuli, such as those measured in the wheel-turn behavioural paradigm of Burgess *et al.* (2017). Comparing behavioural CSF and contrast sensitivity measurements from disease model animals to the behavioural CSF and contrast sensitivity responses measured in patient cohorts would be a useful as a more direct methodological comparison. Furthermore, comparison of the behavioural and neuronally measured CSF and contrast sensitivities from animal disease models could confirm the relevance of using neuronal responses to measure CSF and contrast sensitivity in disease model animals.
Measuring contrast sensitivity and CSF in TS2Neo and WT mice using the optokinetic reflex methods of Cheng *et al.* (2020) would allow one to determine whether visual processing is impacted at the subcortical level, as well as the cortical level, as was shown in this experiment. This would enable us to locate the neural loci of visual processing changes resulting from the classical TS2-type mutation in TS2Neo mice that were indicated by the findings of this study.

A large, multi-centre study which involves testing CSF and contrast sensitivity using reflex response measures and, if possible, conscious behavioural response measures in children with TS would be useful to understand if and how this basic visual function is impacted in the human condition. Completion of a battery of basic sensory processing tests such as that described by Vaughan *et al.* (2020) for each child would also be useful in understanding any TS-related abnormalities in any type of sensory processing and perception. Comparison sensory abnormalities seen in TS patients with those seen in ASD patients would also show whether sensory processing changes seen in TS are like those seen in patients with ASD, or if they are TS-specific.

Human experiments investigating CSF and contrast sensitivity in multiple different, but homogenous large cohorts of ASD patients and age-matched controls should be completed. This would allow us to confirm any ASD-related change in contrast sensitivity and CSF, and to explore any dependence of this change on patient age, comorbidities, and on the methods used to measure CSF and contrast sensitivity.

The methods described in this chapter, and in Appendix 1 could be used to study contrast sensitivity and CSF changes in other animal disease models. One could measure changes in contrast sensitivity and CSF for the BTBR mouse model using neuronal methods. This would be of interest in exploring the visual perceptual changes reported by Cheng *et al.* (2020) for this mouse model of idiopathic ASD. Adaptation of the codes and setup, as well as the methods described in this chapter could produce an experimental protocol by which one could measure neuronal responses in primary sensory areas of the mouse to basic sensory stimuli. The adapted protocol could be used to explore basic sensory perceptual abnormalities in mouse models of disease. This would allow one to test for perceptual abnormalities independent of measuring learned behavioural responses, which rely on animal training, which is typically of a low success rate, or on measuring reflexive behavioural responses which do not sensory processing at the cortical level.

Specifically, exploring changes in neuronal sensory processing in ASD mouse models would be prudent to attempt to understand the physiological basis of any maladaptive sensory processing change caused by ASD-related genetic mutations. Identifying the basis of any ASD-related change in sensory processing could result in a better understanding of disruptive abnormalities in sensory perception often experienced by ASD patients. This could result in the identification of novel lines of treatment which could improve the quality of life of ASD patients, their families, and carers.

The methods described here could be used to explore CSF and contrast sensitivity in mouse models of ophthalmic diseases, such as glaucoma, diabetes related retinopathy, and cataract. Reported experiments aimed to explore changes in CSF and contrast sensitivity in these mouse models have relied on measuring changes in reflexive responses to visual stimuli (Feng *et al.*, 2013; Xiao *et al.*, 2019). The methods could also be used to explore CSF and contrast sensitivity in animal models of neuropsychiatric disease in which we know that CSF and/or contrast sensitivity are disrupted. This includes diseases such as schizophrenia (Skottun and Skoyles, 2007), Fragile X (Kogan *et al.*, 2004), and ADHD (Dönmez *et al.*, 2020).

Conclusion:

I measured contrast sensitivity for visual stimuli of varying SF in TS2Neo and WT mice by functional imaging of visually responsive neurons in L2/3 of V1b of these animals. I successfully obtained CSF and contrast sensitivity measurements from each responsive neuron from each mouse using the methods described in this chapter and in Appendix 1. TS2Neo mice were found to have a significantly different CSF as compared to WT mice. TS2Neo mice had a higher contrast sensitivity to visual stimuli of mid-high SF (0.064cpd and 0.128cpd), and reduced contrast sensitivity to visual stimuli of low SF (0.014cpd) as compared to WT mice. Neurons from TS2Neo mice were found to be significantly more likely to be responsive to visual stimuli of mid-range SFs as compared to those from WT mice. Neurons from TS2Neo mice were less likely to be responsive to visual stimuli of low SF as compared to neurons from WT mice. Classical TS mutations appear to reduce contrast sensitivity to visual stimuli of low SF and increase contrast sensitivity to mid-high SF visual stimuli in the mouse. This should be tested in TS patients. Current evidence from the TS2Neo mouse suggests that TS mutations may impact sensory processing across multiple different sensory modalities, with evidence of such changes now existing for the auditory and visual domains. The methods described in this study can be used and adapted to explore neural processing of sensory stimuli in mouse models of neuropsychiatric and non-neuropsychiatric disorders.

Contributions:

Experiment design and methodology were developed by Rosie Craddock under guidance from Professor Frank Sengpiel. Equipment maintenance and overhaul was performed by Rosie Craddock with assistance from Dr Adam Ranson, Mr Gavin Mills and Mr Diego Sangineto of Thorlabs. Codes for experiment paradigms, data processing and analysis were written largely by Rosie Craddock, with assistance from individuals stated in Appendix 1. Surgeries were carried out by Mrs Fangli Chen. Animal handling and habituation were undertaken by Rosie Craddock with assistance from Mrs Fangli Chen. Experimental recordings were undertaken by Rosie Craddock. Genotyping was performed by Dr Stephanie Bagstaff.

Data Chapter 2: AP duration is increased in pyramidal cells from three cortical regions of TS2Neo as compared to WT mice:

Introduction:

TS is a multisystemic disorder caused by mutations in the *CACNA1C* gene. The *CACNA1C* gene encodes the pore-forming α-1 subunit (CaV1.2) of the L-type voltage-gated calcium channel (Splawski *et al.*, 2004, 2005). In classical TS, expression of mutant *CACNA1C* results in the production of CaV1.2 channel subunits which almost completely lack VDI (Splawski *et al.*, 2004, 2005; Dick *et al.*, 2016). Cardiac cells expressing these mutant channels have been found to have an abnormally long APs (Dick *et al.,* 2016). Pancreatic β cells expressing TS mutant CaV1.2 channel subunits are also predicted to have abnormal electrophysiology (Kummer *et al.*, 2022). In both cardiac and pancreatic β cells, the CaV1.2 channel is substantially electrogenic, and contributes to the depolarisation phase of the AP waveform (Ashcroft and Rorsman, 1989; Hofmann *et al.*, 2014; Tuluc *et al.*, 2021; Shah *et al.*, 2022). It is logical that changes in the CaV1.2 channel function within both cardiac and pancreatic β cells would alter the electrophysiological properties of these cells.

Interestingly, evidence suggests that classical TS mutations also cause prolonged APs in neurons. This evidence comes from a study by Paşca *et al.* (2011) which involved using iPSC-derived neurons from TS1 patients and control subjects to explore the impact of the TS1 mutation on neuronal cellular properties. iPSC-derived neurons from TS patients were found to have a prolonged AP as compared to those from controls. This suggests that the classical TS1 mutation results in increased AP duration for neurons, as it does for cardiac myocytes (Splawski *et al.*, 2004, 2005; Dick *et al.*, 2016). However, this prolonged AP has not been demonstrated in mature neurons which have developed in natural brain tissue from a complete organism. It is possible that the classical TS mutation-related increase in neuronal AP duration found in iPSC-derived neurons by Paşca *et al.* (2011) may not translate into a mutation-related prolongation of AP duration in naturally developed neurons within functional brain tissue.

In this study, I aimed to provide evidence that the classical TS2 mutation causes a prolonged AP in naturally formed neurons in various brain areas of the TS2Neo mouse. Studying the effect of the TS2-type mutation on AP duration in these mice should indicate how classical TS mutations impact neuronal AP duration in the naturally developed mature neuron, generally (Bader *et al.*, 2011; Bett *et al.*, 2012; Calorio *et al.*, 2019). It was not feasible to record AP durations in all cell types from all areas of the brain. I therefore measured AP duration of mature pyramidal cells from three functionally relevant and distinct cortices of the adult mouse brain. Pyramidal cells were used in this study as they are a standard, well-characterised cell type known to express the *CACNA1C* gene (Hell *et al.*, 1993; Erk *et al.*, 2014). Pyramidal cells were sampled from 3 regions of the brain in TS2Neo and WT mice: the CA1 region of the hippocampus, the V1 and the RSC. Pyramidal cells from CA1 were targeted from the pyramidal cell layer of dorsal CA1 of the hippocampus. The cortical pyramidal cells recorded from V1, and RSC areas were sampled from L2-5. Pyramidal cells were targeted based on soma size, location and shape. Pyramidal cell identity was later confirmed after each recording by biocytin-streptavidin labelling and imaging using confocal fluorescence microscopy.

The CA1, RSC and V1 were selected for several reasons. These regions of interest (ROIs) cover a functionally diverse range: a hippocampal region (CA1), a primary sensory cortical area (V1), and an associative cortical area (RSC). The CA1 is part of the hippocampus, which is functionally implicated in ASD; a neurophenotype of TS (Splawski *et al.*, 2004; Banker *et al.*, 2021a). Cells in V1b were evidenced in chapter 1 to have abnormal contrast sensitivity for visual stimuli of high SF in the TS2Neo mouse brain. This TS2-related functional change in V1b neurons suggests that this area is implicated in TS. The RSC is an associative cortex which is connected to both the hippocampus and to V1 (Van Groen and Wyss, 2003). I selected this as a representative associative cortex which may be functionally impacted by the TS2 mutation for this reason.

I measured AP duration for pyramidal cells from each of the 3 areas in TS2Neo and WT mice by use of whole-cell patch clamp electrophysiology. During patch clamp recordings, cells received 14 current step injections between -50pA and 650pA, increasing in 50pA increments. The first AP generated from a current injection was used to measure AP duration. AP half-width was used as a measure of AP duration. The methods used were similar to those described by Paşca *et al.* (2011). I hypothesised that expression of the classical TS2 mutation in TS2Neo mouse pyramidal cells would result in prolonged neuronal AP duration as compared to those cells from WT for all 3 cortical regions sampled. This was my primary hypothesis. Confirmation of the hypothesis would provide evidence that the classical TS2 mutation prolongs neuronal AP in naturally developed mature neurons in functional brain tissue.

I confirmed that AP duration was increased in pyramidal cells for each ROI in TS2Neo as compared to WT mice. I then aimed to explore the mechanism by which the classical TS mutation could impact AP duration in the neuron. I identified three different potential ways in which classical TS mutations might impact AP duration in the neuron.

The first potential mechanism is that the prolonged depolarising calcium current flowing through the mutant CaV1.2 channel subunit results in a prolonged AP in the neuron directly, as is true in the cardiac myocyte (Splawski *et al.*, 2004, 2005; Dick *et al.*, 2016). Storm (1987) found that blocking calcium channels prolongs the neuronal AP, providing some evidence of this being a plausible explanation. However, this prolonged AP appears to be dependent on the function of calcium-dependent big potassium (BK) channels which are coupled to calcium channels. It is typically not thought that currents flowing through calcium channels directly impact the AP duration in the neuron (Bean, 2007).

A second potential mechanism by which TS mutations could impact AP duration is by mutation-related changes in the ability of CaV1.2 channel subunits to interact with calcium-dependent BK channels. BK channels are involved in the repolarisation phase of the neuronal AP (Bean, 2007; Berkefeld, Fakler and Schulte, 2010; Simms and Zamponi, 2014). Blocking BK channels prolongs the neuronal AP, and BK channels are known to be involved in determining AP duration (Storm, 1987). CaV1.2, like other calcium channels, interact with BK channels in the neuronal membrane, forming functional complexes with them. In these CaV1.2-BK channel complexes, the activity of CaV1.2 channels impacts the activity of the BK channel (Berkefeld, Fakler and Schulte, 2010). An increase in calcium influx through the mutant CaV1.2 channel subunit could potentially impact the coupled BK channel function within the complex. However, one might theorise that the increase in calcium influx through mutant TS channels would serve to **increase** BK channel activation which would then **shorten** the AP. This is the opposite of the prolonged AP duration found in this study. It is not clear if classical TS mutations impact BK channel function in any other way. Classical TS mutations may also impact how CaV1.2 channel subunits form complexes with, and interact with, BK channels. These changes could prolong the AP duration in the neuron. It is possible that changes in the CaV1.2 channel subunit caused by classical TS mutations result in unknown changes in BK channel function which could prolong the AP duration. For example, if the mutant CaV1.2 channels impact BK channel density within the neuronal membrane, BK channel inactivation, or calcium-BK channel complex formation within the neuron, these could all potentially cause the prolonged neuronal AP seen in the TS2Neo mouse.

A third potential mechanism by which classical TS mutations could impact AP duration in the neuron is through a mutation-related change in sodium channel density within the neuronal membrane. Calorio *et al.* (2019) found that the AP duration of chromaffin cells in the TS2Neo mouse was prolonged due to a decrease in NaV1 sodium channel density in the membrane. The depolarisation phase of the AP is underpinned by sodium channel currents in the neuron and in the chromaffin cell (Hodgkin and Huxley, 1952; Bean, 2007; Calorio *et al.*, 2019). A reduction in sodium channel density in either cell type would result in longer AP depolarisation phase, and, in turn a longer AP duration. There is precedent to suggest that TS mutations might impact neuronal AP duration by a reduction in sodium channel density within the neural membrane. If TS mutant channels impact NaV1 density in the neuron as they have been shown to in the chromaffin cell, this would likely cause a prolonged AP found in the neuron. CaV1.2 is known to be involved in gene transcription and ion channel trafficking within the neuronal membrane (Tian *et al.*, 2014; Schielzeth *et al.*, 2020; Servili *et al.*, 2020). It is plausible that a mutation-related change in CaV1.2 causes abnormal ion channel trafficking and/or transcription in the neuronal membrane, resulting in a reduced NaV1 ion channel density in the neuron. This mutation-related decrease in NaV1 ion channel density could cause a slower rate of depolarisation during the AP, resulting in a prolonged AP duration in the neuron, as was found in the chromaffin cell by Calorio *et al.* (2019).

I aimed to investigate the impact of the classical TS2 mutation in TS2Neo mice on BK channel function using the data already collected from patch-clamp recording experiments described. To do this, I tested for genotype differences in AP broadening and spike frequency adaptation which result from repetitive cell firing, as measured from cells sampled form each area. AP broadening and spike frequency adaptation are two dynamic electrical cell properties of neurons that are underpinned by BK channel function (Shao *et al.*, 1999; Gu, Vervaeke and Storm, 2007). AP broadening is defined as the increase in AP duration which results from repeated AP firing of the neuron. Spike frequency adaptation is the reduction in AP firing frequency for cells firing repeated APs. Given my theory that classical TS mutations could impact neuronal AP duration through indirect effects of mutant CaV1.2 subunits on BK channel function, I hypothesised that there would be reduced AP broadening and spike frequency adaptation in pyramidal cells of the TS2Neo mice as compared to WT, for all 3 brain areas. AP broadening was measured as the increase in AP width across the first 5 APs in a train of APs. Spike frequency adaptation was measured as the reciprocal of the increase in interval between the first and fifth inter-spike intervals. AP spike broadening and spike frequency adaptation were measured using methods previously described by Tigaret *et al.* (2021).

I further aimed to explore the potential impacts of the classical TS2 mutation on various electrophysiological properties in pyramidal neurons recorded from TS2Neo mice as compared to WT. To do this, I processed and analysed voltage responses in TS2Neo and WT mouse neurons to all current step injections used in the protocol.

I explored the impact of the TS2 mutation on the amplitude of single APs in pyramidal neurons of TS2Neo as compared to WT mice. There was no prior hypothesis. The presence of TS2-type mutant CaV1.2 channel subunits in the membrane of pyramidal cells from TS2Neo was not expected to result in increased or decreased AP amplitude as compared to pyramidal cells from WT mice.

I explored the impact of the TS2 mutation on passive membrane properties, voltage sag and voltage rebound in the pyramidal cells. Voltage responses to the hyperpolarising -50pA current step injection were used to obtain this information. The passive membrane properties which were measured from the cells were membrane input resistance, capacitance, and the membrane time constant. I expected there to be no mutation-related change in passive membrane properties, voltage sag or voltage rebound for these cells. Passive membrane properties are governed by the total number of open ion channels in the membrane at resting potential, which can be impacted by membrane composition and cell size. These properties were not expected to change with the presence of the TS2-type mutant channel within the neural membrane. Voltage sag and rebound are both largely governed by Ih currents flowing through hyperpolarization-activated cyclic nucleotide–gated (HCN) channels (Pape, 1996). Membrane potential rebound is also contributed to by currents flowing through T-type calcium channels. There exists no evidence to suggest that TS mutations might disturb

Ih or T-type calcium channel currents, as such I would expect no genotype effects on voltage sag or on membrane potential rebound.

I explored the impact of the TS2 mutation on various measures of cell excitability for pyramidal cells in the TS2Neo mouse. I tested for genotype differences in the threshold potential for APs from pyramidal cells in each area. The methods used were similar to those used by Paşca *et al.* (2011). I tested for genotype differences in the maximum firing frequency of the cell, the minimum onset latency before AP firing (minimum onset latency), and rheobase. The maximum firing frequency of the cell was measured as the highest instantaneous firing frequency recorded for any current step injection to the cell. The minimum onset latency was measured as the minimum time between current input and AP firing for any current step injection. Rheobase was the measure of the minimum current step injection to the cell required to elicit an AP, this was determined empirically, without extrapolation. Calcium channel currents are known to be involved in regulation of neuronal excitability in burst firing (Cain and Snutch, 2010). There is some evidence to suggest that L-type calcium channels may also impact excitability in the neuron (Moore and Murphy, 2020). It is possible that the TS-related changes in CaV1.2 might impact neuronal excitability. I hypothesised that the TS2 mutation might impact cell excitability in the pyramidal cells of the TS2Neo mice as compared to WT.

Overall, my primary hypothesis was that APs measured from pyramidal cells of all 3 areas of TS2Neo mice would be longer in duration as compared to those from WT. On confirming the primary hypothesis, my secondary hypothesis was that BK channel would be impacted by the TS2-type mutation in the TS2Neo mouse pyramidal cells as compared to WT. A third hypothesis was that the TS2-type mutation would impact cell excitability in the TS2Neo mouse pyramidal cells as compared to WT. I also explored potential impacts of the classical TS2-type mutation on a variety of other electrophysiological properties of pyramidal cells with no prior hypothesis.

Methods:

Animals:

15 mice heterozygous for the TS2Neo mutation, and 11 WT sibling mice were used in this experiment (Jax labs strain #019547, B6.Cg-Cacna1ctm2Itl/J). All mice were between 4-10 weeks old at the time of sacrifice and use. Mice of both sexes were used in this experiment.

Mice were kept in accordance with directives in the UK Animals (Scientific Procedures) Act 1986, and the European Commission Directive 2010/63/EU. Housing and husbandry were provided by Cardiff University Biological Society services. Mice were given regulation food and water ad-libitum and were subject to a normal light/dark cycle (12hours light, 12hrs dark). Mice were single-sex group housed before use in the experiment. I was blinded to animal genotype throughout the duration of the study until the completion of the final data analyses.

Solutions, consumables, and reagents:

Choline-chloride slicing solution:

110mM choline chloride, 25mM D-glucose, 15mM $NaHCO_3$, 2.5mM KCl, 1.25mM NaH_2PO_4, 11.6mM L-ascorbic acid, 2.1mM sodium pyruvate, 0.5mM $CaCl_2$, 7mM $MgCl_2$.

Measured at 310mOsm.

A 1 litre solution was made on the day of, or day before the experiment, and was stored at 4°C until use.

Artificial cerebrospinal fluid (ACSF) solution:

11.9mM NaCl, 10mM D-glucose, 2.6mM $NaHCO_3$, 2.5mM KCl, 1mM NaH_2PO_4, 2.5mM $CaCl_2$, 1.3mM $MgCl_2$.

Measured at 290mOsm.

A 2-litre solution was made on the day of the experiment and stored at 4°C until use.

Internal solution:

117mM $KMeSO_3$, 8mM NaCl, 10mM 4-(2-hydroxyethyl)-1-piperazineethanesulfonic acid (HEPES), 4mM MgATP, 0.3mM NaGTP, and 0.2mM Ethylene Glycol-bis(β-aminoethyl ether)-N,N,N',N'-Tetraacetic Acid (EGTA).

Titrated to pH 7.4.

Measured at 280mOsm.

Biocytin was added at 0.2% weight per volume.

A 500ml solution was made up to 2 months before the experiment, aliquoted, and stored at -20°C. Aliquots of 500µl were defrosted, filtered through a 0.2µm centrifuge tube and used on the day of the experiment.

Poly-L-lysine coverslips:

18 mm round borosilicate glass coverslips.

1mg/ml Poly-L-lysine hydrobromide in borate buffer solution (0.05M boric acid, 0.01M borax).

0.7ml of Poly-L-lysine solution was used to cover 90% of the surface of the glass coverslip

4% Paraformaldehyde (PFA) solution:

4% weight by volume PFA in 1x phosphate buffered saline (PBS) solution.

A 1 litre solution was made up to 3 months before use and stored at 4°C.

Block solution:

10% volume by volume normal goat serum, 0.3 % volume by volume Triton X-100 solution in PBS 1x solution.

Made up to a week before use and stored at 4°C.

Streptavidin solution:

1:1000 AlexaFluor 594-conjugated Streptavidin, 3% volume by volume normal goat serum, 0.3% volume by volume Triton X-100 solution in 1x PBS.

Made up to a week before use and stored at 4°C, covered from light.

Table 3 Reagents used for patch clamp experiments:

Reagents (Patch clamp)				
Reagent nature	**Type**	**Source**	**Manufacturer**	**Identifier**
Choline Chloride	Choline Chloride	Merck	Sigma-Aldrich	C7527-500G
D-glucose	D-glucose anhydrous	Fisher Scientific	Fisher Chemical	10395890
$NaHCO_3$	Sodium Hydrogen Carbonate	Merck	Sigma-Aldrich	S6014-500G
KCl	Potassium Chloride	Merck	Sigma-Aldrich	P5405-500g
NaH_2PO_4	Sodium Phosphate monobasic anhydrous	Fisher Scientific	Fisher BioReagents	10133153
Sodium ascorbate	Sodium L-ascorbate	Merck	Sigma-Aldrich	A4034-500G
Sodium Pyruvate	Sodium Pyruvate	Merck	Sigma-Aldrich	P8574-100G
$CaCl_2$	Calcium chloride dihydrate	Merck	Sigma-Aldrich	C7902-500G
$MgCl_2$	Magnesium chloride hexahydrate	Merck	Sigma-Aldrich	M2393-100g
NaCl	Sodium Chloride ACSF reagent	Merck	Sigma-Aldrich	S9888-10Kg
$KMeSO_3$	Potassium Methanesulfonate	Merck	Sigma-Aldrich	83000-5G-F
HEPES	4-(2-hydroxyethyl)-1-piperazineethanesulfonic acid	Merck	Sigma-Aldrich	H3375-25G
MgATP	Magnesium Adenosine Triphosphate	Merck	Sigma-Aldrich	A9187-1G
NaGTP	Sodium 5'-triphosphate hydrate	Merck	Sigma-Aldrich	51120-100MG

EGTA	Ethylene glycol-bis(2-aminoethylether)-N,N,N',N'-tetraacetic acid	Merck	Sigma-Aldrich	03777-10g
Biocytin	Biocytin	Merck	Sigma-Aldrich	B4261-250mg
Poly-L-lysine	Poly-L-Lysine	Merck	Sigma-Aldrich	P2636-100MG

Table 4 Reagents used for biocytin-streptavidin labelling of pyramidal cells:

Reagents (biocytin staining)					
Reagent nature	**Type**	**Source**	**Manufacturer**	**Identifier**	**Dilution**
Block	Normal Goat Serum	Abcam	Abcam	Ab7481	10% (block solution) 3% (streptavidin solution)
Surfactant	Triton X-100	Thermofisher	ThermoScientific	85111	0.3%
Buffer	PBS 1x	Merck	Sigma-Aldrich	79382	NA
Fixative	Paraformaldehyde	Thermofisher	ThermoScientific Chemicals	416785000	4%
Fluorescence labelled Streptavidin	AlexaFluor 594-Conjugated Streptavidin	Fisher Scientific	Molecular Probes	S32356	1:1000

Table 5 other consumables used in experiments:

Consumables (all)				
Consumable nature	**Type**	**Source**	**Manufacturer**	**Identifier**
Microscope Slide	Superfrost Plus Slide	VWR	VWR	631-0108
Mounting Medium	Fluoromount Aqueous Mounting Medium	Merck	Sigma-Aldrich	F4680
18mm round Coverslips	18mm Coverslips	Fisher Scientific	Epredia	11709875
Glass capillaries for	Glass capillaries,	WPI	WPI	BF150-86-10HP

pulling micropipettes	outer diameter= 1.5mm, inner diameter= 0.86, fire polished, 10cm length			
Bijou tube for post-recording biocytin labelling	Bijou tube	VWR/ Thermo Fisher Scientific	Sterilin	215-0329

Preparation of acute slices from mice:

Mice were sacrificed by use of a lethal dose of inhalatory isoflurane anaesthesia (5% in 95% oxygen for sustained period) followed by decapitation. Brains were removed from the head quickly under ice-cold choline-chloride slicing solution (see “Solutions, consumables and reagents” subsection). After extraction, the brain was rested for up to 1 minute in carboxygenated (95% oxygen, 5% carbon dioxide) cutting solution kept at 4°C. Brains were trimmed using a single-edge razor to remove the cerebellum and olfactory bulbs. Brains were then mounted anterior face down on a vibratome stage using cyanoacrylate glue. Brains were sectioned coronally to a thickness of 400µm using a Vibratome (CI.7000SMZ-2, Campden instruments) filled with carboxygenated choline-chloride slicing solution. Sections were obtained from positions along the anteroposterior axis of the brain which included V1, RSC and/or dorsal CA1. The sections were selected according to visual reference to the Allen Brain Atlas (Sunkin *et al.*, 2013; Wang *et al.*, 2020). Obtained coronal sections were hemi-sectioned mid-sagittaly, and then transferred to a slice holding chamber (BSK1, Brain Slice Keeper) filled with carboxygenated ACSF solution which was incubated at 34°C by use of a water bath (Grant) for 30 minutes. The slice chamber was then removed from the water bath and left to rest at room temperature (RT) for 1 hour. Slices were kept at RT for up to 12 hours before use.

Ex-vivo whole cell patch clamp recording from acute slices:

After slice preparation, slices were mounted onto poly-L-lysine coated 18mm glass coverslips, which were then placed into a submerged recording chamber (Slice Minichamber II, Luigs and Neumann) which was perfused with carboxygenated ACSF at 32°C. Perfusion was controlled by a peristaltic pump (M5-2/12 reglo digital pump, Ismatec). The temperature of the chamber was controlled by use of a temperature control unit (NBD TC2 Bip Temperature Controller, Cell MicroControls equipped with HI-22Dp under-stage heater, and HPRE2 pre-heater units). ROIs (either V1, RSC or CA1 of the dorsal hippocampus) were located by use of infra-red differential interference contrast imaging (BX-51 WT, Olympus), with reference to the Allen Brain Atlas (Sunkin *et al.*, 2013; Wang *et al.*, 2020) and cell bodies were visualized. Cells with large, pyramidal somas were targeted for recording. Pyramidal cell type was confirmed after experimental recording by biocytin-streptavidin labelling and imaging (see “Biocytin staining and imaging to confirm cell type”). Patch pipettes of around 4-5MΩ resistance were pulled (PC-100 pipette puller, Narishige) and filled with internal solution containing biocytin immediately before use for patch-clamp recordings. Pipette resistance was confirmed by use of Clampex and Multiclamp 700B software running on a PC connected to a Multiclamp 700B control unit and amplifier, with data digitized through an Axon Digidata 1550 Data Acquisition System. Once a cell was targeted, a giga-Ω seal was formed, and whole-cell patch was obtained by use of negative pressure. Cells were held at -70mV for 1 minute to assess patch stability. The current required to hold the cell at -70mV was noted and used to assess seal quality. After confirmation of a stable, high-quality patch, the cell was clamped at the current required to hold the membrane at -70mV using Multiclamp700B software. Current clamp experimental protocols were then run, and membrane potentials were lowpass filtered to 6kHz, sampled at 50kHz, and digitized using an Axon Digidata 1550 Data Acquisition System and Clampex 11 software. Stimulation protocols were created and run using Clampex software. Clampex software was also used to record the current input and voltage response traces from cells.

Trains of somatic APs were elicited using a series of 200ms current steps increasing in 50pA increments between -50pA and +650pA. Each current step was followed by a 2s period for which the cell was injected with the holding current. Up to 3 recordings were taken from a single cell, typically the first recording was used for processing to obtain data for the experimental dataset. The -50pA current step was used to assess input resistance of the cell, voltage sag and rebound voltage. Patch stability was not re-assessed during or between experiments as cells were held in the whole-cell patch clamp configuration for a maximum of 15 minutes in each instance.

The head stage used in this experiment was a CB-7B current clamp and voltage clamp head stage, controlled by a Luigs and Neumann micromanipulator. From each experiment, membrane potential traces for current step injections were recorded and saved in the axon binary format using Clampex software. A maximum of 3 cells were recorded from each ROI of a single mouse to minimise issues regarding repeated measures from individual mice.

Biocytin staining and imaging to confirm cell type:

Following recording, cells were held in whole-cell configuration for a further 10 minutes to allow diffusion of biocytin throughout the body of the patched cell. After this period, the patch pipette was carefully retracted, the membrane resealed using a -40mV pulse, and the brain slice was left to rest in the recording chamber for a further 5 minutes. The brain slice was then transferred into a Bijou tube holding 1ml of 4% PFA solution. Brain slices were kept in 4% PFA solution at 4°C for up to 48 hours. Sections were then washed 3 times with PBS 1x solution and stored in PBS 1x for up to one week.

Sections were washed a further 3 times with PBS 1x. Sections were then incubated in block solution for 1hr at RT. Sections were incubated with streptavidin solution overnight at 4°C. Sections were washed a final 4 times in PBS 1x before being mounted onto SuperFrost Plus slides. Slides were cover slipped using Fluoromount aqueous mounting medium. Coverslips were sealed using clear nail polish.

Sections were visualised using a confocal microscope (Zeiss Airyscan LSM880) to image AlexaFluor 594-conjugated Streptavidin-biocytin labelled cells which were patched during the recording experiment. Images were used to confirm pyramidal cell type. Example images are shown in the “Results” section of this chapter. The methods used here are generally based on those of Swietek *et al.* (2016).

Data processing:

Membrane potential data corresponding to each current injection step of the protocol were processed using custom-made python codes. Any cell for which AP amplitude measured under 0mV was excluded from the dataset. Such cells were deemed to be of poor quality. For all other cells, fluorescence images of biocytin-filled bodies were used to confirm pyramidal cell identity, and the ROI to which the cell belonged (V1, RSC, CA1).

Two separate methods were used to process data in this study. One method was used to obtain measures from the first AP fired in the experiment for a given cell. Specifically, the measured properties were AP threshold, amplitude, and half-width values. A second method was used to measure passive membrane properties, voltage sag, membrane potential rebound, cell firing properties, AP broadening and spike frequency adaptation for that cell. The second method involved batch-processing of data. Recordings which were not completed to the end of the 650pA current step injection due to cell death or other recording disruption could not be processed using the second method. The first method was used to extract information regarding the primary hypothesis, as more data could be processed using this basic method, and therefore this avoided data loss. A total of 82 cells were recorded from in experiment. 56 of these 82 cells could be batch-processed, and therefore 56/82 cells were used to obtain measures for passive membrane properties, voltage sag, voltage rebound, firing properties, spike frequency adaptation, and AP broadening. The two methods are detailed in separate subsections below.

Data processing to measure properties of first AP fired by cell:

Experimental data, stored in the axon binary format, were loaded in python using the pyabf package. Traces were visualised, and the portion of the voltage trace containing the waveform of the first AP was sampled manually. From the sampled waveform, a phase-plane plot was generated, where the rate of change of membrane potential (dV/dt) was plotted with respect voltage (V; Bean, 2007). An example of such a plot is shown in Figure 11 below. The phase plane plot was inspected to ensure that the AP waveform was sampled appropriately and was of suitable quality. The threshold of the AP was measured as the voltage at which dV/dt for the AP reached 15.2mV/ms. These were the same defining criteria for AP threshold as those used by Paşca *et al.* (2011). The amplitude of the AP was then found as the maximum voltage the waveform reached within the sampled AP. Both AP threshold and amplitude values were measured in mV. The voltage that was half-way between the threshold and amplitude values of the AP was specified as the AP half-height. The time during which the AP exceeded the AP half-height during the waveform was taken as the AP half-width. The AP half-width was measured in ms. These measurements are shown on the example image in Figure 11.

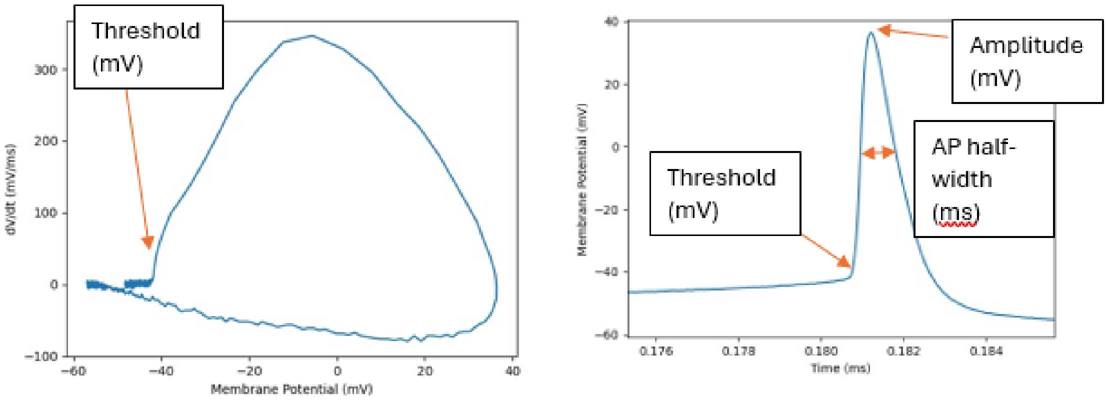

Figure 11 Image showing AP waveform (right) and phase-plane plot (left). The threshold potential was taken as the potential at which dV/dt for the AP upswing reached 15.2mV/ms. The membrane potential halfway between the AP threshold and amplitude values was recorded as the AP half-height, and the duration of time for which the AP waveform exceeded this membrane potential was taken as the AP half-width, in ms.

Data processing to measure passive, firing, broadening and adaption properties of the cell:

Experimental data were processed using software written in Python by Dr Cezar Tigaret.

The voltage trace corresponding to the -50pA current step was used to measure passive membrane properties of the cell as well as voltage rebound and voltage sag. The passive membrane properties measured were membrane input resistance, capacitance, and the membrane time constant. The methods used to obtain these values were based on those reported by Tamagnini *et al.* (2015). An illustration of how these measurements were obtained are shown in Figure 12. Resting membrane potential was taken as the membrane potential of the cell measured 100ms before the onset of the hyperpolarising current. This was typically -70mV, and was not based on empirical measurement.

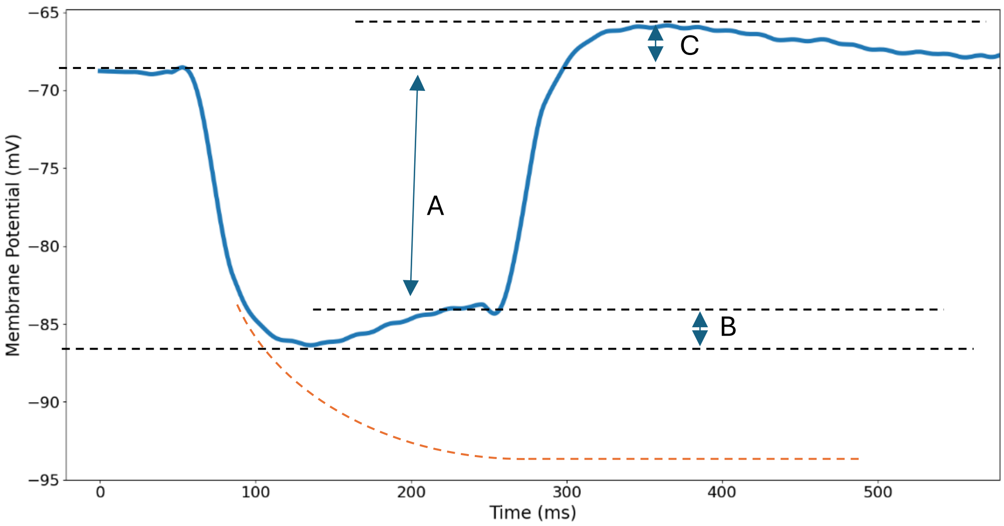

Figure 12 A schematic showing the voltage trace corresponding to a -50pA current injection and the measurements taken to obtain values for passive membrane properties, voltage sag and membrane potential rebound. The voltage difference, A, divided by the input current (-50pA) is taken as the input resistance (MΩ). The measurement B was used to give the voltage sag (mV). The measurement C was used to obtain the membrane potential rebound (mV). An exponential fit of the curve of the depolarisation (fitted based on methods of Tamagnini et al. (2015), indicated by the orange line) was used to obtain a measure of the membrane time constant, τ (ms). Membrane capacitance was taken as τ/input resistance (pF).

Rheobase was measured empirically as the minimum input current required to evoke an AP for the cell, measured in pA. No mathematical calculation was used to estimate rheobase to a higher degree of accuracy. The maximum instantaneous firing frequency of each cell was measured as the reciprocal of the minimum measured time between any two spikes for any input current to the cell. This was measured in Hz. Minimum AP onset latency was measured as the minimum time between stimulus onset and AP firing (taken from AP threshold). Minimum AP onset latency was measured in ms.

AP broadening and firing frequency adaptation in response to repetitive firing required more complex processing. AP trains from each cell were grouped according to the initial instantaneous firing frequency for each current injection step, such that trains for a specific current injection step from a single cell fell in one of four frequency bands. Initial instantaneous firing frequency here is the reciprocal of the firing frequency between the first and second APs in a train of APs which has been elicited by a specified current step injection. The four frequency bands were 10-40Hz, 40-80Hz, 80-120Hz and >120Hz. Trains with initial firing rate of <10Hz were excluded. The difference in firing frequency for the first, second, third, fourth and fifth inter-spike-intervals, and how this varied by genotype and ROI were used to explore genotype effects on spike frequency adaptation. The difference in AP width for the first, second, third, fourth and fifth APs in a train of spikes, and how this varied by genotype and ROI was used to explore genotype effects on AP broadening. The methods used to explore AP broadening and spike frequency adaptation are the same as those used in Dr Cezar Tigaret's lab previously (Tigaret *et al.*, 2021). An illustration of how this data was obtained is shown in Figure 13 and is explained in detail in the paragraph below the figure.

A)

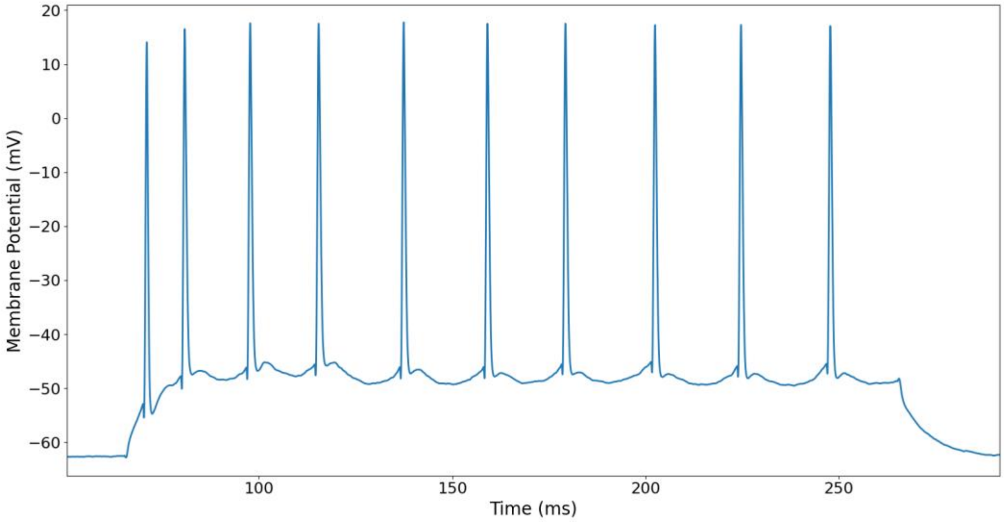

B)

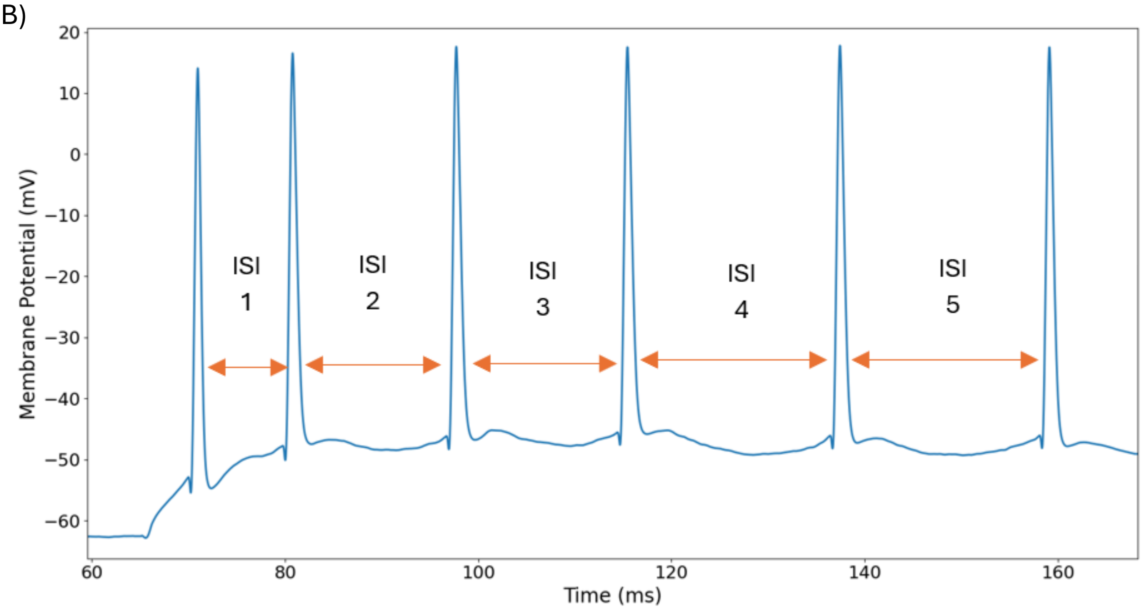

C)

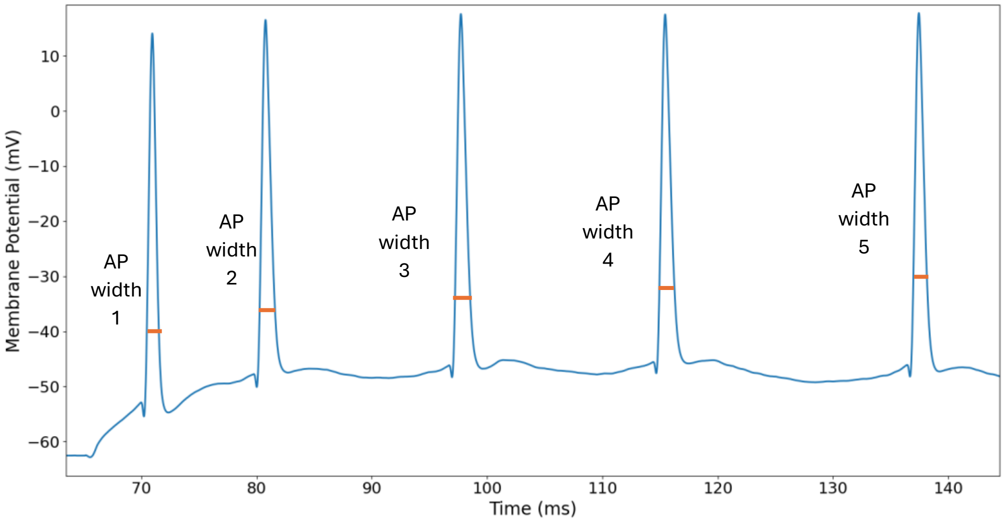

Figure 13 A) Image showing a train of APs being fired in response to a 600pA current step injection. B) Demonstrates how the initial inter spike interval (ISI1) was obtained from this data. The reciprocal of ISI1 was used to find the initial instantaneous firing frequency for this AP train for this cell. This train of APs was found to have an instantaneous firing frequency of >120Hz. This train of APs was processed and analysed to obtain information regarding how genotype impacts spike frequency adaptation and AP broadening when the firing rate is >120Hz. The instantaneous inter spike intervals between the 2nd and 3rd, 4th and 5th, 5th and 6th APs were then obtained, the reciprocals of these were taken to find instantaneous firing frequencies, and the ratio of these values over the initial instantaneous firing frequency was taken to measure spike-frequency adaptation for this spike train for this specific cell. This gave a measure of how the spike frequency changes across the initial stages of a train of APs for this specific cell firing at this specific frequency. Similarly, the width of the first AP in the train was obtained, and the widths of the 2nd, 3rd, 4th and 5th were obtained and were divided by the initial AP width to obtain a measure of AP broadening in response to repeated firing for this cell when firing at >120Hz. In this way, single cells typically were used to obtain multiple measures of spike frequency adaptation and AP broadening. A cell might have an instantaneous firing frequency of 50Hz when receiving a 200pA current step injection but have an instantaneous firing frequency of 125Hz when receiving a 600pA current step injection. Thus, measurements from a single cell were used to contribute to the overall dataset which was used to explore how genotype impacts both AP broadening and spike frequency adaptation across multiple bands of initial firing frequencies. For any cell that produced a train of APs in response to more than one current injection, repeated measures were taken from that cell. These repeated measures were accounted for statistically using mixed effects modelling. In exploring how broadening and firing frequency adaptation were affected by genotype, I used linear modelling to explore how genotype impacts AP width and spike frequency across the first 5 APs/ISIs of the train, while accounting for repeated measures from single cells. This is explained in more detail in the "Data analyses" subsection of this chapter.

Data analyses:

All data analysis was performed using R. The impact of TS2Neo heterozygosity on each measured parameter was estimated by significance testing methods. AP half-width data were compared between the 56 cell and 82 cell sample to verify that the 56-cell subset was representative of the full, 82-cell dataset. AP half-widths measured from the subset of 56 cells did not significantly differ from those measured from the full dataset of 82 cells, as tested by Wilcoxon-signed rank test (W=2412, P=0.6146).

This indicates that the use of the 56-cell subset in analysis of non-single-AP properties and how they vary with genotype should be appropriate.

Data from 82 cells were used to generate linear models of how single AP parameters (amplitude, threshold, and AP half-width) varied with ROI (V1, RSC and CA1) and genotype, with interaction between ROI and genotype being tested for also. Data were transformed before modelling, as appropriate. Details of data transformations are indicated in the results section. Models were tested by plotting to verify that model assumptions were not violated. Models were then assessed for their ability to describe the data by significance testing using base R functions. Adjusted R^2 values were also considered and are reported as appropriate. These values were also generated by base R functions. Models were reduced by drop-wise comparison testing. Drop-wise comparison testing involved use of the drop1 function in base R. The impact of genotype on a specific parameter, either generally, or for a specific ROI (V1, RSC, or CA1) for each maximally reduced model was tested by use of the base R summary function. Any genotype difference on these measures is reported as appropriate. Genotype differences in parameter values are estimated from genotype-significant models, but also given as descriptive statistics from the raw dataset.

AP half-width was hypothesised to be increased in pyramidal cells from TS2Neo as compared to WT mice. Therefore, the impact of the TS2Neo mutation on AP half-width for pyramidal cells was tested for each individual area using Wilcoxon Signed-rank testing as well as by model testing. This was to ensure that the use of high-powered model testing was not responsible for the significant results found. The 3 Wilcoxon signed-rank test results were Bonferroni corrected against one-another.

Data from 56 cells were used to model the impact of ROI and genotype on passive membrane properties, as well as voltage sag and voltage rebound of the cell. The passive membrane properties were input resistance, membrane capacitance, and the membrane time constant. Data were transformed before modelling, as required for data normality. Details of data transformations for each model are indicated in the results section. Models were tested by plotting to verify that assumptions were met in each case. Models were assessed for their ability to describe the data by significance testing. Adjusted R^2 values were also considered and reported as appropriate as a report of model fit. Models were reduced by drop-wise comparison testing as for the single AP parameter models. The impact of genotype on each of the passive parameters either generally, or for each specific ROI was significance tested.

Maximum firing frequency and minimum onset latency of firing for 56 cells were both modelled with respect to genotype and area from which the cell was recorded by linear regression methods. Model assumptions and fit were tested as described for other models generated, data transformations are described in the results section.

The impact of genotype on rheobase for cells recorded from each of the three ROIs was tested by use of Wilcoxon-signed rank methods. Linear regression modelling was not appropriate due to the ordinal spread of the data. Cumulative link mixed modelling- a method for regression of ordinal data- was not deemed appropriate in this instance given the relatively small size of the dataset.

Repeated measures linear models were used to model how AP broadening and spike frequency adaptation varied with ROI and genotype. I modelled how genotype impacted the change in AP width and instantaneous firing frequency across the first 5 APs in the train for cells firing trains of frequency 10-40Hz, 40-80Hz, 80-120Hz and >120Hz for each ROI, while controlling for repeated measures from individual cells. Repeated measures from single animals were also modelled initially, but this led to overfitting and this term was dropped from the model. Model assumptions were tested by graphical visualisation of residuals, and their variance with fitted values of the model. The goodness of fit of each model was confirmed using the r.squaredGLMM function of the MuMIN package in R (Barton, 2023). The impact of genotype was tested by comparison of a reduced model, lacking genotype terms, with the full model which described how each property varied with both genotype and ROI.

The primary hypothesis, being that AP half-width would vary with genotype for each ROI was multiple-test corrected for 3 multiple tests- one for each of the 3 ROIs- using the conservative Bonferroni method. Given that testing genotype effects on all other parameters were not strongly hypothesis-driven, were high in number, and were exploratory in nature, the risk of false-positive findings from these analyses was deemed to be high (Forstmeier, Wagenmakers and Parker, 2017). Therefore, all P values resulting from these exploratory (non-primary hypothesis related) analyses specifically aimed at finding genotype impacts on electrical properties of the cell were multiple comparison corrected using the conservative Bonferroni method.

Descriptive statistics are given either as a mean±standard deviation (SD), or as a median value followed by the interquartile range (IQR) of that value given in brackets.

Results:

Successful recording and staining of pyramidal cells from CA1, V1 and RSC of TS2Neo and WT mouse brains:

Pyramidal cells from V1, RSC and CA1 of acute slices from TS2Neo and WT mouse brains were successfully patched, recorded from, and filled with biocytin. Pyramidal cell type was confirmed by post-recording fluorescence imaging. Example pyramidal cells from each of the 3 different areas are shown in Figures 14, 15 and 16.

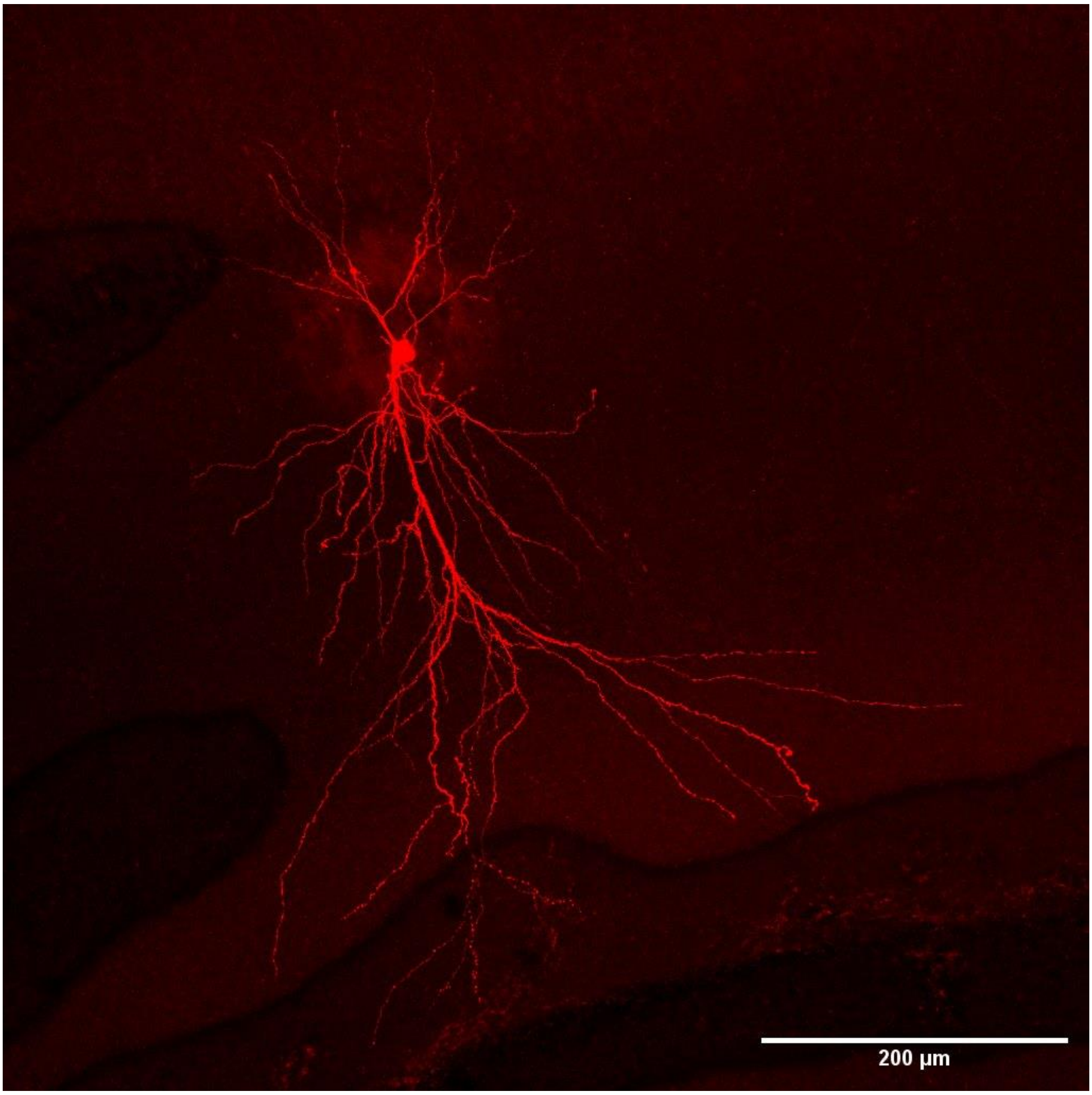

Figure 14 Streptavidin-AlexaFluor594-labelled Biocytin-filled CA1 hippocampal pyramidal cell patched during an electrophysiology experiment. Maximum intensity projection of image taken using a confocal microscope.

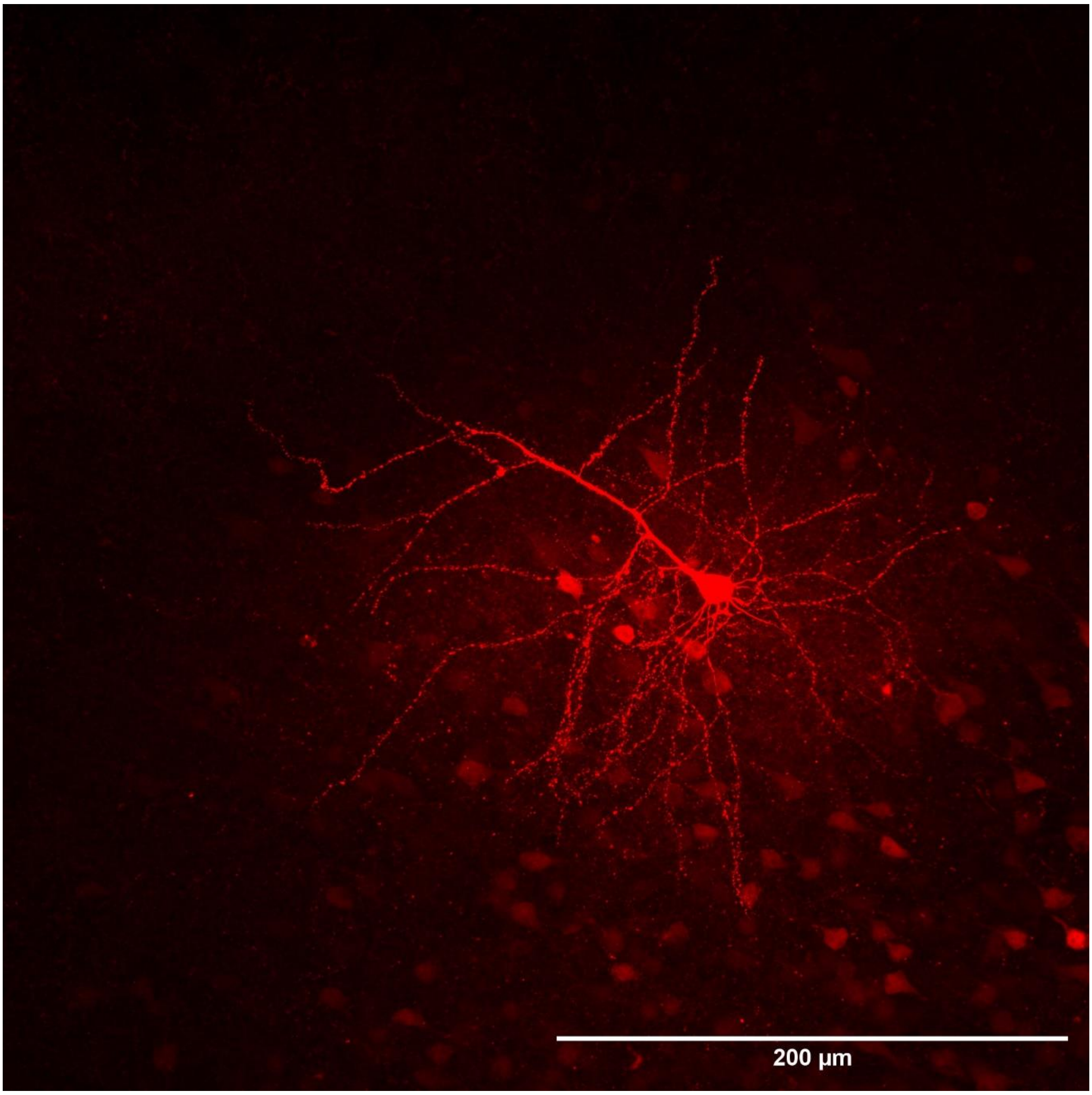

Figure 15 Streptavidin-AlexaFluor594-labelled Biocytin-filled RSC L3 pyramidal cell patched during an electrophysiology experiment. Maximum intensity projection of an image taken using a confocal microscope.

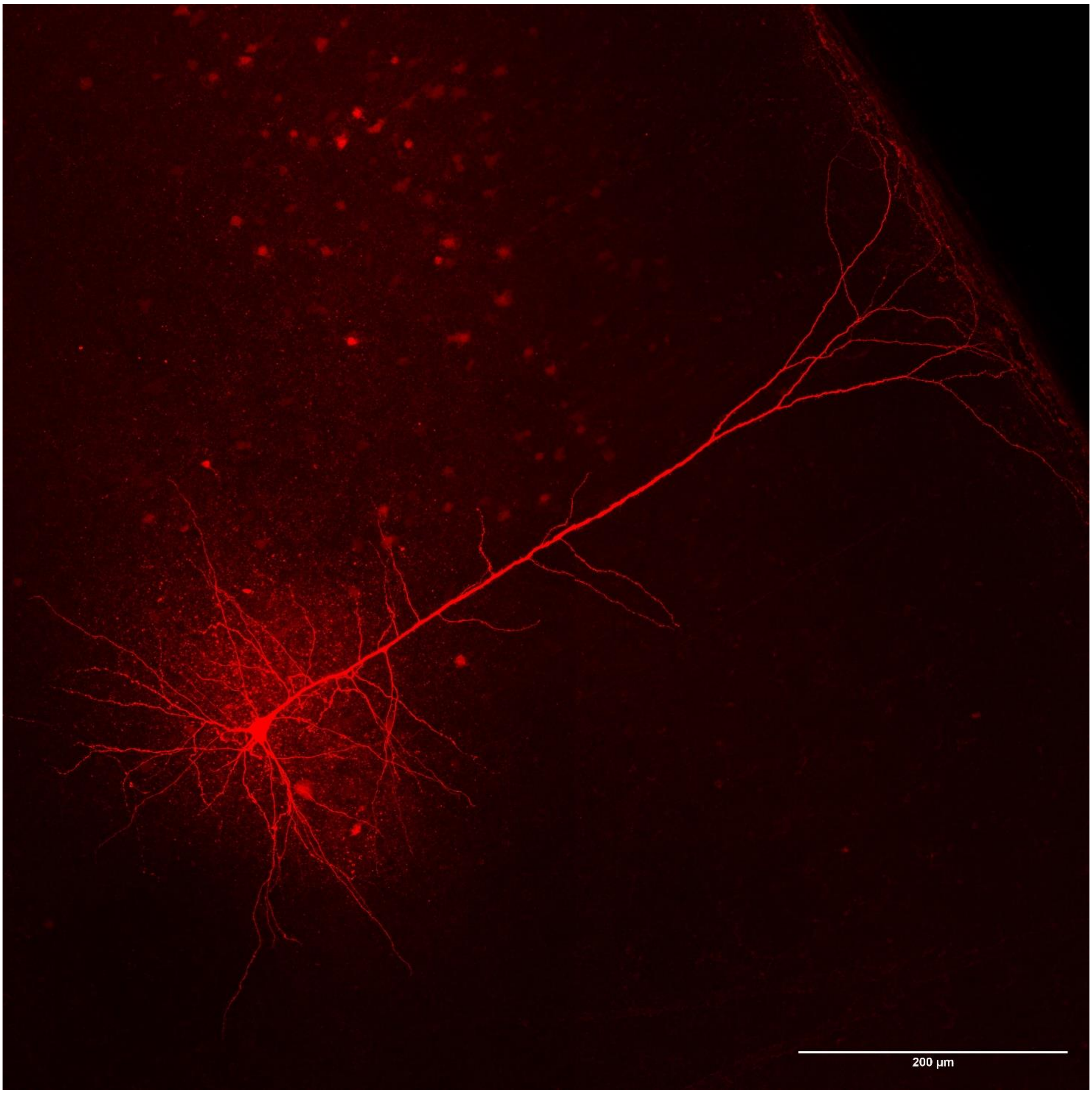

Figure 16 Streptavidin-AlexaFluor594-labelled Biocytin-filled L5 V1 pyramidal cell patched during an electrophysiology experiment. Maximum intensity projection of an image taken using a confocal microscope.

Passive membrane properties not impacted by TS2Neo heterozygosity:

Linear regression was used to generate models describing how specific passive membrane properties varied with ROI and with animal genotype. The passive membrane properties modelled were membrane capacitance, membrane input resistance and membrane time constant. Data required transformation to meet model assumptions. Models predicting membrane capacitance, input resistance and membrane time constant were not found to be significantly superior to null models. ROI nor genotype explained a significant amount of variance in passive membrane properties in any of the models. The statistical results from the testing of these models, and data transformations required for the modelling are shown in the table below. It should be noted that the adjusted R^2 values for each of the models shown in the table below are extremely low, this value is, in fact, negative for the membrane input resistance model. This demonstrates that the models explain a very low proportion of variance in the data.

Table 6 Results from significance testing of models exploring the impact of TS2Neo heterozygosity on passive membrane properties of pyramidal cells in the mouse:

Passive membrane property	**Model terms**	**Data transformation**	**F statistic**	**DF**	**P value**	**Adjusted R^2**
Membrane capacitance	ROI, genotype, ROI-genotype interaction term	Logarithmic	1.58	5 and 50	0.184	0.0498
Membrane input resistance	ROI, genotype, ROI-genotype interaction term	Logarithmic	0.814	5 and 50	0.545	-0.0172 (0)
Membrane time constant	ROI, genotype, ROI-genotype interaction term	Square root	1.81	5 and 50	0.102	0.0800

Table 7 Showing descriptive statistics for passive membrane properties recorded from pyramidal cells of mice from each genotype. The median values of each of these parameters are shown in the table below, alongside the IQR, shown in brackets:

ROI	**Membrane capacitance (pF)**		**Membrane input resistance (MΩ)**		**Membrane time constant (ms)**	
	WT	**HET**	**WT**	**HET**	**WT**	**HET**
CA1	123.7 (79.1-173.7)	140.8 (102.9-161.2)	89.9 (79.7-116.5)	81.2 (64.4-99.4)	11.1 (9.2-13.0)	11.0 (9.9-11.7)
RSC	119.6 (103.2-247.7)	65.2 (41.1-126.5)	60.2 (34.8-100.2)	120.8 (62.9-203.7)	8.6 (6.9-9.5)	7.0 (6.3-11.2)
V1	136.2 (84.1-179.4)	152.2 (99.3-210.2)	106.6 (61.5-127.6)	96.9 (58.6-175.0)	9.6 (8.0-16.2)	14.1 (11.4-18.3)

Overall, the TS2Neo mutation was not found to impact passive membrane properties including membrane input resistance, capacitance, or membrane time constant for pyramidal cells recorded from V1, RSC and CA1 of acute tissue from the mouse brain.

AP width is increased in pyramidal cells from CA1, V1 and RSC of TS2Neo as compared to those from WT mice:

Linear regression was used to model how AP half-width varied with genotype and ROI. AP-half width data required square-root transformation for the data to be modelled without violation of linear model assumptions (as tested graphically). The model was found to be significant, meaning that it fit the data significantly better than a null-fitted model (P=0.000142, F statistic=7.71, DF=2 and 78). The model explained 19.9% of variance in the data (Adjusted R^2=0.199). Transformed AP half-width values were found to significantly vary with genotype based on the model ($P=2.77 \times 10^{-5}$, t=4.45). This finding was based on a linear regression model that explained less than 20% of variance in the data. The model met all required assumptions; however, a sensitivity analysis was performed to confirm that the finding was not purely based on the high-powered statistical methods used in the analysis. Wilcoxon signed-rank methods were used to test for differences in AP half-width from pyramidal cells of each ROI from TS2Neo as compared to WT mice. Pyramidal cells from TS2Neo mice had a significantly higher AP half-width as compared to those from WTs, for each ROI. The results are shown in Table 8.

Table 8 Results from post-hoc testing of linear regression model exploring the genotype impact on AP width for pyramidal cells of each genotype:

ROI	**N WT**	**N TS2Neo**	**W statistic**	**P**	**Adjusted P**
CA1	20	15	77.5	0.00810	0.0243
RSC	10	16	32	0.00611	0.0183
V1	10	11	22	0.0108	0.0324

AP half-width values measured from pyramidal cells of V1, CA1 and RSC from TS2Neo and WT mice are shown in Figure 17. Example AP traces from single WT and TS2Neo mouse V1 pyramidal cells are shown in Figure 18.

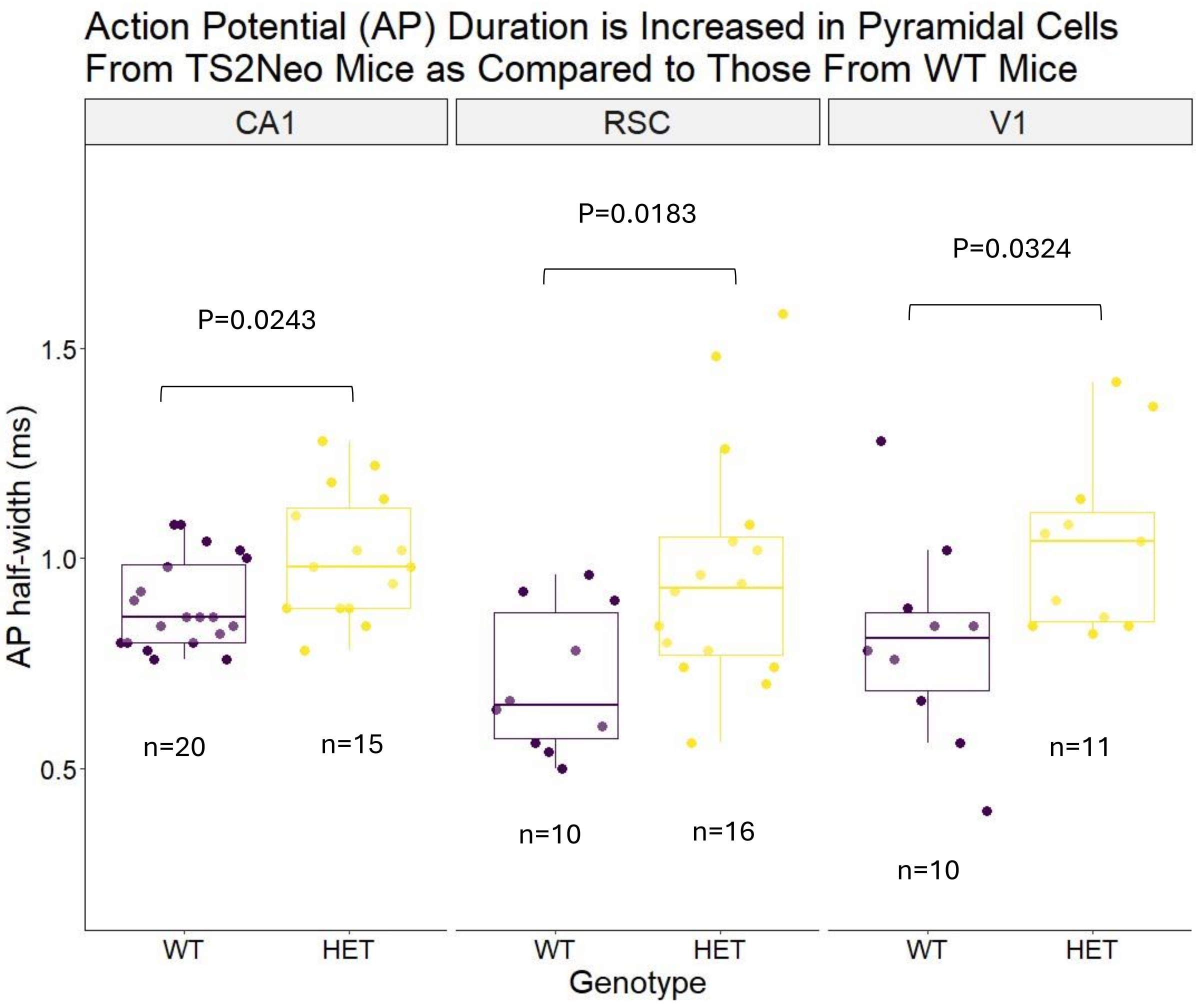

Figure 17 Action potential half-width (ms) is higher in pyramidal cells from CA1, RSC and V1 in acute ex-vivo sections from TS2Neo mice as compared to in pyramidal cells recorded from those areas in acute ex-vivo sections from WT mice. n refers to the number of cells from which the data were obtained. The P values shown on the plots are the Bonferroni corrected P values from Wilcoxon signed-rank testing the differences in values between genotypes for each area. CA1 refers pyramidal cells from the dorsal CA1 region of the hippocampus, RSC refers to pyramidal cells from the retrosplenial cortex, and V1 refers to pyramidal cells from the primary visual cortex.

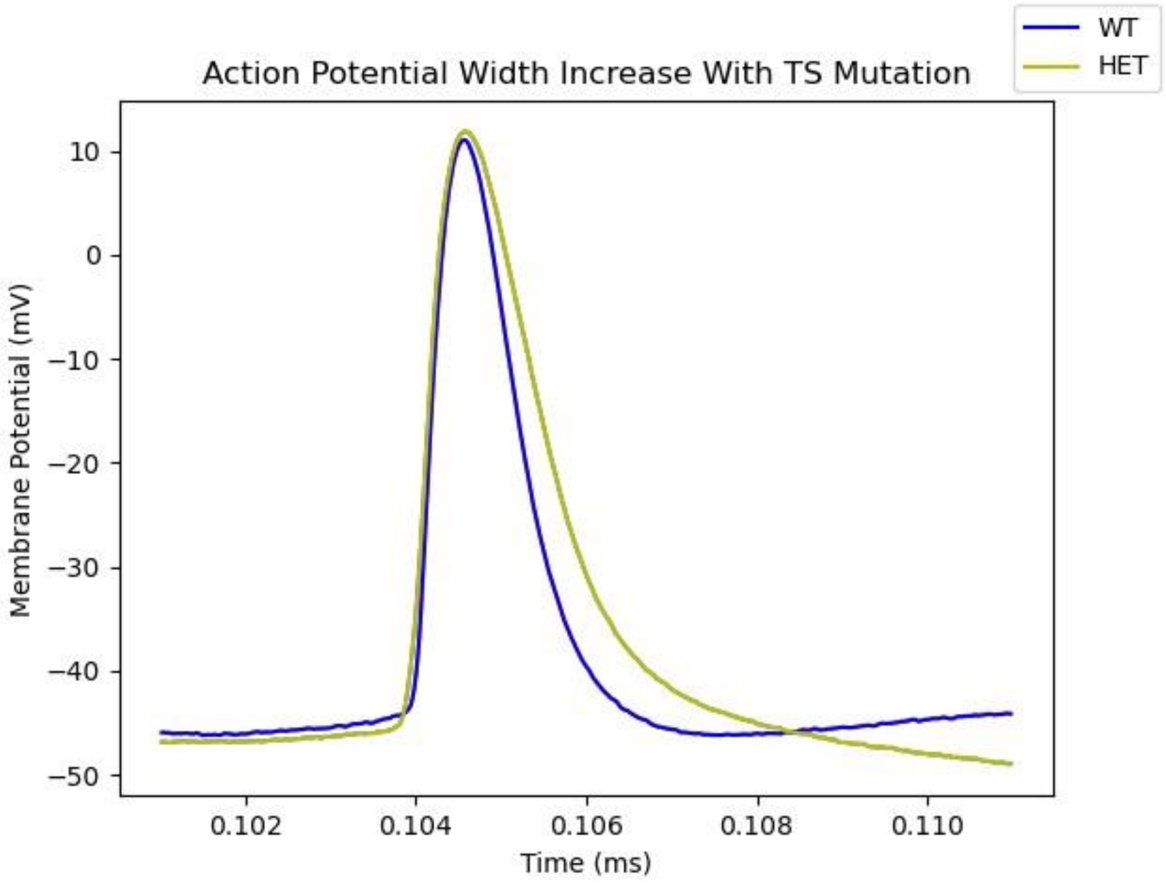

Figure 18 Example AP traces from two single V1 pyramidal cells, one from a WT mouse (blue), the other from a TS2Neo HET (green) mouse. Note how the AP duration is greater for the TS2Neo mouse as for the WT.

TS2Neo heterozygosity is estimated to result in a 23.1% increase in AP half-width based predicted effect sizes of the linear regression model. From the raw data, AP half-width for pyramidal cells of TS2Neo mice are 14.0% higher for CA1, 43.1% higher for RSC, and are 28.4% higher for V1 as compared to those recorded from pyramidal cells from those areas in WT mice (comparing median values from each dataset).

In summary, TS2Neo heterozygosity is significantly related to an increase in AP half-width for pyramidal cells from all 3 areas of the brain studied. TS2Neo heterozygosity results in a 14-43% increase in AP duration in these cells.

TS2Neo mutation does not impact dynamic membrane properties underpinned by BK channel function:

Repeated measures linear regression models were generated to explore the impact of genotype and ROI on AP broadening and spike frequency adaptation. Model testing found that the models were significantly superior to null models in explaining variance in the two parameters. The results of model testing are shown in Table 9 below.

Table 9 Showing the results of model testing for linear regression models exploring the impact of ROI and genotype on AP broadening and spike frequency adaptation in the mouse:

Parameter	**Terms**	**Transformation**	**DF**	**χ2 value**	**P**	**R^2 marginal**	**R^2 conditional**
AP broadening	ROI, genotype	Logarithmic	23	404.4	2.2×10^{-16}	0.219	0.873
Spike frequency adaptation	ROI, genotype	Logarithmic	23	1109.6	2.2×10^{-16}	0.710	0.863

Comparison of reduced models lacking genotype terms with a full model containing terms to describe possible genotype impacts on either AP broadening or spike frequency adaptation were completed. Genotype was not found to impact either property. The results from comparison of reduced and full models are given in Table 10 below.

Table 10 Results of post-hoc testing of linear regression models exploring the potential impact of genotype on AP broadening and spike frequency adaptation for pyramidal cells in acute tissue from the mouse brain:

Parameter	**DF**	**χ2 value**	**P**	**Adjusted P**
AP broadening	5	7.03	0.219	1
Spike frequency adaptation	5	1.21	0.943	1

AP broadening in pyramidal cells from each genotype per ROI is shown in Figure 19. Spike frequency adaptation for pyramidal cells recorded from each ROI of mice from each genotype are shown in Figure 20.

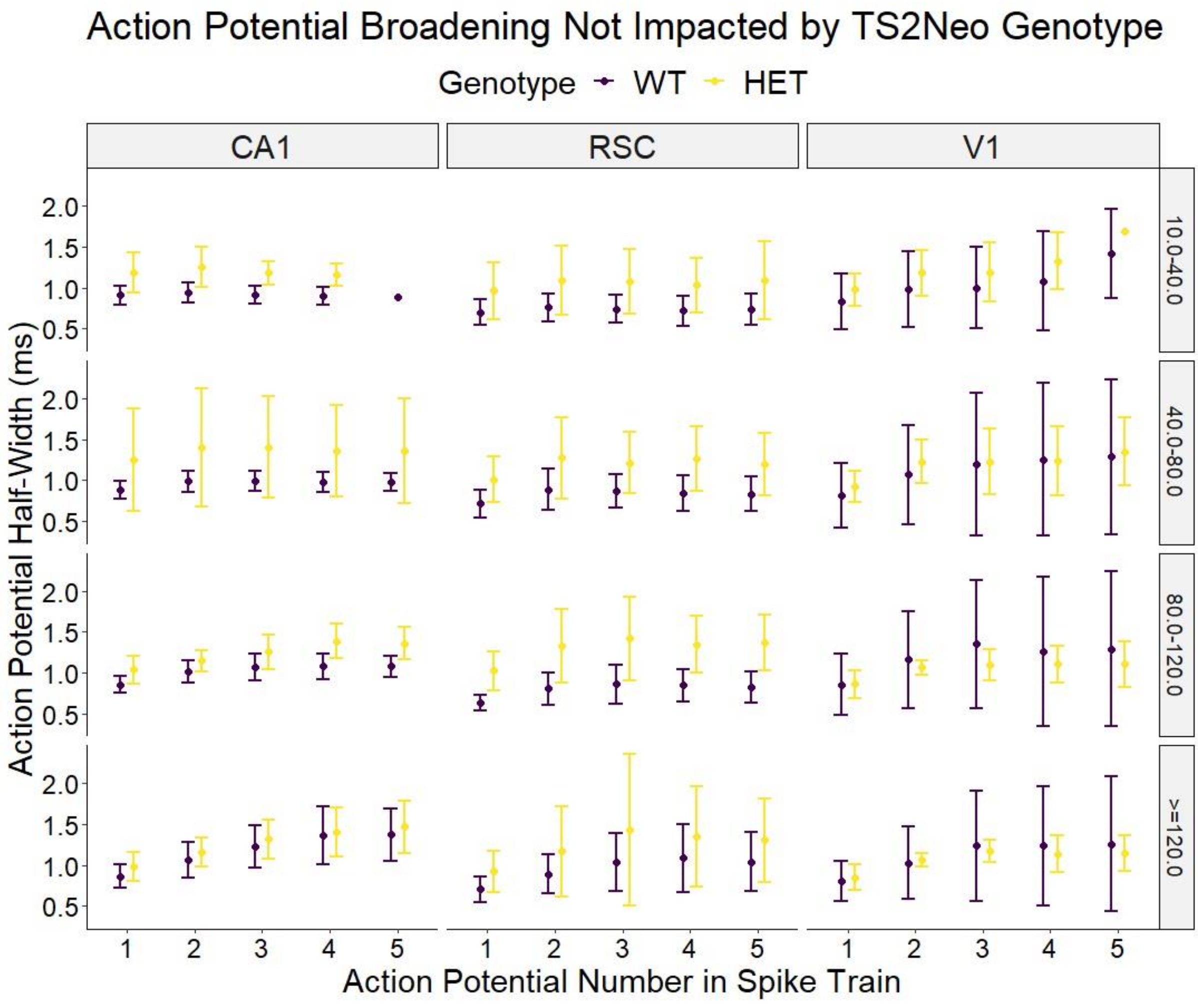

Figure 19 Showing AP broadening across the first 5 APs of spike trains of specific initial firing frequency (shown on right, given in Hz), for cells from each ROI (top) per genotype. Note the lack of genotype effect on broadening in most areas, although AP width is typically greater in TS2Neo HET as compared to WT cells. Points indicate the mean value of the AP half-width, while error bars indicate the standard deviation in this value.

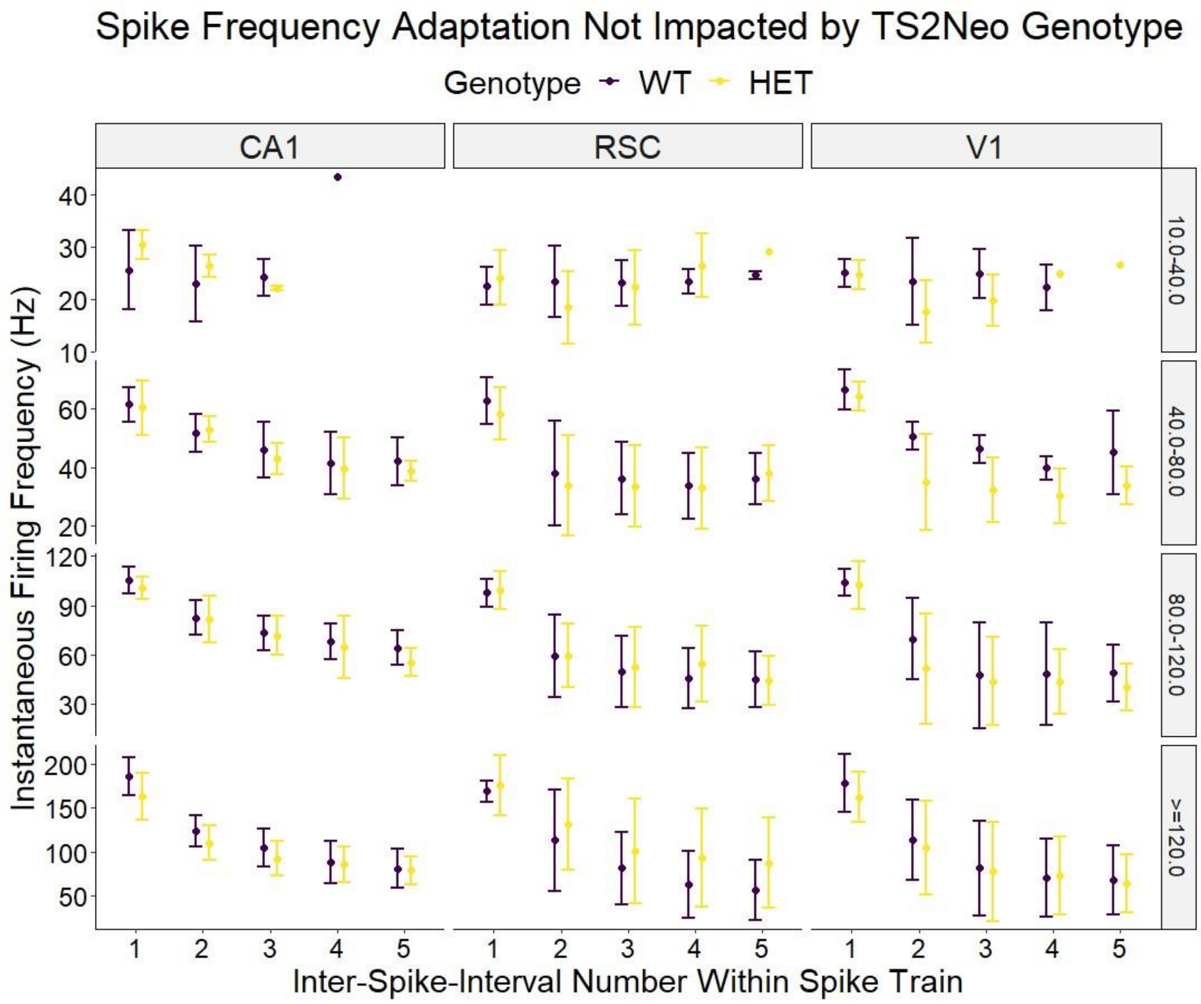

Figure 20 Showing spike frequency adaptation across the first 5 inter-spike-intervals within spike trains of specific initial firing frequency (shown on right, given in Hz), recorded from pyramidal cells of each ROI (top) per mouse genotype. Note the lack of genotype effect on adaptation of the instantaneous firing frequency across the intervals. It should be noted that the scale for instantaneous firing frequency varies across the subplots, for ease of viewing. Points indicate the mean value of the instantaneous firing frequency, while error bars indicate the standard deviation in this value.

Overall, the TS2 mutation was not associated with any significant change in AP broadening or spike frequency adaptation of pyramidal cells from CA1, RSC or V1 of the TS2Neo mouse brain.

Measures of cell excitability not impacted by TS2Neo genotype:

Potential impacts of TS2Neo genotype on AP threshold, minimum onset latency, maximum firing frequency, and rheobase were explored statistically. Linear regression was used to model how AP threshold, minimum onset latency and maximum firing frequency recorded from pyramidal cells varied by ROI and animal genotype. Data were transformed before modelling as indicated in the tables below. The impact of genotype on rheobase was tested by three separate Wilcoxon signed-rank tests; one test being completed per ROI.

The AP threshold model was reduced, but genotype and ROI terms remained in the model. The AP threshold linear model described the variance in the data significantly better than a null model, but post-hoc testing indicated that AP threshold did not vary significantly with animal genotype (adjusted P=1, t value= 0.067, P=0.947).

Table 11 Results of model testing exploring the impact of ROI and genotype on AP threshold for pyramidal cells recorded from acute mouse brain tissue:

AP property	**Model test statistic**	**DF**	**Model P value**
Threshold	15.6	3 and 78	5.09×10^{-8}

Descriptive statistics regarding AP threshold recorded from pyramidal cells from each ROI are shown in Table 12, below.

Table 12 Descriptive statistics for AP threshold values measured from pyramidal cells from CA1, RSC and V1 of WT and TS2Neo mice. The mean and standard deviation in measured AP threshold from each group are shown in the table:

ROI	**AP threshold (mV)**	
	WT	**HET**
CA1	-49.6(±2.7)	-51.5(±5.1)
RSC	-42.6(±3.8)	-40.9(±7.4)
V1	-45.4(±2.9)	-44.9(±6.5)

The models used to describe variance in minimum onset latency and maximum firing frequency did not fit the data significantly better than null models. There is no evidence that these values significantly differ by either ROI or genotype.

Table 13 Results from model testing exploring the impact of genotype and ROI on AP onset latency and maximum instantaneous firing frequency:

Active firing property	**Model terms**	**Data transformation**	**F statistic**	**DF**	**P value**	**Adjusted R^2**
Minimum AP onset latency	ROI, genotype, ROI-genotype interaction term	Logarithmic	1.02	5 and 50	0.414	0.00214
Maximum instantaneous firing frequency	ROI, genotype, ROI-genotype interaction term	None	1.16	5 and 50	0.343	0.0141

The impact of TS2Neo genotype on rheobase recorded for pyramidal cells from each ROI is indicated in Table 14, below.

Table 14 Results of non-parametric testing of the effect of TS2Neo heterozygosity on the obtained measure of rheobase from pyramidal cells of the mouse:

ROI	N WT	N TS2 Neo	W statistic	P value	Adjusted P value
CA1	11	8	64	0.109	1
RSC	9	12	51	0.862	1
V1	8	8	30	0.879	1

Descriptive statistics showing the median and IQR of rheobase values measured from pyramidal cells from each ROI in WT and TS2Neo mice are given in the Table 15, below.

Table 15 Descriptive statistics showing the non-parametric spread of measured rheobase values obtained from pyramidal cells from each ROI for mice of each genotype:

ROI	**Rheobase (pA)**	
	WT	**HET**
CA1	100 (100-200)	200 (150-250)
RSC	150 (150-250)	200 (100-250)
V1	150 (150-200)	150 (100-250)

To summarise, TS2Neo heterozygosity did not significantly impact pyramidal cell excitability by any method of measurement used in this study.

Pyramidal cell AP amplitude not impacted by TS2Neo genotype:

A linear regression was used to model how AP amplitude varied with animal genotype and ROI. Data did not require transformation. Models were reduced using stepwise methods. Reduced models included both genotype and ROI to explain variance in AP amplitude. The model was found to be significantly superior to a null model in describing the data. Genotype as not found to impact AP amplitude on post-hoc testing (adjusted P=1, t value= 1.52, P=0.131). Model significance and the results of genotype testing are shown in Tables 16 and 17, respectively.

Table 16 Results of model testing for a linear regression model exploring the impact of TS2Neo heterozygosity and ROI on AP amplitudes measured from pyramidal cells in acute mouse brain tissue:

AP property	Model test statistic	DF	Model P value
Amplitude	16.8	3 and 78	1.67×10^{-8}

Mean values of AP amplitudes of pyramidal cells from each ROI are shown for HET and WT mice, with the standard deviation of this value shown in brackets.

Table 17 Descriptive statistics showing the spread of AP amplitude data measured from pyramidal cells of each ROI from mice of each genotype:

ROI	**AP amplitude (mV)**	
	WT	**HET**
CA1	32.9(±7.4)	30.1(±9.2)
RSC	25.6(±8.0)	22.8(±8.0)
V1	24.3(±11.4)	22.7(±9.6)

TS2Neo heterozygosity impacts voltage sag for pyramidal cells in mouse RSC, but was not found to impact membrane potential rebound:

Linear regression models describing pyramidal cell membrane potential rebound and voltage sag with respect to animal genotype and ROI to which the cell belonged were generated. The models describing how voltage sag and membrane potential rebound changes with ROI and genotype were found to be significant; the models described variance in the data better than a null fitted model in each case. The results from testing of the fully fitted models are provided in Table 18 below.

Table 18 Results of model testing for linear regression models used to explore how genotype and ROI impact voltage sag and membrane potential rebound for pyramidal cells sampled from the mouse brain:

Property	**Model terms**	**Data transformation**	**F statistic**	**DF**	**P value**	**Adjusted R^2**
Membrane potential rebound	ROI, genotype, ROI-genotype interaction term	Logarithmic	2.82	5 and 50	0.0254	0.142
Voltage sag	ROI, genotype, ROI-genotype interaction term	Square root	5.84	5 and 50	0.000252	0.306

Membrane potential rebound:

Dropwise testing of the membrane potential rebound model found that removal of the genotype-ROI interaction term did not significantly change the models fit; the model's ability to explain the rebound data (P=0.130, F=2.12). The rebound model was reduced such that variance was described by ROI and genotype singularly, without any interaction between the two. The resulting model explained the variance in membrane potential rebound values between cells significantly better than the null test model (P=0.0325, F=3.15, DF=3 and 52, R^2=0.105). Model testing found that the transformed value of membrane potential rebound did not vary with TS2Neo heterozygosity (adjusted P= 1, P=0.24, t=-1.18).

Descriptive statistics showing the median and IQR for voltage rebound measured from pyramidal cells from each ROI in WT and TS2Neo mice are given in Table 19, below.

Table 19 Descriptive statistics showing the distribution of membrane potential rebound values measured from pyramidal cells of each ROI from mice of each genotype:

ROI	**Membrane Potential Rebound (mV)**	
	WT	**HET**
CA1	2.0 (0.9-2.3)	1.4 (1.1-1.5)
RSC	2.4 (1.9-2.8)	1.5 (1.3-1.7)
V1	2.2 (1.3-3.2)	2.5 (2.1-3.8)

Voltage sag:

Dropwise model testing for the voltage sag model determined that removal of the genotype-ROI interaction term significantly impacted the model fit (P=0.00181, F=7.19). Pairwise testing of the model suggested that TS2Neo heterozygosity significantly impacts voltage sag of pyramidal cells in V1 and RSC. The significance of genotype on voltage sag for pyramidal cells in V1 was lost after multiple-comparison correction. The results from the pairwise testing are shown in the table below.

Table 20 Results of pairwise testing showing the significance of TS2Neo heterozygosity on voltage sag values measured from pyramidal cells of each ROI:

ROI	**DF**	**T ratio**	**P value**	**Adjusted P value**
CA1	50	0.685	0.496	1
RSC	50	3.29	0.0018	0.0216
V1	50	-2.15	0.0363	0.436

The estimated effect size of the TS2Neo mutation is a 57.0% reduction in voltage sag for RSC pyramidal cells. Voltage sag measured from pyramidal cells of each ROI from

TS2Neo and WT animals is shown in Figure 21.

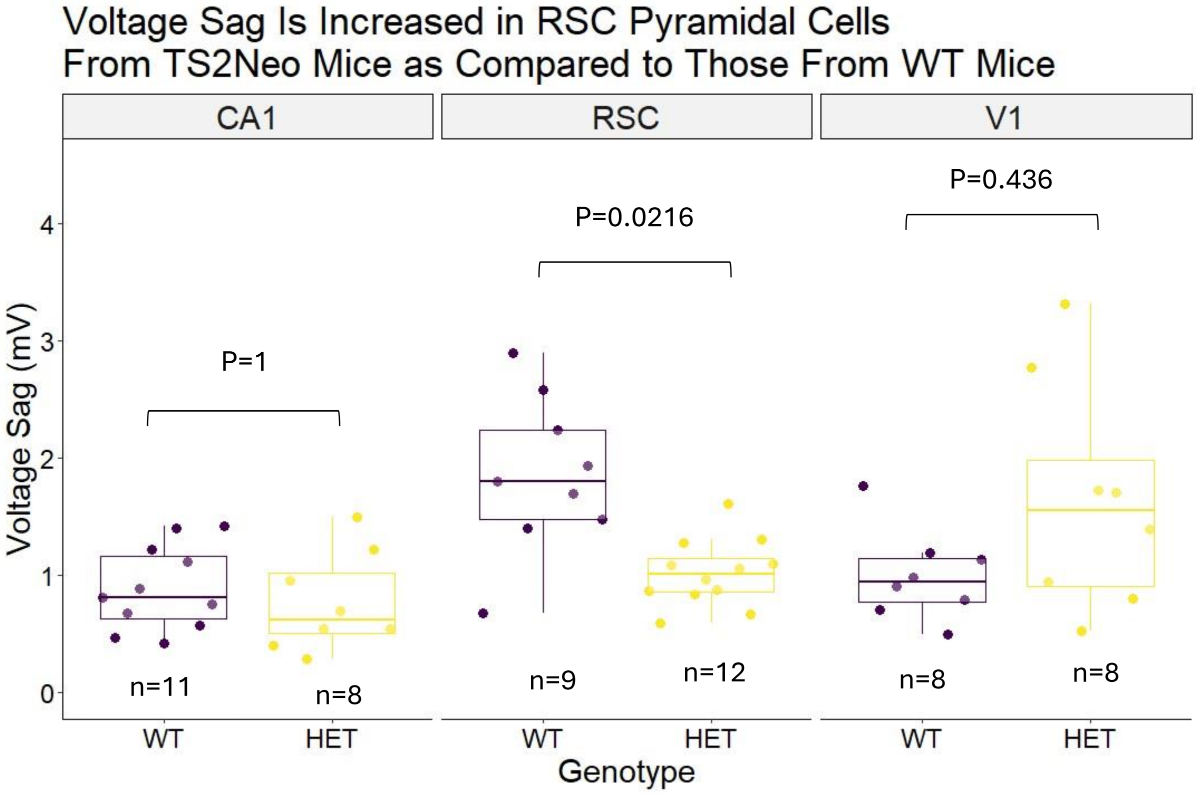

Figure 21 Voltage sag measured from pyramidal cells of CA1, RSC and V1 of TS2Neo HET and WT mice. P values shown on the figure correspond to the Bonferroni adjusted P values from linear regression model testing. n values show the number of cells recorded from in each group. Note that voltage sag measured from RSC pyramidal cells of TS2Neo mice is significantly lower than that measured from WT mice.

Overall, TS2Neo heterozygosity was not found to impact membrane potential rebound for any of the areas tested. TS2Neo heterozygosity was found to be correlated with a significant reduction in voltage sag for pyramidal cells in the RSC region only. TS2Neo heterozygosity does not appear to impact voltage sag for pyramidal cells in V1 or CA1 of the mouse brain.

Discussion:

Classical TS2 -type TS mutation causes prolonged AP in pyramidal cells of TS2Neo mouse:

My primary hypothesis was that the AP duration, measured as AP half-width, would be increased in pyramidal cells from CA1, RSC and V1 of TS2Neo as compared to those from WT mice. This was tested by whole-cell patch clamp electrophysiology experiments using acute ex-vivo slices from TS2Neo and WT mouse brains. I found that pyramidal cells from CA1, RSC and V1 from TS2Neo mice had longer measured AP half-widths as compared to those from WT mice. This suggests that classical TS mutations result in a prolonged AP in naturally developed neurons within functional brain tissue, supporting my primary experimental hypothesis. My findings, together with those of

Paşca *et al.* (2011) provide evidence that classical TS mutations result in a prolonged AP in the neuron as they do in the cardiac myocyte (Splawski *et al.*, 2004, 2005; Dick *et al.*, 2016).

Possible mechanisms by which classical TS mutations prolong the neuronal AP:

As discussed in the introduction, there are three possible mechanisms I have identified by which the TS mutant CaV1.2 channel could prolong the neuronal AP duration. These are A) Directly, with the prolonged depolarising calcium current through the mutant CaV1.2 channel, directly prolonging the neuronal AP; B) through a change in function of calcium-dependent BK potassium channels which associate with CaV1.2 and are known to be involved in AP repolarisation; and C) through a mutation related change in sodium channel density in the neuronal membrane.

This study provided no further evidence to support or contradict the theory that classical TS mutations might impact AP duration directly, with the prolonged depolarising calcium current through the mutant channel directly causing a prolongation of the neuronal AP. It is possible that the prolonged depolarising current flowing through the mutant CaV1.2 channel results in the prolonged AP duration in TS-mutant neurons directly based on the findings of , however L-type calcium channel currents are not typically thought to impact the neuronal AP waveform directly (Bean, 2007).

This study provided no evidence to support the theory that classical TS mutations might impact AP duration indirectly through a mutation-related change in BK channel function. I found no genotype difference in AP broadening and firing frequency adaptation on repetitive neuronal firing. These two dynamic properties are underpinned by BK channel function (Shao *et al.*, 1999; Gu, Vervaeke and Storm, 2007). Differences in BK channel function in TS2Neo as compared to WT pyramidal cells were not tested directly in this study. As such, it cannot be ruled out that classical TS mutations increase neuronal AP duration indirectly through mutation-related changes in BK channel function. However, these findings do provide some evidence to suggest that classical TS mutations prolong the neuronal AP duration by mechanisms that do not involve changes in BK channel function.

This study did not test whether classical TS mutations affect sodium channel currents or density in the TS2Neo vs WT mouse. It remains plausible that classical TS mutations impact AP duration by mutation-related changes in sodium channel density in the neuronal membrane as was found in the chromaffin cell membrane by Calorio *et al.* (2019).

Neuronal AP duration in other ASD-related diseases:

TS is an ASD-related disease of known genetic cause. Here, I found that pyramidal cells from the TS2Neo mouse model of TS had a prolonged AP as compared to those from WT mice. This suggests that ASD-related classical TS mutations result in prolonged AP in pyramidal cells. Other ASD-related genetic models also show prolonged AP in various types of neurons.

Fragile X syndrome is a widely known ASD-related genetic condition of specific and known cause. Fragile X is caused by a loss of function of the *Fragile X Messenger Ribonucleoprotein 1 (FMR1)* gene. CA3 and CA1 Pyramidal cells from the *FMR1* KO mouse model of fragile X syndrome have been demonstrated to have prolonged AP duration as compared to those from WT mice (Deng *et al.*, 2013; Luque *et al.*, 2017). The effect size of the *FMR1* KO on AP duration for CA1 pyramidal cells was found to be a 7% increase (Deng *et al.*, 2013), which is much lower than the increase in AP duration seen in in pyramidal cells from TS2Neo mice as compared to WTs shown here. Abnormalities in firing frequency and in input resistance have also been measured in pyramidal cells from *FRM1* KO mice as compared to WTs (Deng and Klyachko, 2016; Luque *et al.*, 2017). These abnormalities were not found in pyramidal cells from TS2Neo as compared to WT mice in this study. CA3 pyramidal cells from *FMR1* KO mice have been found to have significantly increased AP broadening on repetitive firing (Deng *et al.*, 2013). This contrasts with the lack of AP broadening changes found in pyramidal cells from CA1, V1 and RSC from TS2Neo as compared to WT mice in this study.

Deng *et al.* (2013) found that the increased AP duration and increase in AP broadening seen in CA3 pyramidal cells of *FMR1* KO mice as compared to WTs was dependent on BK channel function. Blockade of BK channels resulted in a loss of genotype effect on AP duration and AP broadening in this study. The findings of Deng *et al.* (2013) suggest that ASD-related mutations can impact AP duration as a result of changes in BK channel function. No change in BK channel function was found in TS2Neo mouse pyramidal cells as compared to WT in this study, although BK channel function was not measured directly in those cells. Further experiments into impacts of the TS mutation on BK channel function are likely warranted, despite the lack of finding in this study.

Rett's syndrome is another widely known ASD-related genetic condition with a specific and known genetic cause, resulting from mutation of the *methyl CpG binding protein 2 (Mecp2)* gene. iPSC-derived neurons from Rett's syndrome patients have recently been found to have prolonged AP as compared to iPSC-derived neurons from control subjects, and compared to isogenic control iPSC-derived neurons (Gomes *et al.*, 2020). AP half-widths measured from iPSC-derived neurons of Rett's syndrome patients were found to be around 3 times greater than controls. This genotype effect is much larger than the 23% increase in AP width reported for pyramidal cells of the TS2Neo mouse as compared to control WT mouse pyramidal cells in this study. The mechanism by which the Rett's syndrome mutation results in prolonged AP has not yet been studied. Increased AP duration has not been reported in the *Mecp2* KO mouse model of Rett's syndrome.

Together with my findings, these observations show that prolonged AP duration is a common neuropathological mechanism in ASD-related genetic disorders, including TS. This neurophysiological change may potentially be of importance in contributing to ASD-type phenotypes seen in these disorders.

No evidence that TS2 mutation in TS2Neo mice impacts passive membrane properties, voltage rebound, cell excitability or AP amplitude for pyramidal cells, but TS2Neo mouse RSC pyramidal cells have increased voltage sag:

Passive membrane properties measured in pyramidal cells of TS2Neo mice were not found to significantly differ from those measured from pyramidal cells of WT mice. This includes membrane input resistance, capacitance, and membrane time constant.

I had originally hypothesised that the TS2 mutation may impact the excitability of pyramidal cells in the TS2Neo mouse. Measures of cell excitability, such as AP threshold, AP onset latency, maximum firing frequency and rheobase were not significantly different between pyramidal cells of TS2Neo as compared to WT mice in this study. Evidence from this study suggests that the TS2 mutation does not impact neuronal excitability in the TS2Neo mouse. It should be noted that other ASD-related genetic mutations do cause alterations in neuronal excitability (Deng *et al.*, 2013; Deng and Klyachko, 2016; Luque *et al.*, 2017). It is possible that classical TS mutations do impact neuronal excitability, but that the reduced expression of TS2-type mutant CaV1.2 channels in the TS2Neo mouse, caused by the inverted neomycin cassette insert, reduced the effect size, resulting in the null finding in this experiment. Overall, the evidence from this study suggests that the TS2 mutation does not impact neuron excitability in the TS2Neo mouse.

Membrane potential rebound was not found to significantly differ by genotype, however, voltage sag was found to be lower in RSC pyramidal cells of TS2Neo as compared to WT mice, but this was not the case in V1 and in the hippocampus. In fact, an opposite, but non-significant increase in voltage sag was seen in the V1 pyramidal cells of TS2Neo as compared to WT mice. It is possible that the expression of and/or distribution of HCN channels in RSC pyramidal cells of the TS2Neo mouse are disrupted by the classical TS2 mutation, but expression of or distribution of T-type calcium channels is similarly disturbed in these cells. This could result in membrane potential rebound not differing significantly between RSC pyramidal cells from TS2Neo and WT mice, while voltage sag—which is not contributed to by currents flowing through T-type calcium channels—is.

Whether the distribution and/or expression of HCN and T-type calcium channels are disrupted in cortical pyramidal cells of the TS2Neo mouse has not been explored and should be investigated in future experiments. A potential impact of the TS2Neo mutation on HCN and/or T-type calcium channel function is interesting, and I suggest this be further researched. The HCN channel has a function in regulating spontaneous cell firing and cell firing properties (Shah, 2014). HCN channel function has also been found to be implicated in several types of epilepsy (Benarroch, 2013), as has the T-type calcium channel (Powell *et al.*, 2014). Epilepsy is a common neurological phenotype of TS (Splawski *et al.*, 2004, 2005; Walsh *et al.*, 2018). However, it is not clear how classical TS mutations might impact HCN channel or T-type calcium channel distribution and function in RSC pyramidal cells. The finding did survive highly conservative Bonferroni correction and is therefore a potentially genuine finding. However, it should be considered that my prior hypothesis was that the TS2Neo mutation would not impact voltage sag or rebound in pyramidal cells for any ROI. Future experiments could provide more evidence to suggest whether the decrease in voltage sag seen in RSC pyramidal cells from TS2Neo as compared to WT mice is a real genotype-related phenomenon, or a spurious finding of this study. This is discussed further in the “Future experiments” subsection.

Limitations:

This study used the TS2Neo mouse model of TS to explore the impacts of the classical TS2-type mutation on pyramidal cell properties. The TS2Neo mutation includes an inverted neomycin cassette which reduces mutant channel expression and mortality of the TS2Neo mouse (Bader *et al.*, 2011). The genetic mutation in TS2Neo mice is therefore slightly different from that which causes TS2 in humans, and the TS2 channel is expressed at lower levels in the mouse. The TS2Neo model mouse is not a perfect genetic model of TS2. This could impact the ability of this study to identify TS2-related changes in the electrical properties of pyramidal cells. It is possible that the TS2 mutation does not cause a prolonged AP in naturally developed neurons in the human brain, as this study only involved the use of mouse brain tissue. The risk of this is low based on Paşca *et al.* (2011) finding a similarly prolonged AP in iPSC-derived human neurons from TS patients as compared to controls.

I used AP broadening and spike frequency adaptation as a way of measuring BK channel function in pyramidal cells from TS2Neo and WT mice but found no difference in these measures between genotypes. These observations suggest that the TS2 mutant CaV1.2 channel could result in prolonged AP in pyramidal cells by mechanisms unrelated to BK channel function. I did not measure BK channel activity directly, nor did I measure any calcium currents directly. This limits my ability to identify or exclude any pathophysiological mechanism whereby the TS2 mutant channel may result in prolonged AP in pyramidal cells in the mouse. Future experiments are required to provide more solid evidence that BK channel function is not impacted by classical TS mutations.

A smaller dataset was used to explore non-single-AP physiological properties than to explore single AP-properties such as AP half-width, threshold, and amplitude. As such, the statistical power available to find genotype effects on these neuronal properties was reduced in this study. The AP half-widths measured from the smaller dataset were compared to those from the full dataset to confirm that the smaller dataset was representative. Statistical testing confirmed no significant differences in AP half-width measured from the data subset used to measure electrical properties not related to the single AP waveform, and the full dataset used to measure electrical properties which were related to the single AP waveform.

The findings of this study are limited in supporting the conclusion that the TS2 mutation impacts AP duration in the neuron in general. I measured membrane properties only in pyramidal cells sampled from just 3 areas of the mouse brain. It is possible that this finding does not generalise across other cell types in the brain.

This experiment did not cover the potential effects of the TS2 mutation on several key electrophysiological properties of the mouse pyramidal cell. These should be explored in the future. I collected no data exploring differences in resting membrane potential for pyramidal cells of mice from each genotype as appropriate data to measure this property were not collected at the time of study. Similarly, data regarding voltage-current relationships for the membrane were not collected and, as such, any differences in V-I curve could not be explored for pyramidal cells of each genotype, per ROI. Measurements of fast after hyperpolarisations (fAHPs) and comparing these for cells from mice of each genotype would have been a useful indicator of genotype-differences in BK channel function. This is because fAHPs are underpinned by BK channel currents (Bentzen *et al.*, 2014). The protocol used to collect the experimental data for this study was based on that used by Paşca *et al.* (2011), and involved constant depolarising step current injections. An accurate measurement of fAHPs was not possible to obtain from the recording data from these experiments as cells were not allowed to return to resting membrane potential immediately after AP firing. To measure fAHPs, measurements of the fAHP duration and magnitude using data from APs elicited by short depolarising pulses as described in Storm (1987) would have been more appropriate. I did not measure APs elicited from this sort of short pulse depolarisation protocol to keep the methods used in line with those of Paşca *et al.* (2011), to make the experiments comparable to those from human-derived iPSCs. Measuring fAHPs and remeasuring single AP properties using short depolarising current pulse injections should be explored in future experiments as described in the "Future experiments" subsection of this chapter.

Future experiments:

The finding that voltage sag was decreased in pyramidal cells of the RSC of TS2Neo as compared to WT mice was an unexpected finding. It is unclear whether this is a real genotype effect, or a spurious result. Repetition of this experiment, using larger sample sizes to measure non-single-AP electrical properties such as voltage sag in pyramidal cells from TS2Neo and WT mice would be useful to resolve this. An experiment involving direct measurements of BK channel currents would be useful in exploring any potential impacts of the mutant CaV1.2 channel on BK channel function. Furthermore, testing for differences in the size of fAHPs measured from pyramidal cells of both TS2Neo and WT mice would be similarly informative. From these studies, a repeated measurement of changes in voltage sag and hyperpolarisation-related membrane potential rebound should be obtained and genotype differences in these measures for pyramidal cells from each ROI should be tested for.

Similar experiments to the ones described here should be completed where a single brief pulse depolarising stimulus current injection should be used in place a continuous depolarising step injection. Measures of fAHPs for cells from mice of each genotype per ROI could be obtained from such experiments. This would indicate if BK channel function is disrupted in T2Neo mice. Measurements of single AP properties, such as AP half-width, AP threshold and AP amplitude should also be obtained from such a study.

A future study exploring NaV1 sodium channel density and currents within pyramidal neurons of the three cortical areas involved in this study from both TS2Neo and WT mice is recommended. If TS mutations impact NaV1 channel density in the neuron, this could then impact the rate of AP depolarisation, and could result in a prolonged AP. I suggest that this be explored using methods similar to those used in Calorio *et al.* (2019). In this study, any differences in HCN and T-type calcium channel density and/or distribution should also be tested for. This would show if and how the TS2 mutation alters the expression and/or distribution of these channels, as suggested by the finding that voltage sag is significantly lower in RSC pyramidal cells of TS2Neo mice as compared to WT.

Studies to examine relative CaV1.2 channel expression in pyramidal cells of the TS2Neo and WT mouse would be useful. This could provide evidence to confirm that the TS2-type channel is expressed in pyramidal cells of the TS2Neo mouse, and at what level the channel is expressed.

Ideally, repetition of this study using the TS2 mouse model described by Matsui *et al.* (2023) should be conducted in the future when this model becomes more widely available and better characterised. The TS2 mouse model which has been recently described has the exact same mutation in the *CACNA1C* gene as TS2 patients, and, unlike the TS2Neo mouse, does not require an inverted neomycin cassette to reduce overall expression of the channel to ensure mouse viability. The TS2 mouse model was not used in the currently described study as it was not available at the time of experiment.

Measuring AP half-width in non-pyramidal cells, and in pyramidal cells from other brain areas would be informative to understand if this genotype effect is cell-type or region specific. Explicitly, I suggest future experiment involve measuring AP half-width in other types of glutamatergic neurons known to express *CACNA1C*, such as hippocampal and cerebellum granule cells (Hell *et al.*, 1993). Measuring AP half-width in mature interneurons would also be informative. Measuring AP half-width of CA3c hippocampal PV+ interneurons from TS2Neo and WT would be especially useful. Mature CA3c hippocampal PV+ interneurons in the adult rodent brain do not express CaV1.2 (Jiang and Swann, 2005). Should PV+ cells in CA3c of TS2Neo mouse brain have a longer AP duration than those in the WT mouse brain, this would indicate that the TS2 mutation results in prolonged neuronal AP by impacts on cell development, as opposed to the presence of the mutant CaV1.2 channel impacting the functionality of the mature neuron through electrogenic mechanisms. Measuring AP in pyramidal cells of the amygdala and in the prefrontal cortex would provide information as to whether the genotype effect on AP duration is functional area and/or cortex specific.

Repetition of this experiment, measuring AP half-widths in pyramidal cells from CA1, RSC and V1 before and then after use of calciseptine is advised. Caliseptine is a recently described toxin found to selectively and specifically block CaV1.2 channel function (Mesirca *et al.*, 2024). Should the AP half-width difference measured between pyramidal cells from TS2Neo and WT mice be lost on application of the toxin, this would suggest that abnormal CaV1.2 channel function underpins the change. Similarly, repetition of the experiment using a BK channel blocker, such as iberiotoxin would suggest whether the genotype-related increase in AP duration is BK-channel dependent. Should the AP duration be equal in cell from TS2Neo as compared to WT mice on application of the BK channel blocker, this would indicate that abnormalities in BK channel function are responsible for the change in AP duration seen in the TS2Neo mouse.

Simple computational experiments to mathematically model neuronal electrical responses to stimulation based on ion channels in the membrane could be completed to explore how the presence of TS2 mutant channels in a pyramidal cell membrane impacts AP half-width.

Conclusion:

The duration of pyramidal cell APs for CA1, RSC and V1 of TS2Neo mice were found to be longer as compared to those from WT mice in this experiment. This study provides the first evidence that classical TS mutations prolong neuronal AP duration in the brain. Pyramidal cells from TS2Neo mice appeared to be otherwise electrically typical as compared to WT. AP amplitude was not affected by the mutation. Measures of cell excitability, including membrane threshold, maximum instantaneous firing frequency, minimum AP onset latency, and rheobase were not significantly different in pyramidal cells from TS2Neo mice as compared to WT. Dynamic firing properties dependent on BK channel function which included AP broadening and spike frequency adaptation were not found to significantly differ by genotype. Passive membrane properties, such as membrane input resistance, capacitance, and membrane time constant, as well as membrane voltage rebound were not found to significantly differ between pyramidal cells from TS2Neo as compared to WT mice. Voltage sag for RSC pyramidal cells was found to be significantly lower in TS2Neo as compared to WT mice. This was an unexpected finding and should be replicated before being accepted as a real genotype effect. Overall, pyramidal cell APs from TS2Neo mouse CA1, RSC and V1 are significantly longer than those from the same areas of WT mice. Together with previous findings, this suggests that classical TS mutations cause prolonged AP in the neuron as it does for other electrical cells. The physiological mechanism by which expression of the TS2-mutant CaV1.2 channel results in a prolonged AP is currently unknown.

Contributions:

Rosie Craddock and Dr Cezar Tigaret were involved in experimental conceptualisation and methodological development. Experiments were completed by, and data were collected by Rosie Craddock. Data processing was completed by Rosie Craddock, under guidance from Dr Cezar Tigaret using software developed by Dr Cezar Tigaret and codes written by Rosie Craddock. Data analysis was completed by Rosie Craddock. Images were acquired by Rosie Craddock. Dr Anthony Hayes aided in microscope optimisation for the acquisition of high-resolution confocal images of fluorescently labelled cells. Electrophysiology equipment was set up and maintained by Dr Cezar Tigaret. Animal genotyping was undertaken by Dr Stephanie Bagstaff. Writing of the manuscript was completed by Rosie Craddock, with advice provided by Dr Cezar Tigaret.

Data Chapter 3: PV+ cell number is differentially altered across multiple brain areas in the TS2Neo mouse:

Introduction:

Patients with TS often present with ASD and/or epilepsy (Splawski *et al.*, 2004, 2005; Walsh *et al.*, 2018). These disorders have been found to be associated with abnormalities in inhibitory interneuron number and development (Hussman, 2001; Paterno, Casalia and Baraban, 2020; Righes Marafiga, Vendramin Pasquetti and Calcagnotto, 2021). PV+ inhibitory interneurons are the most numerous type of inhibitory interneuron in the central nervous system. PV+ cells are implicated in a variety of neurological disorders (Godoy *et al.*, 2022). Specifically, anormal function and distribution of PV+ cells have been found in both ASD and in epilepsy (Hashemi *et al.*, 2017; Filice *et al.*, 2020; Contractor, Ethell and Portera-Cailliau, 2021; Godoy *et al.*, 2022).

Abnormalities in PV+ cell number, function and development have been proposed as potential pathophysiological mechanisms of both epilepsy and ASD (Magloire *et al.*, 2019; Filice *et al.*, 2020). For epilepsy, this theory is supported by evidence from in-vivo optogenetic electrophysiological studies on animals demonstrating that abnormal PV+ cell firing can result in ictogenic neural network activity (Assaf and Schiller, 2016). The theory that PV+ cell abnormalities may result in ASD phenotypes is based on both human and animal studies. Human studies demonstrated abnormalities in PV+ cell number across various brain areas of post-mortem tissue from ASD patients as compared to controls (Hashemi *et al.*, 2017; Ariza *et al.*, 2018). Other human studies have demonstrated that PV messenger ribonucleic acid is the most upregulated transcript in brains of ASD patients as compared to controls (Parikshak *et al.*, 2016; Schwede *et al.*, 2018).

Studies have demonstrated abnormalities in PV+ cell number across various brain regions of ASD model mice as compared to controls (Tripathi *et al.*, 2009; Allegra *et al.*, 2014; Lauber, Filice and Schwaller, 2016; Lee *et al.*, 2019; Paterno *et al.*, 2021; Yang *et al.*, 2021; Kourdougli *et al.*, 2023). Specifically, PV+ cell number has found to be reduced in the CA1 and CA3 areas of the hippocampus in various mouse models of ASD as compared to WT (Tripathi *et al.*, 2009; Paterno *et al.*, 2021). PV+ cell number has been found to be increased in V1 in the *En2* KO mouse model of ASD as compared to WT. The *En2* gene encodes the homeobox protein engrailed-2, which is involved in embryonic development and is implicated in ASD (Allegra *et al.*, 2014). PV+ cell number has also been found to be increased in the RSC in the *SENP1* heterozygous KO mouse model of ASD. *SENP1* encodes a protease enzyme which is implicated in ASD (Yang *et al.*, 2021). The reduction in PV+ cell number found in multiple mouse models within CA1 and CA3 hippocampal regions is of particular interest due the hippocampus being functionally implicated in ASD (Banker *et al.*, 2021a).

Many studies have shown that mouse models of ASD have abnormalities in PV+ cell density across the brain. However, it is important to note that the apparent loss of PV+ inhibitory interneurons from immunological studies may not result from a loss of cells which express PV, but from those cells expressing such low levels of PV that they are no longer detectable as PV+ cells. This can be resolved by double-staining for interneuron specific antibodies (Filice *et al.*, 2016).

PV is a calcium binding protein which is involved in calcium signalling. The development of PV+ cells is regulated by L-type voltage-gated calcium channels, including CaV1.2 (Jiang and Swann, 2005). CaV1.2 is encoded by the *CACNA1C* gene which is functionally mutated in TS. Given that the CaV1.2 channel subunit is involved in PV+ cell development, functional changes in CaV1.2 resulting from TS mutations could impact PV+ cell development and migration. Abnormalities in PV+ cell development and migration could result in abnormal PV+ cell function, but also in an abnormal PV+ cell distribution in the brain, such as those demonstrated in ASD patients and animal models of ASD.

TS mutations have been demonstrated to result in the abnormal migration of inhibitory interneurons within developing human and mouse neural tissue. Abnormalities in inhibitory interneuron migration have been demonstrated in cultured human forebrain spheroids from TS1 patients as compared to those from controls. This suggests that classical TS mutations result in abnormalities in interneuron migration during human brain development (Birey *et al.*, 2017, 2022; Kamijo *et al.* 2018). Abnormalities in interneuron migration have also been demonstrated in the developing brain of TS2Neo HET mice as compared to WTs. This suggests that classical TS mutations can result in abnormal interneuron migration in the mouse brain (Horigane *et al.*, 2020). Together, these findings suggest that classical TS mutations may cause abnormalities in interneuron migration during development.

TS-related abnormalities specifically in the migration and development of PV+ interneurons have not been explored. Based on the role of the CaV1.2 channel subunit in PV+ cell development, I theorise that PV+ cell development may be impacted by the functional changes in that channel known to be caused by classical TS mutations. This could lead to abnormalities in PV+ cell density across different areas of the TS mutant brain, like those found in mouse models of ASD. I hypothesised that PV+ cell density would be abnormal across the brain of the TS2Neo as compared to the WT mouse.

In this study, I aimed to explore the impact of the classical TS2 mutation on PV+ cell number in various areas of the adult brain by comparing the number of immunofluorescence labelled PV+ cells in whole brain sections from heterozygous knock-in TS2Neo and WT mice. The PV+ cell density in CA1, CA3, RSC and V1 were measured and compared between TS2Neo HET and WT mice. These areas were selected as PV+ cell number is known to be altered in these areas in other mouse models of ASD, but also because the ROIs include a) 2 regions of the hippocampus, a structure which is known to be functionally implicated in ASD (Banker *et al.*, 2021a); b) a primary sensory cortex; and c) an associative cortical area. Sections were double stained for glutamate decarboxylase (molecular weight 67; GAD67), which is effectively a non-specific ɣ-aminobutyric acid (GABA) antibody, to label inhibitory interneurons. This was to verify whether any apparent change in PV+ cell number was due to a genuine change in cell number, and not up- or down-regulation of PV expression in those cells. GAD67+ cell staining in this study was unsuccessful so this could not be tested. This is discussed in the “Limitations” subsection of the discussion of this chapter.

My hypothesis was that PV+ cell density would be altered in at least one of the ROIs tested. This would provide evidence of abnormal PV+ cell distribution in the brain caused by the classical TS2 mutation in the TS2Neo mouse. This could indicate that the classical TS2 mutation causes abnormal PV+ cell development and migration in TS2Neo as compared to WT mice.

Methods:

Animals:

7 adult TS2Neo HET mice and 5 WT mice were sacrificed to obtain brain tissue for this study (Jax Labs strain #019547, B6.Cg-Cacna1ctm2Itl/J). The mice used in this study were the same as those used for the in-vivo experiments detailed in chapter 1. Mice of both sexes were used in this experiment. The unbalanced sample sizes were unintentional and were due to a genotyping error. 4 of the 5 WT mice used were non-littermates, as insufficient age-matched WT littermates were available at the time of study. The non-littermates included in the WT group were of the same background as the TS2Neo mice, C57BL/6J (Jax labs; stock number 000664).

One WT mouse, the TS2Neo mouse littermate, was euthanised early during the in-vivo experiment detailed in chapter 1. The cranial window of the mouse became displaced, and the mouse was euthanised for humane reasons. Tissues from this animal were not used in this study as the age of death for this mouse was not comparable to that of the other mice (age 16.5 weeks as compared to 20 weeks), and age is known to impact PV expression (Gray *et al.*, 2013; Honeycutt *et al.*, 2016). Specifically, age has been found to decrease PV+ cell number in the hippocampus of the rat (Honeycutt *et al.*, 2016)..

In total, tissue from 4 WT mice and 7 TS2Neo HET mice was used in this study. Mice were 20 weeks of age at the time of sacrifice and tissue extraction.

All experimental procedures on the mice were carried out in accordance with the UK Animals (Scientific Procedures) Act 1986, and the European Commission Directive 2010/63/EU. Housing and husbandry were provided by Cardiff University Biological Society services. Mice were given standard food and water ad-libitum and were subject to a normal light/dark cycle (12hours light, 12hrs dark). Mice were group housed and kept in enriched housing when not participating in experimental procedures. I remained blinded to animal genotype throughout the experimental procedure and data processing stages. I became unblinded to animal genotype only at the time of the final data analysis for this experiment.

Tissue extraction:

Animals were anaesthetised by use of isoflurane, then sacrificed by intraperitoneal-injected Euthatal overdose. Mice were trans-cardially perfused with 1x PBS, followed by 4% PFA to ensure fast and complete fixation of neural tissue. Whole brains were collected and stored in 4% PFA solution for 48hrs. Brains were then washed 3 times in 1x PBS and stored in 1x PBS for 5 days.

Sectioning and immunofluorescence staining:

Whole brains were sectioned coronally to a thickness of 50μm in ice-cold 1x PBS solution using a Leica LS1000 vibratome equipped with a steel blade. Sections were stored in 1x PBS for up to 56hrs. 1 in 4 sections containing V1, CA1, CA3, or RSC areas were collected, stained, and used to obtain cell counts in this study. Brain areas were identified by comparison of gross anatomy to the reference Allen Brain Atlas (Wang *et al.*, 2020).

Sections were washed 3 times in 1x PBS. Each wash was 10 minutes. Sections were then washed 4 times in 1x PBS containing 0.2% triton to increase tissue permeability. Each wash in 1x PBS with 0.2% triton described here was of 10 minutes duration. Sections were incubated in a blocking solution at RT for 1hr (3% normal goat serum in 1x PBS with 0.2% triton). Blocking solution was then replaced with primary antibody solution (1:1000 Rabbit anti-PV, 1:250 GAD67, 3% normal goat serum in 1x PBS with 0.2% triton), the sections were incubated in this primary antibody solution for 48hrs at 4°C. Sections were washed 3 times in 1x PBS with 0.2% triton, and then incubated in secondary antibody solution (1:500 Goat Anti-Rabbit, 1:200 Goat Anti-Chicken in 1x PBS with 0.2% triton) for 2hrs at RT. Sections were washed 3 time in 1x PBS with 0.2% triton, and then incubated in Hoechst solution (1:1000 Hoechst 33342 in 1xPBS with 0.2% triton) for 7 minutes at RT. Sections were washed 4x in 1x PBS with 0.2% triton, before being mounted onto SuperFrost Plus microscope slides and then cover-slipped using Fluoromount mounting medium. Coverslip edges were sealed for long-term storage using clear nail polish.

Details of the reagents used are given in the table below:

Table 21 Table of reagents used in immunofluorescence studies described in chapter 3:

Antibodies					
Primary/Secondary	**Type**	**Source**	**Manufacturer**	**Identifier**	**Dilution**
Primary	Rabbit Anti PV	Swant	Swant	PV27	1:1000
Primary	Chicken Anti-GAD67	Abcam	Abcam	Ab75712	1:250
Secondary	Goat Anti-Rabbit AlexaFluor 488	Thermofisher	Invitrogen	A-11008	1:500
Secondary	Goat Anti-Chicken AlexaFluor 647	Abcam	Abcam	Ab150171	1:200
Other Reagents and Consumables					
Reagent/Consumable Nature	**Type**	**Source**	**Manufacturer**	**Identifier**	**Dilution**
Block	Normal Goat Serum	Abcam	Abcam	Ab7481	3%
Surfactant	Triton X-100	Thermofisher	ThermoScientific	85111	0.2%
Buffer	PBS 1x	Merck	Sigma-Aldrich	79382	NA
Nuclear Stain	Hoechst 33342	ThermoFisher	ThermoScientific	62249	1:1000
Microscope Slide	Superfrost Plus Slide	VWR	VWR	631-0108	NA
Mounting Medium	Fluoromount Aqueous Mounting Medium	Merck	Sigma-Aldrich	F4680	NA
Razor Blades	Double edge prep razor blade individually wrapped	VWR	Personna	PERS74-0002-0000	NA
Fixative	Paraformaldehyde	Thermofisher	ThermoScientific Chemicals	416785000	4%
Brain Section Storage	24-well plates	Thermofisher	ThermoScientific	142475	NA

Imaging and data acquisition:

Images were obtained using an Olympus VS200 ASW slide scanner at x4 magnification. Images were taken at 1 depth per section only. This depth of focus for imaging was selected automatically by the autofocus feature of the Olympus VS2000 ASW microscope and associated OlyVIA software. Imaged sections were visually inspected to confirm successful labelling of PV+ and GAD67+ cells. GAD67+ labelling was unsuccessful. PV+ cell counts from CA3, CA1, V1 and RSC regions were collected as appropriate from sections obtained from each animal. PV+ cell number in the CA3 region was counted manually using FIJI/ImageJ software by Rosie Craddock. PV+ cell number for the other 3 regions were measured by automated methods using FIJI software as set by Fangli Chen. For each section, cell counts per ROI (CA1, CA3, V1, RSC) were divided by the area of that ROI to obtain a measure of PV+ cell density for that ROI for the given section. The area of a given ROI per section was measured using FIJI/ImageJ software. The eventual measurement taken from each section per ROI was PV+ cell density in PV+ cells/mm^2.

At least 21 sections per animal were used to obtain a measure of PV+ cell density for the CA3 region (range:21-39). For RSC, at least 35 sections per animal were used to obtain PV+ cell density (range:25-41). For CA1, at least 20 sections per animal were used (range: 20-37). For V1, at least 8 sections per animal were used (range: 8-26). All layers of these areas were used in this study. For RSC and V1 this means that counts of PV+ cells in all cortical layers were used. In CA1, PV+ cells from all striata were used to obtain the cell counts.

Data analyses:

PV+ cell density measurements were explored and analysed per ROI using R software. Data were split into 4 datasets, one for each ROI (CA1, CA3, V1, RSC). Data were explored graphically before statistical testing and transformations. Datasets were transformed as appropriate, and the effects of genotype on PV+ cell density for the given ROI were tested by linear mixed modelling, where the animal from which sections were obtained was taken as a random factor to account for between-animal variance. Linear mixed modelling involved the use of the lme4 software package in R (Bates *et al.*, 2015). In total, 4 linear mixed models were generated, one to describe the impact of genotype on PV+ cell density for each ROI. The model assumptions included a normal distribution of model residuals and homoscedasticity. The normality of model residuals were tested both graphically and statistically. Statistical testing of residual normality involved Shapiro-Wilk testing methods. The assumption of homoscedasticity in each model was tested graphically by plotting the residuals against the fitted values of the model. Homoscedasticity was assumed when the distribution of residuals was equal across fitted values, as tested by eye. Details of transformations used for each ROI dataset are provided in the results section appropriate for that ROI. Results from model assumption tests are provided in the results section for each ROI.

For all models, an estimate of conditional and marginal pseudo R^2 were obtained by use of the MuMIn package in R. These values measured how well the model described the variance in the data. In other terms, this was used to estimate the goodness of fit of the model. The conditional R^2 value provided an estimate of how well the model predicted the data when between-animal variance is considered. The marginal R^2 value provided an estimate of how well the model predicted the data based on genotype effects alone. The estimates generated are based on the methods of Nakagawa and Schielzeth (2013). The estimated values for each model are reported in the appropriate results subsection for each ROI.

Following testing of model assumptions and estimating goodness of fit for each model, the effect of genotype on each model was tested. This was achieved by comparing a null model—which accounted for animal variance without modelling genotype effects—to a complete model —where animal variance was accounted for, but genotype effects were also modelled—to see if inclusion of the genotype term significantly impacted model parameters. The recorded P value on comparing the null and complete models by analysis of variance testing was then used as a measure of whether genotype had a significant impact on PV+ cell density for the given ROI. That is whether PV+ cell density significantly differed in TS2Neo HET mice as compared to WTs for the given ROI. These P values were adjusted by the Bonferroni method to correct for multiple-comparison testing. Given the mixed data distributions and related nature of the tests, this conservative method was considered the only appropriate choice for multiple test correction. Following any finding of significant genotype effect on PV+ cell density for an ROI before correction, the effect size was estimated from the model directly. Both adjusted and un-adjusted P values are reported on figures to show potential impacts of the TS2Neo mutation on PV+ cell number. This is because the unbalanced samples, and small sample sizes already reduce the statistical power for finding real genotype effects on PV+ cell density, and conservative multiple comparison corrections will only confound this. Results which lose significance on multiple comparison correction are still considered as positive findings, although corrected P values are reported for completeness.

Results:

Success of PV+ cell labelling, but failure of GAD67+ cell labelling in immunofluorescence study:

Visual inspection of sections labelled using the described immunofluorescence protocol found that PV+ cell labelling was successful, but GAD67+ cell labelling failed in this experiment. This is shown in Figure 22, below. Repetition of the experiment was not possible due to time limitations.

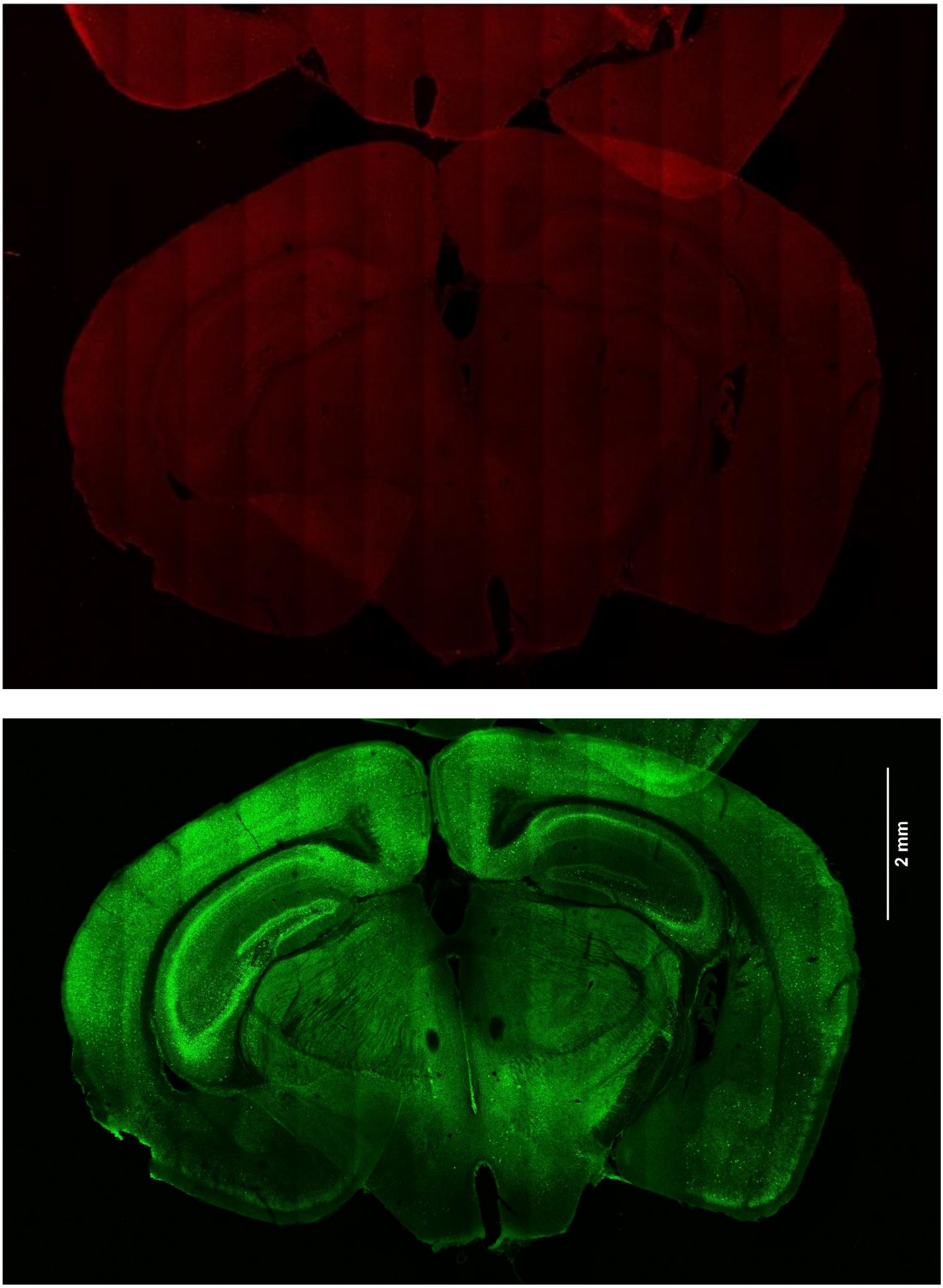
2 mm

Figure 22 Comparison of AlexaFluor488-PV+ (left) and AlexaFluor647-GAD67+(right) images taken of a representative section containing CA1, CA3, RSC and V1 from a WT mouse used in the study. Scale bar represents 2mm. Note the distinct nuclear labelling of AlexaFluor488-PV+ labelled cells and absence of distinct AlexaFluor647-GAD67+ labelled cells. This demonstrates the successful labelling of PV+ interneurons, and failed labelling of GAD67+ neurons in this experiment.

Staining for PV+ was similarly successful in sections of WT and TS2Neo mice. This is illustrated in Figure 23.

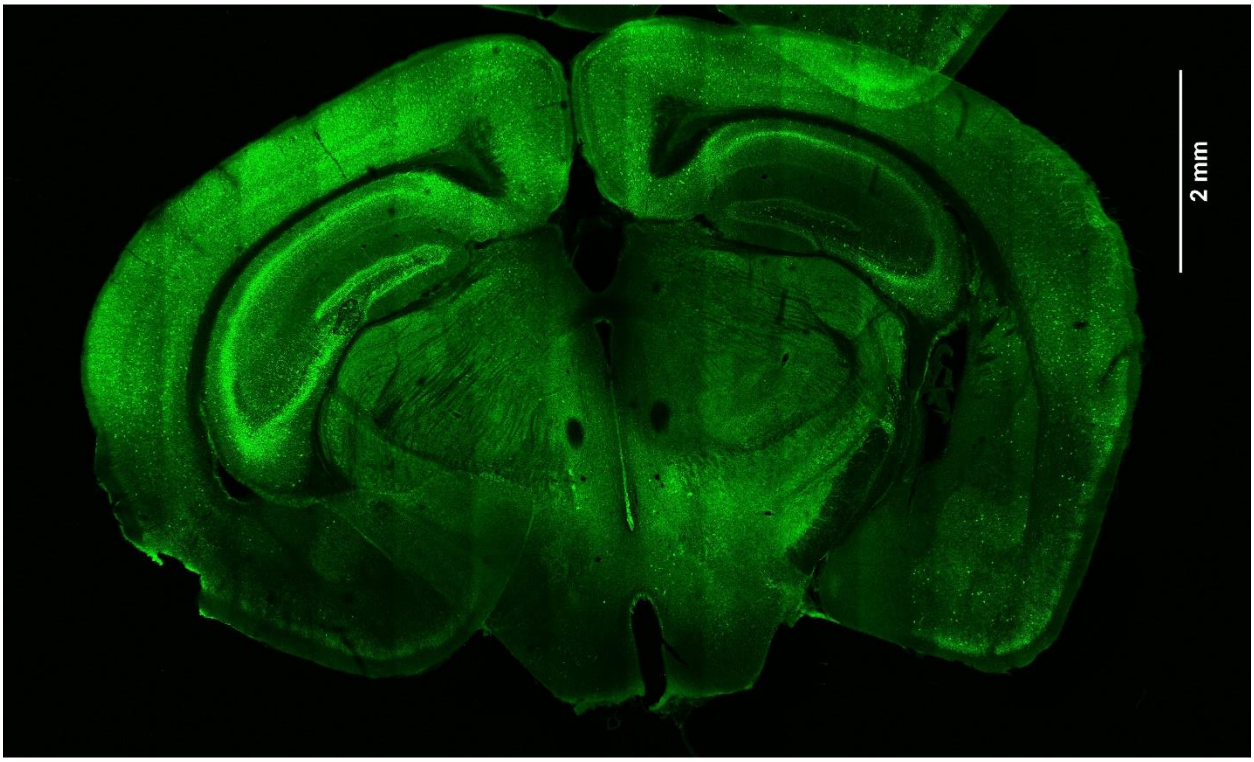
2 mm

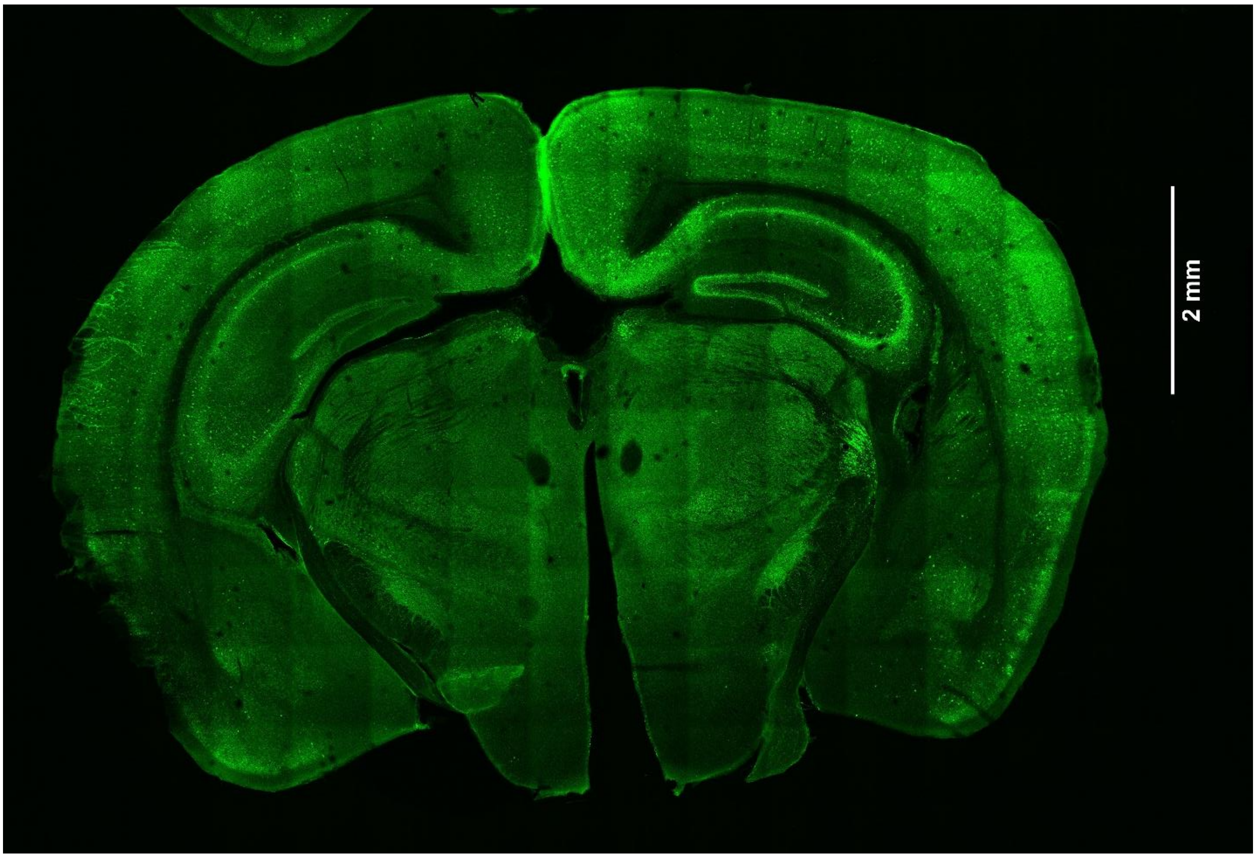
2 mm

Figure 23 AlexaFluor488-PV+ labelled coronal sections from WT (top) and TS2Neo (bottom) mice with scale bars. AlexaFluor-488-PV+ labelling was successful in all ROIs for coronal sections from mice of either genotype.

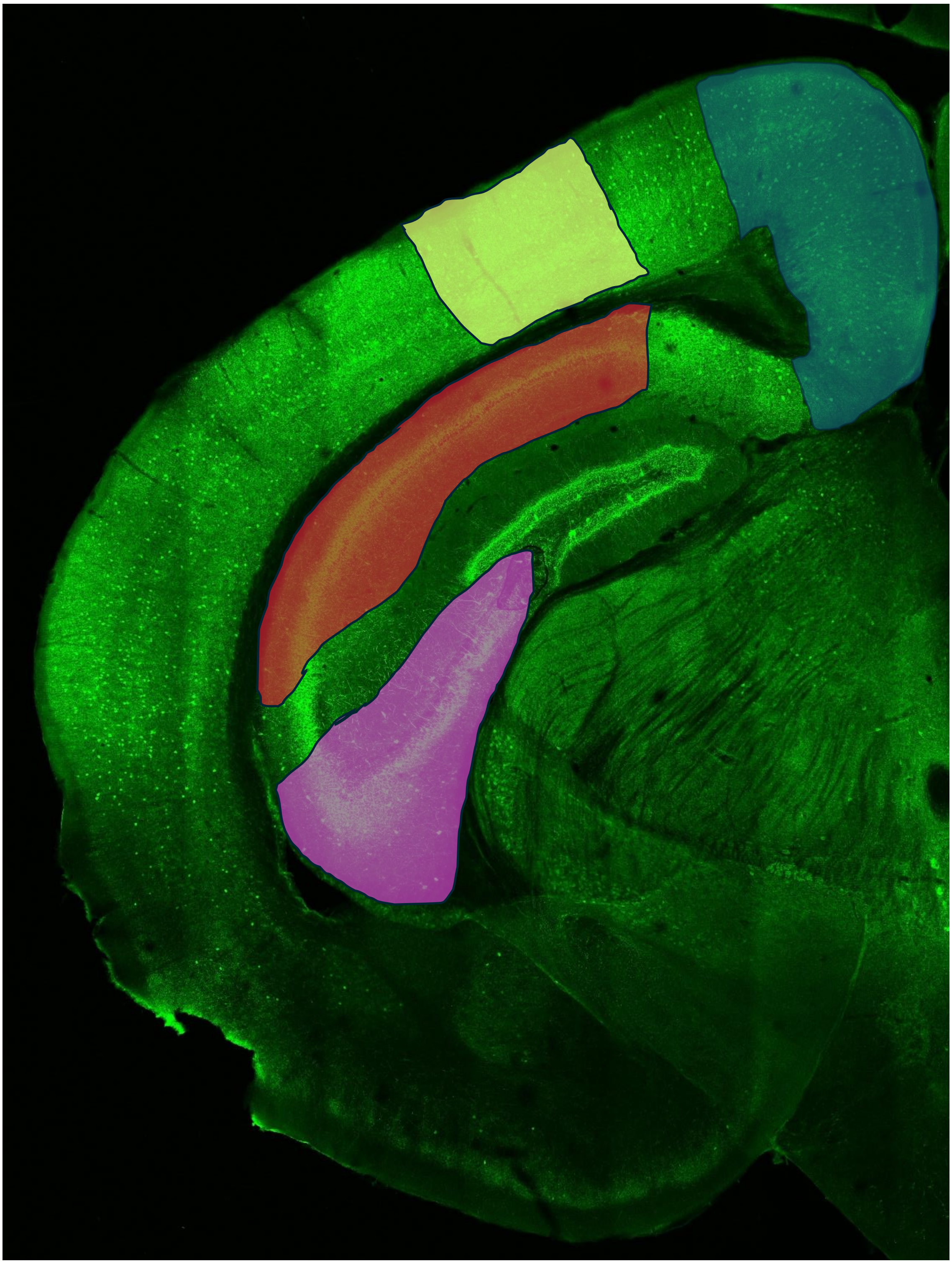

Figure 24 ROIs on image are outlined in different colours. All cells in the blue shaded area are from RSC (all layers) and were used to obtain the RSC PV+ cell count. Yellow indicates V1 (all layers) from which V1 PV+ cell counts were obtained. Red indicates CA1 (all layers) from which CA1 PV+ cell counts were obtained, and pink indicates CA3 (all layers) from which CA3 PV+ cell counts were obtained.

PV+ cell density reduced in CA3 of TS2Neo mice as compared to WTs:

PV+ cell density in the CA3 hippocampal region of TS2Neo and WT mice were compared by linear mixed modelling as described in the methods section. PV+ cell density data were square-root transformed to normalise the data.

Testing of model assumptions demonstrated that all assumptions were sufficiently met. However, model residuals were found to be non-normally distributed by Shapiro-Wilk test (W=0.97, p=1.6×10^{-5}). Homoscedasticity was verified graphically. Linear mixed models are typically robust against failures to meet the assumption of normalised residuals (Schielzeth *et al.*, 2020). Model residuals also appeared mostly normally distributed on visualisation, and so the model was deemed to adequately meet model assumptions, even with the positive Shapiro-Wilk test result.

Testing of the model found that CA3 PV+ cell density significantly differed between TS2Neo HET and WT mice, although significance was lost on adjusting for multiple testing (adjusted P=0.15, χ^2=4.2, P=0.040). This suggests that genotype could have a significant impact on CA3 PV+ cell number. The model described 32% of variance in the data, with genotype explaining 9.9% of the variance in PV+ cell density. The effect size was estimated from the model to be a 23% reduction in PV+ cell density in the CA3 for TS2Neo HET mice as compared to WT. CA3 PV+ density data from sections of animals of each genotype are shown in Figure 25.

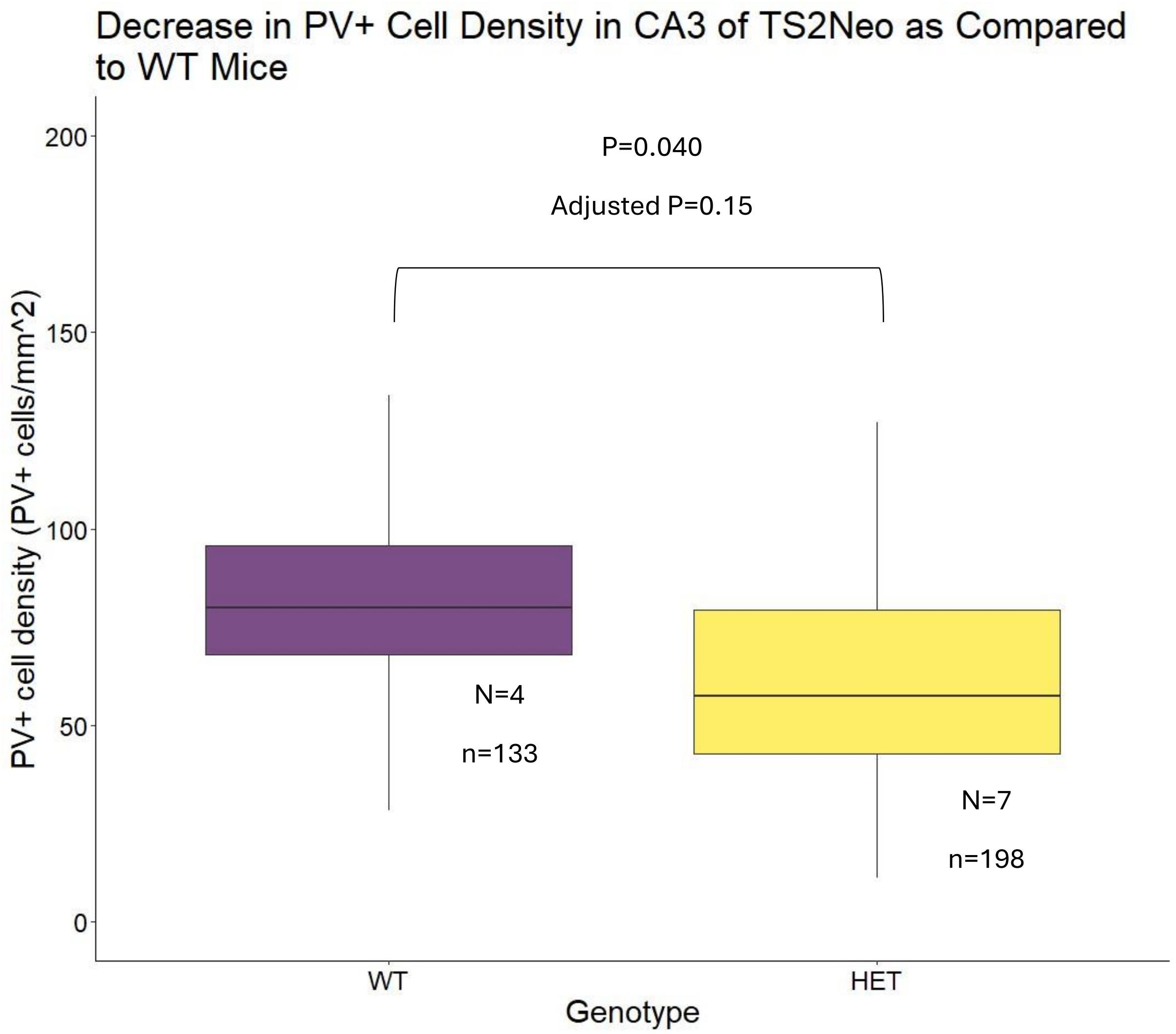

Figure 25 CA3 PV+ cell density for sections from TS2Neo and WT mice. Data displayed here are pooled from mice of each genotype. N values indicate the number of animals from which counts were obtained while n indicates the total number of sections. Note the reduction in PV+ cell density in TS2Neo mice vs WTs. This difference was tested while accounting for between-animal variance and was found to be significant by linear mixed modelling methods after square-root transformation of the data. Significance was lost on Bonferroni correction. The estimated effect size was a 23% reduction in PV+ cell density for the CA3 region of TS2Neo as compared to WT mice. Whiskers show 90% range, the box shows the IQR, and the mid-line shows the median value of PV+ cell density.

Representative images of coronal sections of the CA3 region of a WT and TS2Neo mouse are shown in Figure 26, below.

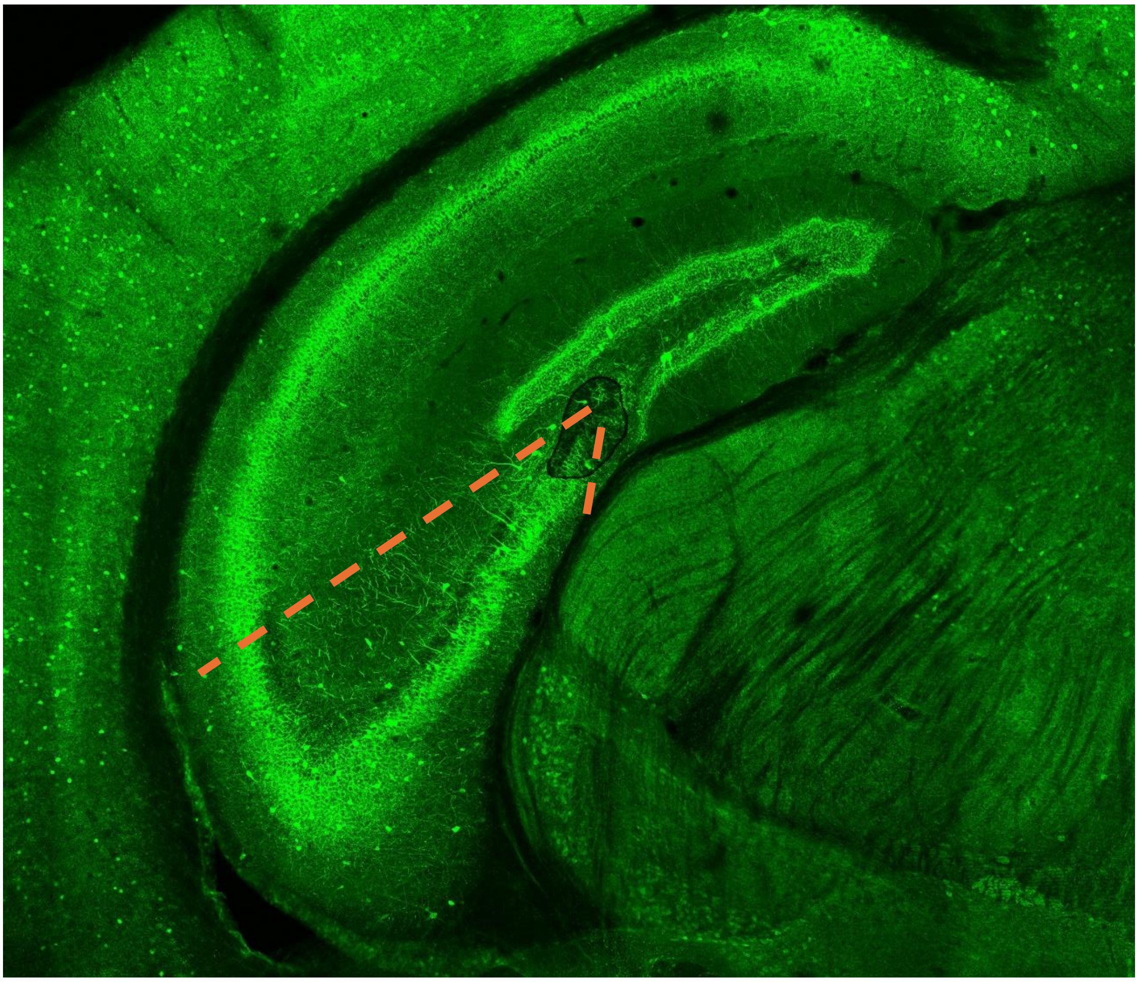

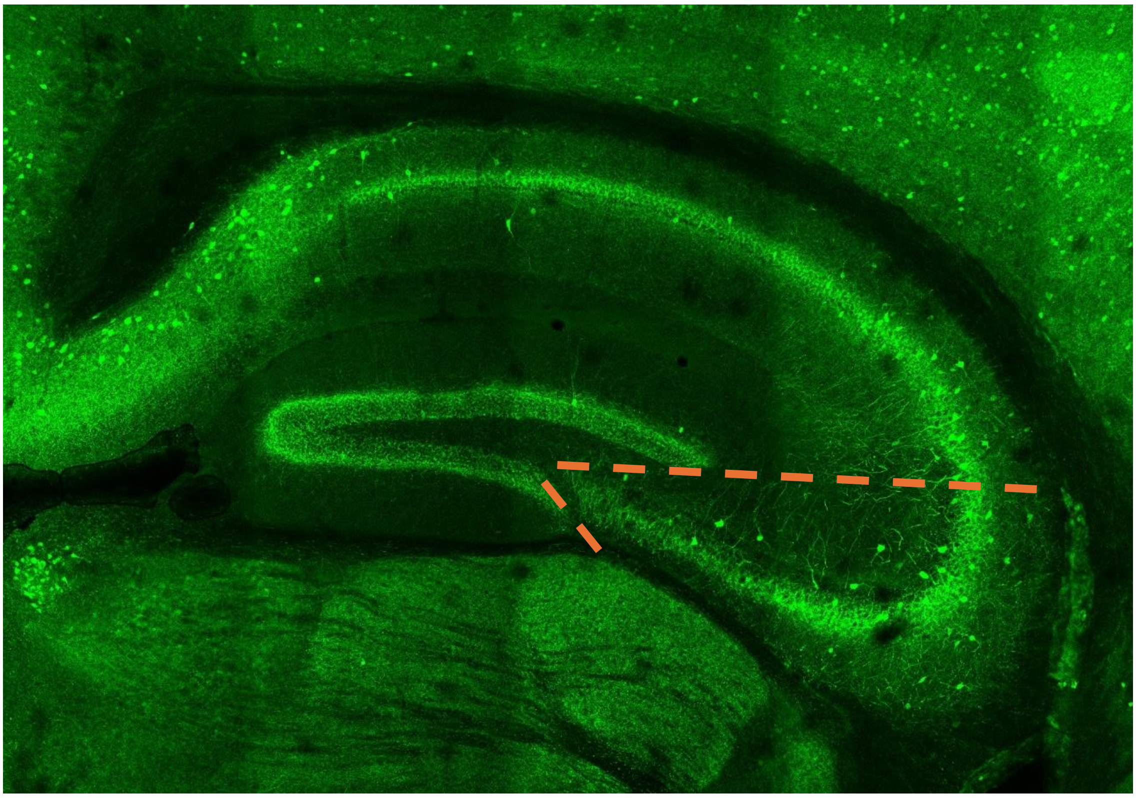

Figure 14 Representative confocal images of PV+AlexaFluor-488 labelled hippocampal coronal sections from WT (top) and TS2Neo (bottom) mice. Note the lower density of PV+ cells in CA3 from the TS2Neo as compared to the WT animal. The CA3 area is indicated by the orange dashed lines.

To summarise, the TS2Neo HET mice had a 23% reduction in CA3 PV+ cell density as compared to WTs. The difference was found to be significant before Bonferroni correction, but not after. This result may be considered positive, regardless of loss of significance on Bonferroni correction.

PV+ cell density significantly increased in V1 of TS2Neo mice as compared to WTs:

PV+ cell density data from V1 of TS2Neo HET and WT were compared as described. PV+ cell density data were not transformed. Testing of the linear mixed model assumptions found that no assumptions were invalidated. Residuals were found to be normally distributed by Shapiro-Wilk testing (W=0.99, P=0.23), and on graphical inspection. Homoscedasticity was verified graphically. The model was deemed to meet specified assumptions and was therefore assumed appropriate for use in testing the effect of genotype on PV+ cell density in V1.

Tests on the model found that genotype significantly impacted PV+ cell density in V1 (adjusted P=0.030, χ^2=7.2, P=0.0075). The model was found to describe 15% of variance in the data, with genotype accounting for 9.2% of data variance. The effect size was estimated to be a 24% increase in PV+ cell density in TS2Neo HET mice as compared to WTs. V1 PV+ cell density data from sections of animals of each genotype are shown in Figure 27.

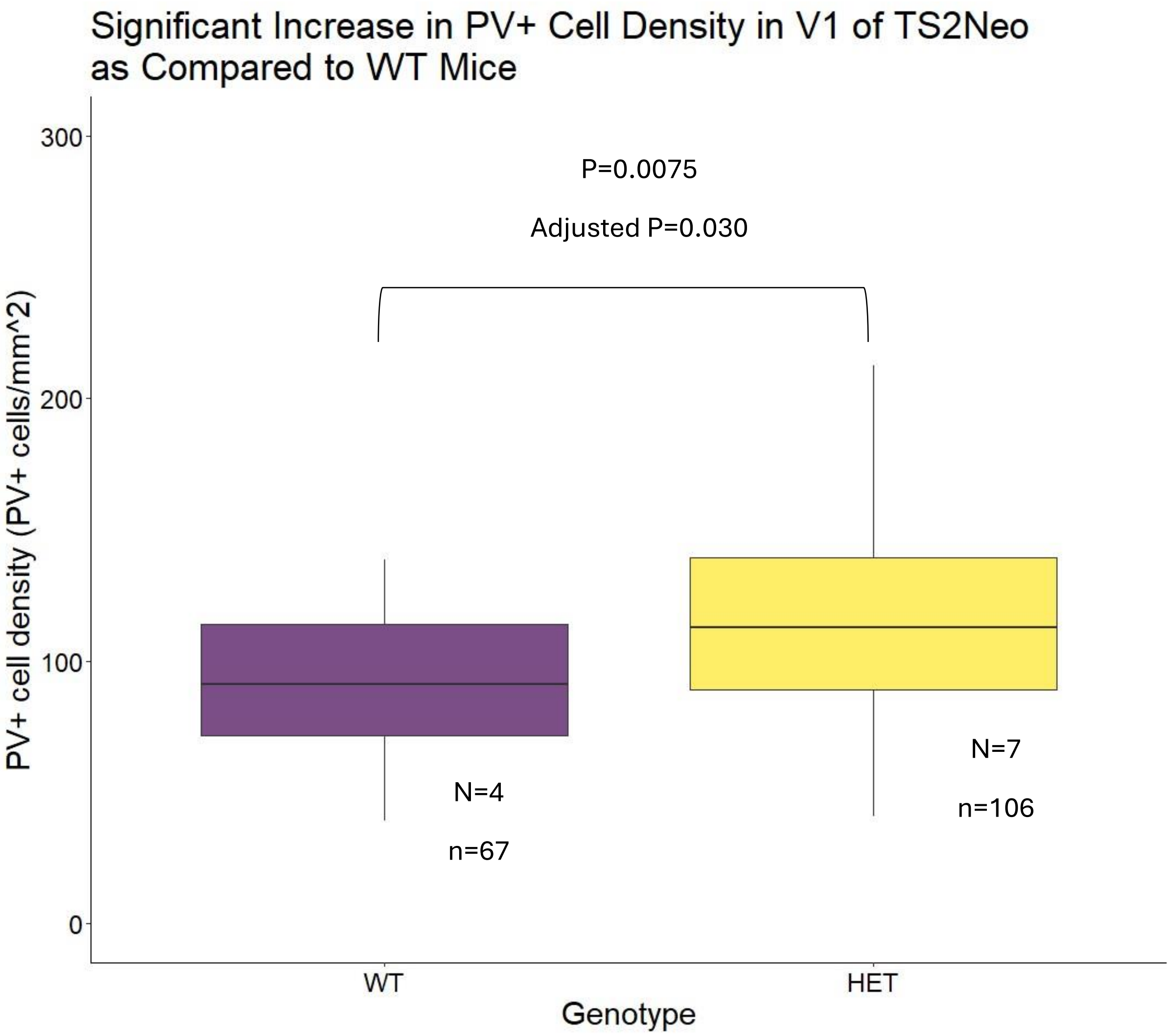

Figure 27 PV+ cell density for sections from TS2Neo HET and WT mice. Data here are pooled from mice of each genotype. N values indicate the number of animals from which counts were obtained while n indicates the total number of sections. Note the increase in PV+ cell density in TS2Neo HETs vs WTs for V1. This difference was tested while accounting for between-animal variance by linear mixed modelling. The estimated effect size was a 24% increase in PV+ cell density for the V1 of TS2Neo HET mice as compared to WTs. Whiskers show 90% range, the box shows the IQR, and the mid-line shows the median value of PV+ cell density.

An example image showing PV+ cells in V1 from a coronal section of a TS2Neo as compared to a WT mouse is shown in Figure 28.

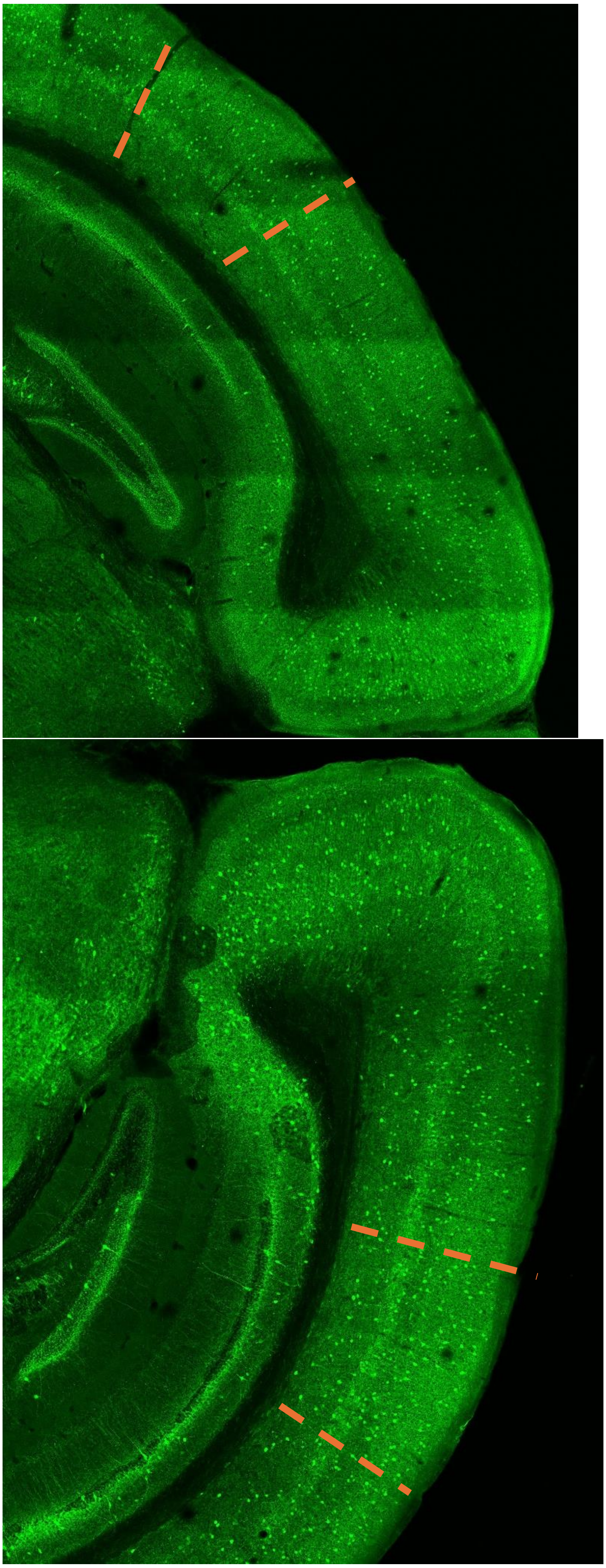

Figure 28 Representative image showing V1 imaged from coronal sections of similar anteroposterior position from a WT (top) and TS2Neo (bottom) mouse. The orange dashed lines indicate the V1 region. Note the higher number of PV+ cells in the TS2Neo mouse V1 as compared to that from the WT.

PV+ cell density not significantly different in CA1 or RSC of TS2Neo mice as compared to WTs:

PV+ cell density data for the CA1 region were log-transformed for normalisation before modelling. PV+ cell density data for CA1 were compared between TS2Neo HET and WT mice by linear mixed modelling methods. Testing of model assumptions found that all assumptions were met. Residuals were found to be normal both on graphical examination and on Shapiro-Wilk testing (P=0.060, W=0.99). Homoscedasticity was confirmed on visual comparison of residuals against fitted values.

The model was tested to explore the effect of genotype on CA1 PV+ cell density. Genotype was found to have no significant impact on PV+ cell density for the CA1 dataset (adjusted P=0.37, χ^2=2.8, P=0.091). The model was found to explain 29% of variance in the dataset, with genotype explaining only 6.1% of this variance. PV+ density measurements taken from CA1 of sections from TS2Neo HET mice as compared to WTs are shown in Figure 29.

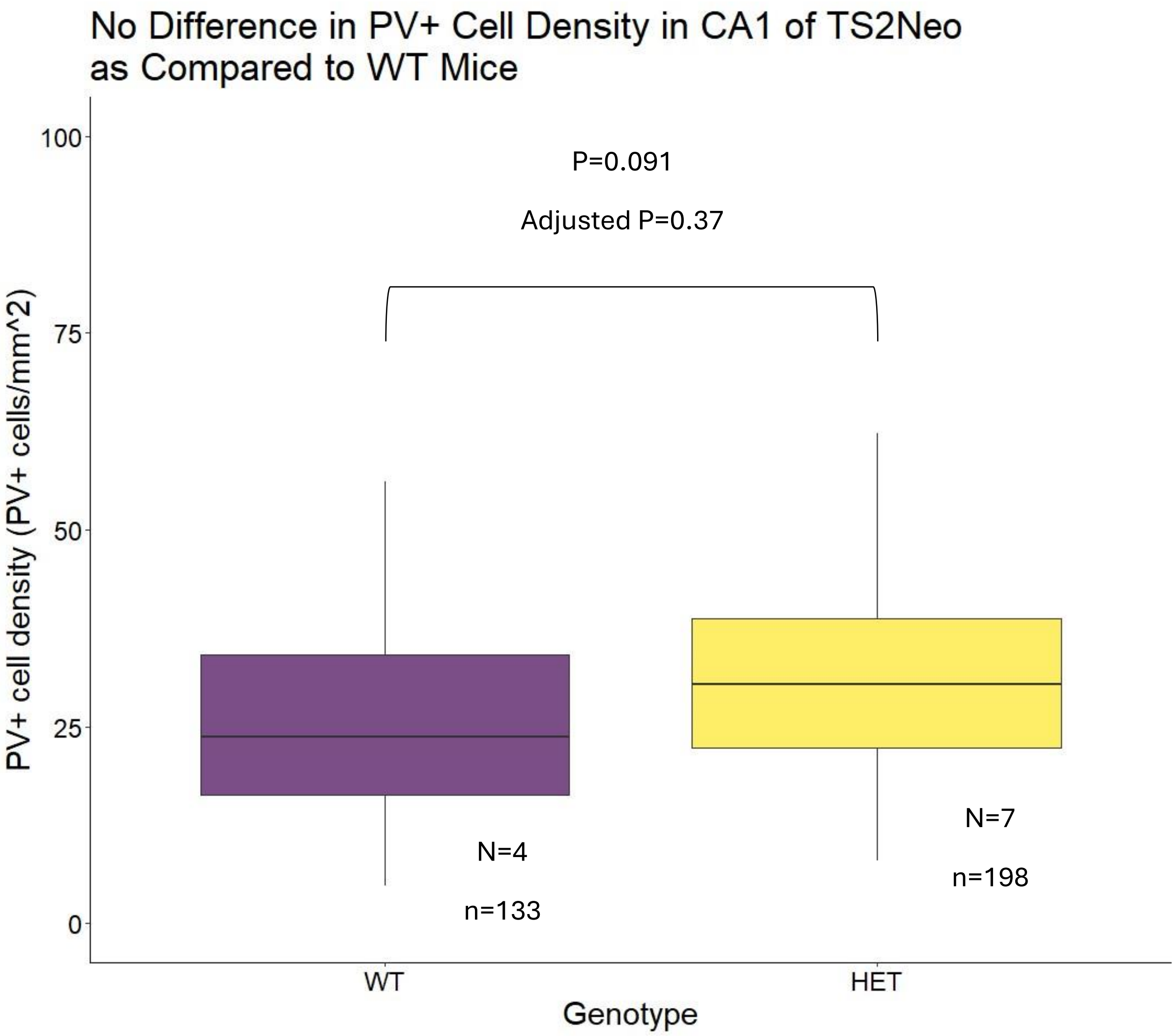

Figure 29 CA1 PV+ cell density for sections from TS2Neo HET and WT mice. Data here are pooled from mice of each genotype. N values indicate the number of animals from which counts were obtained while n indicates the total number of sections. Note the lack of difference in PV+ cell density between TS2Neo HET and WT mouse CA1 regions. Genotype-differences in PV+ cell density for CA1 were tested by linear mixed modelling methods to account for between-animal variance after log-transformation of the data. Uncorrected and Bonferroni-corrected P values are shown. Whiskers show 90% range, the box shows the IQR, and the mid-line shows the median value of PV+ cell density.

PV+ cell density data for RSC were compared between TS2Neo HET and WT mice. PV+ density data were log-transformed for normalisation before modelling. Residuals of the model were found to be non-normally distributed by Shapiro-Wilk testing (P=0.00047, W=0.98). Homoscedasticity was confirmed on visual comparison of residuals against fitted values. Linear mixed models are typically robust against failures to meet the assumption of normalised residuals (Schielzeth *et al.*, 2020). The model residuals appeared mostly normally distributed on graphical examination, and so the model was deemed to adequately meet model assumptions, despite residuals being found to be non-normal by Shapiro-Wilk testing.

The model was tested to explore the effect of genotype on RSC PV+ cell density. Genotype was found to have no significant impact on PV+ cell density in the RSC (adjusted P=1, χ^2= 0.39, P=0.53). The model was found to explain 13% of variance in the dataset, with genotype explaining only 0.47% of the variance in PV+ density. PV+ densities recorded from RSC of TS2Neo HET mice as compared to WTs are shown in Figure 30.

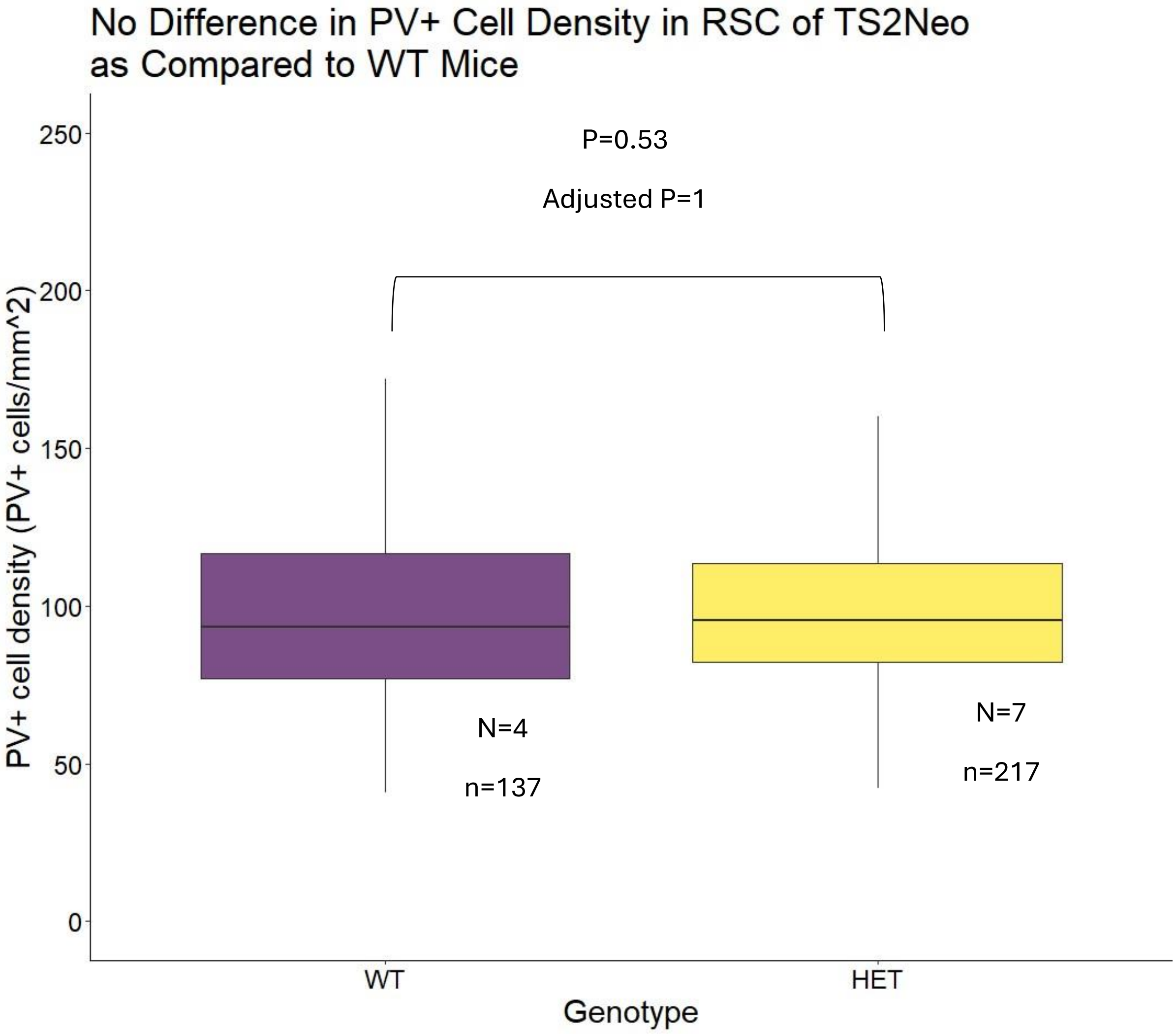

Figure 30 RSC PV+ cell density as measured from sections of TS2Neo HET and WT and mice. Data here are pooled from mice of each genotype. N values indicate the number of animals from which counts were obtained while n indicates the total number of sections. Note the lack of difference in RSC PV+ cell density between sections collected form TS2Neo HET and WT mice. Genotype-differences in PV+ cell density for RSC were tested by linear mixed modelling methods to account for between-animal variance after log-transformation of the data. Uncorrected and Bonferroni-corrected P values are shown. Whiskers show 90% range, the box shows the IQR, and the mid-line shows the median value of PV+ cell density.

PV+ cell densities of RSC and CA1 regions were not found to significantly differ between TS2Neo HET and WT mice before or after Bonferroni correction. A slight increase in PV+

cell number was observed in the CA1 region of the hippocampus of TS2Neo HET mice as compared to WTs.

Discussion:

PV+ cell number reduced in CA3, increased in V1, and unchanged in CA1 and RSC of TS2Neo mouse as compared to WT:

This immunofluorescence study found that labelled PV+ cell density differed in TS2Neo HET mice as compared to WTs in an area-specific way. TS2Neo HET mice had a 23% lower PV+ cell density in CA3, 24% increased PV+ cell density in V1, and an unchanged PV+ cell density in CA1 and RSC areas as compared to WT mice. The evidence from this study suggests that the TS mutation in the *CACNA1C* gene may result in abnormal PV+ cell distribution across the adult mouse brain. Taken with the previous findings that classical TS mutations cause disruptions in interneuron migration across the brain, this could suggest that classical TS mutations disrupt the development and migration of PV+ interneurons within the brain. However, this should be considered alongside the fact that our findings could be explained by TS-related area-specific changes in neuronal PV expression within the brain (Filice *et al.* 2016). A possibility which we have no evidence for or against due to the failure of double staining in this experiment.

The PV+ cell density decreases measured in the CA3 of TS2Neo HET mice as compared to WTs was found to be non-significant after Bonferroni correction of the results. It is my suggestion that this result still be considered a positive finding as the study was probably too underpowered for use of such a conservative multiple-comparison correction method. The finding should, however, be considered with due caution. This and further considerations are discussed in the limitations section of this chapter.

As discussed in the introduction, current evidence suggests that inhibitory interneuron migration is disrupted by classical TS mutations (Birey *et al.*, 2017, 2022; Kamijo *et al.*, 2018; Horigane *et al.*, 2020). I propose that the findings of this study, considered in the context of these previous findings, suggest that classical TS mutations cause disruptions in PV+ interneuron migration throughout the brain.

PV+ cell density changes in TS2Neo mouse model and potential impacts on neurological function:

As discussed in the introduction, evidence suggests that PV+ cell function and distribution are disrupted in ASD, which led to the PV hypothesis of ASD; suggesting that ASD symptoms arise due to abnormalities in PV+ cells.

A similar theory exists suggesting that abnormal PV+ cell activity may result in epileptiform neural activity in the brain (Magloire *et al.*, 2019). PV+ cells are known to control the discharge rates of various types of neurons including pyramidal cells, resulting in synchronous neural activity such as network oscillations (Kalaska *et al.*, 1995). Aberrant synchronous activity in neural networks can result in epilepsy (Jiruska *et* *al.*, 2013). The theory that abnormal PV+ cell activity could result in epileptiform neural activity sees support from the finding that stimulation of PV+ cells in the primary somatosensory cortex (S1) of the mouse brain can result in ictogenic neural activity in-vivo (Assaf and Schiller, 2016).

Overall, the current literature in the field suggests that abnormalities in PV+ cell function, development and distribution across the brain may result in abnormal neurological function as seen in ASD and in epilepsy, two phenotypes presented by TS patients. Although there is likely to be more than one mechanism involved in the development of ASD and of epilepsy (Geschwind, 2008), generally. This study has provided evidence that classical TS mutations such as the TS2 mutation in the TS2Neo mouse can result in abnormal PV+ cell distribution across the brain. Abnormalities in PV+ cell distribution caused by classical TS mutations may lead to ASD and epileptiform symptoms, according to the PV theories of ASD and epilepsy.

Suggested mechanism by which the TS mutation could result in abnormal PV+ cell distribution:

The mechanism by which the TS2 mutation may result in abnormal PV+ cell distribution was not addressed in this study. I propose that changes in CaV1.2 function resulting from the TS2 mutation causes abnormal PV+ cell development and migration, resulting in the abnormal PV+ cell distribution seen in the TS2Neo HET mouse brain.

Classical TS mutations are known to result in the expression of functionally abnormal CaV1.2 channel subunits, lacking VDI (Splawski *et al.*, 2004, 2005). PV+ cell development is known to be regulated by the function of L-type voltage-gated calcium channels, such as CaV1.2 (Jiang and Swann, 2005). Studies have shown that classical TS mutations can impact neuronal development in various animal models of TS (Krey *et al.*, 2013; Buddell *et al.*, 2019; Buddell and Quinn, 2021). It is plausible that the functional changes in CaV1.2 caused by classical TS mutations lead to abnormal PV+ cell development.

Classical TS mutations have been evidenced to disrupt the migration of inhibitory interneurons in general. PV+ cells are a type of interneuron, the migration of which could be impacted by TS mutations. Interestingly, studies involving generation of forebrain organoids from patients with Rett's syndrome have suggested that this ASD related genetic disorder is associated with abnormalities in interneuron migration also (Gomes *et al.*, 2020). This could potentially indicate that any changes in interneuron migration found to result from TS mutations may be relevant to the aetiology of ASD.

I theorise that the functional changes in CaV1.2 resulting from classical TS mutations may impact both PV+ cell development and migration. This could explain the area-specific abnormalities in PV+ cell density found across the brain of TS2Neo HET as compared to WT mice in this study. This theory would need testing, recommended future experiments are found in the "Future experiments" subsection of this chapter.

Comparison of PV+ cell density changes found in the TS2Neo mouse model as compared with those found in ASD patients, in ASD animal models and in the *CACNA1C* HET KO rat:

PV+ cell density has been found to be altered in various brain areas of patients with ASD, in mouse models of ASD, in the *CACNA1C* HET KO rat, and now in the TS2Neo mouse model of TS. Below I have summarised the changes in PV+ cell density (or number) found so far in ASD patients, in ASD mouse models, in the *CACNA1C* model rat and in the TS2Neo mouse by histological study of CA1, CA3, RSC and V1.

Table 22 Table comparing findings from studies exploring changes in PV+ cell density measured in the ROIs explored in this study from ASD patients with controls, ASD model animals with WTs, CACNA1C heterozygous KO rats against WTs, alongside the findings from this study:

Area	**Study type (ASD patient/ ASD mouse model/ TS mouse model/ *CACNA1C* KO Rat)**	**Study specifics**	**PV+ cell number/density change**	**Reference**
CA1	ASD patient	5 ASD patients, 5 Controls	Increase	(Lawrence *et al.*, 2010)
	ASD mouse model	4 *Contatactin-associated protein-like* 2 (*Cntnap2*) KO mice, 6 WT mice	Decrease	(Paterno *et al.*, 2021)
	TS mouse model	7 TS2Neo HET mice, 4 WT mice	No effect	This study
	CACNA1C KO rat	8 *CACNA1C* HET KO rats, 8 WT rats	Decrease	(Moon *et al.*, 2018)
CA3	ASD patient	5 ASD patients, 5 Controls	Increase	(Lawrence *et al.*, 2010)
	ASD mouse model	7 *En2* KO mice, 5 WT mice	Decrease (not tested for significance)	(Tripathi *et al.*, 2009)
	ASD mouse model	4 *Cntnap2* KO mice, 6 control mice	Non-significant decrease	(Paterno *et al.*, 2021)

	TS mouse model	7 TS2Neo HET mice, 4 WT mice	23% decrease (significance uncertain)	This study
	CACNA1C KO rat	8 *CACNA1C* HET KO rats, 8 WTs	Non-significant decrease	(Moon *et al.*, 2018)
RSC	ASD mouse model	3 *SENP1* HET KO mice, 3 WT mice	Increase	(Yang *et al.*, 2021)
	TS mouse model	7 TS2Neo HET mice, 4 WT	No effect	This study
V1	ASD mouse model	3 *En2* KO mice, 3 WT mice (age P30)	20% increase	(Allegra *et al.*, 2014)
	TS mouse model	7 TS2Neo HET mice, 4 WT mice	24% increase	This study

For completeness, abnormalities in PV+ cell densities found for other ASD-relevant brain areas of ASD mouse models and ASD patients are listed in the table below.

Table 23 Findings from studies looking at ASD-related changes in PV+ cell density in areas not explored in this experiment:

Area	**Study type (ASD patient/ ASD mouse model/ TS mouse model)**	**Study specifics**	**PV+ cell number/density change**	**Reference**
Prefrontal Cortex (PFC)	ASD patient	10 ASD patients, 10 Controls	Decrease AND Decrease in PV+ Chandelier cell number Non-significant decrease in basket cell number	(Ariza *et al.*, 2018)
	ASD patient	11 ASD patients, 10 Control	Decrease	(Hashemi *et al.*, 2017)

S1	ASD patient	8 Fragile X patients, 8 Controls	Decrease (Supragranular layer)	(Kourdougli *et al.*, 2023)
	ASD Mouse model	8 *FMR1* KO mice, 9 WT mice	Decrease (L2/3 of S1)	(Kourdougli *et al.*, 2023)
Cortex (general)	ASD Mouse Model	20-24 *FMR1* KO mice, 20-24 WT mice	Decrease	(Lee *et al.*, 2019)
Striatum	ASD mouse model	5 Valproic acid (VPA)-treated mice, 5 controls	Decrease	(Lauber, Filice and Schwaller, 2016)

It is worth emphasising how heterogeneous these results are.

ASD patients have been found to have an overall decrease in PV+ cell number specifically in the PFC and S1 areas of the brain (Hashemi *et al.*, 2017; Ariza *et al.*, 2018; Kourdougli *et al.*, 2023). However, an increase was found in PV+ cell number for the CA1 and CA3 regions of the hippocampi of ASD patients (Lawrence *et al.*, 2010).

Decreases in PV+ cell number were found in the cortex and S1 areas of various mouse models of ASD (Lee *et al.*, 2019; Kourdougli *et al.*, 2023). These changes in PV+ cell number reflect those found in those brain areas in ASD patients.

However, the increase in CA1 and CA3 PV+ cell number found by Lawrence *et al.* (2010) in ASD patients has not been replicated in animal models of ASD.

The *Cntnap2* mouse model of ASD had a decrease in PV+ cell number in the CA1 (Paterno *et al.*, 2021). In this study, I found no significant impact of the TS2 mutation on PV+ cell number in the CA1 brain area of the TS2Neo mouse as compared to WT. *CACNA1C* HET KO rats had a decrease in PV+ cell number for this area as compared to WT (Moon, 2018). The *CACNA1C* HET KO rat is not an ASD animal model, but the changes in PV+ cell number found in the CA1 of these rats demonstrate that changes in the *CACNA1C* gene could impact CA1 PV+ cell number, although this was not found in the TS2Neo mouse in this study.

En2 and *Cntnap2* KO mouse models of ASD were both found to have a reduction in PV+ cell number of the CA3 (Tripathi *et al.*, 2009; Paterno *et al.*, 2021). In this study, the TS2Neo mouse model was found to have a reduction in PV+ cell number in the CA3 also. *CACNA1C* HET KO rats also had a reduction in PV+ cell number in the CA3 (Moon, 2018).

The abnormalities in PV+ cell number in the CA1 and CA3 regions of the hippocampus for all these animal models do not reflect the increase in PV+ cell number reported in these areas of ASD patient brains.

The reported changes in PV+ cell number in the hippocampi of ASD patients, and ASD animal models are very heterogenous. Further studies exploring PV+ cell distribution in the hippocampus of ASD model animals and in ASD patients are warranted to provide further evidence of ASD-related changes in PV+ cell number in specific hippocampal regions.

The changes in RSC PV+ cell number found in the *SENP1* HET KO mouse by Yang *et al.* (2021) was not found in the TS2Neo mouse, but the increase in V1 PV+ cell number found in the *En2* KO mouse (Allegra *et al.*, 2014) was found in the TS2Neo mouse in this study. Changes in PV+ cell number in the V1 and RSC of ASD and TS patients should be explored.

Limitations:

This study was originally designed such that sample sizes were small, but balanced. The sample sizes used were based on those used by Moon (2018) which found genotype-differences in PV+ cell densities for various brain areas of the *CACNA1C* HET KO rat. The statistical power for testing the hypothesis in the designed, balanced experiment was estimated to be sufficient, to find any genotype-related difference in PV+ cell number. The designed study sample size allowed minimization of unnecessary animal usage, while providing enough power to find significant genotype differences in PV+ cell number across areas tested, given the predicted effect size based on Moon (2018). Unfortunately, a genotyping error and the early sacrifice of one animal resulted in unbalanced sample sizes being used in this study, with the WT group being 34% smaller than originally planned. The WT small sample size used in this study could result in both type I and type II statistical errors in the analysis of the data. The risk of both false-positive and false-negative findings from this study is therefore relatively high (Serdar *et al.*, 2021). Furthermore, the TS2Neo HET mouse sample size was 17% greater than originally planned, making the groups substantially unbalanced. Comparing data of unbalanced sample sizes reduces the statistical power of the study even more (Serdar *et al.*, 2021). Thus, the ability to find genotype effects on PV+ cell density for each ROI in this study was low. The Bonferroni method I used to correct for the multiple comparisons in this study is conservative but would have been appropriate for the sufficiently powered study that was planned. However, Bonferroni correction can result in false-negative findings when the statistical power of the study is already low, as in the case of this experiment (Perneger, 1998). Overall, the reduction in PV+ cell density in CA3 of TS2Neo HET as compared to WT mice should be taken as a real effect of the TS2Neo mutation on PV+ cell density. However, I suggest that this finding be considered with due caution. The findings of this study should be considered alongside the caution that false positives and false negatives are likely given the nature of the study.

A further potential limitation of this study was that PV+ cells were labelled with a AlexaFluor-488, which is a fluorophore of similar wavelength emission to that of green fluorescent protein (GFP). The mice used in this study were the same as those used in the experiment detailed in chapter 1. As such, the mice used in this experiment expressed GFP-type fluorescent calcium indicator, GCaMP6f, in neurons of V1b. Should the internal calcium level in neurons of V1b be high enough to be detected on imaging Alexa-Fluor-488 neurons in V1, this may have impacted the cell count from this region. In other words, the PV+ cell count for V1 may have also included GCaMP6f-expressing neurons in V1b also. It is unlikely that internal calcium levels would be high enough for visualisation of GCaMP6f-expressing cells in this study. This is based on our previous fluorescence imaging of post-mortem GCaMP6f labelled neural tissues (data not shown or published). However, the predicted impact of any such cross-over, if present, would presumably be a systematic increase in PV+ cell number counted from V1 in mice of both genotypes. This systematic increase would also be expected to impact the PV+ cell count from V1 of only one hemisphere in each animal.

In this study, I aimed to double-label the PV+ stained sections for GAD67 to ensure that any genotype difference in PV+ cell density was because of a genuine difference in the density of PV+ type inhibitory interneurons. Filice *et al.* (2016) previously found that apparent reduction in PV+ cell number in ASD model mice can result from a PV+ type cells expressing such low levels of PV that they are not detected by PV+ antibody labelling. To resolve this, double staining is required. I planned to stain for GAD67 in this study, to allow verification that any change in PV+ cell density was due to a loss of GABAergic interneurons, and not due to a reduction in PV expression. Although, changes in GAD67+ cell number may indicate a change in the number of other types of inhibitory interneuron. GAD67 labelling was unsuccessful in this experiment and so this could not be tested. The genotype-differences in PV+ cell density measured in this study were assumed to result from a true genotype-difference in the number of PV+ inhibitory interneurons. This assumption should be considered when interpreting the results of this study. Future studies should use double staining to determine if there is a true change in PV+ cells in TS2Neo mice in V1 and CA3, or if this is due to up and downregulation of PV expression in neurons of these areas. This is discussed further in the “Future experiments” subsection of this chapter.

Sections in this study were imaged at a single depth, the depth selected was based on autofocusing of the microscope on the maximally fluorescent depth of the tissue. This is sufficient for a quick overview of changes in PV+ cell number, but the automated imaging could theoretically introduce a systematic error in how the data were sampled.

PV+ cell counting was performed by two different investigators, using two different methods. PV+ cell density for the CA3 region was measured manually by myself, Rosie Craddock, whereas PV+ cell density measurements for the CA1, V1 and RSC regions were taken by Fangli Chen, using partially automated methods. This difference in measurement method and personnel could have resulted in the CA3 dataset not being comparable to the CA1, V1 and RSC datasets.

Future experiments:

Based on the findings of this study, I suggest that further experiments be completed to determine whether PV+ cell density is truly increased in V1 and decreased in CA3 of the TS2Neo mouse brain as compared to WT.

I suggest that this experiment, investigating the impact of TS2Neo heterozygosity on PV+ cell density in the CA1, CA3, RSC and V1 brain areas of mice be repeated by an independent investigator using increased and balanced sample sizes. The use of double-staining with GAD67 or Vicia villosa agglutin (a lectin which is specific to the extracellular matrix which surrounds typically-expressing PV+ cells) in this recommended study would be prudent to ensure that any difference in PV+ cell density represents a true change in PV+ interneuron number, and not a reduction in PV expression. The use of a standardised cell-count protocol as well as cross-sectional imaging of brain sections is also recommended. Exploring any changes in PV+ cell density in areas of the brain known to have abnormal PV+ cell number and function in ASD and in other ASD mouse models should also be considered. I suggest measuring PV+ cell density in S1, PFC and in the striatum of TS2Neo and WT mice using methods similar to those described here.

It is important to understand whether classical TS mutations disrupt the development or migration of any other specific types of interneuron in the brain. Reports of Birey *et al.* (2022) found no difference in the numbers of calretinin, calbindin or somatostatin expressing neurons in cultured human forebrain spheroids from TS patients. This suggests that the development and migration of these cell types are unlikely to be affected by classical TS mutation. However, *CACNA1C* is known to be expressed by vasoactive intestinal polypeptide-expressing (VIP+) neurons (Goff and Goldberg, 2021). TS-related changes in the *CACNA1C* gene could potentially result in abnormal VIP+ cell development and/or migration. I suggest future experiments involving TS2Neo mice aim to find if other inhibitory interneuron cell types, specifically VIP+ cells, are impacted by the TS2 mutation, both in terms of distribution in the adult mouse brain, and in terms of development at various stages of embryonic development.

As TS is a human condition, it is of great importance to understand whether PV+ or other interneurons are abnormally distributed across the brains of TS patients. Histological study of post-mortem brain tissue from TS patients would allow the exploration of this. I suggest that a multi-centre effort which works closely with the families of affected children be set up to obtain neurological tissues and complete these studies. This would help us to understand any developmental abnormality resulting from TS mutations which may result in the neurological phenotypes seen in this disease. Such a study would require appropriate funding, ethical review, and continued contact with families of children with TS.

Changes in PV+ cell number can impact synchronous neural activity, including network oscillations. The changes in PV+ cell number found in this study could impact functional network oscillations in neural circuits involving these brain areas (Buzsáki and Wang, 2012). This could result in abnormal function of that neural circuitry (Fernández-Ruiz *et al.*, 2021). In chapter 4 I describe an experiment in which I explored how the TS-related reduction in PV+ cell density found in the CA3 region in this study and/or the expression of the TS-mutant CaV1.2 channel in pyramidal cells might alter functionally important ɣ oscillations in a well-characterised CA3 neural network.

Conclusion:

Comparison of the density of immunofluorescence-stained PV+ cells in various areas of the TS2Neo HET as compared WT mouse brain demonstrated that PV+ cell density is impacted by the TS-type mutation differentially across the mouse brain. PV+ cell density was decreased in the CA3 hippocampal region of TS2Neo HET mice as compared to WTs. PV+ cell density was increased in the V1 of TS2Neo HET mice as compared to WTs. PV+ cell density was not significantly changed in CA1 and RSC areas of the TS2Neo HET mouse brain as compared to WT. This study has several limitations which are discussed in detail including low study power. Replication of this study with increased sample size is recommended. It is suggested that classical TS mutations may impact PV+ cell development and migration, thus resulting in the abnormal distribution of PV+ cells seen in the brains of TS2Neo HET mice. Changes in interneuron development resulting from classical TS mutations could potentially be related to the development of ASD-type phenotypes seen in patients with classical TS mutations.

Contributions:

Experimental design and protocols were developed by Rosie Craddock. ROIs were selected based on conversations with Professor Frank Sengpiel, Dr Cezar Tigaret and Professor Jeremy Hall. Perfusion and tissue extraction was completed by Rosie Craddock with assistance by Dr Bethany Frost. Sectioning, immunofluorescence staining and imaging was completed by Rosie Craddock. Cell count for CA3 was completed by Rosie Craddock. Cell counts for CA1, RSC and V1 were completed by Fangli Chen. Animal genotyping was performed by Dr Stephanie Bagstaff.

Data Chapter 4: ɣ oscillation abnormalities predicted to result from TS-type changes in a simple computational model of a CA3 neural network:

Introduction:

ɣ oscillations are rhythmic waves of synchronous activity across networks of neurons in the central nervous system that fall within the 30-100Hz frequency band. ɣ oscillations which are generated by specific neural circuits are thought to be related to the function of those circuits, modulating communication between neural structures within those circuits (Fernandez-Ruiz *et al.*, 2023). Specifically, ɣ oscillations in the hippocampus are believed to be related to the structure's role in learning and memory (Colgin and Moser, 2010). ɣ oscillations have been found to be perturbed in various brain areas of patients with a variety of different neurological and psychiatric diseases, including ASD (Uhlhaas and Singer, 2010; Rojas and Wilson, 2014; Mably and Colgin, 2018; Guan *et al.*, 2022). Studies into ɣ oscillation abnormalities in patients with neuropsychiatric diseases could help us understand the mechanisms by which those diseases result in aberrant brain processing and function at a circuit level, and even identify potential novel treatments (Mably and Colgin, 2018).

A high percentage of TS patients meet diagnostic criteria for ASD (Splawski *et al.*, 2004). All TS2 patients surviving beyond early infancy have been found to have some neurological abnormality at the time of publication of this thesis (see general introduction). Patients with TS often present with learning difficulties and ASD which are both associated with abnormal hippocampal function (Banker *et al.*, 2021a; Banker *et al.*, 2021b). I therefore decided to explore the impact of TS-related changes on ɣ oscillations generated by a model CA3 hippocampal neural network.

Research suggests that modifications in L-type calcium channel currents may impact ɣ oscillations. Experiments have found that blocking or otherwise disrupting L-type calcium channels, like CaV1.2—which is disrupted in TS— results in perturbed ɣ oscillations in-vitro (Kumar *et al.*, 2015; Zhang *et al.*, 2021). Furthermore, experiments modelling the impact of *CACNA1C* mutations on ɣ oscillations found that a inclusion of a different disease-relevant mutant CaV1.2 channel in cells of a neural network model resulted in production of ɣ oscillations of abnormally low power by the network (Metzner *et al.*, 2022). The L-type voltage-gated CaV1.2 channel is expressed in many neurons including pyramidal cells (Hell *et al.*, 1993). Pyramidal cells are involved in ɣ oscillation production (Buzsáki and Wang, 2012). Modelling the classical TS-type mutant CaV1.2 channel within pyramidal cells of a CA3 network model would result in abnormal L-type calcium channel currents in these neurons. This abnormality in calcium channel currents could disrupt network ɣ oscillations.

Furthermore, direct electrophysiological evidence from Birey *et al.* (2022) found that the TS1 mutation not only impairs interneuron migration in cultured forebrain spheroids, but also impacts the synchronous activity in these structures. Specifically, the TS mutation increased synchronous activity in the network. This suggests that classical TS mutations can alter neural network synchronous activity through impacts of the mutation on interneuron migration. My research in chapter 3 found that the density of PV+ cells is reduced in the CA3 region of the hippocampus in TS2Neo mice as compared to WTs. PV+ cells are known to be involved in the generation of ɣ oscillations in neural circuits (Buzsáki and Wang, 2012). TS-related changes in PV+ cell number in the CA3 region of the hippocampus could result in abnormal ɣ oscillations of that circuitry.

Overall, I hypothesise that TS-related changes in a CA3 neural network, including mutant channel expression and a reduction in PV+ cell number, might result in abnormal ɣ oscillations generated by that network. These changes could be aetiologically relevant and inform us of important neural circuit processing abnormalities which are related to the neuropathophysiology of TS.

Here, I used a simple computational modelling approach to explore how TS-related changes in a CA3 neural network— namely inclusion of classical TS mutant CaV1.2 channels in pyramidal cells, and reduction of PV+ cell number in the network— could impact ɣ oscillations generated by the network. The neural network model used was based on that of Betterton *et al.* (2017), being adapted such that pyramidal cells contained CaV1.2 channels which could be modelled as having either WT or classical TS-type channel kinetics. The CaV1.2 channel and TS-mutation related changes in equations and parameters used to model the channels are taken from by Kummer *et al.* (2022). They are also described in Appendix 2 of this thesis. Appendix 3 of this thesis shows a similar experiment where I explored how heterozygous KO of *CACNA1C* impacts ɣ oscillations generated by a CA3 network.

Methods:

General details of computational model:

A simple CA3 neural network, containing 100 pyramidal cells and 10 PV+ interneurons, was used to explore the impact of CaV1.2 mutant channel and TS-mutation-related PV+ cell reduction on the power and frequency distribution of ɣ oscillations generated by the CA3 neural network.

All neurons were modelled as single compartments containing ion channel modelled using Hodgkin-Huxley type ordinary differential equations. The CA3 neural network model used was based on that of Betterton *et al.* (2017; see also Kopell *et al.*, 2010), and was written in MATLAB 2021a. All simulations and data processing were completed using MATLAB 2021a.

Pyramidal cells of the Betterton *et al.* (2017) model were altered to include the L-type calcium channel current of Kummer *et al.* (2022). The maximum conductance for the channel was set to 1mS/cm^2 as per Ermentrout and Kopell (1998). The pyramidal cell: PV+ interneuron ratio was adjusted from 80:20 to 100:10 for physiological accuracy (Traub and Miles, 1991).

All cells in the network were synaptically interconnected in an all-to-all configuration. All cells received an external input current to simulate θ-oscillatory drive from the dentate gyrus. This θ oscillatory drive is known to elicit ɣ oscillations in the CA3 network. The θ-oscillatory input was modelled as an alternating current with sinusoidal waveform of amplitude 2.5μA/cm^2 and frequency 5Hz (Betterton *et al.*, 2017). A separate input to each cell was also modelled to simulate network noise (Kopell *et al.*, 2010).

Four conditions were simulated using the base model described above to allow testing of how classical TS mutations might impact ɣ oscillations in the CA3 neural network. These four conditions were: 1) a WT condition where the pyramidal cell: PV+ interneuron ratio was 100:10, and pyramidal cells contained only non-mutant CaV1.2 channels (WT condition), 2) a WT with reduced PV+ cell number Condition, where pyramidal cells contained only non-mutant channels, but the pyramidal cell: interneuron ratio was 100:8 (WT with PV+ reduction condition), 3) a WT with mutant channel condition, where pyramidal cells contained 50% mutant and 50% non-mutant CaV1.2 channel currents. This was appropriate to simulate the co-expression of mutant and non-mutant CaV1.2 channels in neurons of TS patients. The pyramidal cell: interneuron ratio was 100:10 (WT with mutant channel condition); and 4) a WT with mutant Channel and PV+ reduction condition, where pyramidal cells contained both mutant and non-mutant channels, but there was also a 100:8 pyramidal cell: PV+ interneuron ratio (WT with mutant channel and PV+ reduction condition). I compared properties of ɣ oscillations from 20 different simulated CA3 neural networks per condition. The aim was to test for any difference in ɣ oscillation power or in the power distribution amongst oscillations in the ɣ frequency band across the different conditions modelled to determine whether TS-related changes in CA3 neural network properties could result in abnormalities in ɣ oscillations for this neural network.

On initialisation of the network model, membrane potentials of each neuron were set to between -50 and -80mV. Simulations were 2 seconds long and consisted of 2x10^5 time steps (timestep=0.1ms).

Local field potential (LFP) recording data were generated from the simulated neural network. The peak frequency, maximum PSD, maximum power, and average power of the ɣ oscillations for the network were measured from the simulated LFP data. These were then compared between modelled conditions to test the impact of TS-related changes in the CA3 neural network on the properties of ɣ oscillations generated by the network. Average ɣ power is defined as the band-wide average power of ɣ oscillations. Comparison of peak frequency and maximum PSD for ɣ oscillations generated by CA3 neural network models for different conditions were used to measure how TS-type changes in CA3 neural network properties impacts the distribution of ɣ oscillatory power across frequencies. Comparison of maximum and average power of the ɣ oscillations between simulations of differing conditions were used to measure how TS-type changes in a CA3 neural network might impact the power of ɣ oscillations generated by that network.

Pyramidal cells were modelled by the following equation:

$$C\frac{dV}{dt} = I_{Na} + I_{K} + I_{Km} + I_{Kahp} + I_{CaL} + I_{L} + I_{syn} + I_{input}$$

Pyramidal cells containing TS-type mutant L-type channel currents were modelled by the following equation:

$$C\frac{dV}{dt} = I_{Na} + I_{K} + I_{Km} + I_{Kahp} + I_{CaL} + I_{CaLMut} + I_{L} + I_{syn}$$

The equations used to model sodium, potassium and leak currents were taken from Ermentrout and Kopell (1998). An M-type potassium channel current and an AHP current were included to the pyramidal cell models as per Ermentrout, Pascal and Gutkin (2001). An L-type calcium channel was included in model pyramidal neurons. This was taken from Kummer *et al.* (2022), which is based on the model for an L-type calcium channel from a pancreatic β cell (Riz, Braun and Pedersen, 2014). The maximum conductance for each channel and a list of equations used for modelling are detailed in “Appendix 2: Modelling parameters and equations”. The parameters used in modelling the mutant L-type calcium channel current differed from those used to model the non-mutant L-type channel current as described in Appendix 2. This modelled an adjustment in the steady-state voltage dependent inactivation, the inactivation time constants, and the current amplitudes. This is described in detail in Kummer *et al.* (2022). PV+ fast-spiking inhibitory interneurons were modelled using the Hodgkin-Huxley-type equation below as described in Betterton *et al.* (2017). See also (Wang and Buzsáki, 1996; Kopell *et al.*, 2010) . All current equations were as listed in Betterton *et al.* (2017), and are listed in “Appendix 2: Modelling parameters and equations”.

$$C\frac{dV}{dt} = I_{Na} + I_{K} + I_{L} + I_{syn} + I_{input}$$

Details of simulated TS mutant CaV1.2 channel:

In WT and WT with PV+ reduction conditions, pyramidal cells contained non-mutant CaV1.2 channels only. The equations used to model the channels are described in Appendix 2. The maximum channel conductance for L-type calcium channels in the model pyramidal cells was set to 1mS/cm^2 as per Ermentrout and Kopell (1998).

Mutant channel conditions— specifically WT with Mutant Channel and WT with mutant channel and PV+ reduction conditions—contained L-type calcium channel currents with a total maximal channel conductance of 1mS/cm^2 as for the WT condition. The L-type channel used in this model was not specific to currents carried by either CaV1.2 or CaV1.3 channels. 75% of L-type calcium channel currents in pyramidal neurons of CA3 are underpinned by CaV1.2 channels (Hell *et al.*, 1993). The TS2 mutation is heterozygous, carried in 50% of all *CACNA1C* genes, and 77.2% of all CaV1.2 channels that are created by the mutant *CACNA1C* gene will express the alternatively spliced exon 8 region (Splawski *et al.*, 2005). Therefore 71.05% of the total maximum calcium channel conductance was set to be carried by non-mutant channels and 28.95% of the total maximum channel current was set to be carried by mutant channels. Mutant calcium channels therefore had a maximum conductance of 0.2895mS/cm^2, and non-mutant calcium channels were then set a maximum channel conductance of 0.7105mS/cm^2.

LFP calculations and spectral analyses:

LFP recording data and spectral analyses were performed in MATLAB 2021a. LFP recording data were generated from the simulated neural network using mathematical methods of Bédard *et al.* (2010), where LFP was calculated as:

$$LFP = \frac{R_e}{4\pi}\sum\nolimits_j \frac{I_j}{r_j}$$

Where R_e is the resistivity of the extracellular medium, assumed to be =230Ωcm, I_j is the sum of all current inputs to cell j, where synaptic influence is 95%, and intrinsic ion channel currents have 5% influence over I_j, and r_j is the distance between cell j and the recording electrode, specified as 75±6μm.

LFP recording data generated were then down-sampled 10 times and used to assess properties of the network's activity oscillations. ɣ oscillations were defined as lying within oscillation frequency 30-100Hz. The Chronux toolkit was used for all LFP data analysis and spectral analyses (Bokil *et al.*, 2010).

Down-sampled LFP data underwent fast Fourier transform (FFT) to generate a single PSD plot which showed how the power of oscillations (mV^2/Hz) related to the frequency of oscillation (Hz) for all ɣ oscillations (30-100Hz), averaged across the entire simulation period. Spectral data was smoothed using a moving average filter, spanning 35 datapoints. FFT methods involved use of a 5-taper multi-taper estimate (30s time-bandwidth per taper). All other parameters are described in the section "Parameters for Fourier transform", below. From the PSD generated, the oscillatory frequency at which maximum oscillatory power was seen (within the ɣ range) was identified, as was the average power of this frequency oscillation across the simulation period. These two measurements are termed 'peak frequency' of oscillation and 'maximum PSD', respectively. These two parameters describe the properties of the strongest ɣ oscillations, considering oscillation persistence throughout the simulation.

Down-sampled LFP data from the 2 second simulation period were then grouped by time, using a moving window (length 0.5s, timestep 0.1ms). FFT for each group were then performed using similar parameters as for PSD generation. The spectral density data for each group were then used to create a spectrogram (see below for parameters), describing ɣ oscillatory power at each frequency in ɣ range, per time (as defined by the moving time-window detailed in the tables below). From this spectrogram, the maximal power of any oscillation in the ɣ range at any timepoint was found, as was the ɣ-band-wide average oscillatory power was calculated. These two measurements are termed 'maximum ɣ power' and 'average ɣ power', respectively.

Parameters for Fourier transform:

Table 24 Showing parameters for the generation of oscillatory PSD (averaged across all timepoints):

Parameter	Value
Sampling frequency	5000Hz
Band-pass filtering	0-200Hz
FFT padding factor	1
Down-sampling	10x
Span of moving average filter used for spectral smoothing	35 data points

Table 25 showing parameters for the generation of oscillatory power spectrogram:

Parameter	Value
Sampling frequency	5000Hz
Band-pass filtering	31-101Hz
FFT padding factor	0
Down-sampling	10x
Span of moving average filter used for spectral smoothing	None
Span of moving time window for averaging	0.5s
Window-step for moving time window used for averaging	1ms

Statistical analyses:

All statistical analyses of data regarding neural network ɣ oscillations were performed in R, using the 'tidyverse' package (Wickham *et al.*, 2019). For each measurement of ɣ oscillations compared between models, the data were tested for normality graphically, and equality of variances between simulation types was determined using Bartlett's test.

Following testing of parametric modelling assumptions, between-condition differences in the maximum PSD for ɣ oscillations generated by the modelled CA3 neural networks were tested for by Analysis of Variance Analysis (ANOVA). Between-condition differences in maximum ɣ power, average ɣ power and peak spectral frequency for ɣ oscillations generated by the modelled CA3 neural networks were tested by Kruskal-Wallis testing. This is because normality and equality of variance assumptions were not met. Where significant between-condition differences in ɣ oscillation properties were found, post-hoc pairwise testing was used to test for differences in ɣ oscillation properties. For maximum PSD this involved parametric estimated marginal means comparison testing. When performing pairwise comparisons for effect of condition on maximum power and average power of ɣ oscillation, non-parametric post-hoc Dunn testing was used. Due to the exploratory nature of this experiment, and the lack of prior hypothesis, all P values obtained from testing were corrected for multiple comparisons using the Bonferroni method.

Results:

Adaptation of a computational model of a CA3 neural network to test impacts of TS-related changes on properties of ɣ oscillations generated by the network:

I visually compared several network activity properties for the modelled WT CA3 neural network against those reported in the literature. This provided evidence that the WT model generates normal network activity. This therefore suggests that the model is appropriate for use in exploring how TS-type changes in a CA3 neural network model might impact activity of the network, including ɣ oscillations.

Membrane potential traces generated by single pyramidal cells and interneurons of the base WT model were compared to traces measured from typical hippocampal neurons by electrophysiological recording, as reported in the literature.

Modelled CA3 pyramidal cell spiking was found to be appropriately synchronised to θ stimulation input in the model network. This resembles the synchronous activity of pyramidal cells in the adjacent CA1 area which has been reported in the literature from ex-vivo experiments (Bland, Konopacki and Dyck, 2005; see Figure 31). Comparative data for the CA3 region of the hippocampus were not available, which limits my ability to ensure that CA3 pyramidal cell activity on θ stimulation for the model correctly simulates in-vivo/ in-vitro CA3 pyramidal cell activity.

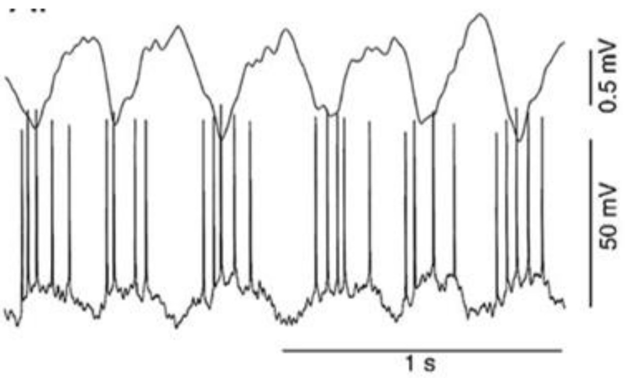
0.5 mV
50 mV
1 s

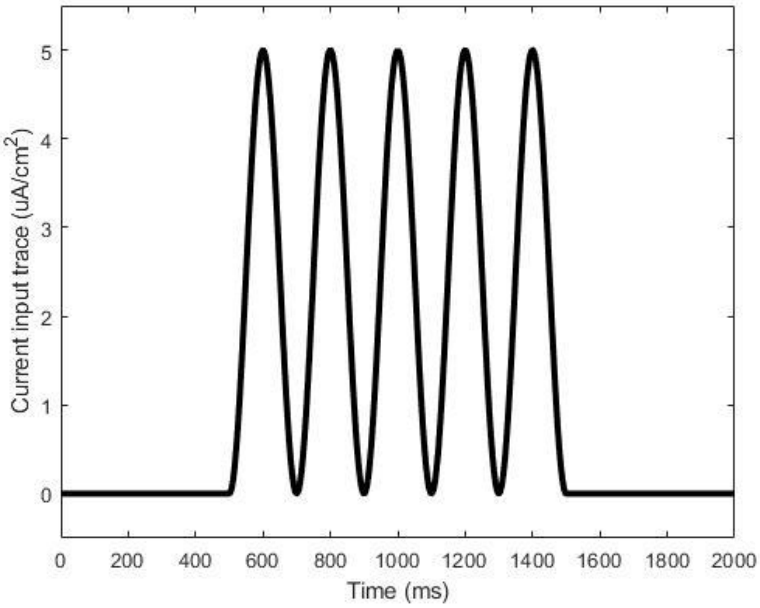
Current input trace (uA/cm^2)
5
4
3
2
1
0
0
200
400
600
800
1000
1200
1400
1600
1800
2000
Time (ms)

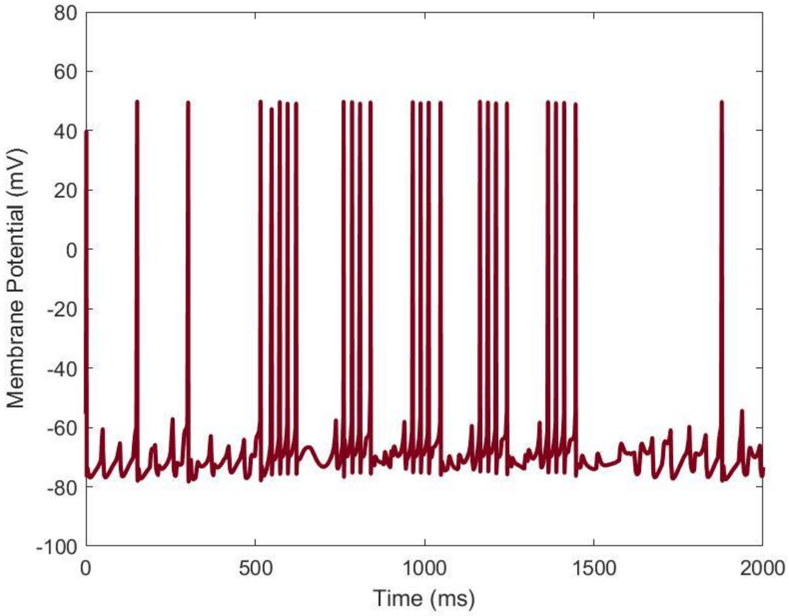
Membrane Potential (mV)
80
60
40
20
0
-20
-40
-60
-80
-100
0
500
1000
1500
2000
Time (ms)

Figure 31 A 3 panel figure with the top panel showing θ frequency waves recorded from the CA1 of the hippocampus, and the θ phase-locked firing of a CA1 pyramidal cell taken from Bland, Konopacki and Dyck (2005), the bottom two panels showing the θ-frequency current input simulated in this experiment, and the θ phase-locked firing of a modelled CA3 pyramidal cell of the WT model. Data showing CA1 pyramidal cell θ phase-locked pyramidal cell firing was used for comparison due to a lack of CA3 data being found in the literature, and due to the similar firing properties of both CA1 and CA3 pyramidal neurons (Traub and Miles, 1991).

Spiking of modelled CA3 PV+ interneurons was found to be appropriately driven by θ oscillation in a manner comparable to that reported by electrophysiological data from the literature for PV+ interneurons in the CA1 region of the hippocampus (Huh *et al.*, 2016; see Figure 32). Again, comparative data from electrophysiological experiments in the CA3 region were not available.

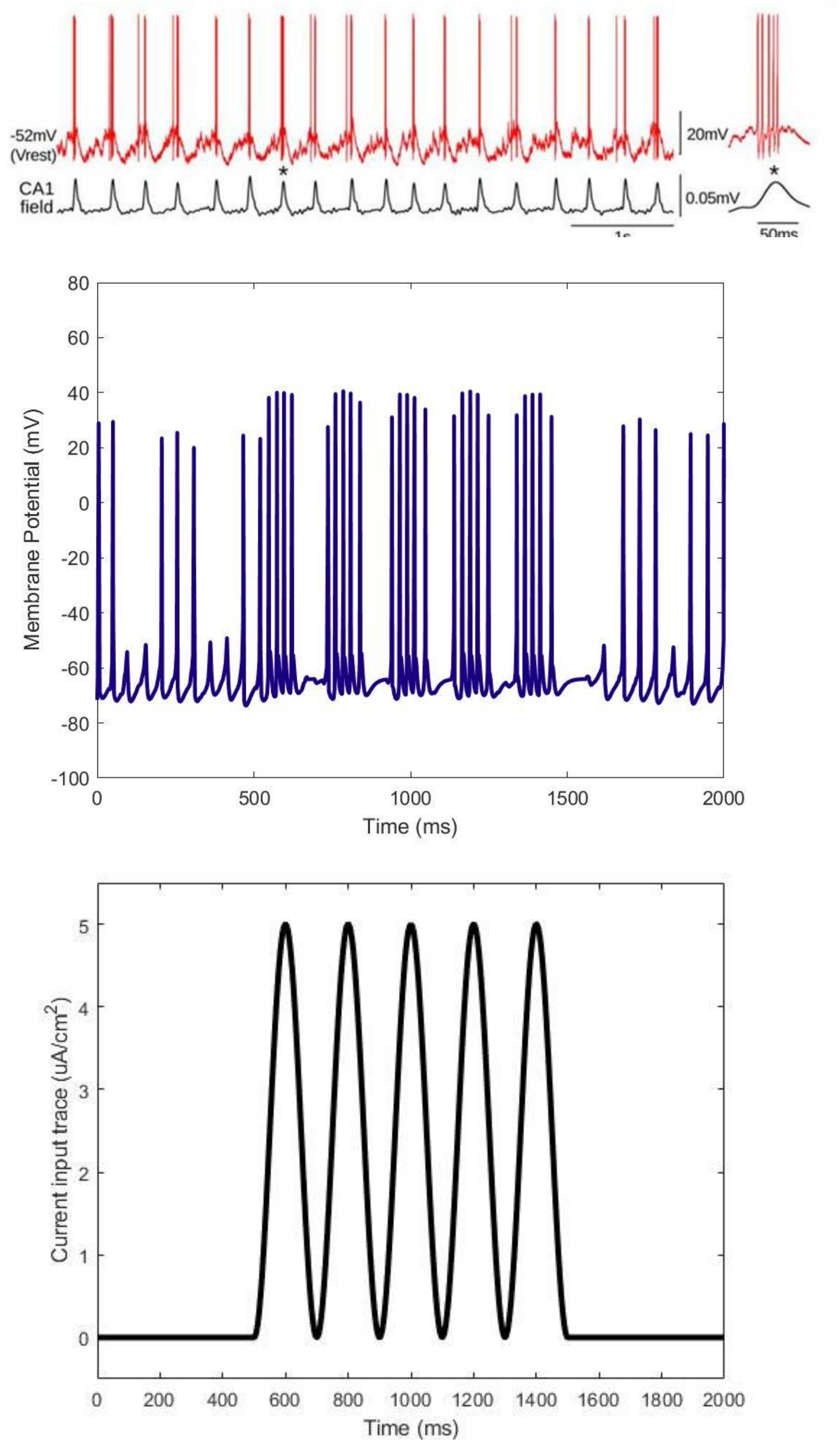

Figure 32 A 3-panel figure with the top panel showing data from Huh et al. (2016) of a CA1 parvalbumin interneuron demonstrating phase-locked firing with a θ frequency oscillation in the CA1, as measured by LFP recording. The middle panel shows a membrane potential trace from a CA3 parvalbumin interneuron displaying phase-locked firing to the θ-frequency current input to the modelled CA3 neural network in this experiment. Again, no CA3 specific data was available for a direct comparison.

Visual comparison between LFP data recorded from θ-frequency stimulated CA3 slices in ex-vivo recordings (taken from Betterton *et al.,* 2017) and LFP data generated from my WT network simulation demonstrated the model was able to emulate real CA3 neural network oscillatory behaviour, as shown in Figure 33. Note the θ-phase-locked oscillatory activity in each instance.

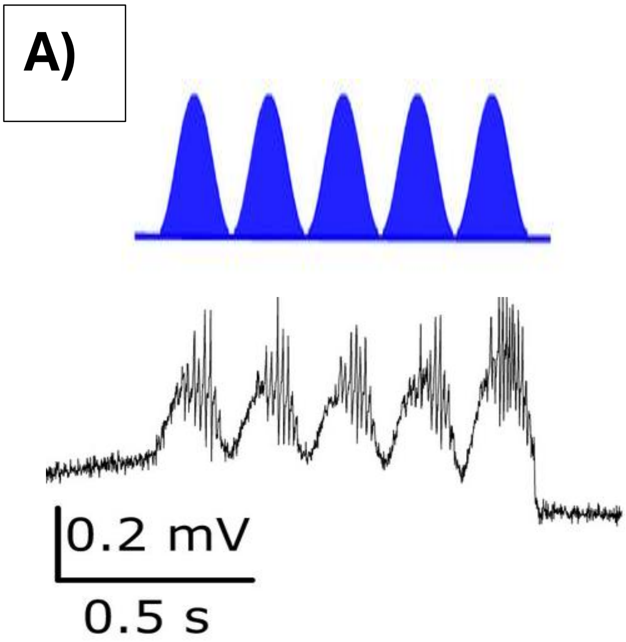

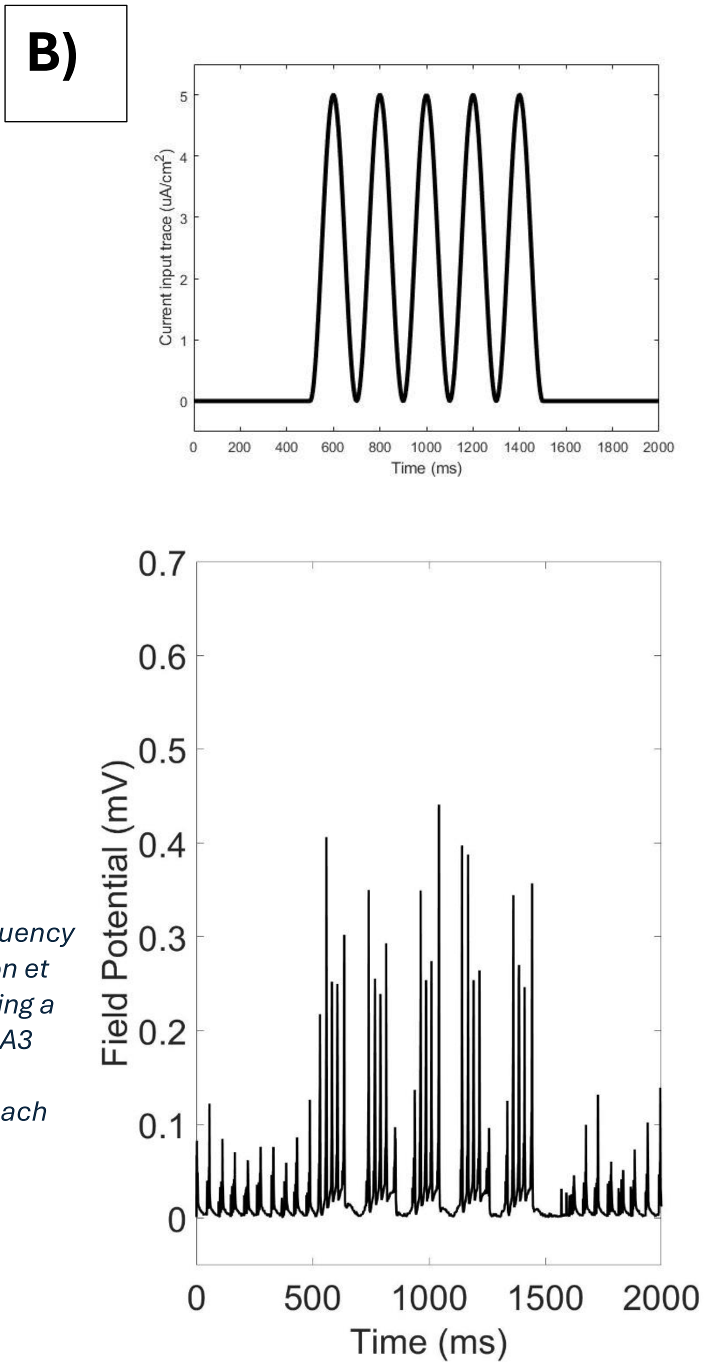

Figure 33 A) Recorded LFP from acute CA3 hippocampal sections of mouse receiving θ-frequency sinusoidal current input (left; taken from Betterton et al., 2017) B) estimated LFP generated by simulating a θ-frequency sinusoidal current input to the WT CA3 hippocampal neural network described in this experiment (right). Note the θ-nested spiking in each instance.

Overall, the model appeared to emulate the expected CA3 neural network activity based on comparison of simulated data with data taken from the literature. This suggests that the model is appropriate for use in exploring how TS-type changes in the network might impact network activity, including ɣ oscillations.

ɣ oscillation power decreased on simulating TS-type changes in CA3 neural network:

The average power of ɣ oscillation generated by the CA3 neural network model significantly varied between conditions modelled as by Kruskal-Wallis testing (adjusted $P=7.2x10^{-5}$, $P=3.8x10^{-6}$, KW $\chi^2=27.9$, DF=3). Post-hoc pairwise Dunn testing found that the TS-related reduction in PV+ cell number significantly impacted the average ɣ power for models where pyramidal cells lacked mutant calcium channels (adjusted P=0.023, P=0.0012, Z=-3.03, shown in Figure 34), and where the pyramidal cells were modelled to contain mutant calcium channels (adjusted $P=5.0x10^{-4}$, $P=2.6x10^{-5}$, Z=4.05). The average ɣ power elicited by models with reduced PV+ cell number decreased in both cases. The average power of ɣ oscillation elicited by the networks with reduced PV+ cell number and TS-type calcium channels differed significantly from that elicited by the WT model, however, this difference became non-significant after multiple comparison testing (adjusted P=0.13, P=0.0071, Z=-2.45). Inclusion of mutant calcium channels within pyramidal cells of the CA3 neural network model did not significantly impact the average power of ɣ oscillations generated by the model as compared to the WT model (adjusted P=1, P=0.056, Z=1.59).

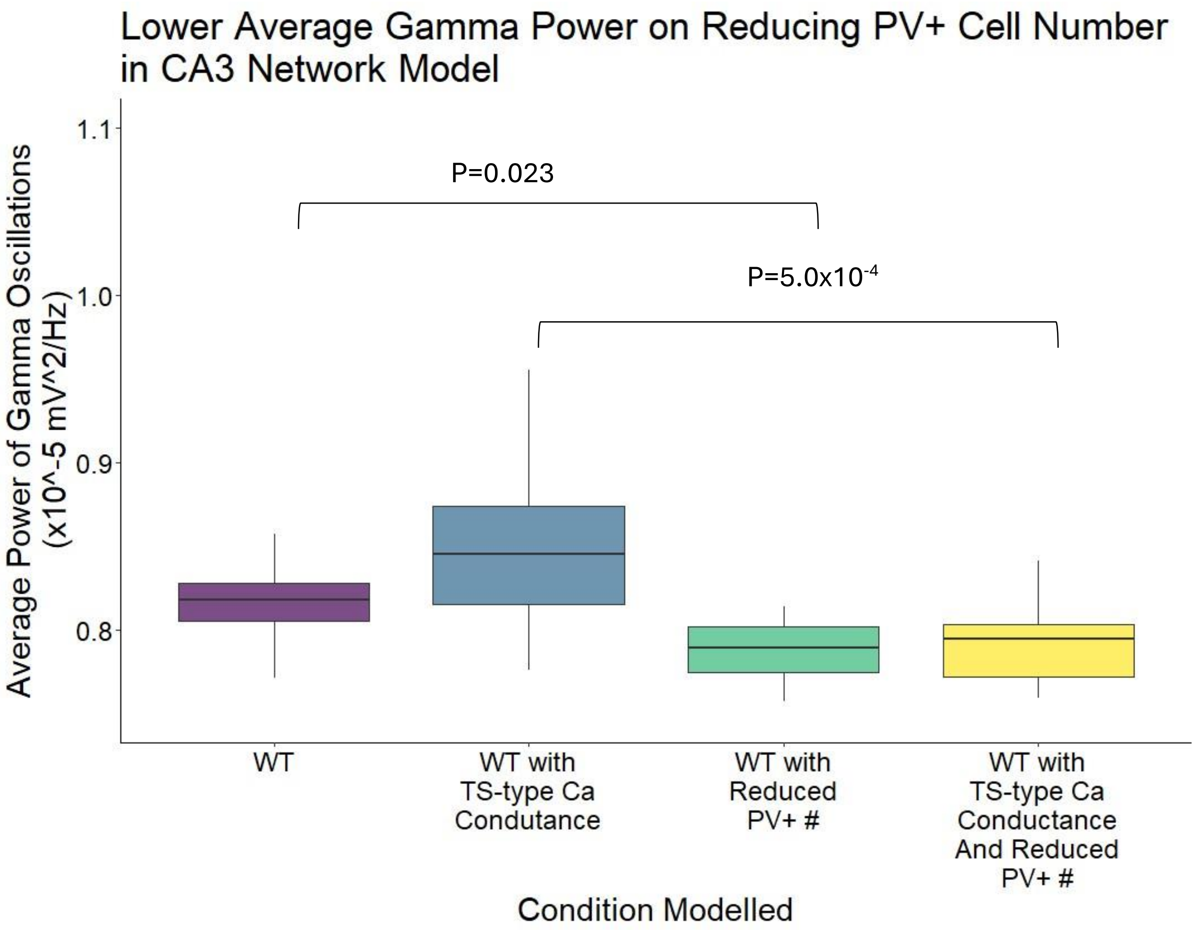

Figure 34 Band-wide average power of ɣ oscillations varies significantly between conditions modelled (KW between-condition testing: adjusted P=7.2x10—5, P=3.8x10-6, KW χ^2=27.9, DF=3). This suggests that TS-type changes in CA3 neural network could result in reduced ɣ oscillatory power. Brackets show between-condition comparisons which yielded significant results after multiple comparison adjustments. Non-significant between-condition comparison results are not shown. TS-related reduction in PV+ cell number results in ɣ oscillations of significantly lower average power being produced by modelled CA3 neural network.

The maximum power of ɣ oscillations generated by neural network models varied significantly by condition modelled (adjusted P=0.026, P=0.0014, KW χ^2=15.6, DF=3). Post-hoc Dunn testing found that the maximum power of ɣ oscillations differed significantly on reduction of PV+ cell number when pyramidal cells in the network model contained the TS-type mutant channels (adjusted P=0.0095, P=0.0005, Z=3.31, shown in Figure 35). Reduction in PV+ cell number in models that lacked mutant channels did change maximal ɣ power generated by the network, but this difference became non-significant after adjusting for multiple comparisons (adjusted P=0.59, P=0.031, Z=-1.81). Reduction in PV+ cell number and expression of mutant channels in pyramidal cells significantly impacted the maximum power of ɣ oscillations generated by the network as compared to the WT model. This difference became non-significant after correction for multiple testing (adjusted P=0.65, P=0.034, Z=-1.82). Inclusion of a mutant calcium channel in pyramidal cells of the model did not significantly impact the maximal power of ɣ oscillations generated for conditions where PV+ cell number was unchanged (adjusted P=1, P=0.068, Z=1.49), and for conditions where PV+ cell number was reduced (adjusted P=1, P=0.48, Z=-0.44).

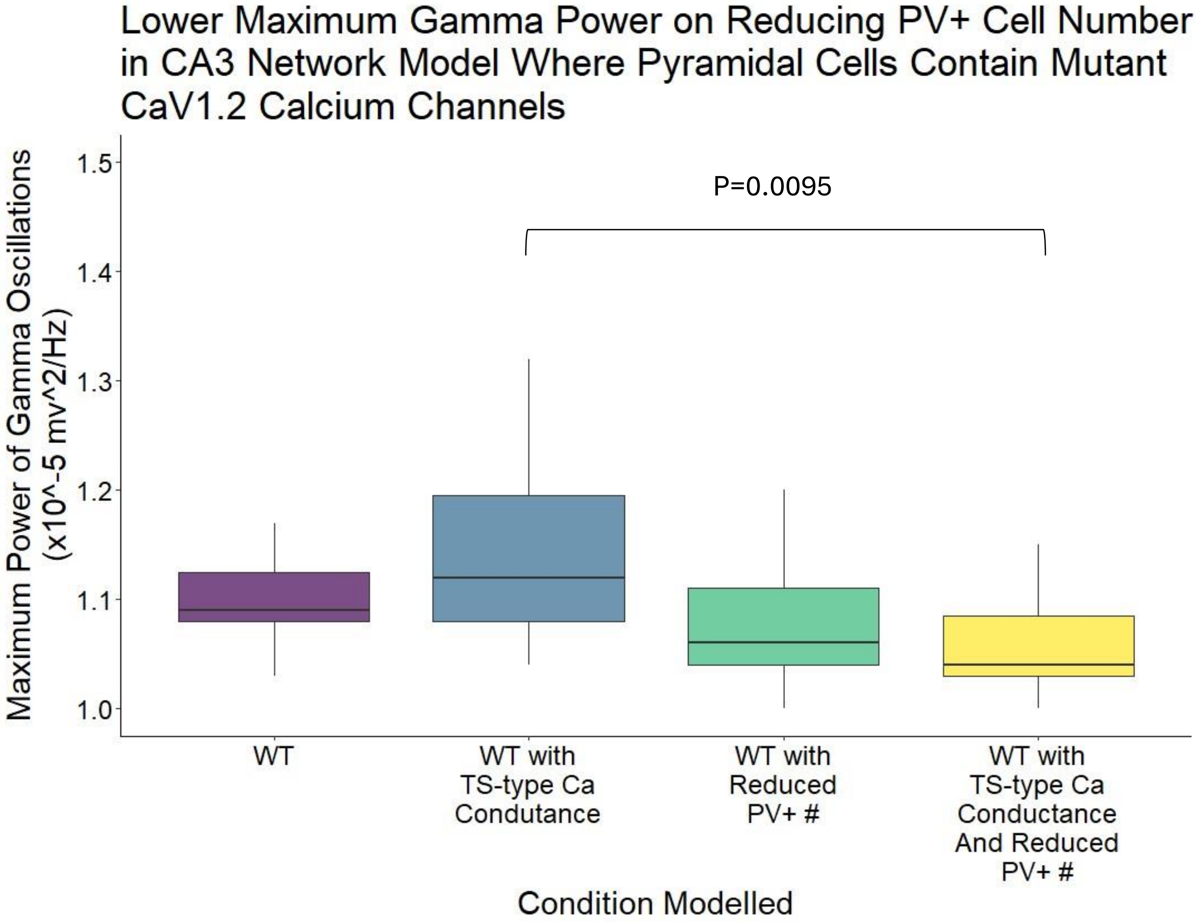

Figure 35 Maximum power of ɣ oscillations generated by CA3 neural network model varies significantly by condition modelled (adjusted P=0.026, P=0.0014, KW χ^2=15.6, DF=3). This suggests that TS-related changes in CA3 neural network may significantly impact oscillation power. The maximum power of ɣ oscillations generated by the CA3 network model were reduced on TS-related reduction in PV+ cell number, but only when pyramidal cells of the model contain TS-type mutant channels. Brackets show between-condition comparisons which yielded significant results after multiple comparison adjustments. Non-significant between-condition comparison results are not shown.

Overall, the power of ɣ oscillations produced by the modelled CA3 neural network were seen to decrease because of a TS-related reduction in PV+ cell number. This difference appeared more prominent when pyramidal cells of the model also contained TS-type mutant calcium channels. Modelling TS-type mutant channel within pyramidal cells of the CA3 neural network model without reducing CA3 PV+ cell number did not significantly impact the power of oscillations generated by the network.

ɣ oscillation maximum PSD impacted on modelling TS-type changes in CA3 neural network:

An ANOVA model describing variance in ɣ oscillation maximum PSD by modelled condition was generated. ANOVA model assumptions were met on testing. Residuals were tested for normality graphically, and variances found to be equal by Bartlett test (P=0.52, K^2=2.3, DF=3).

The maximum PSD for ɣ oscillations generated by models of differing condition varied significantly (ANOVA: adjusted P=0.0034, P=0.00018, F=7.516, DF=3). Modelling both TS-type changes in CA3 neural network—both reducing PV+ cell number and including mutant calcium channels in pyramidal cells—resulted in the network generating ɣ oscillations of significantly decreased maximal PSD as compared to those generated by the WT model (adjusted P=0.0019, P=0.0001, t=4.0, DF=76). TS-related reduction in PV+ cell number led to a significant decrease in maximum PSD of ɣ oscillations generated by the model when the pyramidal cells of the model contained mutant channels (adjusted P=0.0038, P=0.0002, t=4.0, DF=76). Reduction in PV+ cell number also led to decrease in maximum PSD of ɣ oscillations generated by models that did not contain mutant calcium channels, however, this effect became non-significant after correcting for multiple comparisons (adjusted P=0.46, P=0.024, t=2.3, DF=76). Inclusion of mutant TS-type calcium channels in pyramidal cells of the CA3 network model without reducing PV+ cell number did not significantly impact maximal PSD for ɣ oscillations generated by the network (adjusted P=1, P=0.094, t=-1.7, DF=76). The maximum PSDs of ɣ oscillations generated by each modelled condition are shown in Figure 36.

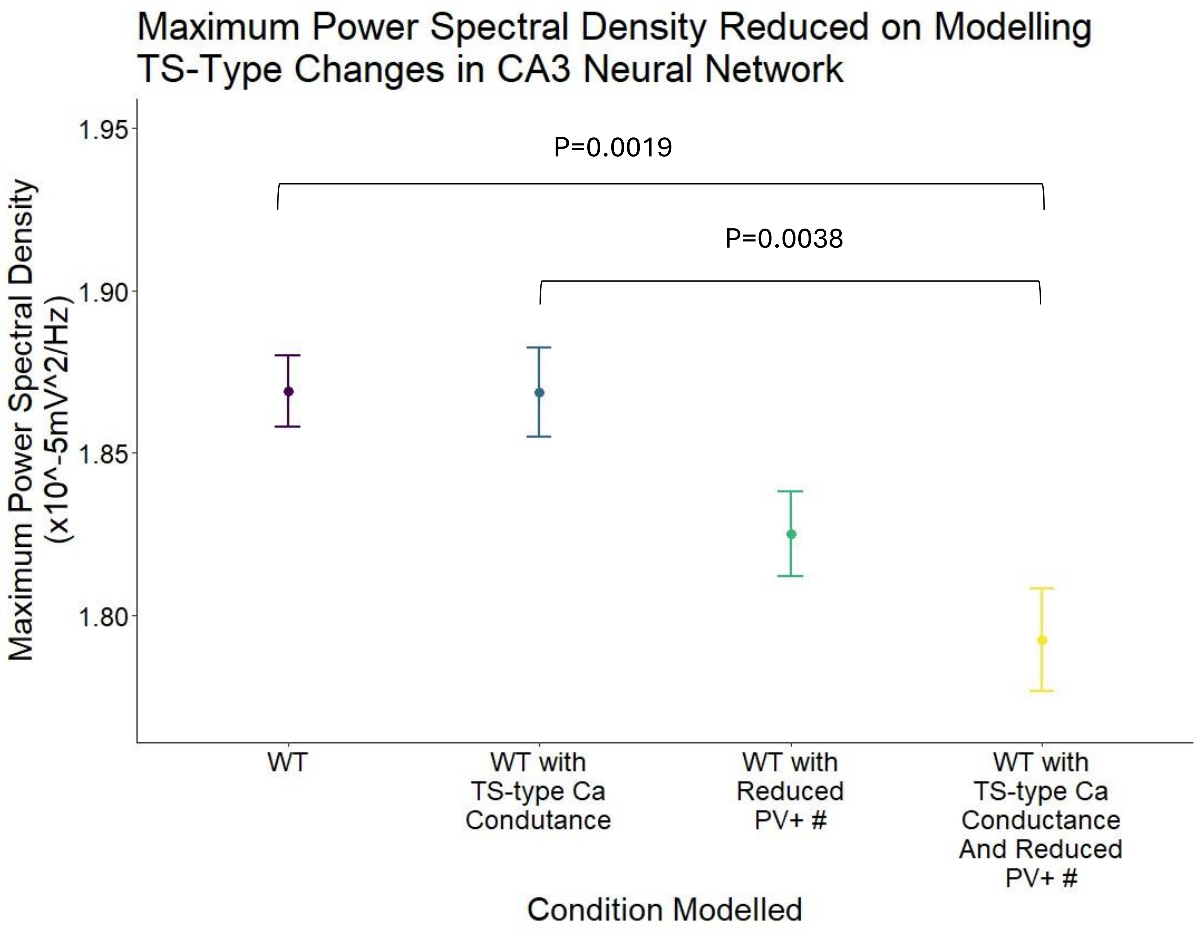

Figure 36 Maximum PSD of ɣ oscillations generated by the CA3 model varied significantly between conditions modelled (ANOVA: adjusted P=0.0034, P=0.00018, F=7.516, DF=3). This suggests that TS-type changes in the CA3 neural network could impact ɣ oscillation power distribution. The maximum PSD was reduced in modelled conditions involving a TS-related reduction in PV+ cell number as compared to WT, regardless of whether pyramidal cells contained TS-type mutant channels.

Overall, the TS-related reduction in PV+ cell number in the CA3 neural network impacted the maximum PSD of ɣ oscillations generated by the network. This suggests that TS-type changes in the network can impact the distribution of power across the ɣ oscillatory frequency. This impact specifically results from the TS-related reduction in PV+ cell number in this model.

No change in peak frequency of ɣ oscillations on modelling TS-type changes in CA3 neural network:

No significant difference in peak frequency of ɣ oscillations elicited by the CA3 neural network model were found between models of differing condition (KW testing: adjusted P=1, P=0.61, KW χ^2=1.8, DF=3). This suggests that TS-type changes in the CA3 neural network, including PV+ cell number reduction and inclusion of TS-type mutant calcium channels in pyramidal cells of the model, do not impact the frequency at which ɣ oscillations are strongest. No post-hoc testing was completed following the null-finding. This is shown in Figure 37.

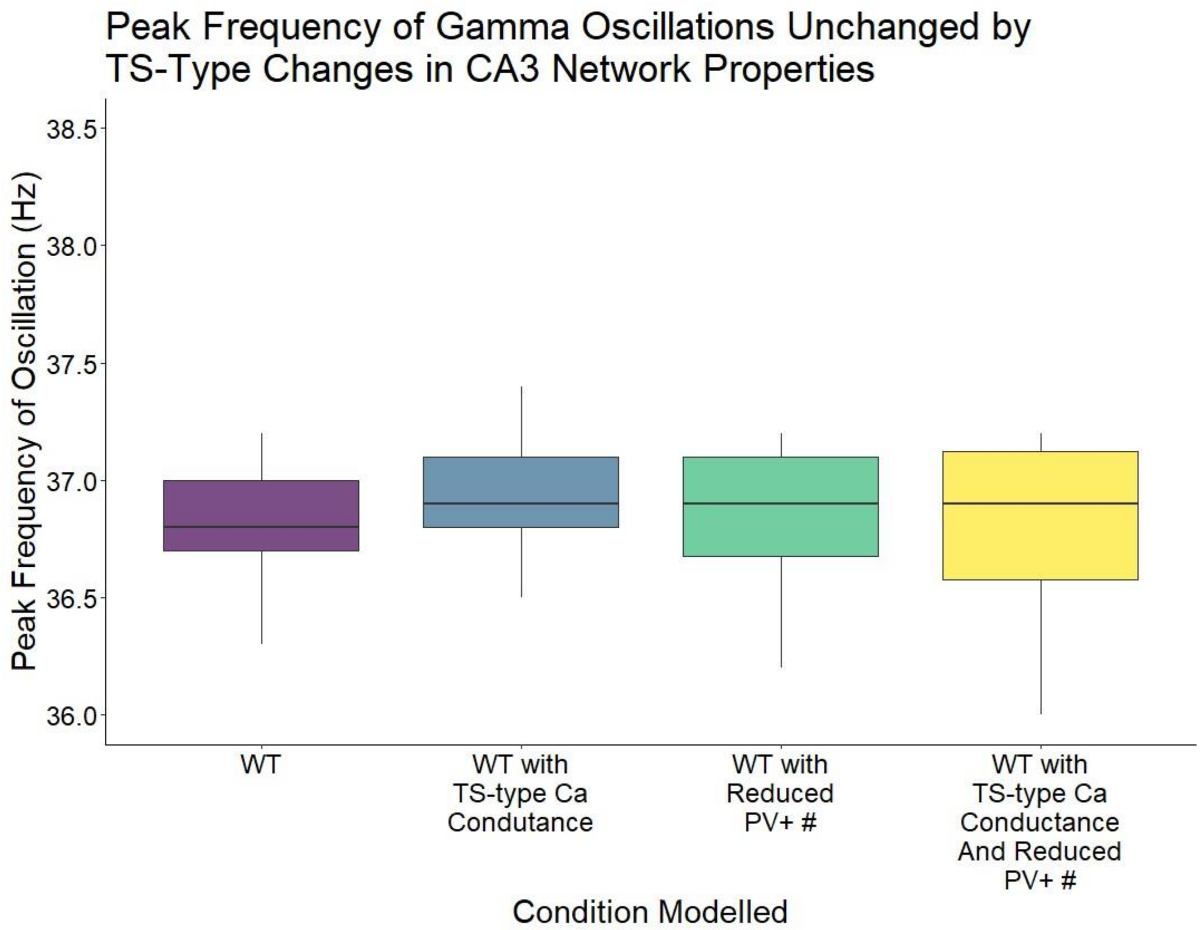

Figure 37 No significant differences between models of differing condition found when comparing peak frequency of ɣ oscillations generated (KW testing: adjusted P=1, P=0.61, KW χ^2=1.8, DF=3). This suggests that TS-related changes in the CA3 neural network are unlikely to impact the frequency at which maximum power ɣ oscillations are generated.

Discussion:

TS-type changes in CA3 neural network model result in generation of ɣ oscillations of reduced power, and abnormal PSD:

Simulating TS-related changes in a CA3 neural network reduced the power and maximum PSD of ɣ oscillations generated by the network. The main causative factor for these changes was found here to be the TS-related reduction in PV+ cell number in the modelled neural network. The presence of mutant CaV1.2 channels in pyramidal cells of the model did not appear to impact ɣ oscillations significantly, contrary to my original expectations.

This experiment provides evidence that TS-related changes in the network could result in abnormal ɣ oscillatory activity in the neural circuitry of the CA3 in TS patients, and of TS2Neo mice as compared to controls and WTs, respectively. The findings of this study, together with those of Birey *et al.* (2022) suggest that classical TS mutations may impact synchronous neural network activity in the brain through mutation-related changes in interneuron number within specific neural network circuitry, including the CA3.

Abnormal ɣ oscillations resulting from TS mutations could be indicative or causative of abnormal neural network function:

It is important to note that the increase in CA3 network ɣ oscillatory power predicted to result from classical TS may merely be indicative of abnormalities in the function and processing of the CA3. It is not clear at this time if changes in ɣ oscillatory activity seen in neuropsychiatric disease are related to neurological dysfunction in that disease (Fernandez-Ruiz *et al.*, 2023). However, recent studies have provided evidence to suggest that disrupting ɣ wave oscillations in specific circuits within the brains of awake, behaving mice can disrupt functions related to that circuitry (Fernández-Ruiz *et al.*, 2021; Guan *et al.*, 2022), supporting the notion that changes in ɣ oscillations may cause alterations in brain function. Therefore, identifying ɣ oscillatory abnormalities, and developing targeted treatment of these using deep brain stimulation or similar methods could be of potential therapeutic value. Should ɣ oscillations merely indicate abnormal circuit function, studying them would still provide a useful insight into the neurophysiological impacts of TS mutations.

Studying the mechanisms and types of changes in ɣ oscillations within different neural circuits which result from neurologically important genetic mutations is of potential use in understanding the neurological function of specific genes, but also in better understanding the neurophysiology of genetic diseases. The TS-related changes in ɣ oscillatory activity noted here may indicate neuropathological changes in hippocampal function caused by classical TS mutations.

Abnormal ɣ oscillations in ASD-related TS mouse model similar to those found in other ASD-related mouse models:

Many TS patients meet diagnostic criteria for ASD (Splawski *et al.*, 2004). ɣ oscillations in various neural circuits are found to be disrupted in ASD patients (Gogolla *et al.*, 2009; Rojas and Wilson, 2014), although the exact nature of the disruptions reported often differ between studies. This may be due to the currently non-standardised methods of measuring and reporting ɣ oscillation results (see Fernandez-Ruiz *et al.*, 2023 for an overview).

Interestingly, ɣ oscillations generated by various neural networks have been found to be disrupted in several mouse models of ASD. The environmental VPA exposure mouse model of ASD was found to have whole-brain ɣ oscillatory activity of lower power as compared to WT mice, as measured by in-vivo electroencephalogram (EEG) recording (Gandal *et al.*, 2010). ASD model mice with KO of the ASD-related *Neuroligin-4* gene (*Nlgn4* KO mice) were found to have reduced CA3 ɣ oscillatory power as compared to WTs by in-vitro LFP recording (Hammer *et al.*, 2015). Another genetically modified ASD mouse model having KO of the *Cntnap2* gene was found to have abnormal ɣ oscillations in the CA1 of the hippocampus as compared to WT mice by in-vivo LFP experiment. The

Cntnap2 gene encodes a synaptic cell adhesion molecule (Paterno *et al.*, 2021). The *FMR1* KO mouse model of the ASD-related condition, Fragile-X, has been found to have abnormal ɣ oscillatory activity across multiple neural circuits by use of in-vivo and in-vitro methods (Gibson *et al.*, 2008; Kozono *et al.*, 2020; Pollali, Hollnagel and Çalışkan, 2021). Of note, ɣ oscillations in the CA3 neural network of *FRM1* KO mice are of increased power as compared to WTs as measured by in-vitro LFP recording (Pollali, Hollnagel and Çalışkan, 2021).

ASD-related genetic mutations impact ɣ oscillation in many neural circuits in the brain, including the CA3. The findings from this computational study predict that TS-related changes in a CA3 neural network would cause abnormal reduction in ɣ oscillation power and PSD which supports this conclusion.

Lack of impact of TS-type changes in CaV1.2 model on CA3 neural network ɣ oscillations:

My study found that inclusion of the TS2-type channel in pyramidal cells of the CA3 network model did not significantly impact neural network ɣ oscillations. Findings from other studies which involve manipulation of CaV1.2 channels, or L-type channel function generally, suggest that TS-related changes in calcium channel currents of the neuron could result in abnormalities in ɣ oscillations generated by neural networks including those cells. Metzner *et al.* (2022) showed that genetic disease related changes in CaV1.2 channel conductance could result in a reduction in ɣ oscillation power within cortical neural networks. Heterozygous KO of *CACNA1C* was found by EEG study to reduce whole-cortex ɣ oscillation power in the mouse (Kumar *et al.* 2015). Further to this, blocking L-type calcium channels has also been found to impact ɣ oscillations in a CA3 neural network in-vitro (Zhang *et al.*, 2021).

One could therefore expect that TS-type changes in CaV1.2 channel expression within pyramidal cells would disrupt ɣ wave oscillations of the associated networks, contrary to the predictions of this model. The potential reasons for this are discussed in the "Limitations" section of this chapter.

Reduced PV+ cell number is related to abnormal ɣ oscillations in TS and in other ASD-related mouse models:

My finding that a TS-related reduction in PV+ cell number leads to the generation of ɣ oscillations of reduced power in a CA3 neural network is of interest. Many mouse models of ASD have been found to have reduced PV+ cell number in various areas of the brain (Gogolla *et al.*, 2009; Filice *et al.*, 2020). The VPA mouse model of ASD which was found to have reduced ɣ oscillatory power in the cortex was also found to have a reduced number of neocortical PV+ interneurons (Gogolla *et al.*, 2009; Gandal *et al.*, 2010).The *Cntnap2* mouse has mid-range ɣ oscillations of reduced power in CA1, but also a reduced number of PV+ interneurons in the CA1 (Paterno *et al.*, 2021). *FMR1* KO mice have been found to have reductions in PV+ cell numbers across various brain areas which also show aberrant ɣ oscillations (Lee *et al.*, 2019; Filice *et al.*, 2020).

Together with the findings from this study, this suggests that PV+ cell reduction found in several ASD models, including the TS2Neo mouse, may result in abnormal ɣ oscillations in various neural circuits of the brain. It is likely that increases in PV+ cell number— such as those found in V1 in chapter 3— would also impact ɣ oscillations also.

Limitations:

There are several limitations to this study. The study was computational in nature and therefore all results are merely predictive. Pyramidal cells of the model were modelled as simple single electrical compartments containing various channels, but notably lacking BK channels. Zhang *et al.* (2021) showed that blocking L-type calcium channels in a CA3 neural network reduces the power of ɣ oscillations of the network. However, they found that this effect was dependent on the function of calcium-dependent BK channels. Modelling pyramidal cells without BK channels may have led to a false negative finding for classical TS-type mutant channel presence in pyramidal cells of the model impacting ɣ oscillations. The TS mutation may also impact sodium and/or potassium channel function and/or density in an unknown way that requires future investigation. This is discussed in chapter 2. Any potential TS-related changes in sodium and potassium channel density and/or dynamics have not been modelled here. Should the TS mutation impact sodium channel density or dynamic properties, this would likely impact ɣ oscillations (Kaplan, Isom and Petrou, 2016). The change in calcium channel conductance and reduction in PV+ cell number in CA3 which was designed to model the TS condition may not accurately represent all the genotype changes in this network. This needs to be appreciated when considering the result of this study.

My L-type calcium channel model was based on kinetics of the channel as expressed in a pancreatic β cell, not in a neuron (Riz, Braun and Pedersen, 2014). Should the channel kinetics differ substantially between cell types, my use of an inappropriate calcium channel model could also result in an erroneous finding (Petkov, 2009).In my qualitative analysis of the data, the firing properties simulated by the modelled pyramidal cells and PV+ interneurons appeared to replicate those recorded by electrophysiological studies as reported in the literature. However, exact data from θ-frequency stimulated pyramidal and PV+ cells were not available at the time of study. I could not directly compare CA3 cell activity with recorded data from CA3 neurons, instead comparing them against those for CA1 cells. Therefore, I cannot be entirely confident that the model cell faithfully replicates real-life firing properties for CA3 neurons exactly. LFP data generated from the modelled network showed θ-nested bursting as is seen in ex-vivo LFP recordings of the CA3 network in electrophysiological experiments. Overall, this suggests that the model faithfully replicates firing properties of CA3 neurons, as well as their synchronous activity. This reduces the concern of this model being inappropriate for the intended purpose.

The model was used in this study in line with its primary design purpose, to explore changes in the network on its synchronous activity, notably ɣ oscillations. The model appeared to replicate expected cell firing and synchronous network activity. Together this suggests that the simplicity of the model may not be problematic, although the potential for missing nuanced changes is always present in any modelling study.

In this study, I assumed that TS-type mutant CaV1.2 channels were expressed in pyramidal cells of the CA3 region. It was assumed that 28.95% of the CaV1.2 channels present in those cells were mutant-type, reflecting heterozygous expression of the channel. The splice ratio of exons 8:8a were not considered in modelling the CaV1.2 channel current, as it was predicted that a high proportion of the CaV1.2 channel current would be carried by the mutant channel. This was based on the finding of Panagiotakos *et al.* (2019) that classical TS mutation causes an upregulation of expression of the mutant exon, and that the splice ratio of exons 8:8a is usually 5:1, so the >80% expression ratio was high enough to assume ≈1:0 exon 8:8a for simplicity. However, Calorio *et al.* (2019) found that TS2Neo mice had a reduced exon 8:8a alternative splice ratio as compared to WT. Also Panagiotakos *et al.* (2019) found that the TS1 mutation in exon 8a of *CACNA1C* also caused a reduced exon 8:8a splice ratio. This change in splicing may only be true for the classical TS1 mutation, not the classical TS2 mutation which is modelled here. The expression of classical mutant CaV1.2 channels within the neuronal membrane as compared to unaffected L-type channels has not been explored. My modelling 28.95% of all CaV1.2 as having the mutation is based on an untested assumption, which may not be valid based on the findings of others reported above. This could limit the physiological appropriateness of my model.

The TS-related reduction in PV+ cell number was based on the findings from my immunofluorescence studies reported in chapter 3 which have not been replicated by an independent investigator. It is well known that biological science findings are often not reproducible (Baker and Penny, 2016), replication of this study would increase confidence in the conclusion that TS2Neo heterozygosity leads to a reduction in PV+ cell density in the CA3 region of the hippocampus.

Future experiments:

I suggest that classical TS mutant channel expression be explored by transcriptome study, to confirm the level of mutant TS channels in CA3 pyramidal cells of the hippocampus of TS2Neo mice described by Bader *et al.* (2011) and the TS2 mouse model described by Matsui *et al.* (2023). My immunofluorescence study (detailed in chapter 3), which provided evidence that PV+ cell number is reduced in the CA3 of TS2Neo HET mice as compared to WT, should be replicated by an independent investigator using larger sample sizes. Future studies should aim to explore how classical TS mutations might impact neural network oscillations in-vivo and in-vitro, using EEG and LFP recording techniques respectively. Understanding if classical TS mutations impact ɣ oscillations in TS patients by use of non-invasive EEG techniques would be of great interest and direct relevance to the human condition. Exploring how TS mutations impact ɣ oscillations by use of LFP recording in ex-vivo acute slices of CA1 and CA3 regions of TS2Neo and TS2 and WT mice would be of great interest going forward to test the predictions from this modelling study. I suggest θ-frequency oscillatory drive be used to elicit the ɣ oscillations in CA3 studies.

ɣ oscillations generated by other neural networks should be explored in TS2Neo mice using in-vivo, in-vitro, and computational modelling methods to understand if any differences in oscillations are area-specific or generalise to other neural networks in the brain. The PV+ cell number reduction noted in CA3 hippocampus of TS2Neo mice as compared to WTs could be explored in TS patients by post-mortem study of neurological tissues as described in chapter 3. Effects of TS-type changes in neural circuitry on ɣ oscillations should also be performed using a network model that accurately replicates the prolonged AP seen in TS mutant neurons, such as the TS2Neo pyramidal cells. Use of a more complex computational model, like that of Zou *et al*. (2011) could uncover TS-related ɣ oscillation abnormalities which are not observed due to the simplicity of the model used. Similarly, using a CaV1.2 channel model derived from electrophysiological data collected from the neuron in any future model would be of great benefit.

Conclusion:

The current computational modelling study has demonstrated that TS-related changes in a simple CA3 neural network results in reduced ɣ oscillatory power and reduced PSD. The TS-related reduction in PV+ cell number appeared to impact ɣ oscillation power and PSD more than inclusion of classical TS-type calcium channel currents in pyramidal cells of the model. I suggest that more complex computational modelling studies be completed, where pyramidal cells include BK channel currents, include other potential genotype-related changes in ion channel expression and contain neuron-appropriate CaV1.2 channel currents to further explore the possible impact of TS-mutant channel currents within pyramidal cells on CA3 network oscillations. Electrophysiological studies would be pertinent to explore the impact of classical TS mutations on network activities ex-vivo and in-vivo. Study of the effects of ASD-related mutations on the power and power-distribution of ɣ oscillations, likely through PV+ cell functional abnormalities, is an important avenue to explore to better understand the pathophysiological mechanisms by which ASD-related mutations might impact brain function and processing.

Contributions:

Dr Cezar Tigaret and Rosie Craddock were involved in experimental design. Computational modelling, data acquisition and analyses were performed by Rosie Craddock.

General discussion:

Key findings:

The overall aim of my PhD was to undertake research to gain a better understanding of the neurophysiology of TS. This is a broad aim with a wide scope. I focused on 4 specific key aims, addressed using various methodologies as discussed in the introduction. Each aim was addressed by a separate experiment, each being detailed in a data chapter of this thesis.

In data chapter 1, I provided evidence that TS2Neo mice have a specific visual perceptual abnormality as compared to WT mice. TS2Neo mice had superior contrast sensitivity to visual stimuli of high SF as compared to WT mice. TS2Neo mice also had a significantly different CSF as compared to WT. This suggests that the classical TS2 mutation results in abnormal basic sensory processing in the visual domain of the mouse. Work by Rendall *et al.* (2017) has provided evidence that TS2Neo mice also have an auditory processing enhancement as compared to WT mice. Together, this suggests that classical TS mutations, such as the TS2 mutation may impact sensory processing generally, across multiple sensory modalities.

Data chapter 2 provided evidence that pyramidal cells from 3 different cortical areas of the TS2Neo mouse have prolonged AP duration as compared to those from WT. These areas were V1, RSC and CA1. Previous work by Paşca *et al.* (2011) provided evidence that the classical TS1 mutation prolongs the AP duration in human iPSC-derived neurons. Together, this suggests that the classical TS mutations prolong the AP in the neuron.

Data chapter 3 provided evidence that PV+ cell number was increased in V1 and decreased in CA3 in the TS2Neo mouse brain as compared to WT. There was no change in PV+ cell density in the CA1 or RSC regions. This suggests that the TS2 mutation causes abnormal PV+ cell distribution across the TS2Neo mouse brain. The mechanism by which this happens was not explored. Classical TS mutations have previously been shown to disrupt inhibitory interneuron migration (Birey *et al.*, 2017, 2022; Horigane *et al.*, 2020), and the CaV1.2 channel has also been shown to play a role in PV+ cell development (Jiang and Swann, 2005). It seems likely that the mechanism by which classical TS mutations impact PV+ cell distribution across the brain may involve changes in PV+ cell development, interneuron migration, or both.

In chapter 4, I use computational modelling which predicted that the classical TS2 mutation would cause abnormalities in ɣ oscillations generated by a CA3 neural network, decreasing the power of ɣ oscillations and altering the distribution of ɣ oscillatory power across the ɣ frequency band. The TS-related reduction in PV+ cell number which was included in the CA3 network model was largely responsible for the TS-related changes in ɣ oscillations predicted by the model. The inclusion of a mutant CaV1.2 channel in the pyramidal cells barely impacted ɣ oscillatory activity within the model network. This provides some evidence that the classical TS2 mutation can impact ɣ oscillatory activity within functional neural networks of the brain, largely by the TS-related impact on PV+ interneuron distribution in the brain. Birey *et al.* (2022) found evidence that the classical TS1 mutation causes abnormal inhibitory interneuron migration which then results in abnormal synchronous activity in a cultured neural network. My findings together with those of Birey *et al.* (2022) suggest that classical TS mutations can impact neural network synchronous activity including network oscillations by mechanisms likely involving abnormal inhibitory interneuron distribution within those networks.

Important potential TS-related changes in neurophysiology not covered in the scope of thesis:

TS patients tend to exhibit hypoglycaemia and cardiac abnormalities (Splawski *et al.*, 2004, 2005; Dufendach *et al.*, 2018; Walsh *et al.*, 2018), these may well lead to neurological damage, the impacts of which were not studied in this body of work. It is important to note the potential contribution of syncope-related hypoxic brain injury, falls and circulatory disruptions to TS-related changes in neurological function. Indirect mechanisms by which the mutation could result in neurological disturbances or dysfunction were not addressed here but must be considered.

I did not explore the impact of classical TS mutations on glia function within the brain in this body of work. Glia are an understudied and critical functional component of all nervous systems. Astrocytes are known to be critically involved in the maintenance of synapses in the central nervous system (Chung, Allen and Eroglu, 2015). Oligodendrocytes are involved in neuronal myelination and controlling the rate of electrical transmission within the brain. Classical TS mutations have previously been shown to impact oligodendrocyte maturation and myelination in the TS2Neo mouse brain (Cheli *et al.*, 2018). Astrocytes are known to express high levels of CaV1.2 channels, and calcium signalling is critical for astrocyte function (Cheli *et al.*, 2016b). Abnormalities in astrocyte and oligodendrocyte function are thought to be pathologically relevant to TS and ASD (Cheli *et al.*, 2018; Chung and Son, 2020). Specifically, abnormalities in myelination and astrocyte function have been reported in patients with ASD, neurodevelopmental disorder and epilepsy (Sloan and Barres, 2014; Patel *et al.*, 2019; Galvez-Contreras *et al.*, 2020; Knowles *et al.*, 2022), all of which are neurophenotypes of TS. Changes in oligodendrocyte development which were demonstrated by Cheli *et al.,* (2018), and changes in astrocyte function which could result from TS mutations were not explored in this study. These changes and the functional implications of these changes should be explored in the future to gain a more holistic understanding of the pathophysiology of the neurological changes seen in TS.

Abnormalities in the neuronal structures at the microscopic and macroscopic levels were not explored in this study but have previously been reported to result from classical TS mutations (Krey *et al.*, 2013; Rendall *et al.*, 2017; Buddell *et al.*, 2019). It is likely that these abnormalities also contribute to the neurophenotypes of TS. Similarly, disruptions in chemical neurotransmitter systems caused by classical TS mutations have also been reported (Paşca *et al.*, 2011; Ehlinger and Commons, 2017). The resultant functional changes caused by these physiological abnormalities, and mechanisms by which classical TS mutations impact neurotransmitter signalling and systems in the brain were not explored here but may be critical to the neurological and neuropsychiatric abnormalities seen in TS patients.

General limitations of the experiments described in the thesis:

The methods used in this body of work involved either computational modelling or the use of an animal model to study mutation-related changes in neurophysiology which are likely to contribute to the neurophenotypes seen in TS patients. Computational modelling is, by nature, predictive, with models being based on previously acquired data. As such, modelling studies always involve assumptions and simplifications of the systems studied (Teufel and Fletcher, 2016). Any study involving an animal model of a human condition should be considered with the understanding that human and animal physiology are somewhat different, often in ways we do not yet know or understand (Hartung, 2008). To address these limitations, studies using human post-mortem or iPSC-derived neurons should be conducted, and results of such studies be considered alongside computational modelling and/or animal model study findings.

Key future studies:

Key future studies related to work in this thesis:

There is much left to understand regarding the neurophysiology of TS. There are several key questions directly related to the findings described in this thesis which have yet to be addressed. Below I discuss the top five questions related to the work in this thesis which I believe are most critical to our understanding of the neurophysiology of TS.

Key question 1:

First, current evidence suggests that there exist basic sensory processing abnormalities which result from the classical TS2 mutation in the TS2Neo mouse. A multicentre international study of TS patients in which the patients undergo a battery of standardised sensory function tests, as well as genetic testing to confirm the causative mutation in each patient is recommended. This would provide evidence as to which, if any, TS mutations result in basic sensory processing abnormalities in humans. I suggest the use of the standardised sensory integration and praxis test (Ayres, 1996).

Key question 2:

Secondly, the mechanism by which classical TS mutations prolong the neuronal AP are yet unclear. Calorio *et al.* (2019) found that the classical TS2 mutation decreases sodium channel density, resulting in prolonged AP in chromaffin cells of the TS2Neo mouse. A reduction in sodium channel density resulting from the TS2 mutation in neurons of the TS2Neo mouse is a strong candidate mechanism by which the mutation might cause prolonged AP in the neuron. Studies involving measuring sodium channel density and currents in pyramidal cells in V1, RSC and CA1 of TS2Neo mice should be conducted to explore this possibility. Other studies involving measuring potassium and specifically BK channel density and function in TS2Neo and WT mice would demonstrate whether the classical TS2 mutation could impact AP duration by altering potassium channel function in the neuron. I propose that these studies use methods based on those described by Calorio *et al.* (2019).

Key question 3:

Evidence now suggests that classical TS mutations can prolong AP duration in the neuron as it does in the cardiac myocyte. The prolonged AP in the cardiomyocyte has a direct contribution to the pathophysiology of the cardiac phenotypes seen in TS (Splawski *et al.*, 2004, 2005; Drum *et al.*, 2014; Dick *et al.*, 2016). Studies are required to understand the impact of the prolonged AP on pathologically important functions of the nervous system. The prolonged AP could potentially impact neurotransmitter release as it does in the *FMR1* KO mouse (Deng *et al.*, 2013). Transmission electron microscopy studies should be used to measure neurotransmitter release in neurons with and without a classical TS mutation. This would indicate whether classical TS mutations impact neurotransmission in general within the brain. I suggest the use of methods described in Deng, Sojka and Klyachko (2011) in evaluating whether classical TS mutations impact neurotransmitter release.

Key question 4:

The distribution of PV+ cells was evidenced to be altered by the classical TS2 mutation in the mouse brain. The two proposed mechanisms by which classical TS mutations could impact PV+ cell distribution in the brain are: a) by mutation-related changes in PV+ cell development, or b) by mutation-related changes in interneuron migration during embryogenesis. Embryological studies using TS2Neo and WT mice, alongside the study of iPSC-derived neurons from TS patients and a genetically corrected control line would be useful in exploring whether PV+ cell development, PV+ cell migration, or both, are disrupted by classical TS mutations, and how this may result in the abnormal PV+ cell distribution across the brain which was demonstrated in this study.

Key question 5:

It should be confirmed that TS-related changes in the neural networks of the mouse brain cause the predicted alterations in CA3 neural network activity by use of in-vivo or ex-vivo electrophysiological recording techniques inTS2Neo and WT mice. These studies would also provide evidence of the ability of the computational model described in data chapter 4 to predict any changes in ɣ oscillatory activity caused by the classical TS2 mutation.

Key future studies unrelated to the work described in this thesis:

There are several important avenues not explored in this thesis which should be addressed to better our understanding of the neurophysiology of TS. Below, I have outlined two key questions that I suggest should be addressed to expand our understanding of the disease and of neurophysiological function of the *CACNA1C* gene.

Key question 6:

CaV1.2 channels play an important role in calcium signalling within the astrocyte (Cheli *et al.*, 2016b). Functional imaging of a fluorescent calcium indicator expressed in astrocytes of the WT and TS2Neo or TS2 mouse brain should be used to explore whether the mutation alters calcium signalling in the astrocyte. It is also important to understand how classical TS mutations might impact astrocyte development and distribution across the brain. Immunohistological study should be used to explore if and how the development, migration and final distribution of astrocytes differs across the brains of TS model mice as compared to WT. Changes in astrocyte function or distribution within the brain could be of pathophysiological relevance to the neurological components of TS.

Key question 7:

Findings by Cheli *et al.* (2018) suggested that excessive myelination is caused by the classical TS2 mutation in the TS2Neo mouse. Immunohistological study of post-mortem tissue from TS patients with classical TS mutations would be useful to confirm whether classical TS mutations impact myelination and oligodendrocyte development in the human brain as it does in the mouse. Study of the implications of enhanced myelination in the brain on neurological function would be informative.

Overall conclusion:

The overall aim of my doctoral research was to provide evidence to inform a better understanding of the neurophysiology of TS. Together with previous research, my findings suggest that classical TS mutations, specifically the TS2 mutation, causes abnormal sensory processing in at least two sensory domains in the mouse. I provide the first published evidence that the classical TS2 mutation causes prolonged AP in mature neurons of functional brain tissue in the mouse as it does in other functionally important electrical cells of the body. The mechanism by which the TS2-type mutant CaV1.2 channel causes prolonged AP in the neuron is unknown and requires resolution. I have suggested several experiments which may be used to indicate the mechanism by which the TS2 mutation leads to prolonged AP duration in the neuron. I provide evidence that the classical TS2 mutation causes abnormal PV+ cell distribution across the adult TS2Neo mouse brain, causing an increase in PV+ cell density in V1, a reduced PV+ density in CA3, but no change in PV+ cell density in CA1 or RSC. This suggests that classical TS mutations can impact interneuron distribution throughout the brain. Computational neural network modelling predicted that the TS mutation would increase the power of—and alter the PSD of—CA3 neural network ɣ oscillatory activity largely due to the effect of mutation-related reduction in PV+ inhibitory interneuron number within the CA3. My research on the neurophysiology of a mouse model of TS has been fruitful in indicating potential avenues of research to follow to better our understanding of the aetiology of the neuropsychiatric components of TS.

Appendix 1: Original in-vivo two-photon imaging experiment, equipment overhaul and instructions for setting up and running the experiment described in chapter 1:

Original experiment setup:

Overview of original experiment:

As in chapter 1, I aimed to explore how the TS2 mutation impacts a specific visual processing ability—contrast sensitivity to visual stimuli of varying SF, and the resulting CSF—in TS2Neo mice. TS is an ASD-associated disease of specific genetic cause (Splawski *et al.*, 2004). Patients with ASD have been found to have abnormal CSFs as compared to controls (Kéïta *et al.*, 2014). ASD patients were found to have an increased contrast sensitivity to visual stimuli of high SF. A recent study has found that a mouse model of ASD also has increased contrast sensitivity to visual stimuli of high SF (Cheng *et al.*, 2020). This finding relied upon optokinetic reflex responses behavioural of mice to various visual stimuli. The optokinetic reflex response involves the function of lower brain areas, and not on cortical function (Distler and Hoffmann, 2011). The human experiments showing that ASD patients have abnormal CSF involved measuring conscious behavioural responses from subjects which are dependent on the function of V1 (Leopold, 2012). I designed an experiment based on the equipment available in Professor Frank Sengpiel's lab to measure V1-dependent CSF in a mouse which involved recording a mouse's behavioural and V1b neuronal responses to visual stimulation in such a way that CSF could be measured for TS2Neo and WT mice, and then compared.

I describe here the experiment setup, explain briefly what a CSF is, and the methods by which I had originally aimed to measure this in the mouse. I explain the equipment malfunctions that resulted in failure of the pilot experiment, how the equipment was then overhauled, and the setup used for the final experiment which is detailed in chapter 1. The final experiment was completed after equipment overhaul. The final experiment did not involve measuring mouse behavioural responses to visual stimuli due to insufficient time remaining within the PhD. Detailed instructions on hardware and software requirements, setup and experimental procedures required to repeat the final experiment (which is presented in chapter 1 of this thesis) are provided. Codes required to run the experiment, and to process resulting data are also provided on the GitHub pages indicated within the text. This GitHub page will be monitored infrequently, but bug fixes may be provided in the future.

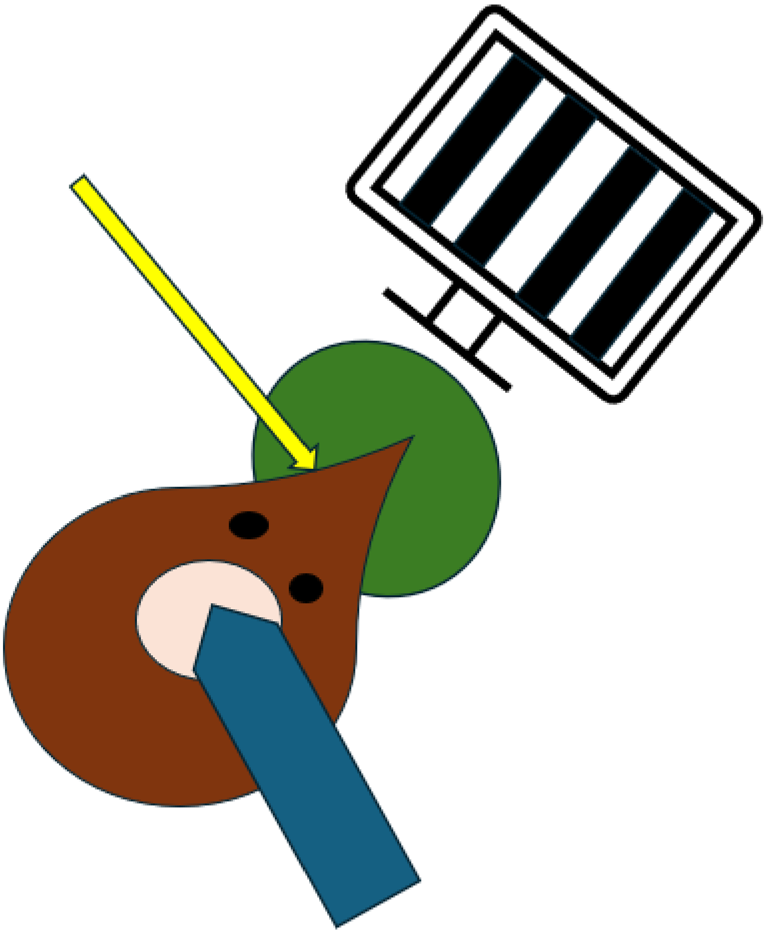

Figure S1 Image showing mouse (brown) positioned in front of an LCD screen on which gratings stimuli are presented, with a microscope objective (blue) focused on a cranial window (pink) over V1b of the mouse, and a steering wheel (green) positioned directly in front of the mouse, below eye level. The reward dispense system is shown in yellow. This was the general setup of the original experiment. Visual stimuli were presented to the mouse using the LCD screen, if the mouse turned the steering wheel (green) when the stimulus was shown on the LCD screen, then a liquid reward was given to the mouse through the reward system (yellow). Images of GCaMP6f-labelled neurons in V1b were recorded through the microscope objective (blue) throughout this experiment.

Figure S1 shows the overview of the pilot experiment setup. The mouse was placed on a custom-made mouse holder, which was equipped with a steering wheel. The steering wheel was just below the mouse's field of vision, in a position at which the mouse would rest its paws. The position of the steering wheel was recorded by a rotary encoder. The mouse was positioned facing an LCD screen. When the mouse correctly turned the steering wheel while visual stimuli were presented on the LCD screen, a liquid reward (Koolaid) was dispensed via the reward system to a spout placed in front of the mouse's mouth (indicated on Figure S1 in yellow). The reward dispense was controlled by a solenoid valve interfaced with PC-connected hardware. GCaMP6f-labelled neurons of L2/3 of V1b of the mouse brain were recorded throughout the experiment paradigm by use of two-photon calcium imaging. The imaging described is similar to that used in our lab previously (Craddock *et al.*, 2023), for a more detailed representation of the steering wheel and reward dispense setup, see Burgess *et al.* (2017).

The visual stimuli shown on the LCD screen were gratings of varying SFs and contrasts. The aim was to produce both a behavioural and a neuronal-response CSF from each mouse. Data from mice of each genotype would be compared to test how the TS2 mutation impacts CSF in TS2Neo as compared to WT mice.

CSF is a function of contrast sensitivity to stimuli of varying SFs. Typically, one can see gratings bars of low SF at low contrasts (high contrast sensitivity), can see gratings bars of mid SF at very low contrasts (very high contrast sensitivity), and can see gratings bars of high SF at only higher contrasts (low contrast sensitivity). The CSF plots how contrast sensitivity changes as a function of SF.

The experiment involved training mice to respond to stimuli of a range of SFs at 100% contrast- stimuli the mice should be able to see. Full-screen gratings stimuli of 7 SFs across the mouse's visual range were presented at 100% contrast for 3 seconds, followed by a 3 second grey-screen. If the mouse turned the steering wheel during visual stimulus presentation, the reward valve was opened, and a liquid reward (Koolaid) was dispensed to the mouse. Should the mouse turn the wheel on presentation of the grey-screen, the grey-screen period would restart, to provide a sort of 'time-out' reinforcement to avoid the mouse constantly turning the wheel regardless of stimulus presentation. This was to be repeated until the mouse obtained 80% success rate of turning the steering wheel when each stimulus was presented. Once the mice were trained for this visual stimulus detection task, they would be shown stimuli of all 7 SFs, but at varying contrasts between 100% and 3.4%. The behavioural responses of the mouse to stimuli of each SF shown at each contrast level would indicate the contrasts at which each mouse could see the gratings at each SF. From this, I could obtain a behavioural CSF for the mouse.

During experimental sessions, I would also record from neurons of V1b as visual stimuli of each SF at each contrast level were presented. From this I could generate a CSF for each neuron of an animal as described in chapter 1. This was the neuronal CSF. Neuronal CSFs from mice of each genotype, and behavioural CSF from mice of each genotype could then be compared to explore how TS2Neo mutation impacts CSFs in the mouse.

To complete this experiment data regarding steering-wheel position, neuronal fluorescence (from 2-photon image recording), reward dispense, and visual stimulus presentation were recorded. This information was sampled by use of DAQ hardware from NI. The timestamps of DAQ hardware sampling were also required, such that all this information could be integrated so I could know how neurons responded to each visual stimulus as it was shown, how the mouse responded behaviourally to the stimuli, and to ensure reward dispense for correct response to visual stimuli during the training period. I used a 3-PC setup which involved various hardware components to achieve this. The setup for control of the visual stimulation and behavioural part of the experiment was generally based on the Rigbox setup described by Burgess *et al.* (2017). The setup for the imaging part of the experiment was generally based on that indicated for use of ScanImage r4.2 software (Pologruto, Sabatini and Svoboda, 2003).

The 3 PCs used in the setup were named VS PC, 2P PC, and Master PC. The 2P PC controlled 2-photon image acquisition through the microscope objective focused on V1b. The Master PC determined which visual stimuli were to be presented, set the experiment name based on the animal's identifier (provided manually), and controlled time-synced initiation of all parts of the experiment by simultaneous sending of User Datagram Protocol (UDP) signals to the VS and 2P PCs. On receiving the start signal from the Master PC, the VS PC started sampling data from associated DAQ hardware and generated visual stimuli to be presented during the experiment. Through interaction with DAQ hardware, the VS PC was able to record the order and timings of visual stimuli shown in the experiment, control reward-dispense, record the timings of reward dispense, sample information regarding steering wheel position with associated timestamps, and collect timestamps for 2-photon imaging frames. At the end of the experiment, the VS PC generated a data file containing information regarding behavioural, stimulus and imaging data collected during the experiment, alongside associated data sampling timestamps. This involved the use of the time-syncing 'timeline' function of Rigbox (Burgess *et al.*, 2017). On receiving the UDP signal from the Master PC, the 2P PC started 2-photon image acquisition via ScanImage (Pologruto, Sabatini and Svoboda, 2003) software, which controlled DAQ hardware which interacted with the electronic control unit (ECU) of the THORLABS B-SCOPE 2-photon imaging hardware used in this experiment.

The hardware used in this experiment is detailed in the "Hardware" subsection of this appendix. Hardware wiring is as described in subsection "Hardware wiring". The software used in this experiment is detailed in the subsection "Software". The command flow between hardware in this experiment is as shown in "Hardware command flow".

A power outage during training of the mice for the pilot experiment resulted in equipment malfunction and failure. A power surge within the ECU of the 2-photon microscope rendered the equipment unusable for several months as a like-for-like replacement of the ECU was no longer available. Further damages to the microscope optics occurred also. The 2-photon associated PC (2P PC) was also damaged in the power outage. Equipment failure occurred before mice had finished behavioural training. The experiment was therefore unsuccessful, and no useful data was recorded. The equipment was overhauled, and the experiment was redesigned and then completed as described in chapter 1. Details of the overhaul, the final experiment setup, codes, and how to repeat the experiment described in chapter 1 is provided in the second half of this appendix.

List of hardware used:

Optics:

Table S1 Optics for original experiment setup:

General description	**Name**	**Brand**	**Details**
Resonant scanner	B-SCOPE	THORLABS	Single-package multiphoton resonant scanner
Resonant scanner associated optics	Appropriate for B-SCOPE setup	THORLABS	Collective optics of B-SCOPE package
Resonant scanner associated power control unit	ECU	THORLABS	Part of B-SCOPE package
Pockels cell control unit	302-RM	Conoptics	linear HV differential amplifier
Pockels cell	350-380	Conoptics	Phase modulator
Objective	LWD 16x0.8W DIC N2	Nikon	Water-immersion objective
Photomultiplier tube (PMT)	7422pa-40	Hamamatsu	Connected to B-SCOPE-type THORLABS amplifiers (green channel fitted with filter of excitation/emission wavelengths: 525/550nm)
PMT	7422pa-40	Hamamatsu	Connected to B-SCOPE-type THORLABS amplifiers (red channel fitted with filter of excitation/emission wavelengths: 607/670nm)
Laser	Chameleon	Coherent	Controlled by Separate Control unit- part of chameleon package

NI boards and associated hardware for experiment:

Table S2 NI boards and associated hardware for original experiment:

General description	**Name**	**Brand**	**Details/other**
Rack-mount connector accessory for E/M series DAQ device	Bayonet-Neill-Concelman (BNC)-2090A	National Instruments	Name: Dev1 VS
Rack-mount connector accessory for E/M series DAQ device	BNC-2090A	National Instruments	Name: SI4
Rack-mount connector accessory for E/M series DAQ device	BNC-2090A	National Instruments	Name: SI4 2
PC-related DAQ card	PCIe-6321	National Instruments	Connects SI4 2 to 2P PC
PC-related DAQ card	PCIe-6323	National Instruments	Connects Dev1 VS to VS PC
PC-related DAQ card	PCIe-6321	National Instruments	Connects ECU to 2P PC
Steering wheel	LEGO parts 86652 and 32019	LEGO	
Rotary encoder for steering wheel	05.2400 incremental encoder	Kubler	Shaft encoder
Reward dispense vale	161T011	Neptune Research	Solenoid pinch valve which controls release of reward
Custom-Made Mouse holder			
LCD screen	B2080HS	Iiyama	Used for presentation of visual stimuli. Associated with VS PC. Width × height: 26 × 47 cm^2

PCs:

Table S3 details of PCs used in original setup:

Name	**Details**	**Brand**	**Storage**	**Source**	**RAM**	**VRAM**	**Processor**	**DAQ port**

					(GB)			
2P PC	2P-associated PC. 2 DAQ card ports. 32GB RAM. 2TB SSD. Intel i8.	HP	2TB SSD	Thorlabs	32	NA	Intel i8	2x PCIe6321
VS PC	Visual Stimulus Generation PC. Acquires timestamps for all data input.	Stone	1TB SSD	Cardiff University	16	8	Intel i6	PCIe6323
Master PC	Specify visual stimuli and start experiment	Stone	1TB SSD	Cardiff University	8	NA	Intel i6	NA

RAM is Random Access Memory.

VRAM is Video RAM.

Wiring of hardware:

Much of the wiring was based on that suggested for ScanImage r4.2 setup (Pologruto, Sabatini and Svoboda, 2003). ScanImage is now a paid-for software, and information regarding the r4.2 version of the software (previously free) is no longer available online. The wiring has therefore been described below.

NI 2090A boards and the ECU were rack-mounted for ease of setup. The connections between PCs and hardware are all specified below. Please refer to the BNC2090A user manual for a visual reference for sockets referred to in this setup. https://www.ni.com/docs/en-US/bundle/bnc-2090a-feature/resource/372101a.pdf Please refer to the B-SCOPE user guide for a visual reference of the ECU sockets referred to in this setup. This is available on request from THORLABs.

BNC Connections:

Table S4 BNC Connections used in original experiment setup:

Input device	**Input socket**	**Output device**	**Output socket**	**Notes**
Dev1	AI2	SI4-2	AI0	

Dev1	AI3	SI4-2	AO0	
Solenoid Valve	NA	Dev1	AI0	
Dev1	USER2	SI4	USER1	Shared
Dev1	USER2	ECU	Frame Trigger Output	Shared
ECU	Tigger input	SI4	PFI0	
SI4	USER1	ECU	Frame trigger output	
SI4	USER2	ECU	Line trigger output	

68-pin PCIe connections:

Dev1 VS→ PCIe-6323→ VS PC

SI4-2→PCIe-6321→2P PC

ECU→PCIe-6321→2P PC

PINOUT connections:

Table S5 PINOUT connection details for original experiment setup:

Input device	Input socket	Output device	Output socket
Dev1	+5 (USER2)	Rotary encoder	Brown
Dev1	PFI3 (USER2)	Rotary encoder	Gray
Dev1	PFI10 (USER2)	Rotary encoder	Green
Dev1	DGND (USER2)	Rotary encoder	White
Dev1	PFI8	Dev1	USER2
SI4-2	USER1	SI4-2	PO0
SI4-2	PFI3	SI4-2	USER2
SI4-2	PFI2	SI4	PFI2
SI4-2	PFI3	SI4	PFI3
SI4	PFI3	SI4	USER2
SI4	PFI2	SI4	PO0
SI4	PFI4	SI4	USER2

Other connections:

Table S6 Other connections between devices used in original experiment setup:

Input device	Input socket	Output Device	Output socket
2P PC	PMT	ECU	PMT
ECU	Line trigger o	2P PC	Line trigger input
2P PC	Line trigger i	ECU	Line trigger output

List of software used:

VS PC:

Table S7 List of PC software used in original experiment for VS PC:

Type	**Software**	**Version**	**Details**	**Reference**
Operating system	Windows	7		
DAQ software	NI DAQmx	4.2	For reading data from DAQ cards	
MATLAB	MATLAB	2013b	Used to write all experiment codes	
Daq toolkit	Data acquisition toolkit	Correct for 2013b	Used to obtain reading from DAQ cards in MATLAB	
Experiment time sync and control software	Rigbox	2013	Used to time-sync all data collected in the experiment, and also control reward dispense	(Burgess *et al.*, 2017)
Visual Stimulus Generation	Psychtoolbox 3	2013	Used to generate all visual stimuli in the experiment	(Kleiner *et al.*, 2007)

2P PC:

Table S8 List of PC software used in original experiment for 2P PC:

Type	**Software**	**Version**	**Details**	**Reference**
Operating system	Windows	7		
DAQ software	NI DAQmx	4.2	For reading data from DAQ cards	
MATLAB	MATLAB	2013b	Used to run ScanImage4 for control of 2-photon equipment	
2-Photon image acquisition software	ScanImage	R4.2	Used to control scanmage4 in a time-synced way	(Pologruto, Sabatini and Svoboda, 2003)

Daq toolkit	Data acquisition toolkit	Correct for 2013b	Used to obtain reading from DAQ cards in MATLAB	

Master PC:

Table S9 List of PC software used in original experiment for Master PC:

Type	**Software**	**Version**	**Details**
Operating system	Windows	7	
MATLAB	MATLAB	2013b	Used for control of experiment
Experiment Control	bGUI	1	Home-made code written by Adam Ranson for time-synced starting of data acquisition on 2P and VS PCs

Command flow between hardware:

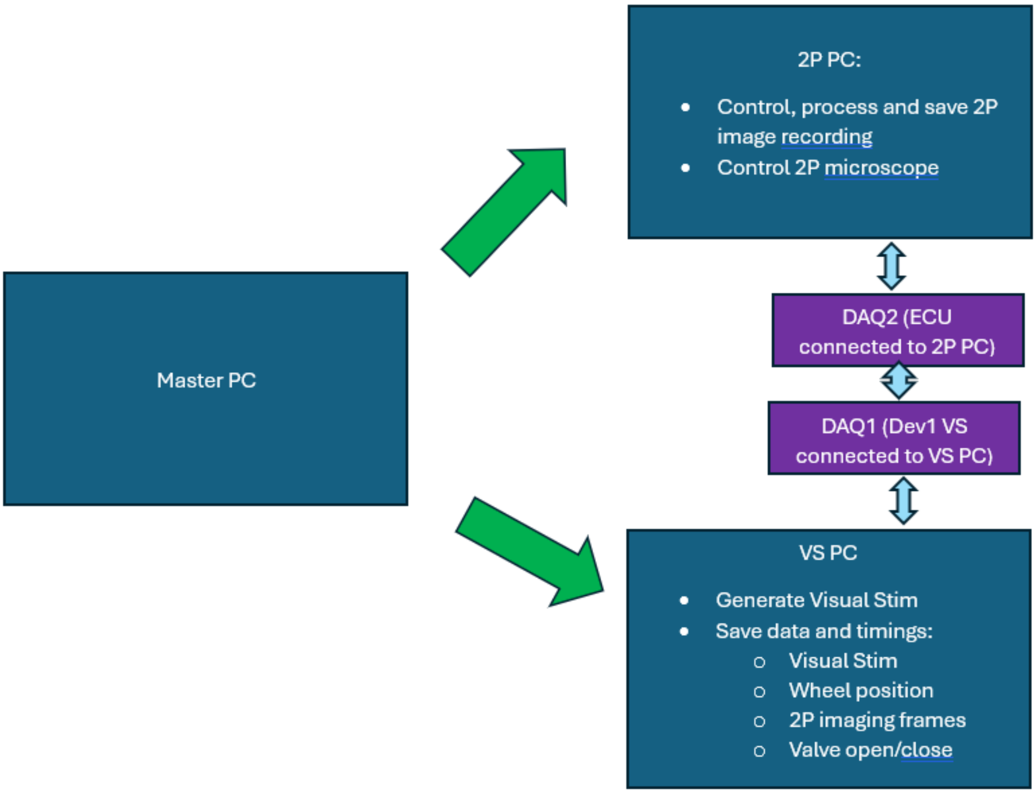

Figure S2 Master PC sends UDP signals (green) to start experimental procedures controlled by the 2P and VS PCs. The 2P PC interacts with the ECU-related DAQ, which reads and processes 2P imaging information, but also controls the ECU of the 2P microscope (not shown). The 2P works to control, process, and save 2P image recordings. The VS PC generates the visual stimuli on receiving input from the Master PC, but also interacts with the DAQ entitled Dev1 VS to sample data and store timestamps for each sample for visual stimuli, wheel positional information, valve voltage outputs (open/closed; 5V/0V). DAQ1 and DAQ2 interact such that the VS PC receives timestamps for 2P imaging frames. All interactions shown in aqua are via hard-wired interfaces, interactions shown in green are UDP signals across an internal network. Devices shown in dark blue are PCs. Devices shown in purple represent DAQ cards and associated hardware.

Optics setup:

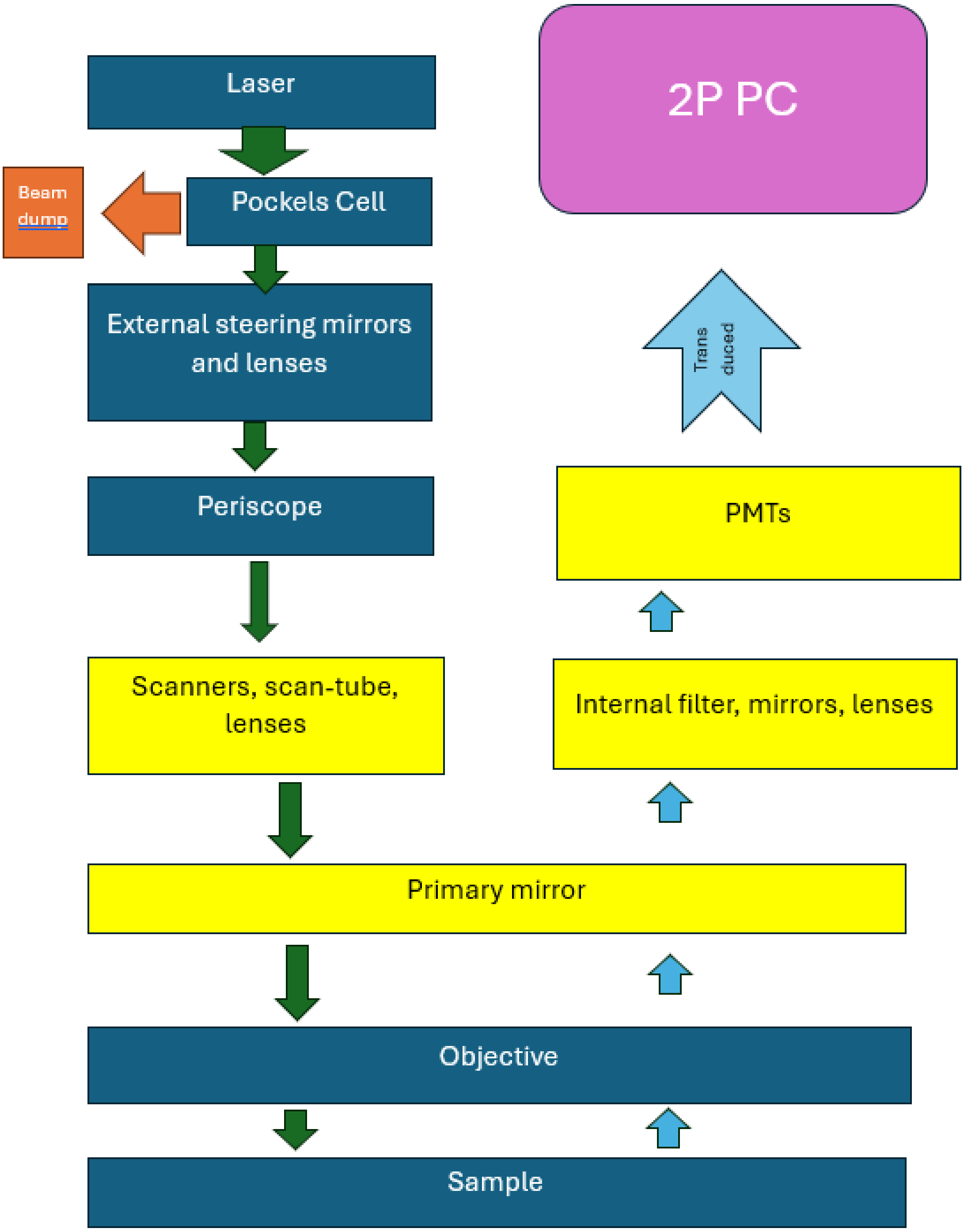

Figure S3 Optics setup schematic. Green arrows show the 2 photon laser pulses coming from the laser to the sample (V1b). Blue arrows show the GCaMP6f emissions from the sample (V1b), and the path of the emitted light to the PMTs (photo multiplier tubes) before transduction to the electrical signal, read by the 2P PC. The orange arrow shows the fraction of the laser beam that is dumped after the laser beam passes through the Pockel's cell. All boxes in blue show optics components which were not controlled by the THORLABS ECU (electronic control unit) and were stand-alone pieces of equipment. Boxes in yellow show the components of the optics *setup which were controlled by the ECU. The orange box shows the beam-dump. The purple box indicates the 2P PC. Note that the signal from the PMTs must be amplified, transduced, and read through the NI PCI component before being able to be read into the 2P PC.*

Overhaul:

Malfunctioning equipment was troubleshooted and overhauled by myself, other lab members, and by the Thorlabs support team. See the “Contributions” subsection of this appendix for full details.

Hardware malfunctions were addressed first, as these were most obvious at the time of experiment failure. Troubleshooting indicated that the power supply unit for the PMT within the ECU was malfunctioning. The ECU was returned to Thorlabs for replacement. No like-for-like replacement was possible, so ECU2 hardware was modified and placed into the shell of an ECU, which effectively functioned as a standard ECU. B-SCOPE associated optics were also badly misaligned following troubleshooting. Laser alignment was completed by myself, under the direction of Diego Sangineto of Thorlabs. Internal optics within the periscope of the B-SCOPE microscope were found to be misaligned. A replacement periscope was purchased from Thorlabs.

The 2P PC was found to have hard-drive failure, and required replacement. Cardiff University further required all network-connected PCs (including the VS and Master PCs) to be updated to Windows 10. The 2P PC was replaced by Thorlabs, and setup at Cardiff University. All PCs were updated to run on Windows 10 operating system.

Running previous experimental software in compatibility mode on the PCs was not feasible due to processing constraints of the hardware. All PCs required software upgrades. NI MAX software was used in place of NI DAQmx software (auto installed with DAQ device drivers). MATLAB 2022a was installed in place of MATLAB 2013b (MATLAB 2013b is not Windows 10 compatible) on all PCs. MATLAB 2022a could not be used to run the free version of ScanImage (r4.2, Pologruto, Sabatini and Svoboda, 2003), and so the 2P PC required new software for 2-photon image acquisition. Other issues with the updated data acquisition toolkit package for MATLAB also prevented us from being able to use Rigbox software for collection of timestamps for sampled data on the VS PC (Burgess *et al.*, 2017). This meant I was unable to generate a datafile holding all behavioural, imaging and stimulus information timestamped in a way where the information could be used to understand how the mouse responded to each stimulus. Furthermore, UDP communications could no longer be initiated using MATLAB via previously used communications functions.

It was clear that software changes were required on all PCs so I could collect data needed for the completion of the experiment, to obtain CSFs for the mice. I estimated that the required software changes would leave me with insufficient time to complete the behavioural training required to measure behaviourally defined CSFs for each mouse. I decided to omit behavioural training and recording of behavioural responses in the final experiment. Therefore, I only needed to track visual stimulus presentation timings, collect 2-photon image recordings from V1b, and collect timestamps of each 2-

photon imaging frame in such a way that I could know which frame corresponded to the presentation of each stimulus.

I wrote codes for the Master PC which allowed us to be able to: a) generate an appropriate experimental name from a manually input animal identifier code (in form AAAA123); b) send and receive UDP signals to start experiment data acquisition; and c) set the experiment parameters.

I designed and wrote codes for the VS PC, such that it could receive a UDP input from the Master PC, relay this UDP signal to the 2P PC, generate visual stimuli (by use of PTB3 MATLAB package; Kleiner *et al.*, 2007) and sample timestamps for visual stimulus presentations, but also sample timestamps of the first 200 frames of 2-photon image recording. These frames were sampled correct to the VS PC internal clock.

I set up the 2P PC such that I could use it to collect 2-photon image recordings, but also collect timestamps from each frame correct to the 2P PC internal clock. ThorImage 4.1.2021.9131 and ThorSync 4.1.2020.1131 software were acquired from THORLABs on request. These were installed on the 2P PC and set up by myself with help from Thorlabs. ThorImage software was used to control 2-photon hardware, but also to collect 2-photon image recordings. ThorSync software was used to collect timestamps of each image frame, correct to the internal clock on the 2P PC. With the assistance of a contracted software developer, I produced an app which could receive UDP signals from the VS PC which would then trigger ThorImage software to begin 2-photon image recording 5 seconds before visual stimulus presentation was to begin. This software was named “ThorClient”. ThorSync software was started manually before the Master PC was set to start the experiment.

Timestamps of the first 200 frames of the 2-photon image recording were collected by the VS PC. These timestamps could be compared to those measured by the 2P PC using ThorSync software. This allowed calibration of the timestamp data collected on the 2P PC such that I could obtain timestamps for all frames of the 2-photon image recording correct to the VS PC internal clock. The VS PC internal clock was also used to obtain timestamps for when visual stimuli were presented, and when that stimulus presentation ended. This timestamp calibration was completed using custom-made data processing codes post-hoc. Timestamps for only the first around 200 frames of the 2-photon image recording (typically the first 20 seconds of the recording) could be collected on the VS PC, due to limited functionality in the NI data acquisition toolkit available for MATLAB 2022a.

Data processing codes previously used in our lab, originally written by Dr Adam Ranson, were rewritten to accept the data generated by the new experimental setup. This data was in a different format due to the change in software and timestamp collection methods used for the new vs the original experiment. Much of the processing methodology was unchanged from that previously used in our lab (Ranson, 2017; Broom *et al.*, 2022; Craddock *et al.*, 2023).

The result of the overhaul was that 2-photon microscope resumed functionality and could be used in experiments which involve recording visual stimulus evoked neuronal responses in the cortex. Behavioural elements involved in the pilot experiment could easily be included by simple modification of my codes, however, this would involve time-consuming animal training so was omitted in the experiment detailed in chapter 1. The overhaul allowed me to image V1b of TS2Neo and WT mice viewing stimuli of varying SFs and contrasts, to generate a CSF based on the responses of neurons in L2/3 of V1b. This meant that I could compare CSFs between mice of differing genotypes. This experiment is described in chapter 1.

The setup for the experiment described in chapter 1 is detailed in the subsection “Final experiment described in chapter 1” below. All codes written for data acquisition during the experiment, and those used to process the data obtained to generate the CSF described in chapter 1 are available on GitHub. Links to repositories are provided as appropriate.

Final experiment described in chapter 1:

Overview of experiment:

My aim was still to explore how the TS2 mutation impacts CSF in TS2Neo mice. In this experiment I used the overhauled 2-photon imaging setup to measure the CSFs of V1b neurons from TS2Neo and WT mice. I compared these neuronal CSFs to explore the impact of genotype on this visual processing property.

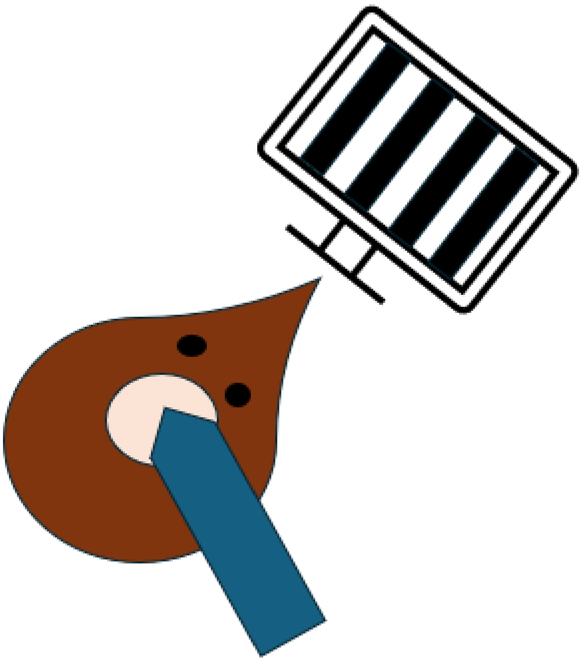

Figure S4 Image showing mouse (brown) positioned in front of an LCD screen on which gratings stimuli are presented, with a microscope objective (blue) focused on a cranial window (pink) over V1b of the mouse. Stimuli were presented to the mouse using the LCD screen while 2-photon recordings of GCaMP6f-labelled neurons were taken through the microscope objective (blue), which was focused through the cranial window (pink) at L2/3 of V1b of the mouse brain throughout this experiment.

Figure S4 shows the overview of the final experiment setup. The mouse was positioned on a treadmill (not shown) on which the mouse was freely able to run throughout the experiment. In front of the mouse was an LCD screen on which visual stimuli, which consisted of gratings bars were shown. As in the original experiment, stimuli of SFs across the range detectable by mice were presented. Stimuli of each of the 7 SFs selected were shown at one of 6 contrasts between 100 and 3.4% (decreasing exponentially). The objective, attached to the 2-photon microscope, was focused through the cranial window onto GCaMP6f-labelled neurons of L2/3 of V1b in the mouse brain. The optical setup was similar to that described by Craddock *et al.* (2023). In this experiment, I recorded neuronal responses to visual stimuli of varying contrasts and spatial frequencies to generate a neuronal CSFs for each mouse. Neuronal CSFs were compared by genotype, while accounting for between-animal variance.

During the experiment, I collected 2-photon image recordings, timestamps of 2-photon image recording frames, and timestamps for visual stimulus presentation. This information was collected by the VS and 2P PCs. Integration of the data to understand neuronal responses to each visual stimulus was performed post-hoc. This was required so I could compare responses of each cell to stimuli of each SF and contrast, to obtain a CSF.

I, again, used a 3-PC setup to achieve my aim. The PC names were unchanged (VS PC, Master PC, 2P PC). The Master PC determined which visual stimuli were to be presented, set the experiment name based on the animal's identifier (provided manually), and initiated the start of the experiment by sending a UDP signal to the VS PC. On receiving the start UDP signal from the Master PC, the VS PC sent a UDP start signal to the 2P PC. The 2P PC, already set to sample 2-photon imaging frames, received this signal and started image acquisition using ThorImage software. The VS PC also sampled the first 200 frames of the 2-photon image recording, before beginning to generate and present visual stimuli as part of the experiment. Timestamps of visual stimulus presentations were collected by the VS PC. At the end of the experiment, the VS PC generated a datafile containing information regarding stimulus data, stimulus timings, and timings for the first 200 frames of the 2-photon imaging correct to the VS PC internal clock. The 2P PC held the 2-photon image recording, and all timeframes of the 2-photon image recording correct to the 2P PC internal clock. Comparison of timestamps of the first 200 frames of 2-photon imaging collected from the VS and 2P PCs allowed post-hoc calibration of timestamp data, such that I could generate a single file holding timestamps for visual stimulus presentation and imaging frames correct to just one PC, the VS PC. Using this integrated metadata file alongside the 2-photon image recording, I could measure single neuron responses to each visual stimulus type.

Two-photon imaging data was acquired using the overhauled B-SCOPE microscope, and its associated optics setup. The optics setup was relatively unchanged from that used in the original experiment, and therefore no dedicated subsection is provided here regarding the optics setup. For details on how the optics setup was changed during the equipment overhaul, please refer to the subsection “Overhaul”. The 3 PCs were interconnected with experiment hardware, as described in the subsection “Hardware”. The wiring and interconnection between the hardware is described in the subsection “Hardware wiring”. The software used in this experiment is as described in the subsection “Software”. The flow of commands between hardware involved in the experiment is shown in the subsection “Hardware command flow”. Instructions for setup of PCs and codes required to run the experiment detailed in chapter 1 are provided in subsection “Setting up and running CSF experiment described in chapter 1”. Instructions for setup and running of the processing pipeline required to obtain CSF data from the raw experiment files is provided in subsection "Instructions for setting up and running CSF experiment processing pipeline”. General instructions on how to analyse the processed data are provided in subsection “Instructions for analysis of pre-processed files output from the experiment”.

List of hardware used:

Optics:

Table S10 Optics setup for final experiment:

General description	**Name**	**Brand**	**Details**
Resonant scanner	B-SCOPE	THORLABS	Single-package multiphoton resonant scanner
Resonant scanner associated optics*	Appropriate for B-SCOPE setup	THORLABS	Collective optics of B-SCOPE package
Resonant scanner associated power control unit*	ECU 2 hardware board custom-wired into an ECU shell. This is read into THORIMAGE as a standard ECU.	THORLABS	Part of B-SCOPE package
Pockels cell control unit	302-RM	Conoptics	linear HV differential amplifier
Pockels cell	350-380	Conoptics	Phase modulator
Objective	LWD 16x0.8W DIC N2	Nikon	Water-immersion objective
PMT	7422pa-40	Hamamatsu	Connected to B-SCOPE-type THORLABS amplifiers (green channel fitted with filter of excitation/emission wavelengths: 525/550nm)
PMT	7422pa-40	Hamamatsu	Connected to B-SCOPE-type THORLABS amplifiers (red channel fitted with filter of excitation/emission wavelengths: 607/670nm)
Laser	Chameleon	Coherent	Controlled by Separate Control unit- part of

			chameleon package

*denotes equipment that was replaced and/or modified during equipment overhaul. Details are provided in the "Overhaul" subsection of this appendix.

NI boards and associated hardware for experiment:

Table S11 NI boards and associated hardware for final experiment:

General description	**Name**	**Brand**	**Details/other**
Rack-mount connector accessory for E/M series DAQ device	BNC-2090A	National Instruments	Name: Dev1 VS
Rack-mount connector accessory for E/M series DAQ device	BNC-2090A	National Instruments	Name: SI4
Rack-mount connector accessory for E/M series DAQ device	BNC-2090A	National Instruments	Name: SI4 2
PC-related DAQ card	PCIe-6321	National Instruments	Connects SI4 2 to 2P PC
PC-related DAQ card	PCIe-6323	National Instruments	Connects Dev1 VS to VS PC
PC-related DAQ card	PCIe-6321	National Instruments	Connects ECU to 2P PC
Custom-made mouse treadmill**			
LCD screen	B2080HS	Iiyama	Used for presentation of visual stimuli. Associated with VS PC. Width × height: 26 × 47 cm^2

** This replaced the steering-wheel setup used in the original experiment. No rotary encoder etc was required, as behavioural responses were no longer recorded. Reward valve was not required either.

PCs:

Table S12 PCs used for final experiment:

Name	**Details**	**Brand**	**Storage**	**Source**	**RAM (GB)**	**VRAM**	**Processor**	**DAQ port**

2P PC*	2P-associated PC. 2 DAQ card ports. 32GB RAM. 2TB SSD. Intel i8.	HP	2TB SSD	Thorlabs	32	NA	Intel i8	2x PCIe6321
VS PC	Visual Stimulus Generation PC. Acquires timestamps for all data input.	Stone	1TB SSD	Cardiff University	16	8	Intel i6	PCIe6323
Master PC	Specify visual stimuli and start experiment	Stone	1TB SSD	Cardiff University	8	NA	Intel i6	NA

Wiring of hardware:

The wiring between hardware within this experiment was unchanged from that used in the original experiment. The rotary encoder and reward dispense valve could be removed from the setup (these are shown in red). The connections between hardware in the final experiment setup are all specified below.

BNC Connections:

Table S13 BNC connections used in final experiment:

Input device	**Input socket**	**Output device**	**Output socket**	**Notes**
Dev1	AI2	SI4-2	AI0	
Dev1	AI3	SI4-2	AO0	
Solenoid Valve	NA	Dev1	AI0	
Dev1	USER2	SI4	USER1	Shared
Dev1	USER2	ECU	Frame Trigger Output	Shared
ECU	Tigger input	SI4	PFI0	
SI4	USER1	ECU	Frame trigger output	
SI4	USER2	ECU	Line trigger output	

68-pin PCIe connections:

Dev1 VS→ PCIe-6323→ VS PC

SI4-2→PCIe-6321→2P PC

ECU→PCIe-6321→2P PC

PINOUT connections:

Table S14 PINOUT connections used in final experiment:

Input device	**Input socket**	**Output device**	**Output socket**
Dev1	+5 (USER2)	Rotary encoder	Brown
Dev1	PFI3 (USER2)	Rotary encoder	Gray
Dev1	PFI10 (USER2)	Rotary encoder	Green
Dev1	DGND (USER2)	Rotary encoder	White
Dev1	PFI8	Dev1	USER2
SI4-2	USER1	SI4-2	PO0
SI4-2	PFI3	SI4-2	USER2
SI4-2	PFI2	SI4	PFI2
SI4-2	PFI3	SI4	PFI3
SI4	PFI3	SI4	USER2
SI4	PFI2	SI4	PO0
SI4	PFI4	SI4	USER2

Other connections:

Table S15 Other connections used in final experiment:

Input device	**Input socket**	**Output Device**	**Output socket**
2P PC	PMT	ECU	PMT
ECU	Line trigger o	2P PC	Line trigger input
2P PC	Line trigger i	ECU	Line trigger output

List of software used:

VS PC:

Table S16 Software used on VS PC for final experiment:

Type	**Software**	**Version**	**Details**	**Reference**
Operating system*	Windows	10		
DAQ software*	NI MAX	18.5	For reading data from DAQ cards	
MATLAB*	MATLAB	2022a	Used to write all experiment codes	
Daq toolkit*	Data acquisition toolkit	Correct for 2022a	Used to obtain reading from	

			DAQ cards in MATLAB	
Experiment time sync and control scripts**	Scripts only	NA	Collects timestamps regarding visual stimuli, collects timestamps for the initial ~200 frames of 2 photon image recording	
Visual Stimulus Generation*	Psychtoolbox 3 (PTB3)	2022	Used to generate all visual stimuli in the experiment	(Kleiner *et al.*, 2007)

*indicates where software was updated during the overhaul. **indicates where software was replaced/rewritten for use in overhaul.

2P PC:

Table S17 Software used on 2P PC for final experiment:

Type	**Software**	**Version**	**Details**
Operating system*	Windows	10	
DAQ software*	NI MAX	18.5	For reading data from DAQ cards
2-Photon image acquisition software*	ThorImage	4.1.2021.9131	Used for 2-photon image acquisition and control of 2-photon equipment.
2-photon timestamp acquisition software*	ThorSync	4.1.2020.1131	Used to record timestamps of 2-photon image frames later used to align 2-photon recordings to visual stimulus presentation timestamps recorded on the VS PC.
Communications and imaging control app**	ThorClient	1.7	GUI for reading UDP inputs from VS PC and triggering 2-photon image acquisition

*indicates where software was updated during the overhaul. **indicates where software was replaced/rewritten for use in overhaul.

Master PC:

Table S18 Software used on Master PC for final experiment:

Type	Software	Version	Details
Operating system*	Windows	10	
MATLAB*	MATLAB	2022a	Used for control of experiment
Experiment Control scripts**	Scripts Only	NA	Home-made code used to set visual stimulus parameters, and start the time-synced experiment across the distributed PC network

*indicates where software was updated during the overhaul. **indicates where software was replaced/rewritten for use in overhaul.

Command flow between hardware:

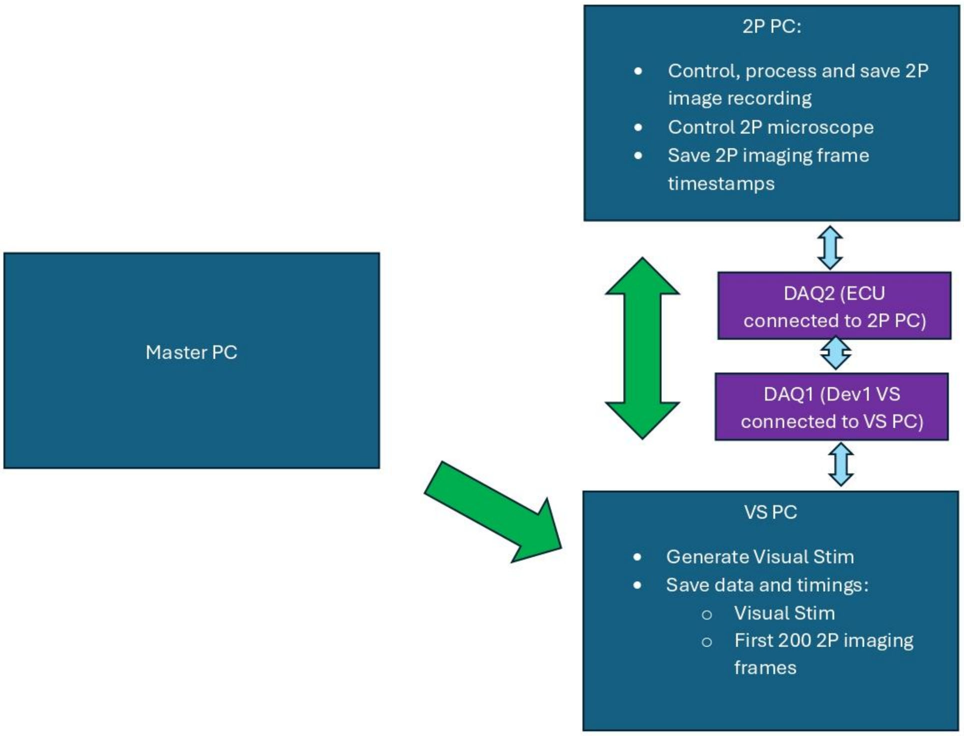

Figure S5 ThorSync software is started to allow sampling of any 2-photon image recording frame timestamps on the 2P PC, as recorded on the ECU-related DAQ2. The Master PC sends UDP *signal (green) to VS PC to start the experiment. The VS PC interacts with DAQ hardware (Dev1 VS, DAQ1) to start a listener to allow the recording of the timestamps of the first 200 2-photon image frames. The 2P PC then interacts with ECU-related DAQ2 to start 2-photon image acquisition by control of the 2-photon microscope (not shown). The VS PC then generates visual stimuli shown in the experiment. Timings of visual stimulus presentation, and timestamps of the first 200 2-photon imaging frames are collected on the VS PC, correct to the VS PC internal clock. Timings of all 2-photon imaging frames and 2-photon image recording files are stored on the 2P PC, correct to the 2P PC internal clock. PCs are shown in dark blue. DAQ hardware is shown in purple. UDP signals are shown in green, with the arrow showing the direction of signal transmission. Aqua arrows indicate hardware interaction.*

Setting up and running CSF experiment described in Chapter 1:

The experiment described in chapter 1 involves open-source software. The details of how to set up the experiment, including obtaining and installing the required software and code are provided here. Instructions on how to run the experiment are also provided, as are details on how the experiment can be adapted and changed.

Instructions for experiment setup:

1. Obtain all hardware described in the “Hardware” subsection of this appendix. Note any PCs with similar specifications should be able to run this experiment.
2. Align laser path as appropriate (may not be required).
3. Wire-up hardware as indicated in the “Hardware wiring” subsection.
4. Install all software described in the “Software” subsection. On the 3 PCs as indicated.
    a. VS PC:
        i. Install MATLAB software (licence required).
        ii. The data acquisition toolkit is available in the MATLAB toolkits repository.
        iii. NI MAX will be installed on installation of NI drivers.
        iv. Setup your DAQ cards as required (naming etc).
        v. PTB3 code is available online. http://psychtoolbox.org/download
        vi. VS PC codes are available on GitHub https://GitHub.com/craddr/CreateVisStim_VSPC. Please follow all instructions on the GitHub information page to download and change the codes as required for the experiment to run on your PC.
    b. 2P PC:
        i. NI MAX will be installed on installation of NI drivers.
        ii. Setup your DAQ cards as required (naming etc).
        iii. ThorImage and ThorSync software are available on request from THORLABs. Assistance with setup can be provided by THORLABs on request.
        iv. Source code for the ThorClient app is available on GitHub https://GitHub.com/craddr/CSF_2P. Clone the repository to obtain the source code. This app must be built using Visual Studio 2018 app, and the associated .NET PC developer package. To build the

        app, open the ThorClient.sln from rosie-scripts-src-1.7\ThorClient (once cloned from GitHub). It is recommended to make changes to the code indicated on the GitHub information page before building the app. It is recommended to move the app to a sensible location.
    c. Master PC:
        i. Install MATLAB software (licence required).
        ii. Download Master PC code from GitHub (https://GitHub.com/craddr/GenerateStimuli_MasterPC_CSF) and follow information page instructions to change codes and files as required for the experiment to run on your PC.
5. Adjust settings in THORIMAGE software, focusing on sample tissue, until ThorImage software is optimised for your imaging setup.
6. Follow the instructions indicated on the VS PC GitHub page to change the rigConfig.mat file as required for your LCD display screen.
7. Check all GitHub pages to ensure all required code changes have been made, and all codes and dependencies have been added to the MATLAB paths on both VS and Master PCs.

Running the experiment:

1. Set up your imaging equipment. Ensure ECU is on.
2. Open ThorImage, ThorSync and ThorClient on the 2P PC, in that order, and initialise equipment as prompted by the ThorImage software.
3. Visualise GCaMP6f-labelled cortical tissue as required for imaging of neuronal responses using ThorImage software.
4. Ensure the zoom is set to x1, with two-way alignment, and frame averaging is set to 6 cumulative frames (final frame rate 9.6fps).
5. Enter Animal identifier followed by _1 into ThorSync filename (form AAAA123_1). Ensure that the save directory is as appropriate.
6. Ensure that the save directory indicated by ThorImage software is appropriate, and that there is >100GB data empty storage on the drive to which data will be saved.
7. Enter the capture tab of ThorImage, ensure the finite recording is selected, the file type is RAW, and the maximum frame length is sufficiently high that it will not be reached (e.g. 999999999).
8. Click “Start” on ThorClient software.
9. Ensure that the “Remote connection” checkbox of ThorImage is now checked.
10. Start the recording on ThorSync software on the 2P PC.
11. Start MATLAB 2022a on the VS PC.
12. Type “RosieNewlisten” into the MATLAB command-line on the VS PC.
13. Start MATLAB 2022a on the Master PC.
14. Type “rosieProtocol1(animal Identifier, 1, bRosieTesting2023_1) into the MATLAB command-line on the Master PC. AnimalID must be in form: AAAA123, and be the same as that input to the ThorSync software.

The experiment should run as appropriate for the experiment described in chapter 1 of this PhD thesis. The experiment lasts 43 minutes and involves 5 repetitions of 42 different visual stimuli which are presented in a pseudo-random order. Each stimulus is shown for 3 seconds, followed by a 3 second inter-trial interval.

Modifying the experiment:

Should you wish to run a short version of the experiment for troubleshooting reasons or otherwise, this can be achieved. Open the file C:\\Code\pFiles\bRosieTesting2023_1 in MATLAB 2022a. Change Pstate.globalParasVals(24) to the number of repetitions required to run in the experiment.

The experiment can also be changed in other ways. The stimulus can be shown as a small circular patch instead of full screen. The gratings bars can be of a square-waveform The orientation of the grating-stimulus can be changed. The spatial frequences, temporal frequencies, duty, and stimulus contrast can all be changed. The time for which the stimulus is shown, and the inter-trial interval can also both be adjusted. Details on the changes that can be made, and how to make them are given on the GitHub page https://GitHub.com/craddr/GenerateStimuli_MasterPC_CSF.

Use of experiment codes with other imaging methods:

Any other imaging method which involves the use of ThorImage software can be used in place of two-photon imaging in this experiment, so long as:

- Timestamps for image frames can be acquired in a similar manner to that described in this experiment. (trigger output from the imaging control apparatus exists and can be read into the NI DAQ hardware of both 2P and VS PCs in a similar manner to that described in this appendix).
- Imaging is of a sufficiently high rate (at least 5 frames per second).

Adaptation of the experiment to allow for measurement of a behavioural CSF:

Obtain the hardware for the LEGO steering-wheel, the rotary encoder, the custom-made mouse holder, and the reward dispense valve (with tubing).

Complete wiring to the rotary encoder and to the reward dispense valve as indicated for the original experiment setup.

Amend segments of the RosieNewListen.m code on the VS PC to allow for reading of the rotary encoder data. The saveData2 file must be amended to save rotary encoder data. Where the encoder position reaches the threshold value, which was set as 420 in the parameter file bRosieTesting2023_1, a 5V pulse lasting 0.5 seconds should be provided to the reward dispense valve, and reaching the threshold must be noted and timestamped using GetSecs function. Reward delivery must be noted and timestamped using GetSecs function.

Many of the commands required are found already in the RosieNewListen.m code but have been commented out. Behavioural training should involve a protocol similar to that reported by Aguillon-Rodriguez *et al.* (2021). Mice should be trained to respond to stimuli of 100% contrast only. On reaching 80% success rate for each stimulus type, the mice should be tested on their ability to respond to each stimulus at each of the contrasts suggested in this experiment.

Processing experimental data obtained from experiment described in chapter 1:

The data obtained from the experiment described in chapter 1 must be processed before analysis to obtain a neuronal CSF as described in the experiment.

The data obtained from the experiment should be found in an experiment-entitled subdirectory within a parent folder containing experimental files for the animal:

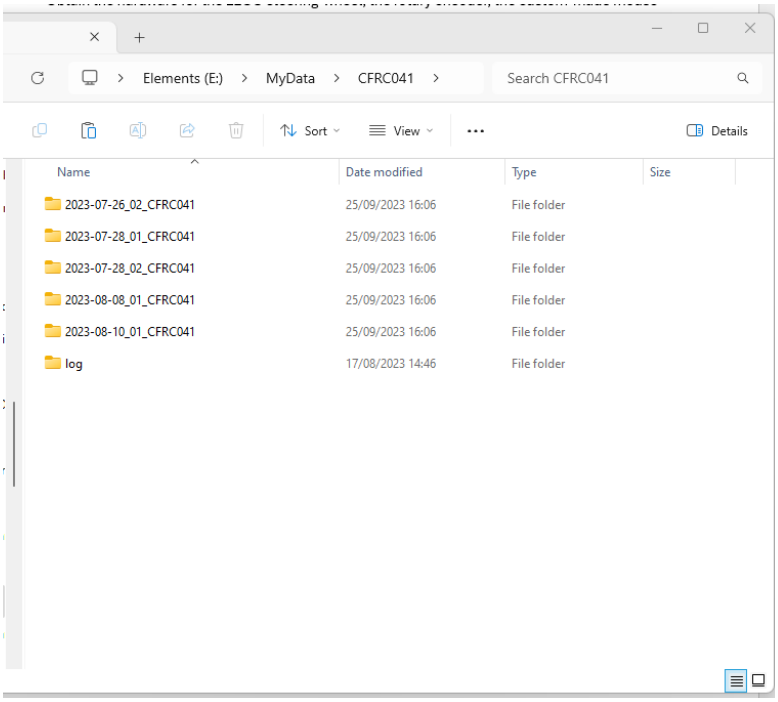

Name	Date modified	Type	Size
2023-07-26_02_CFRC041	25/09/2023 16:06	File folder	
2023-07-28_01_CFRC041	25/09/2023 16:06	File folder	
2023-07-28_02_CFRC041	25/09/2023 16:06	File folder	
2023-08-08_01_CFRC041	25/09/2023 16:06	File folder	
2023-08-10_01_CFRC041	25/09/2023 16:06	File folder	
log	17/08/2023 14:46	File folder	

Figure S6 Example contents of parent directory for experimental animal, containing experiment files.

The experimental directory of interest should contain the following:

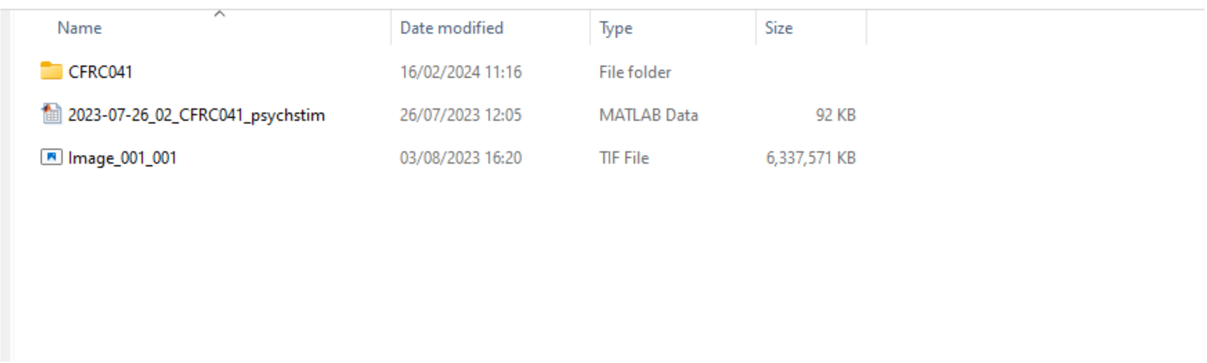

Name	Date modified	Type	Size
CFRC041	16/02/2024 11:16	File folder	
2023-07-26_02_CFRC041_psychstim	26/07/2023 12:05	MATLAB Data	92 KB
Image_001_001	03/08/2023 16:20	TIF File	6,337,571 KB

Figure S7 Example contents of experiment folder.

An image.tif file which contains 2-photon image recording frames.

An experiment _psychstim.mat file which contains timestamp data for the presentation of all visual stimuli during the experiment, and timestamps for the first ~200 frames of the two-photon imaging recording.

A folder which is labelled with the animal's ID, which contains two files. A H5 file containing 2-photon image recording timestamps for every imaged frame of the recording (correct to the 2P PC clock, and to the DAQ card), and an XML settings file which contains timestamp recording meta data.

This data is processed using the pipeline available on GitHub https://GitHub.com/craddr/CSF_AnalysisMod , to produce a table for each experiment which lists the minimum contrast to which each cell was able to respond to stimuli of the specified SFs. This is output as a table which looks as follows:

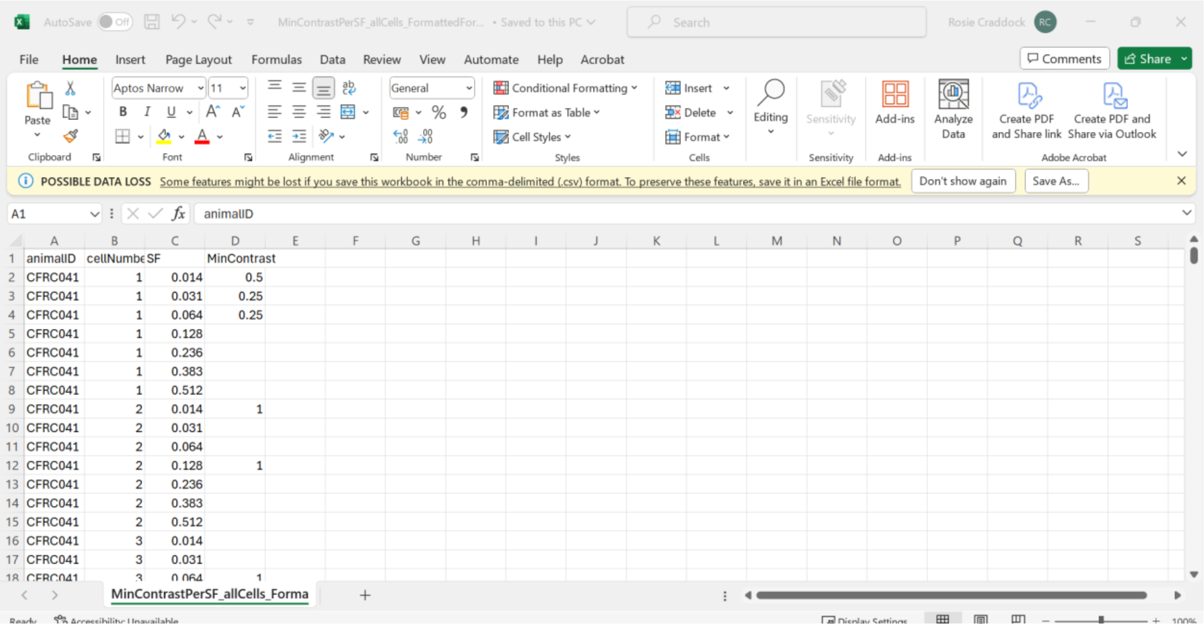

POSSIBLE DATA LOSS Some features might be lost if you save this workbook in the comma-delimited (.csv) format. To preserve these features, save it in an Excel file format.

animalID	cellNumbe	SF	MinContrast
CFRC041	1	0.014	0.5
CFRC041	1	0.031	0.25
CFRC041	1	0.064	0.25
CFRC041	1	0.128	
CFRC041	1	0.236	
CFRC041	1	0.383	
CFRC041	1	0.512	
CFRC041	2	0.014	1
CFRC041	2	0.031	
CFRC041	2	0.064	
CFRC041	2	0.128	1
CFRC041	2	0.236	
CFRC041	2	0.383	
CFRC041	2	0.512	
CFRC041	3	0.014	
CFRC041	3	0.031	
CFRC041	3	0.064	1

Figure S8 Example data frame showing the minimum contrast to which each cell from an animal responded to when presented with visual stimuli of given SFs (in cpd). Empty cells indicate that the cell was not responsive to visual stimuli of that SF.

The data processing pipeline is as shown in the flowchart below:

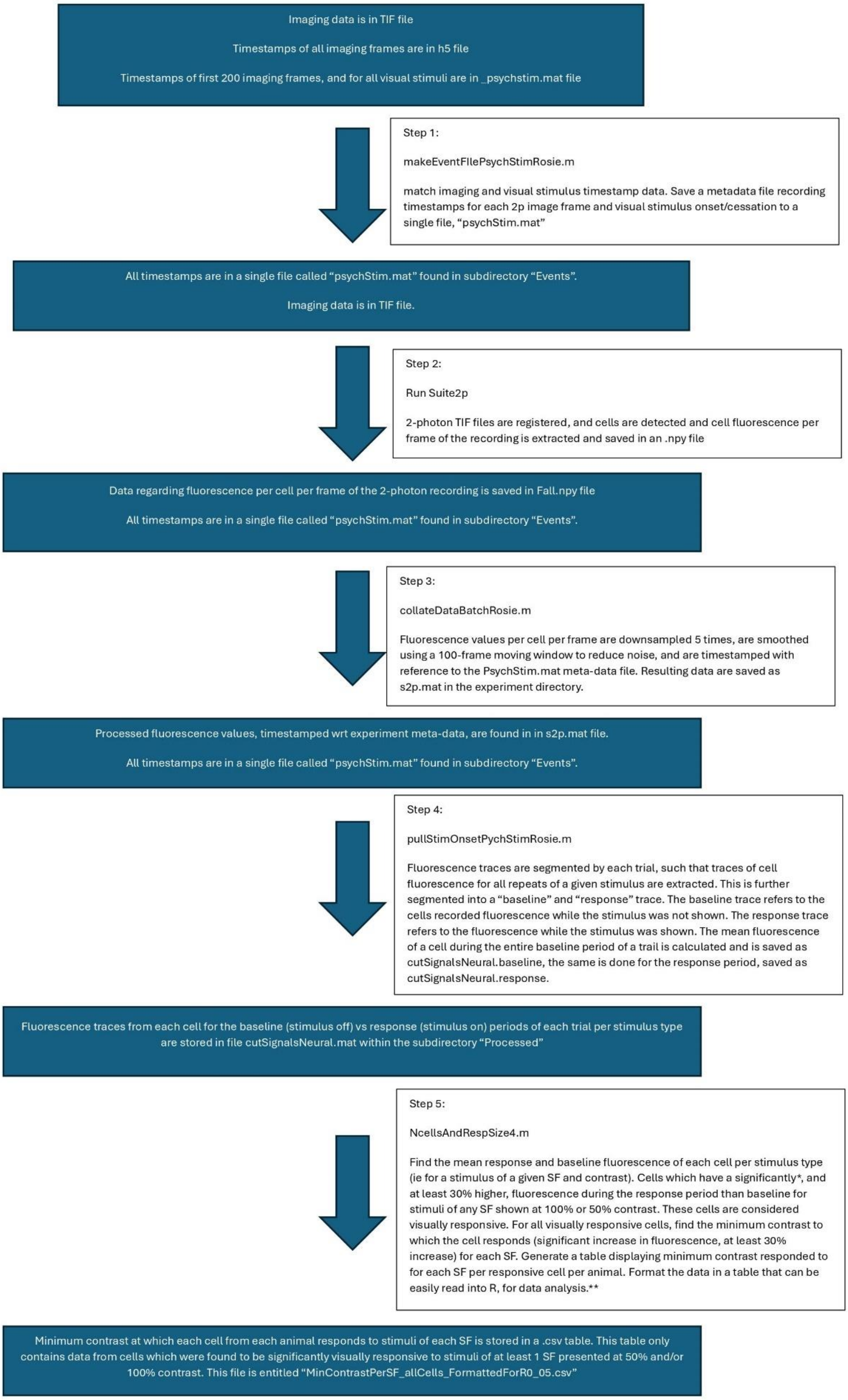

Imaging data is in TIF file

Timestamps of all imaging frames are in h5 file

Timestamps of first 200 imaging frames, and for all visual stimuli are in _psychstim.mat file

Step 1:

makeEventFIlePsychStimRosie.m

match imaging and visual stimulus timestamp data. Save a metadata file recording timestamps for each 2p image frame and visual stimulus onset/cessation to a single file, “psychStim.mat”

All timestamps are in a single file called “psychStim.mat” found in subdirectory “Events”.

Imaging data is in TIF file.

Step 2:

Run Suite2p

2-photon TIF files are registered, and cells are detected and cell fluorescence per frame of the recording is extracted and saved in an .npy file

Data regarding fluorescence per cell per frame of the 2-photon recording is saved in Fall.npy file

All timestamps are in a single file called “psychStim.mat” found in subdirectory “Events”.

Step 3:

collateDataBatchRosie.m

Fluorescence values per cell per frame are downsampled 5 times, are smoothed using a 100-frame moving window to reduce noise, and are timestamped with reference to the PsychStim.mat meta-data file. Resulting data are saved as s2p.mat in the experiment directory.

Processed fluorescence values, timestamped wrt experiment meta-data, are found in in s2p.mat file.

All timestamps are in a single file called “psychStim.mat” found in subdirectory “Events”.

Step 4:

pullStimOnsetPychStimRosie.m

Fluorescence traces are segmented by each trial, such that traces of cell fluorescence for all repeats of a given stimulus are extracted. This is further segmented into a “baseline” and “response” trace. The baseline trace refers to the cells recorded fluorescence while the stimulus was not shown. The response trace refers to the fluorescence while the stimulus was shown. The mean fluorescence of a cell during the entire baseline period of a trail is calculated and is saved as cutSignalsNeural.baseline, the same is done for the response period, saved as cutSignalsNeural.response.

Fluorescence traces from each cell for the baseline (stimulus off) vs response (stimulus on) periods of each trial per stimulus type are stored in file cutSignalsNeural.mat within the subdirectory “Processed”

Step 5:

NcellsAndRespSize4.m

Find the mean response and baseline fluorescence of each cell per stimulus type (ie for a stimulus of a given SF and contrast). Cells which have a significantly*, and at least 30% higher, fluorescence during the response period than baseline for stimuli of any SF shown at 100% or 50% contrast. These cells are considered visually responsive. For all visually responsive cells, find the minimum contrast to which the cell responds (significant increase in fluorescence, at least 30% increase) for each SF. Generate a table displaying minimum contrast responded to for each SF per responsive cell per animal. Format the data in a table that can be easily read into R, for data analysis.**

Minimum contrast at which each cell from each animal responds to stimuli of each SF is stored in a .csv table. This table only contains data from cells which were found to be significantly visually responsive to stimuli of at least 1 SF presented at 50% and/or 100% contrast. This file is entitled “MinContrastPerSF_allCells_FormattedForR0_05.csv”

Figure S9 Flow diagram describing experimental data files collected during the experiment, how they are processed at each stage of the processing procedure and all intermediate file types and *their contents. *significance is tested using Wilcoxon signed-rank methods, with a threshold value of α=0.01.*

Instructions for setting up and running the processing pipeline are found in subsection "Instructions for setting up and running CSF experiment processing pipeline". These are also outlined on the GitHub page https://GitHub.com/craddr/CSF_AnalysisMod.

Instructions for setting up and running CSF experiment processing pipeline:

Setup of data processing pipeline:

On any PC with 8GB+ RAM and 100GB+ hard drive storage, the data processing pipeline can be set up and run.

On such a PC follow the following instructions to set up the data processing pipeline required to process experimental data obtained:

1. Install MATLAB 2022a
2. Clone code from GitHub repository https://GitHub.com/craddr/CSF_AnalysisMod to C:\\Analysis
3. Add C:\\Analysis directory and all subdirectories to MATLAB path.
4. Follow the information file instructions on the GitHub page to change required codes where indicated to direct the codes toward the file in which your data is stored.
5. Install suite2p software by following the online instructions referred to in their GitHub page https://GitHub.com/MouseLand/suite2p.

Running data processing pipeline:

1. Open MATLAB
2. Run "makeEventFilePsychStimRosie.m". When prompted, enter animalID (form AAAA123) and select the appropriate experiment for processing.
3. Open Anaconda3 prompt and run suite2p as per instructions on suite2p GitHub page https://GitHub.com/MouseLand/suite2p.
4. Load the ops file now found in your C:\\Analysis directory. Change this file if using alternative imaging methods, or neuronal activity indicator other than GCaMP6f.
5. Select your experimental TIF in suite2p and run the pipeline. Select cells manually after registration and auto-cell detection. Exit suite2p on completion of cell selection. Exit Anaconda3.
6. In MATLAB, run "collateDataBatchRosie.m". When prompted, enter animalID (form AAAA123) and select the appropriate experiment for processing.
7. In MATLAB, run "pullStimOnsetPsychStim_s2pRosie.m" When prompted, enter animalID (form AAAA123) and select the appropriate experiment for processing.
8. In MATLAB, run "NcellsAndRespSize4.m". When prompted, enter animalID (form AAAA123) and select the appropriate experiment for processing.

To plot response traces for each cell to each stimulus type (optional graphic), then, in MATLAB, run “plotTracesRosie.m”. When prompted, enter animalID (form AAAA123) and select the appropriate experiment for processing. This code will take a long time to run and is greedy with respect to PC resources.

Instructions for analysis of pre-processed files output from the experiment:

To complete analysis of the resulting pre-processed files, the use of R is required. .csv files from all experiments should be collated using the read_csv and rbind functions of the dplyr package. Label data from each animal with the appropriate genotype using the tidyverse package (Wickham *et al.*, 2019). Calculate the log2 inverse of the minimum contrast value to obtain a measure of contrast sensitivity per cell of each animal using base R. Use the ordinal package in R to generate a cumulative link mixed model of contrast sensitivity by Genotype, SF, and Genotype:SF, with animal being taken as a random factor (Christensen, 2023). Use the Anova.clmm function of the RVAideMemoire package in R to test the impact of each term, including genotype terms, on contrast sensitivity (Herve, 2023). Any effect of genotype would indicate that the genotype impacts contrast sensitivity regardless of SF, whereas significant effect of the interaction term would suggest that genotype impacts the CSF. A lack of effect of SF on contrast sensitivity would be a cause for concern. The nagelkerke function of the rcompanion package should be used to test the goodness of fit of the model. I suggest using the Cox and Snell pseudo-R^2 value returned by the function (Mangiafico, 2023). The emmeans and multcomp packages will allow to compare probabilities of a cell being of a specific contrast sensitivity for each specific SF tested, based on genotype, and significance of any such difference (Hothorn *et al.*, 2023; Searle, Speed and Milliken, 2024). Nominal_test and scale_test functions of the ordinal package can be used to test the assumptions of the cumulative link mixed model generated from the dataset (Christensen, 2023). However, these tests can be very conservative, failure of these tests should not lead to the conclusion that the proportional odds assumption of the cumulative link model has been violated. Instead, the failure of these tests should be considered alongside the graphical examination of the fitted vs predicted model values.

Contributions:

Thorlabs replaced the light path periscope, ECU hardware and 2-photon microscope associated PC in the experiment overhaul. The laser path was aligned by myself, under direction of Diego Sangineto of Thorlabs. Troubleshooting of equipment malfunctions involved multiple lab group members including Professor Frank Sengpiel, Dr Bethany Frost, Mrs Fangli Chen, and myself. Codes written in the overhaul and used in the final experiment were written by me. Some codes were based on those written by Chris Burgess used as part of Rigbox software (Burgess *et al.*, 2017). Some codes were based on those written by Dr Adam Ranson, previously at Cardiff University. Some codes were unchanged from the original setup, and therefore had been written by people outside our lab. These include dependent functions written by Kothe (2024), based on those written by Tim Hutt, and functions which were originally included as part of the Rigbox package (Burgess *et al.*, 2017). Professor Frank Sengpiel and Dr Adam Ranson provided advice and support during the overhaul process. The ThorClient application was developed under my direction and were written by an externally contracted freelance software engineer. I later completed minor bug fixes to the ThorClient application software.

Appendix 2: Modelling parameters and equations:

Computational models used in this thesis were based on previously described CA3 neural network models (Ermentrout and Kopell, 1998; Kopell *et al.*, 2010; Betterton *et al.*, 2017). Pyramidal cells and interneurons were modelled as single compartments, with all channels modelled using Hodgkin-Huxley type equations. The ratio of pyramidal cells: PV+ interneurons was adapted for physiological accuracy (Traub and Miles, 1991) to be 100:10, and the L-type calcium channel current of Riz, Braun and Pedersen (2014) was added to the model with maximum conductance, g_{Ca}, set as 1mS/cm^2 (Ermentrout and Kopell, 1998) for modelling experiments described in chapter 4. L-type channel equations were adapted using methods described by Kummer *et al.* (2022) to simulate TS-type mutant channels, and PV+ number was varied to model the effect of TS-related PV+ cell reduction on various electrical properties of the CA3 neural network and of pyramidal cells.

Model parameters specific to each experiment are as stated in the appropriate methods section.

Parameters and equations:

Pyramidal neuron:

Pyramidal cell membrane potential was modelled by equation 1 for cells lacking TS-mutant CaV1.2 channels, or by equation 2 in cells containing both mutant and non-mutant channels.

Equation 1:

$$C\frac{dV}{dt} = I_{Na} + I_K + I_{Km} + I_{Kahp} + I_{CaL} + I_L + I_{syn}$$

Equation 2:

$$C\frac{dV}{dt} = I_{Na} + I_K + I_{Km} + I_{Kahp} + I_{CaL} + \ I_{CaLMut} + I_L + I_{syn}$$

Where capacitance, C=1 µF/cm^2, V is voltage and is measured in mV, t is time, and is measured in seconds, and channel currents, I_x, were measured in pA and were defined by the below equations:

$$I_{Na} = \ g_{Na} m_{\infty}^3(V)h(V - V_{Na})$$

$$I_K = g_K n^4 \ (V - V_k)$$

$$I_{Km} = \ g_{Km} w(V - V_k)$$

$$I_{Kahp} = \ g_{Kahp}\frac{[Ca^{2+}]i}{[Ca^{2+}]i + 1}(V - V_k)$$

$$I_{Ca} = g_{Ca} m_{l\infty} h_l (V - V_{Ca})$$

$$I_{CaMut} = g_{CaMut} m_{lMut\infty} h_{lMut} (V - V_{Ca})$$

$$I_L = g_L (V - V_L)$$

Where all maximum conductances, g_x, have the unit mS/cm^2, and were as listed in the table below:

Table S19 Table listing the values for maximum conductance for each ion channel (mS/cm^2) for pyramidal cells simulated in each condition:

Condition	g_{Na}	g_K	g_{Km}	g_{Ca}	g_{CaMut}	g_L	g_{AHP}
WT	50	40	0.1	1	0	0.1	1
WT With Mutant Channel and PV+ Reduction	50	40	0.1	0.7105	0.2895	0.1	1
WT With Mutant Channel	50	40	0.1	0.7105	0.2895	0.1	1
WT With PV+ Reduction	50	40	0.1	1	0	0.1	1
Increased Calcium Channel Conductance	50	40	0.1	2	0	0.1	1

All reversal potentials, V_x have the unit mV, and were as listed below:

Table S20 Table listing the values for reversal potential for each ion (mV) for pyramidal cells simulated in each condition:

Condition	V_{Na}	V_K	V_{Ca}	V_L
All conditions	50	-90	120	-67

All gating variables m_∞, h, n, w, $m_{l\infty}$, h_l, $m_{lMut\infty}$, h_{lMut} and calcium concentration were calculated as follows:

$$\frac{dy}{dt} = \frac{y_\infty(V) - y}{\tau_y}$$

Where y= h, n, w, h_l and h_{lMut}.

$$\frac{d\left[Ca^{2+}\right]i}{dt} = -0.002(Ica) - \frac{\left[Ca^{2+}\right]i}{80}$$

And starting $\left[Ca^{2+}\right]$i= 0mM.

With

$$x_{\infty}(V) = \frac{\alpha_x(V)}{\alpha_x(V) - \beta_x(V)}$$

For x=m, h, n, where

$$\alpha_m(V) = \frac{0.032(V+54)}{1 - e^{\left(-\frac{(V+54)}{4}\right)}}$$

$$\beta_m(V) = \frac{0.28(V+27)}{e^{(\frac{V+27}{5})} - 1}$$

$$\alpha_h(V) = 0.128e^{(-\frac{V+50}{18})}$$

$$\beta_h(V) = \frac{4}{1 + e^{(-\frac{V+27}{5})}}$$

$$\alpha_n(V) = \frac{0.032(V+52)}{1 - e^{(-\frac{V+52}{5})}}$$

$$\beta_n(V) = 0.5e^{(-\frac{V+57}{40})}$$

And

$$\tau_x(V) = \frac{1}{\alpha_x(V) - \beta_x(V)}$$

And other gating variables specified as follows:

$$w_{\infty}(V) = \frac{1}{1 + e^{\left(-\frac{V+35}{10}\right)}}$$

$$m_{l\infty}(V) = \frac{1}{1 + e^{\left(-\frac{V+25}{-6}\right)}}$$

$$h_{l\infty}(V) = \max\left[0, \min\left\{1,1 + \frac{mL\infty(Vm - ECa)}{57}\right\}\right]$$

$$m_{lMut\infty}(V) = \frac{1}{1 + e^{\left(-\frac{V+18.54}{-7.36}\right)}}$$

$$h_{lMut\infty}(V) = \max\left[0, \min\left\{1,1 + \frac{mL\infty(Vm - ECa)}{243.01}\right\}\right]$$

With gating time constants τ_{hl}=20ms, τ_{hlMut}=20ms, and τ_W being specified by:

$$\tau_w(V) = \frac{100}{(3.3e^{\left(\frac{V+35}{20}\right)} + e^{\left(-\frac{V+52}{20}\right)})}$$

I_{syn} is the synaptic current modelled as described by the subsection of this appendix, entitled “Synaptic model”.

The parameters which were adjusted between the L-type channel and the mutant L-type channel include the normalisation factor (changed from 57mV to 243.01mV), a slope parameter (changed from -6mV to -7.36mV), and a factor related to the voltage at which half the peak value of conductance occurs (changed from-25mV to -18.54mV). The adjustments made to these parameters are described in more detail in Kummer *et al.* (2022).

PV+ interneuron:

PV+ interneuron membrane potential was defined in each case by equation 3 below:

Equation 3:

$$C\frac{dV}{dt} = I_{Na} + I_K + I_L + I_{syn}$$

Where capacitance, C=1 μF/cm²

$$I_{Na} = g_{Na}m_{\infty}^3(V)h(V - V_{Na})$$

$$I_K = g_K n^4\,(V - V_k)$$

$$I_L = g_L(V - V_L)$$

Where all maximum conductances, g_x, have the unit mS/cm², and were as listed in the table below:

Table S21 Table listing the values for maximum conductance for each ion channel (mS/cm²) for PV+ cells simulated in each condition:

Condition	g_{Na}	g_K	g_L
All Conditions	35	9	0.1

Where all reversal potentials V_x, have the unit mV, and were as listed below:

Table S22 the values for reversal potential for each ion (mV) for PV+ cells simulated in each condition:

Condition	**V_{Na}**	**V_K**	**V_L**
All Conditions	50	-90	-67

And where gating variables m_∞, h and n were calculated using the following:

$$\frac{dy}{dt} = \frac{y_\infty(V) - y}{\tau_y}$$

For y= h, n

With

$$x_\infty(V) = \frac{\alpha_x(V)}{\alpha_x(V) - \beta_x(V)}$$

For x=m, h, n

And

$$\tau_y(V) = \frac{0.2}{\alpha_y(V) - \beta_y(V)}$$

For y=h, n

Where

$$\alpha_m(V) = \frac{0.1(V + 35)}{1 - e^{(-\frac{V+35}{10})}}$$

$$\beta_m(V) = 4e^{(-\frac{V+60}{18})}$$

$$\alpha_h(V) = 0.07e^{(-\frac{V+58}{20})}$$

$$\beta_h(V) = \frac{1}{e^{(-0.1(V+28))} + 1}$$

$$\alpha_n(V) = \frac{0.01(V + 34)}{1 - e^{(-0.1(V+34))}}$$

$$\beta_n(V) = 0.125e^{(-\frac{V+44}{80})}$$

I_{syn} is the synaptic current modelled as described by the subsection of this appendix, entitled “Synaptic model”.

Synaptic model:

Synaptic currents, I_{syn} were modelled by methods described by Ermentrout and Kopell (1998). The current is described by the equation below:

$$I_{syn_{(ij)}} = g_{ij} s_i(t)(V_{rev} - V_j)$$

Where s_{ij} is a synaptic gating variable associated with presynaptic neuron I, and postsynaptic neuron, j, where:

$$\frac{ds}{dt} = \rho(V_i)\frac{1-s}{\tau_R} - \frac{s}{\tau_D}$$

Where τ_R and τ_D are synaptic rise and decay time constants with units ms, and τ_R=0.1 and τ_D=3 where cell j is a pyramidal neuron, τ_R=0.3 and τ_D=9 where cell j is an interneuron.

With ρ denoting the smoothed Heaviside function (to model all-or-nothing synaptic stimulation):

$$\rho(V_i) = \frac{1 + \tanh\left(\frac{V_i}{4}\right)}{2}$$

g_{ij} described maximal synaptic conductance, and has units mS/cm^2. V_{rev} is the reversal potential for the synapse, and has the units mV. Both g_{ij} and V_{rev} are defined per synapse type as stated in the table below:

Table S23 maximum conductance (mS/cm^2) and reversal potential (mV) for synapses between pre and post synaptic cells per synapse type in all simulated conditions:

Synapse Type	**g_{ij}**	**V_{rev}**
PV+ Interneuron→ PV+ Interneuron	0.7	-80
PV+ Interneuron→Pyramidal	1.5	-80
Pyramidal→ PV+ Interneuron	0.8	0
Pyramidal→ Pyramidal	0.5	0

Stochastic input to each cell was modelled as per Kopell *et al.* (2010).

The experiment described in Appendix 3 uses the same equations and parameters used here except where explicitly specified.

Appendix 3: Reduced PV+ interneuron number as a possible compensatory mechanism against impacts of reduced dosage of psychiatric-risk gene, *CACNA1C*, on neural network ɣ activity:

Introduction:

ɣ oscillations are known to be implicated in schizophrenia (Spencer *et al.*, 2003; Hong *et al.*, 2004; Hall MH *et al.*, 2009; Kikuchi *et al.*, 2011; Spencer, 2012). Mutations in the *CACAN1C* gene have been found to be significantly associated with schizophrenia by GWAS study (Ripke *et al.*, 2014). An animal model of reduced *CACNA1C* gene dosage has been created to study the potential effects of this reduced gene dosage on neurophysiology, to inform the potential roles of *CACNA1C* mutations in schizophrenia (Sykes *et al.*, 2019). The animal model is a rat with heterozygous KO of the *CACNA1C* gene. A previous study by Moon (2018) found that the *CACNA1C* heterozygous KO rat has a 20% reduced PV+ density in the CA3 as compared to WT. In-vitro experiments have previously found that acute block of L-type calcium channels causes an increase in synchronised bursting activity of iPSC-derived neural populations in-vitro (Plumbly *et al.*, 2019). However, the work of Kumar *et al.* (2015) found that HET *CACNA1C* KO mice have a reduction in cortical ɣ oscillatory power, not increase as was suggested by the in-vitro experiments of Plumbly *et al.* (2019). This could be due to the genotype-related reduction in PV+ cell number as found by Moon (2018).

I aimed to explore the impacts of reduced *CACNA1C* gene dosage and reduced PV+ cell number which are correct to the *CACNA1C* HET KO rat on ɣ oscillations generated by a model neural network. I modelled a CA3 neural network similar to that described in chapter 4. I simulated θ-evoked ɣ oscillations in the model network for four different conditions: 1) WT; 2) WT with reduced CaV1.2 conductance; 3) WT with reduced PV+ cell number; 4) WT with reduced CaV1.2 conductance and PV+ cell number. I compared the ɣ oscillations generated by the network simulations of these modelled conditions in terms of their oscillatory power, peak frequency and PSD. This would allow me to explore how *CACNA1C*-hemizygosity might affect ɣ oscillations, and how the reduction in CaV1.2 channel density, and the genotype-related reduction in PV+ cell density contributes to this.

Methods:

The methods of this study were similar to those used in chapter 4, differences in parameters and methods are as indicated below.

Four conditions were modelled: 1) A WT model, 2) a WT with heterozygous *CACNA1C* KO and PV+ reduction, 3) a WT model with PV+ reduction, 4) a WT model with heterozygous *CACNA1C* KO.

All parameters and equations used in this experiment were the same as those used in chapter 4 and Appendix 2 except where explicitly stated below.

L-type calcium channel currents within pyramidal CA3 cells were modelled by the equation below.

$$I_{Ca} = g_{Ca} m_{l\infty}(V - V_{Ca})$$

Where:

$$m_{l\infty}(V) = \frac{1}{1 + e^{\left(-\frac{V+25}{2.5}\right)}}$$

This equation is not used in chapter 4 and is not described in Appendix 2 as it lacks an inactivation gating variable. The equation is taken from Ermentrout, Pascal and Gutkin (2001) and was derived using data from studies which measured L-type channel kinetics in the neuron. The values for maximum conductance for each channel were based on those used in previous studies (Ermentrout, Pascal and Gutkin, 2001; Traub and Miles, 1991; Wang and Buzsáki, 1996; Ermentrout and Kopell, 1998).

g_{AHP} was 0.5mS/cm^2 for all conditions modelled here, instead of being 1mS/cm^2 as it was in the work described in chapter 4. g_{Ca} also differed in this model from that used in the previously described work, the values for g_{Ca} are as indicated below, in mS/cm^2.

Table S24 Table showing the maximum calcium channel conductance used in the experiment detailed (mS/cm^2). No other conductances are detailed as they are the same as shown in Appendix 2.

Condition	**g_{Ca}**
WT	0.3
WT with heterozygous *CACNA1C* KO and PV+ reduction	0.19
WT with PV+ reduction	0.3
WT with heterozygous *CACNA1C* KO	0.19

Synaptic connections were modelled as described in chapter 4 and Appendix 2, but with the maximal synaptic conductance (mS/cm^2) between cells i and j, g_{ij} being as listed below. The conductances which differ between the two experimental models are indicated in bold italics:

Table S25 Table showing synaptic conductance for all conditions per synapse type (mS/cm^2):

Synapse Type:	**g_{ij}**
PV+ Interneuron→PV+ Interneuron	***0.5***
PV+ Interneuron→Pyramidal	1.5
Pyramidal→PV+ Interneuron	***0.5***
Pyramidal→Pyramidal	***0.1***

These parameters were kept within the ranges used in previous modelling studies (Ermentrout, Pascal and Gutkin, 2001; Traub and Miles, 1991; Wang and Buzsáki, 1996; Ermentrout and Kopell, 1998).

The 4 modelled conditions differed from one another as follows:

WT condition modelled as described above with 100 pyramidal cells and 10 interneurons.

WT with heterozygous *CACNA1C* KO and PV+ reduction was modelled as above, but with 8 interneurons, and g_{Ca} of 0.19mS/cm^2.

WT with heterozygous *CACNA1C* KO was modelled as the WT condition but with g_{Ca} of 0.19mS/cm^2.

WT with PV+ reduction was modelled as the WT condition, with 8 interneurons.

Data processing was as described in chapter 4 and Appendix 2. Data analyses involved exploring the data for normality and equality between groups graphically and statistically using Shapiro-Wilk and Levene's tests.

Testing for between-condition differences in maximum PSD and band-wide ɣ power were tested using ANOVA. Between-condition differences in maximum ɣ power and peak frequency of oscillation were tested using the non-parametric Kruskal-Wallis method. Pairwise between-condition differences in maximum ɣ PSD and band-wide ɣ power values were tested for using Wilcoxon signed rank testing, while pairwise between-condition differences in maximum ɣ power and in peak frequency of oscillation were tested using multiple t-tests. The Holm method was used to correct for multiple testing, the threshold for significance was set at 0.05.

Results:

Creation of a functioning computational CA3 network model:

The computational model described produced appropriate stimulus-evoked responses in CA3 pyramidal and PV+ interneurons as indicated in Supplemental Figures S10, S11 and S12, below.

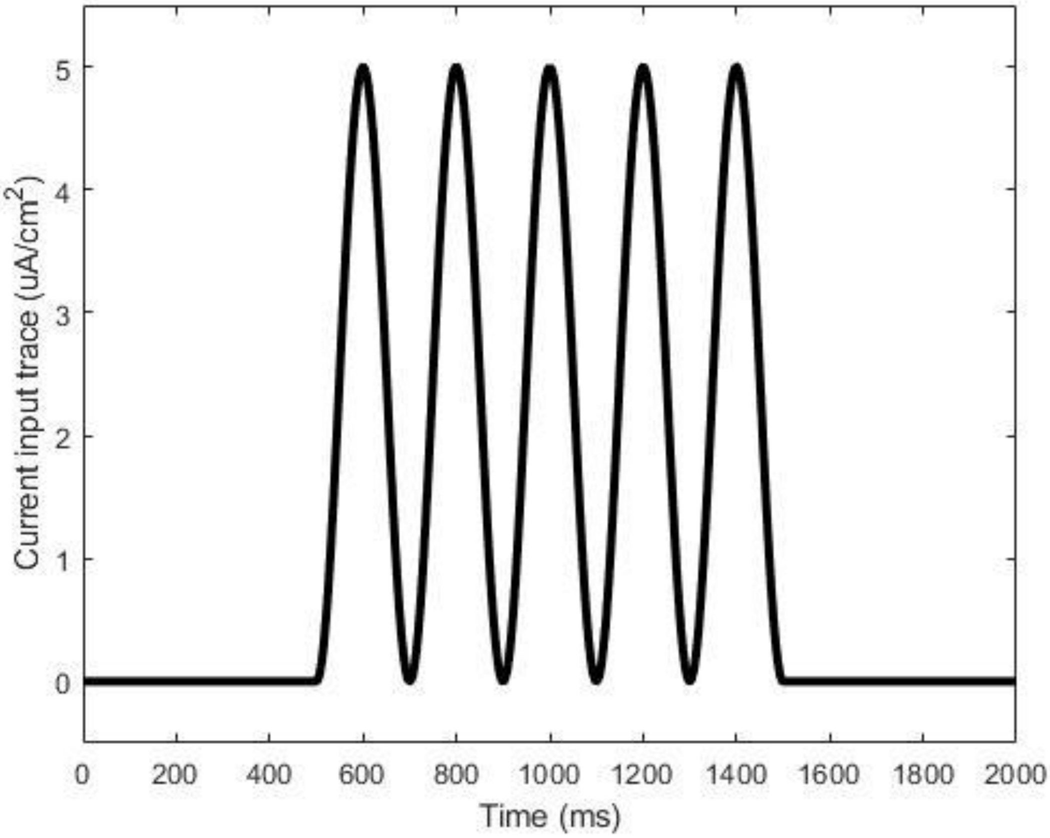

Figure S10 θ frequency current input which was delivered to all pyramidal cells in network to elicit synchronous firing.

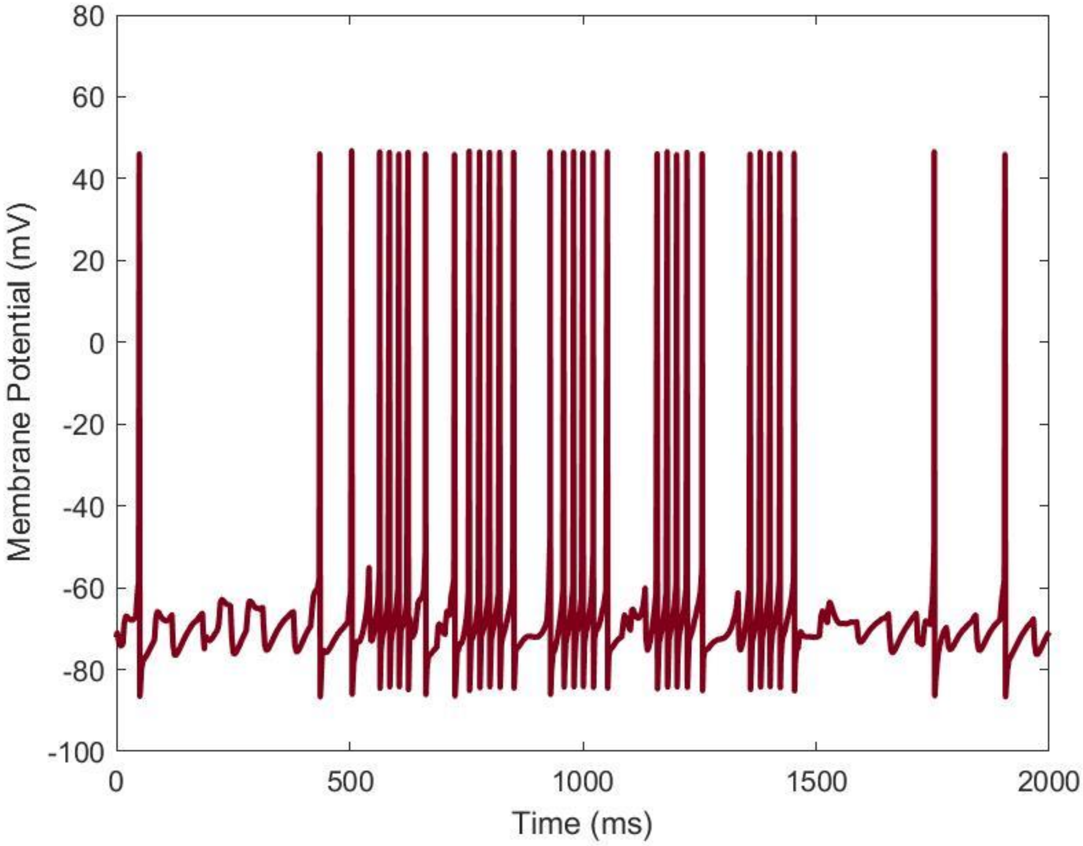

Figure S11 Membrane potential trace of a pyramidal cell during the experiment. The firing pattern demonstrates burst firing corresponding to θ frequency input as shown in Figure S10.

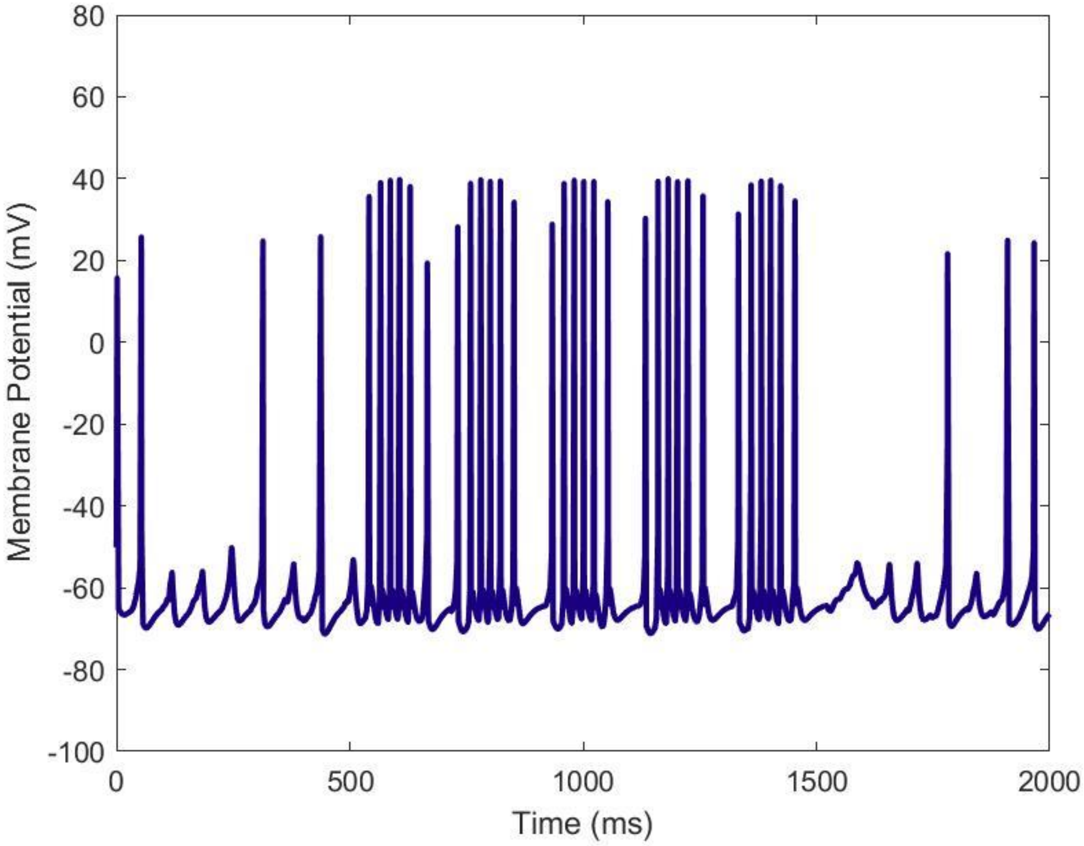

Figure S12 Membrane potential trace of a PV+ cell during the experiment. The firing pattern demonstrates burst firing corresponding to θ frequency input as shown in Figure S10.

LFP-type data was obtained from the simulated network model successfully, as is shown in Supplemental Figure S13.

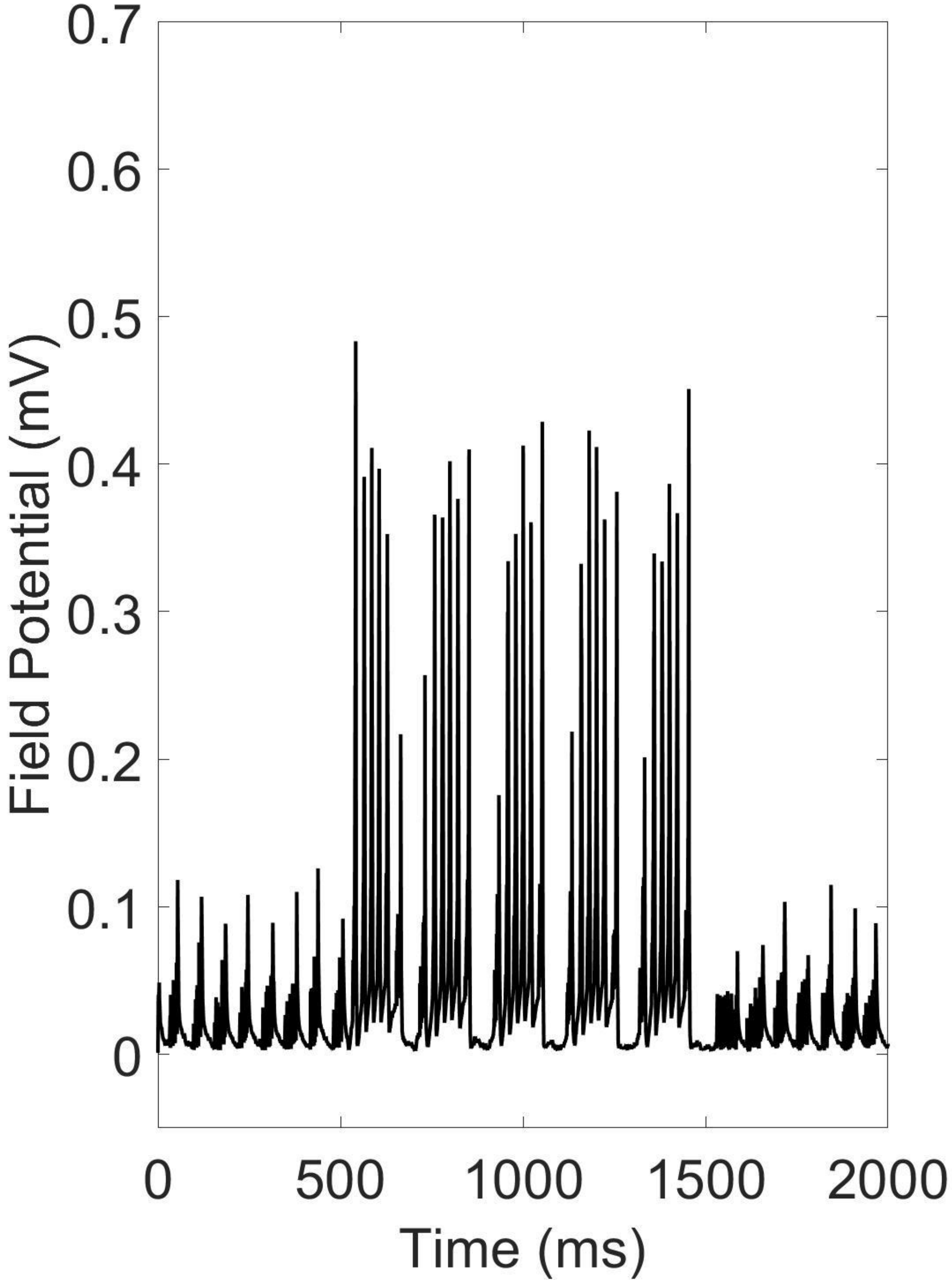

Figure S13 LFP trace generated from a WT simulation experiment.

Maximum ɣ oscillation power, average ɣ oscillation power, maximum PSD and peak frequency of ɣ oscillations are all significantly impacted by model type:

Kruskal-Wallis testing demonstrated that all aspects of network ɣ oscillatory output significantly differed by simulation type (**maximum ɣ power**: corrected P= 3.2X10^{-8}, P=4.1x10^{-9}, DF=3, H=42.0; **peak frequency:** corrected P=1.03X10^{-7}, P=1.23x10^{-9}, DF=3, H=44.4; **maximum PSD:** corrected P=6.41X10^{-26}, P=1.83x10^{-27}, DF=3, 56, F value= 160; **band-wide oscillatory power**: corrected P=3.3X10^{-21}, P= 9.71x10^{-23}, DF=3, 56, F value= 103). As such, between-condition ɣ outputs were examined by all parameters tested.

Heterozygous *CACNA1C* KO increases ɣ oscillation power, but associated PV+ cell loss causes a compensatory reduction in ɣ oscillation power:

The maximum and average power of ɣ oscillations were not significantly changed by modelling the heterozygous KO of *CACNA1C* with the genotype-associated reduction in PV+ cell number (**maximum ɣ power tested by Wilcoxon signed rank test:** corrected P value=0.776, P=0.0706, W=3.27; **average ɣ power tested by t test**: corrected P value= 0.186, P=0.0155, t=2.58).

Maximum and average ɣ power were both significantly increased by the reduction in calcium channel conductance which was used to model the WT with *CACNA1C* HET KO condition (**maximum ɣ power tested by Wilcoxon signed rank test**: corrected P value=6.34x10^{-5}, P= 2.88x10^{-6}, W= 21.9 ; **average ɣ power tested by t test**: corrected P value= 1.39x10^{-16}, P=4.22x10^{-18} , t=-19.97). A reduction in PV+ cell number also increased maximum ɣ power non-significantly (corrected P=1, P=0.900, W=0.0157), and significantly decreased the average power of ɣ oscillations generated by the network model (corrected P value= 3.91x10$^{=7}$, P= 1.63x10^{-8}, t=-7.82) as compared to WT. When heterozygous KO of *CACNA1C* was modelled with the genotype-associated reduction in PV+ cell number, maximum and average ɣ power were **not** significantly different from the WT condition (**maximum ɣ power tested by Wilcoxon Signed Rank Test:** corrected P value=0.776, P=0.0706, W=3.27; **average ɣ power tested by t test:** corrected P value= 0.186, P=0.0155, t=2.58). Including a reduction in PV+ cell density in models including the reduced calcium conductance significantly reduced the maximum and average power of ɣ oscillations (**maximum ɣ Power:** corrected P= 0.0022, P=0.000157, W=14.3; **average ɣ Power**: corrected P value=8.23x10^{-6}, P=3.58x10^{-7}, t=6.61). The effects of *CACNA1C* hemizygosity and PV+ cell density reduction on maximum and average ɣ power are shown in supplementary figures S14 and S15, respectively.

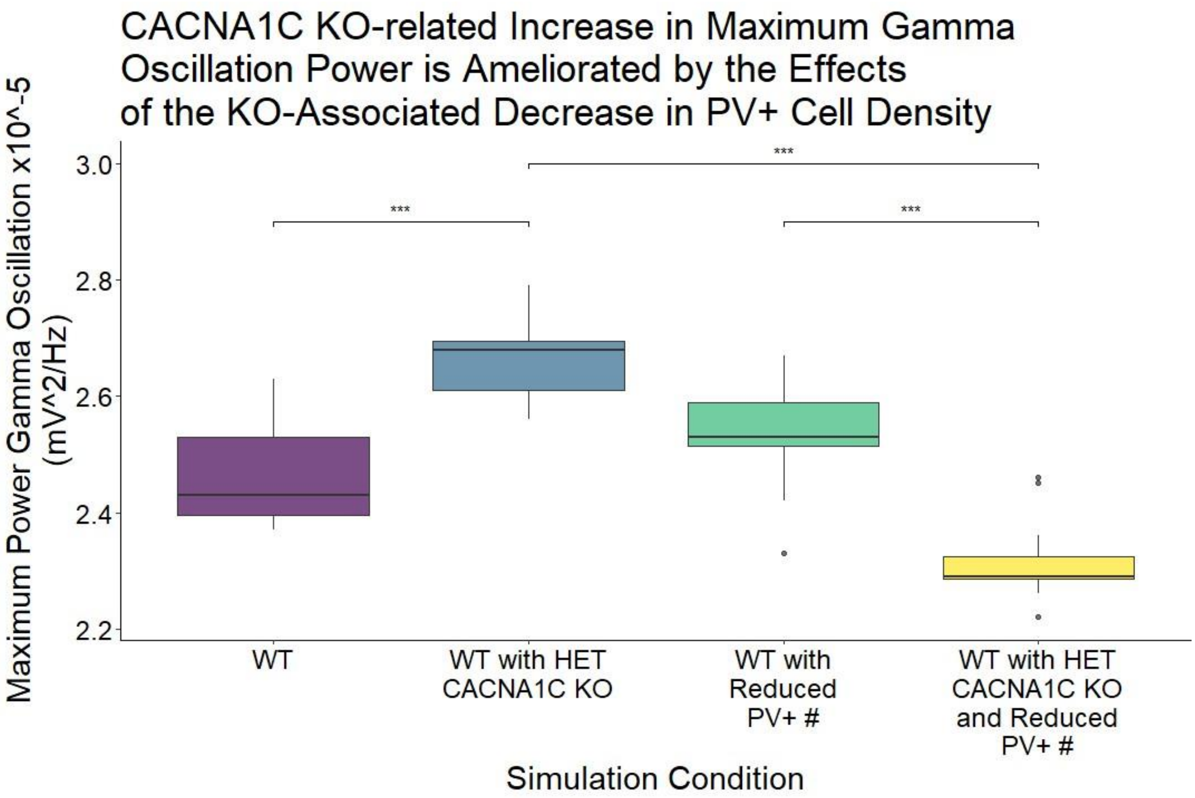

Figure S14 Maximum ɣ power varying with simulated condition modelled. One significance star indicates P<0.05. Two significance stars indicates P<0.01. Three significance stars indices P<0.001.

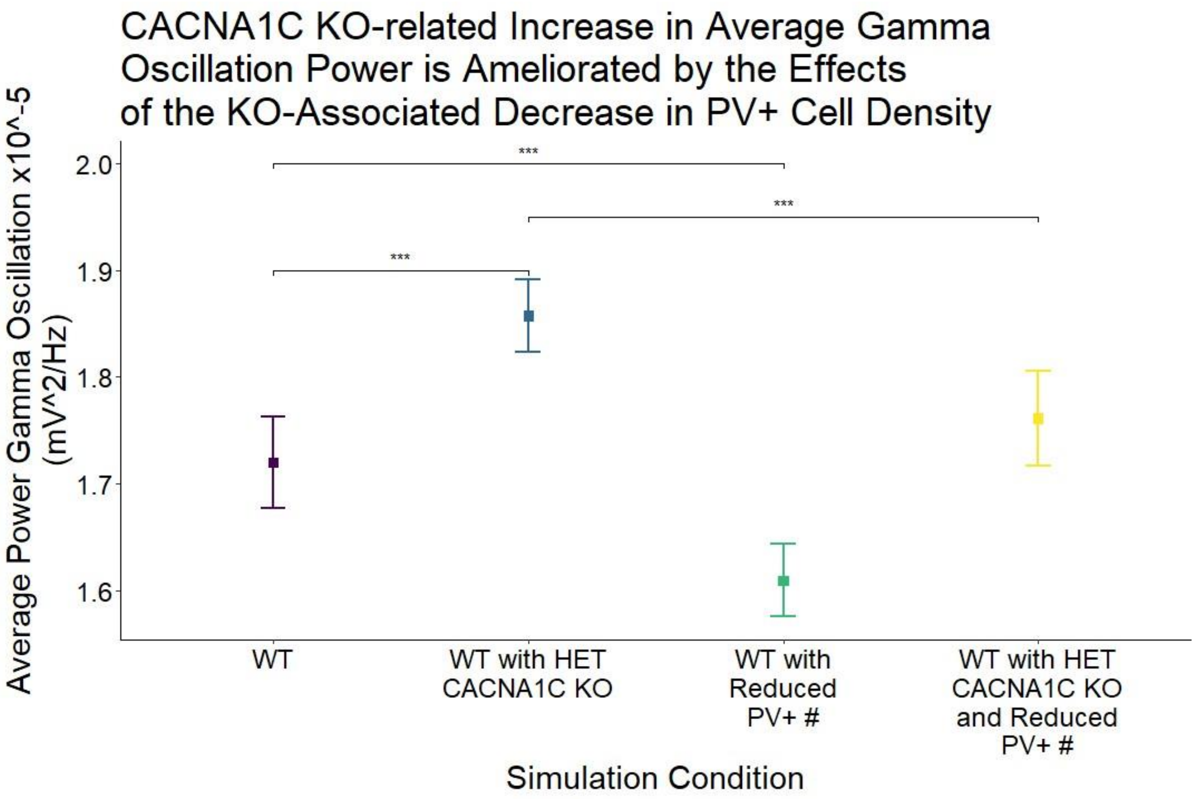

Figure S15 Average ɣ power varying with simulated condition modelled. One significance star indicates $P<0.05$. Two significance stars indicates $P<0.01$. Three significance stars indices $P<0.001$.

Overall, the power of ɣ oscillations is increased by *CACNA1C* HET KO, but this increase is ameliorated by the effects of the genotype-related reduction in PV+ cell number. This suggests that the loss of PV+ cells could compensate for the impacts of reduced *CACNA1C* dosage within the CA3 neural network.

Reduction in CaV1.2 channel conductance resulting from *CACNA1C* hemizygosity reduces maximum PSD and peak frequency of ɣ oscillations:

Modelling the heterozygous *CACNA1C* KO led to an increase in maximum PSD and peak frequency of ɣ oscillations as compared to WT when the genotype-associated PV+ cell number reduction was also modelled (**maximum PSD:** corrected P= $5.58\text{x}10^{-15}$, P=$1.86\text{x}10^{-16}$, t=17.3; **peak frequency:** corrected P value= $6.34\text{x}10^{=5}$, P=$2.93\text{x}10^{-6}$, W=21.9). Heterozygous *CACNA1C* KO alone also led to an increase in maximum PSD and peak frequency of ɣ oscillations as compared to WT (**maximum PSD:** corrected P value=$2.67\text{x}10^{-13}$, P=$6.06\text{x}10^{-13}$, t=12.5; **peak frequency:** corrected P=0.00115, P=$2.88\text{x}10^{-6}$, W=21.9). The genotype-related decrease in PV+ cell number reduced the maximum PSD (corrected P value= 0.00238, P=$1.83\text{x}10^{-4}$, t=-4.31), and marginally but significantly increased the peak frequency of ɣ oscillations (corrected P value=0.00180, P= 0.000120, W=14.8) as compared to WT. The difference in maximum PSD and in peak frequency of ɣ oscillation between simulated conditions are shown in supplementary figures S16 and S17, respectively.

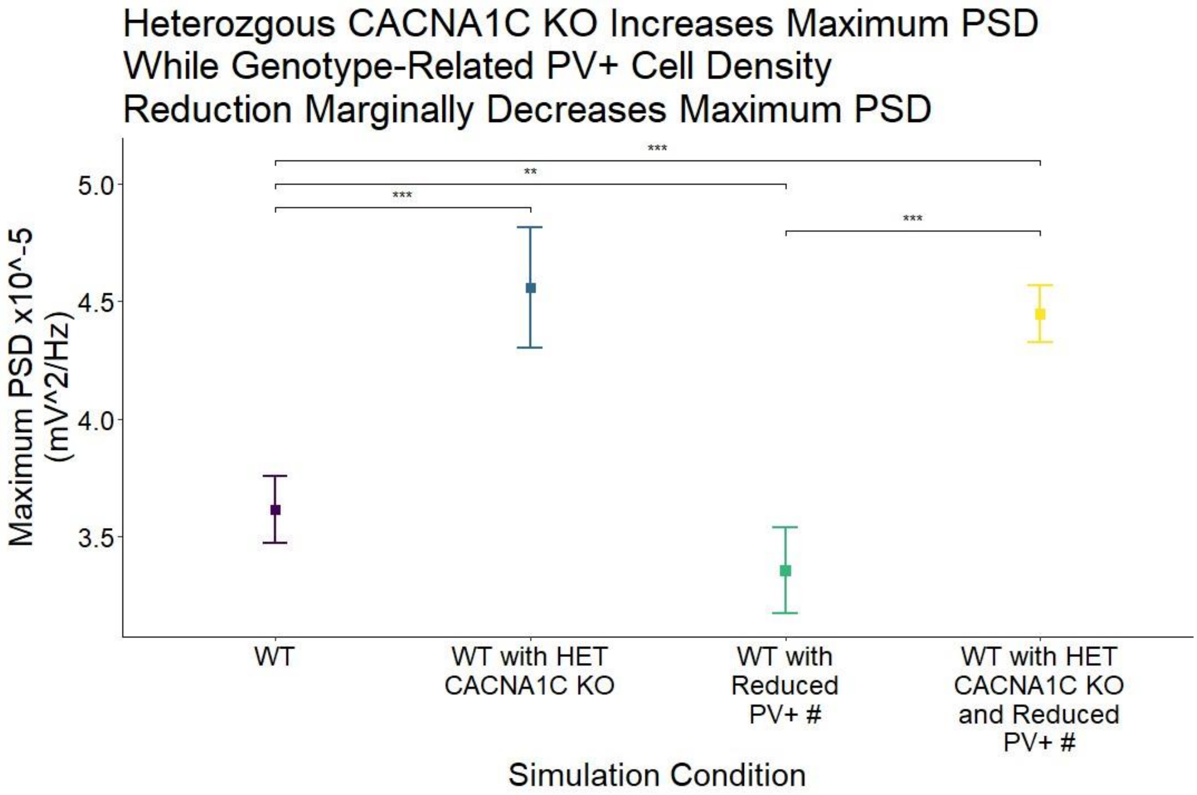

Figure S16 Maximum PSD varies with simulated condition of the CA3 network model.

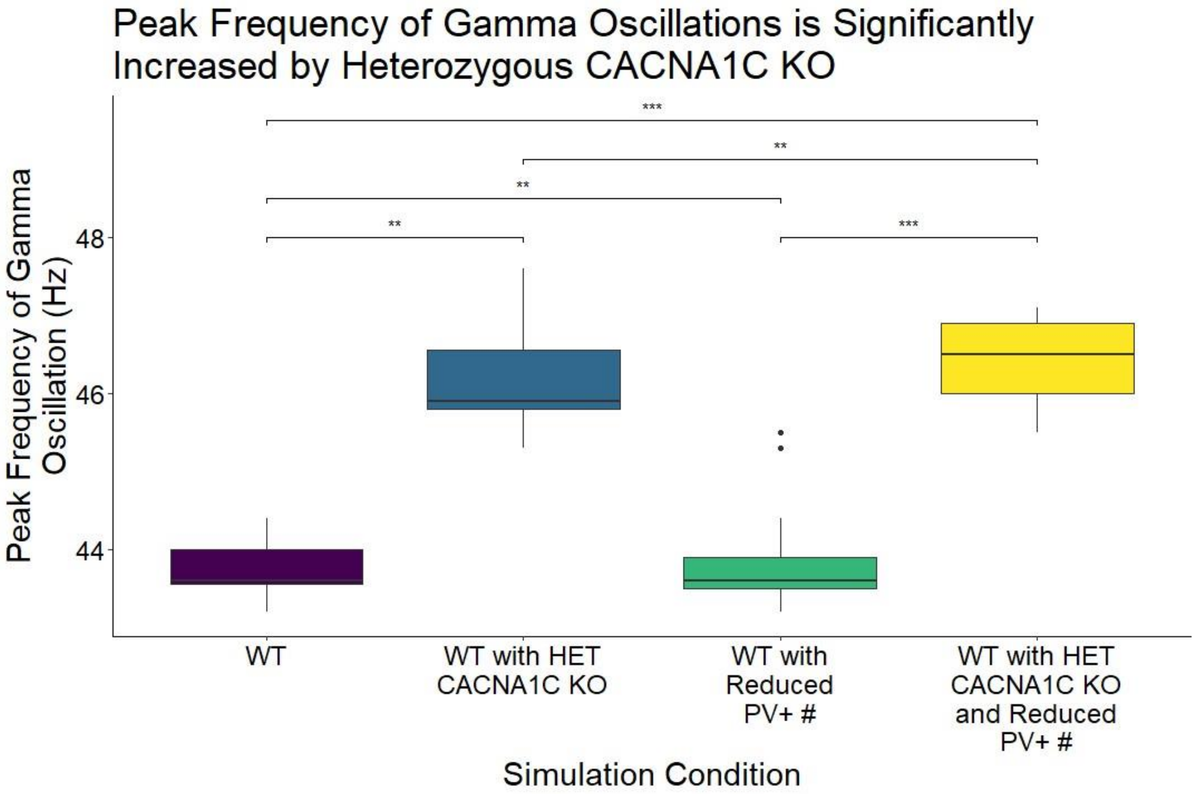

Figure S17 The peak frequency of ɣ oscillations generated by the model varies with simulated condition of the CA3 network model.

Discussion and Conclusion:

Heterozygous KO of *CACNA1C* is predicted here to increase the power of ɣ oscillations in the CA3 in a way that is counteracted by a decrease in power caused by the genotype-related reduction in PV+ cell number. This PV+-reduction related effect on ɣ oscillatory power may explain why Plumbly *et al.* (2019) found that acute blockage of L-type calcium channels increases the power of synchronous activity in neural networks, but Kumar *et al.* (2015) found that heterozygous *CACNA1C* KO reduces cortical ɣ oscillatory power measured in the cortex of the mouse. Based on the results of this study, heterozygous *CACNA1C* KO is expected to increase maximum PSD and increase the peak frequency of ɣ oscillations in the CA3. Overall, heterozygous *CACNA1C* KO and the associated reduction in PV+ cell number are expected to alter the frequency:power distribution of ɣ oscillations in the CA3. These model predictions should be tested by θ-stimulation of acute sections of CA3 from WT and *CACNA1C* Het KO rats, using LFP recordings to measure ɣ oscillations produced in each case. Acute partial block of CaV1.2 channels using a low dose of wash-in Caliseptine would enable us to explore the contribution of reduced CaV1.2 channel conductance as compared to PV+ cell reduction in any resulting changes in ɣ oscillations.

Bibliography:

Aguillon-Rodriguez, V. *et al.* (2021) 'Standardized and reproducible measurement of decision-making in mice', *eLife*, 10. doi: 10.7554/ELIFE.63711.

Al-Beltagi, M. (2021) 'Autism medical comorbidities', *World Journal of Clinical Pediatrics*, 10(3), p. 15. doi: 10.5409/WJCP.V10.I3.15.

Allegra, M. *et al.* (2014) 'Altered GABAergic markers, increased binocularity and reduced plasticity in the visual cortex of engrailed-2 knockout mice', *Frontiers in Cellular Neuroscience*, 8(JUN). doi: 10.3389/FNCEL.2014.00163/ABSTRACT.

American Psychiatric Association (2013) 'DSM-5 Diagnostic Classification', in *Diagnostic and Statistical Manual of Mental Disorders*. American Psychiatric Association. doi: 10.1176/appi.books.9780890425596.x00diagnosticclassification.

An, H. S. *et al.* (2013) 'Sudden cardiac arrest during anesthesia in a 30-month-old boy with syndactyly: A case of genetically proven timothy syndrome', *Journal of Korean Medical Science*, 28(5), pp. 788–791. doi: 10.3346/jkms.2013.28.5.788.

Ariza, J. *et al.* (2018) 'The Number of Chandelier and Basket Cells Are Differentially Decreased in Prefrontal Cortex in Autism', *Cerebral Cortex (New York, NY)*, 28(2), p. 411. doi: 10.1093/CERCOR/BHW349.

Ashcroft, F. M. and Rorsman, P. (1989) 'Electrophysiology of the pancreatic β-cell', *Progress in Biophysics and Molecular Biology*, 54(2), pp. 87–143. doi: 10.1016/0079-6107(89)90013-8.

Assaf, F. and Schiller, Y. (2016) 'The antiepileptic and ictogenic effects of optogenetic neurostimulation of PV-expressing interneurons', *Journal of Neurophysiology*, 116(4), p. 1694. doi: 10.1152/JN.00744.2015.

Ayres, A. (1996) *Sensory integration and praxis tests (SIPT)*. Available at: http://v-psyche.com/doc/MENTAL ABILITY/Sensory Integration and Praxis Test-2.doc (Accessed: 19 March 2024).

Bader, P. L. *et al.* (2011) 'Mouse model of Timothy syndrome recapitulates triad of autistic traits', *Proceedings of the National Academy of Sciences of the United States of America*, 108(37), pp. 15432–15437. doi: 10.1073/pnas.1112667108.

Baker, M. and Penny, D. (2016) 'Is there a reproducibility crisis?', *Nature*, 533(7604), pp. 452–454. doi: 10.1038/533452A.

Banker, S. *et al.* (2021a) 'Hippocampal contributions to social and cognitive deficits in autism spectrum disorder', *Trends in Neurosciences*. NIH Public Access, pp. 793–807. doi: 10.1016/j.tins.2021.08.005.

Banker, S. *et al.* (2021b) 'Altered structure and functional connectivity of the hippocampus are associated with social and mathematical difficulties in nonverbal learning disability', *Hippocampus*, 31(1), pp. 79–88. doi: 10.1002/hipo.23264.

Barrett, C. F. and Tsien, R. W. (2008) ‘The Timothy syndrome mutation differentially affects voltage- and calcium-dependent inactivation of CaV1.2 L-type calcium channels’, *Proceedings of the National Academy of Sciences of the United States of America*, 105(6), pp. 2157–2162. doi: 10.1073/pnas.0710501105.

Barton, K. (no date) ‘CRAN - Package MuMIn’. Available at: https://cran.r-project.org/web/packages/MuMIn/index.html (Accessed: 29 February 2024).

Bates, D. *et al.* (2015) ‘Fitting Linear Mixed-Effects Models Using lme4’, *Journal of Statistical Software*, 67(1), pp. 1–48. doi: 10.18637/JSS.V067.I01.

Bauer, R., Timothy, K. W. and Golden, A. (2021) ‘Update on the Molecular Genetics of Timothy Syndrome’, *Frontiers in Pediatrics*, 9, p. 435. doi: 10.3389/FPED.2021.668546/BIBTEX.

Bean, B. P. (2007) ‘The action potential in mammalian central neurons’, *Nature reviews. Neuroscience*, 8(6), pp. 451–465. doi: 10.1038/NRN2148.

Bédard, C. *et al.* (2010) ‘Evidence for frequency-dependent extracellular impedance from the transfer function between extracellular and intracellular potentials: Intracellular-LFP transfer function’, *Journal of Computational Neuroscience*, 29(3), pp. 389–403. doi: 10.1007/s10827-010-0250-7.

Behrmann, M., Thomas, C. and Humphreys, K. (2006) ‘Seeing it differently: visual processing in autism’, *Trends in Cognitive Sciences*, 10(6), pp. 258–264. doi: 10.1016/J.TICS.2006.05.001.

Benarroch, E. E. (2013) ‘HCN channels: function and clinical implications’, *Neurology*, 80(3), pp. 304–310. doi: 10.1212/WNL.0B013E31827DEC42.

Bentzen, B. H. *et al.* (2014) ‘BK channel activators and their therapeutic perspectives’, *Frontiers in Physiology*, 5(OCT). doi: 10.3389/FPHYS.2014.00389.

Berkefeld, H., Fakler, B. and Schulte, U. (2010) ‘Ca2+-activated K+ channels: From protein complexes to function’, *Physiological Reviews*, 90(4), pp. 1437–1459. doi: 10.1152/PHYSREV.00049.2009/ASSET/IMAGES/LARGE/Z9J0041025620007.JPEG.

Bertone, A. *et al.* (2005) ‘Enhanced and diminished visuo-spatial information processing in autism depends on stimulus complexity’, *Brain : a journal of neurology*, 128(Pt 10), pp. 2430–2441. doi: 10.1093/BRAIN/AWH561.

Bett, G. C. L. *et al.* (2012) ‘A Mouse Model of Timothy Syndrome: a Complex Autistic Disorder Resulting from a Point Mutation in Cav1.2’, *North American journal of medicine & science*, 5(3), p. 135. doi: 10.7156/NAJMS.2012.053135.

Betterton, R. T. *et al.* (2017) ‘Acetylcholine modulates gamma frequency oscillations in the hippocampus by activation of muscarinic M1 receptors’, *European Journal of Neuroscience*. Edited by P. Poirazi, 45(12), pp. 1570–1585. doi: 10.1111/ejn.13582.

Birey, F. *et al.* (2017) ‘Assembly of functionally integrated human forebrain spheroids’, *Nature 2017 545:7652*, 545(7652), pp. 54–59. doi: 10.1038/nature22330.

Birey, F. *et al.* (2022) ‘Dissecting the molecular basis of human interneuron migration in forebrain assembloids from Timothy syndrome', *Cell stem cell*, 29(2), pp. 248-264.e7. doi: 10.1016/J.STEM.2021.11.011.

Bland, B. H., Konopacki, J. and Dyck, R. (2005) 'Heterogeneity among hippocampal pyramidal neurons revealed by their relation to theta-band oscillation and synchrony', *Experimental Neurology*, 195(2), pp. 458–474. doi: 10.1016/j.expneurol.2005.06.007.

Bokil, H. *et al.* (2010) 'Chronux: A platform for analyzing neural signals', *Journal of Neuroscience Methods*, 192(1), pp. 146–151. doi: 10.1016/j.jneumeth.2010.06.020.

Bozarth, X. *et al.* (2018) 'Expanding clinical phenotype in CACNA1C related disorders: From neonatal onset severe epileptic encephalopathy to late-onset epilepsy', *American journal of medical genetics. Part A*, 176(12), pp. 2733–2739. doi: 10.1002/AJMG.A.40657.

Broom, E. *et al.* (2022) 'Recruitment of frontal sensory circuits during visual discrimination', *Cell Reports*, 39(10), p. 110932. doi: 10.1016/j.celrep.2022.110932.

Buddell, T. *et al.* (2019) 'An autism-causing calcium channel variant functions with selective autophagy to alter axon targeting and behavior', *PLOS Genetics*, 15(12), p. e1008488. doi: 10.1371/JOURNAL.PGEN.1008488.

Buddell, T. and Quinn, C. C. (2021) 'An autism-associated calcium channel variant causes defects in neuronal polarity in the ALM neuron of C. elegans', *microPublication Biology*, 2021. doi: 10.17912/MICROPUB.BIOLOGY.000378.

Buraei, Z. and Yang, J. (2010) 'The β Subunit of Voltage-Gated Ca2+ Channels', *Physiological reviews*, 90(4), p. 1461. doi: 10.1152/PHYSREV.00057.2009.

Burgess, C. P. *et al.* (2017) 'High-Yield Methods for Accurate Two-Alternative Visual Psychophysics in Head-Fixed Mice', *Cell Reports*, 20(10), pp. 2513–2524. doi: 10.1016/j.celrep.2017.08.047.

Buzsáki, G. and Wang, X.-J. (2012) 'Mechanisms of Gamma Oscillations', *Annual Review of Neuroscience*, 35(1), pp. 203–225. doi: 10.1146/annurev-neuro-062111-150444.

Cain, S. M. and Snutch, T. P. (2010) 'Contributions of T-type calcium channel isoforms to neuronal firing', *Channels*, 4(6), p. 475. doi: 10.4161/CHAN.4.6.14106.

Calorio, C. *et al.* (2019) 'Impaired chromaffin cell excitability and exocytosis in autistic Timothy syndrome TS2-neo mouse rescued by L-type calcium channel blockers', *The Journal of Physiology*, 597(6), pp. 1705–1733. doi: 10.1113/JP277487.

Catterall, W. A. (2011) 'Voltage-gated calcium channels', *Cold Spring Harbor perspectives in biology*, 3(8), pp. 1–23. doi: 10.1101/CSHPERSPECT.A003947.

Cens, T. *et al.* (2006) 'Voltage- and calcium-dependent inactivation in high voltage-gated Ca2+ channels', *Progress in Biophysics and Molecular Biology*, 90(1–3), pp. 104–117. doi: 10.1016/J.PBIOMOLBIO.2005.05.013.

Cheli, V. T. *et al.* (2016a) 'Conditional deletion of the L-type calcium channel cav1.2 in oligodendrocyte progenitor cells affects postnatal myelination in mice', *Journal of*

Neuroscience, 36(42), pp. 10853–10869. doi: 10.1523/JNEUROSCI.1770-16.2016.

Cheli, V. T. *et al.* (2016b) 'L-type voltage-operated calcium channels contribute to astrocyte activation in vitro', *Glia*, 64(8), p. 1396. doi: 10.1002/GLIA.23013.

Cheli, V. T. *et al.* (2018) 'Enhanced oligodendrocyte maturation and myelination in a mouse model of Timothy syndrome', *GLIA*, 66(11), pp. 2324–2339. doi: 10.1002/glia.23468.

Chen, T. W. *et al.* (2013) 'Ultrasensitive fluorescent proteins for imaging neuronal activity', *Nature 2013 499:7458*, 499(7458), pp. 295–300. doi: 10.1038/nature12354.

Cheng, N. *et al.* (2020) 'Atypical visual processing in a mouse model of autism', *Scientific Reports*, 10(1), p. 12390. doi: 10.1038/s41598-020-68589-9.

Chokron, S. *et al.* (2020) 'The inter-relationships between cerebral visual impairment, autism and intellectual disability', *Neuroscience and biobehavioral reviews*, 114, pp. 201–210. doi: 10.1016/J.NEUBIOREV.2020.04.008.

Chokron, S., Kovarski, K. and Dutton, G. N. (2021) 'Cortical Visual Impairments and Learning Disabilities', *Frontiers in Human Neuroscience*, 15, p. 713316. doi: 10.3389/FNHUM.2021.713316/BIBTEX.

Christensen, R. H. B. (2023) 'Regression Models for Ordinal Data [R package ordinal version 2023.12-4]'. Available at: https://cran.r-project.org/package=ordinal (Accessed: 16 February 2024).

Chung, S. and Son, J. W. (2020) 'Visual perception in autism spectrum disorder: A review of neuroimaging studies', *Journal of the Korean Academy of Child and Adolescent Psychiatry*, 31(3), pp. 105–120. doi: 10.5765/jkacap.200018.

Chung, W. S., Allen, N. J. and Eroglu, C. (2015) 'Astrocytes Control Synapse Formation, Function, and Elimination', *Cold Spring Harbor Perspectives in Biology*, 7(9). doi: 10.1101/CSHPERSPECT.A020370.

Clark, M. B. *et al.* (2019) 'Long-read sequencing reveals the complex splicing profile of the psychiatric risk gene CACNA1C in human brain', *Molecular Psychiatry 2019 25:1*, 25(1), pp. 37–47. doi: 10.1038/s41380-019-0583-1.

Colgin, L. L. and Moser, E. I. (2010) 'Gamma oscillations in the hippocampus', *Physiology (Bethesda, Md.)*, 25(5), pp. 319–329. doi: 10.1152/PHYSIOL.00021.2010.

Consortium, S. W. G. of the P. G. (2014) 'Biological insights from 108 schizophrenia-associated genetic loci', *Nature*, 511(7510), pp. 421–427. Available at: http://dx.doi.org/10.1038/nature13595.

Contractor, A., Ethell, I. M. and Portera-Cailliau, C. (2021) 'Cortical interneurons in autism', *Nature neuroscience*, 24(12), pp. 1648–1659. doi: 10.1038/S41593-021-00967-6.

Corona-Rivera, J. R. *et al.* (2015) 'Unusual retrospective prenatal findings in a male newborn with Timothy syndrome type 1', *European journal of medical genetics*, 58(6–7), pp. 332–335. doi: 10.1016/J.EJMG.2015.04.001.

Costain, G. *et al.* (2016) ‘Rare copy number variations in an adult with transposition of the great arteries emphasize the importance of updated genetic assessments in syndromic congenital cardiac disease’, *International journal of cardiology*, 203, pp. 516–518. doi: 10.1016/J.IJCARD.2015.10.216.

Coulter, R. (2009) ‘Understanding the Visual Symptoms of Individuals with Autism Spectrum Disorder (ASD)’.

Craddock, R. *et al.* (2023) ‘Experience dependent plasticity of higher visual cortical areas in the mouse’, *Cerebral Cortex*, 33(15), pp. 9303–9312. doi: 10.1093/CERCOR/BHAD203.

Dalton, K. M. *et al.* (2005) ‘Gaze fixation and the neural circuitry of face processing in autism’, *Nature Neuroscience 2005 8:4*, 8(4), pp. 519–526. doi: 10.1038/nn1421.

Davis, R. A. O. *et al.* (2006) ‘Subjective perceptual distortions and visual dysfunction in children with autism’, *Journal of autism and developmental disorders*, 36(2), pp. 199–210. doi: 10.1007/S10803-005-0055-0.

Dedic, N. *et al.* (2018) ‘Cross-disorder risk gene CACNA1C differentially modulates susceptibility to psychiatric disorders during development and adulthood’, *Molecular Psychiatry*, 23(3), p. 533. doi: 10.1038/MP.2017.133.

Delinière, A. *et al.* (2023) ‘Phenotypic Characterization of Timothy Syndrome Caused by the CACNA1C p.Gly402Ser Variant’, *Circulation. Genomic and precision medicine*, 16(3), pp. 280–282. doi: 10.1161/CIRCGEN.122.004010.

Deng, P. Y. *et al.* (2013) ‘FMRP regulates neurotransmitter release and synaptic information transmission by modulating action potential duration via BK channels’, *Neuron*, 77(4), pp. 696–711. doi: 10.1016/J.NEURON.2012.12.018.

Deng, P. Y. and Klyachko, V. A. (2016) ‘Increased Persistent Sodium Current Causes Neuronal Hyperexcitability in the Entorhinal Cortex of Fmr1 Knockout Mice’, *Cell Reports*, 16(12), pp. 3157–3166. doi: 10.1016/J.CELREP.2016.08.046.

Deng, P. Y., Sojka, D. and Klyachko, V. A. (2011) ‘Abnormal Presynaptic Short-Term Plasticity and Information Processing in a Mouse Model of Fragile X Syndrome’, *Journal of Neuroscience*, 31(30), pp. 10971–10982. doi: 10.1523/JNEUROSCI.2021-11.2011.

Dick, I. E. *et al.* (2016) ‘Arrhythmogenesis in Timothy Syndrome is associated with defects in Ca2+-dependent inactivation’, *Nature Communications*, 7. doi: 10.1038/ncomms10370.

Diep, V. and Seaver, L. H. (2015) ‘Long QT syndrome with craniofacial, digital, and neurologic features: Is it useful to distinguish between timothy syndrome types 1 and 2?’, *American Journal of Medical Genetics, Part A*, 167(11), pp. 2780–2785. doi: 10.1002/ajmg.a.37258.

Distler, C. and Hoffmann, K. P. (2011) ‘The optokinetic reflex’, *The Oxford Handbook of Eye Movements*. doi: 10.1093/OXFORDHB/9780199539789.013.0004.

Dolphin, A. C. (2012) ‘Calcium channel auxiliary α2δ and β subunits: trafficking and one step beyond’, *Nature Reviews Neuroscience 2012 13:8*, 13(8), pp. 542–555. doi:

10.1038/nrn3311.

Dönmez, Y. E. *et al.* (2020) ‘Is contrast sensitivity a physiological marker in attention-deficit hyperactivity disorder?’, *Medical hypotheses*, 145. doi: 10.1016/J.MEHY.2020.110326.

Drum, B. M. L. *et al.* (2014) ‘Cellular mechanisms of ventricular arrhythmias in a mouse model of Timothy syndrome (long QT syndrome 8)’, *Journal of molecular and cellular cardiology*, 66, pp. 63–71. doi: 10.1016/J.YJMCC.2013.10.021.

Dufendach, K. A. *et al.* (2013) ‘Maternal mosaicism confounds the neonatal diagnosis of type 1 Timothy syndrome’, *Pediatrics*, 131(6). doi: 10.1542/PEDS.2012-2941.

Dufendach, K. A. *et al.* (2018) ‘Clinical Outcomes and Modes of Death in Timothy Syndrome: A Multicenter International Study of a Rare Disorder’, *JACC: Clinical Electrophysiology*, 4(4), pp. 459–466. doi: 10.1016/j.jacep.2017.08.007.

Ehlinger, D. G. and Commons, K. G. (2017) ‘Altered Cav1.2 function in the Timothy syndrome mouse model produces ascending serotonergic abnormalities’, *European Journal of Neuroscience*, 46(8), pp. 2416–2425. doi: 10.1111/ejn.13707.

Ergül, Y. *et al.* (2015) ‘A rare association with suffered cardiac arrest, long qt interval, and syndactyly: Timothy syndrome (LQT-8)’, *Anadolu Kardiyoloji Dergisi*. AVES Ibrahim Kara, pp. 672–674. doi: 10.5152/AnatolJCardiol.2015.6315.

Erk, S. *et al.* (2014) ‘Replication of brain function effects of a genome-wide supported psychiatric risk variant in the CACNA1C gene and new multi-locus effects’, *NeuroImage*, 94, pp. 147–154. doi: 10.1016/J.NEUROIMAGE.2014.03.007.

Ermentrout, B., Pascal, M. and Gutkin, B. (no date) *The Effects of Spike Frequency Adaptation and Negative Feedback on the Synchronization of Neural Oscillators*.

Ermentrout, G. B. and Kopell, N. (1998) ‘Fine structure of neural spiking and synchronization in the presence of conduction delays’, *Proceedings of the National Academy of Sciences of the United States of America*, 95(3), pp. 1259–1264. doi: 10.1073/pnas.95.3.1259.

Etheridge, S. P. *et al.* (2011) ‘Somatic mosaicism contributes to phenotypic variation in Timothy syndrome’, *American Journal of Medical Genetics, Part A*, 155(10), pp. 2578–2583. doi: 10.1002/ajmg.a.34223.

Fam, J. *et al.* (2013) ‘Visual contrast sensitivity in major depressive disorder’, *Journal of psychosomatic research*, 75(1), pp. 83–86. doi: 10.1016/J.JPSYCHORES.2013.03.008.

Feng, L. *et al.* (2013) ‘A Laser-induced Mouse Model of Chronic Ocular Hypertension to Characterize Visual Defects’, *Journal of Visualized Experiments : JoVE*, (78), p. 50440. doi: 10.3791/50440.

Fernandez-Ruiz, A. *et al.* (2023) ‘Over and above frequency: Gamma oscillations as units of neural circuit operations’, *Neuron*, 111(7), pp. 936–953. doi: 10.1016/J.NEURON.2023.02.026.

Fernández-Ruiz, A. *et al.* (2021) ‘Gamma rhythm communication between entorhinal cortex and dentate gyrus neuronal assemblies', *Science (New York, N.Y.)*, 372(6537). doi: 10.1126/SCIENCE.ABF3119.

Filice, F. *et al.* (2016) 'Reduction in parvalbumin expression not loss of the parvalbumin-expressing GABA interneuron subpopulation in genetic parvalbumin and shank mouse models of autism', *Molecular Brain*, 9(1), pp. 1–17. doi: 10.1186/S13041-016-0192-8/METRICS.

Filice, F. *et al.* (2020) 'The Parvalbumin Hypothesis of Autism Spectrum Disorder', *Frontiers in Cellular Neuroscience*, 14, p. 577525. doi: 10.3389/FNCEL.2020.577525/BIBTEX.

Forstmeier, W., Wagenmakers, E. J. and Parker, T. H. (2017) 'Detecting and avoiding likely false-positive findings – a practical guide', *Biological Reviews*, 92(4), pp. 1941–1968. doi: 10.1111/BRV.12315.

Fröhler, S. *et al.* (2014) 'Exome sequencing helped the fine diagnosis of two siblings afflicted with atypical Timothy syndrome (TS2)', *BMC Medical Genetics*, 15(1), p. 48. doi: 10.1186/1471-2350-15-48.

Galvez-Contreras, A. Y. *et al.* (2020) 'Role of Oligodendrocytes and Myelin in the Pathophysiology of Autism Spectrum Disorder', *Brain Sciences*, 10(12), pp. 1–17. doi: 10.3390/BRAINSCI10120951.

Gandal, M. J. *et al.* (2010) 'Validating gamma oscillations and delayed auditory responses as translational biomarkers of autism', *Biological psychiatry*, 68(12), p. 1100. doi: 10.1016/J.BIOPSYCH.2010.09.031.

Gao, Y. *et al.* (2013) 'Inhibition of late sodium current by mexiletine: a novel pharmotherapeutical approach in timothy syndrome', *Circulation. Arrhythmia and electrophysiology*, 6(3), pp. 614–622. doi: 10.1161/CIRCEP.113.000092.

Gershon, E. S. *et al.* (2014) 'A rare mutation of CACNA1C in a patient with bipolar disorder, and decreased gene expression associated with a bipolar-associated common SNP of CACNA1C in brain', *Molecular Psychiatry*, 19(8), pp. 890–894. doi: 10.1038/mp.2013.107.

Geschwind, D. H. (2008) 'Autism: Many Genes, Common Pathways?', *Cell*, 135(3), p. 391. doi: 10.1016/J.CELL.2008.10.016.

Gibson, J. R. *et al.* (2008) 'Imbalance of neocortical excitation and inhibition and altered UP states reflect network hyperexcitability in the mouse model of fragile X syndrome', *Journal of neurophysiology*, 100(5), pp. 2615–2626. doi: 10.1152/JN.90752.2008.

Gillis, J. *et al.* (2012) 'Long QT, syndactyly, joint contractures, stroke and novel CACNA1C mutation: Expanding the spectrum of Timothy syndrome', *American Journal of Medical Genetics, Part A*, 158 A(1), pp. 182–187. doi: 10.1002/ajmg.a.34355.

Godoy, L. D. *et al.* (2022) 'Parvalbumin Role in Epilepsy and Psychiatric Comorbidities: From Mechanism to Intervention', *Frontiers in Integrative Neuroscience*, 16, p. 765324. doi: 10.3389/FNINT.2022.765324/BIBTEX.

Goff, K. M. and Goldberg, E. M. (2021) 'A Role for VIP Interneurons in

Neurodevelopmental Disorders', *Developmental neuroscience*, 43(3–4), p. 168. doi: 10.1159/000515264.

Gogolla, N. *et al.* (2009) 'Common circuit defect of excitatory-inhibitory balance in mouse models of autism', *Journal of neurodevelopmental disorders*, 1(2), pp. 172–181. doi: 10.1007/S11689-009-9023-X.

Gomes, A. R. *et al.* (2020) 'Modeling Rett Syndrome With Human Patient-Specific Forebrain Organoids', *Frontiers in Cell and Developmental Biology*, 8, p. 610427. doi: 10.3389/FCELL.2020.610427/BIBTEX.

Gray, D. T. *et al.* (2013) 'Parvalbumin increases in the medial and lateral geniculate nuclei of aged rhesus macaques', *Frontiers in Aging Neuroscience*, 5(NOV), p. 63795. doi: 10.3389/FNAGI.2013.00069/BIBTEX.

Van Groen, T. and Wyss, J. M. (2003) 'Connections of the retrosplenial granular b cortex in the rat', *The Journal of Comparative Neurology*, 463(3), pp. 249–263. doi: 10.1002/cne.10757.

Gu, N., Vervaeke, K. and Storm, J. F. (2007) 'BK potassium channels facilitate high-frequency firing and cause early spike frequency adaptation in rat CA1 hippocampal pyramidal cells', *The Journal of Physiology*, 580(Pt 3), p. 859. doi: 10.1113/JPHYSIOL.2006.126367.

Guan, A. *et al.* (2022) 'The role of gamma oscillations in central nervous system diseases: Mechanism and treatment', *Frontiers in Cellular Neuroscience*, 16. doi: 10.3389/FNCEL.2022.962957.

Guy, J. *et al.* (2016) 'The developmental trajectory of contrast sensitivity in autism spectrum disorder', *Autism Research*, 9(8), pp. 866–878. doi: 10.1002/AUR.1579.

Hall MH *et al.* (2009) 'The early auditory gamma-band response is heritable and a putative endophenotype of schizophrenia.', *Schizophrenia Bulletin*, 37(4), pp. 778–787. doi: 10.1093/SCHBUL.

Hammer, M. *et al.* (2015) 'Perturbed Hippocampal Synaptic Inhibition and γ-Oscillations in a Neuroligin-4 Knockout Mouse Model of Autism', *Cell reports*, 13(3), p. 516. doi: 10.1016/J.CELREP.2015.09.011.

Han, H. *et al.* (2020) 'Clinical characterization and outcome of prolonged heart rate-corrected QT interval among children with syndactyly', *Medicine*, 99(42). doi: 10.1097/MD.0000000000022740.

Hartung, T. (2008) 'Thoughts on limitations of animal models', *Parkinsonism & Related Disorders*, 14(SUPPL.2), pp. S81–S83. doi: 10.1016/J.PARKRELDIS.2008.04.003.

Hashemi, E. *et al.* (2017) 'The Number of Parvalbumin-Expressing Interneurons Is Decreased in the Prefrontal Cortex in Autism', *Cerebral Cortex*, 27(3), pp. 1931–1943. doi: 10.1093/CERCOR/BHW021.

Hell, J. W. *et al.* (1993) 'Identification and differential subcellular localization of the neuronal class C and class D L-type calcium channel α1 subunits', *Journal of Cell Biology*, 123(4), pp. 949–962. doi: 10.1083/jcb.123.4.949.

Hennessey, J. A. *et al.* (2014) ‘A CACNA1C Variant Associated with Reduced Voltage-Dependent Inactivation, Increased CaV1.2 Channel Window Current, and Arrhythmogenesis’, *PLoS ONE*, 9(9). doi: 10.1371/JOURNAL.PONE.0106982.

Hermida, A. *et al.* (2021) ‘Long-term follow-up of a patient with type 2 Timothy syndrome and the partial efficacy of mexiletine’, *Gene*, 777. doi: 10.1016/J.GENE.2021.145465.

Hermida, A. *et al.* (2022) ‘Use of ranolazine as rescue therapy in a patient with Timothy syndrome type 2’, *Revista espanola de cardiologia (English ed.)*, 75(5), pp. 447–448. doi: 10.1016/J.REC.2021.11.003.

Herve, M. (2023) *CRAN - Package RVAideMemoire*. Available at: https://cran.r-project.org/web/packages/RVAideMemoire/index.html (Accessed: 20 February 2024).

Hiippala, A. *et al.* (2015) ‘Expanding the phenotype of Timothy syndrome type 2: an adolescent with ventricular fibrillation but normal development’, *American journal of medical genetics. Part A*, 167A(3), pp. 629–634. doi: 10.1002/AJMG.A.36924.

Hodgkin, A. L. and Huxley, A. F. (1952) ‘A quantitative description of membrane current and its application to conduction and excitation in nerve’, *The Journal of Physiology*, 117(4), pp. 500–544. doi: 10.1113/jphysiol.1952.sp004764.

Hofmann, F. *et al.* (2014) ‘L-type CaV1.2 calcium channels: From in vitro findings to in vivo function’, *Physiological Reviews*, 94(1), pp. 303–326. doi: 10.1152/PHYSREV.00016.2013/ASSET/IMAGES/LARGE/Z9J0011426780003.JPEG.

Hollins, B. and Ikeda, S. R. (1996) ‘Inward currents underlying action potentials in rat adrenal chromaffin cells’, *https://doi.org/10.1152/jn.1996.76.2.1195*, 76(2), pp. 1195–1211. doi: 10.1152/JN.1996.76.2.1195.

Honeycutt, J. A. *et al.* (2016) ‘Developmental Age Differentially Mediates the Calcium-Binding Protein Parvalbumin in the Rat: Evidence for a Selective Decrease in Hippocampal Parvalbumin Cell Counts’, *Developmental neuroscience*, 38(2), pp. 105–114. doi: 10.1159/000444447.

Hong, L. E. *et al.* (2004) ‘Evoked gamma band synchronization and the liability for schizophrenia’, in *Schizophrenia Research*, pp. 293–302. doi: 10.1016/j.schres.2003.12.011.

Horigane, S. ichiro *et al.* (2020) ‘A mouse model of Timothy syndrome exhibits altered social competitive dominance and inhibitory neuron development’, *FEBS Open Bio*, 10(8), pp. 1436–1446. doi: 10.1002/2211-5463.12924.

Hothorn, T. *et al.* (2023) ‘Simultaneous Inference in General Parametric Models [R package multcomp version 1.4-25]’. Available at: https://cran.r-project.org/package=multcomp (Accessed: 16 February 2024).

Huh, C. Y. L. *et al.* (2016) ‘Excitatory inputs determine phase-locking strength and spike-timing of CA1 stratum oriens/alveus parvalbumin and somatostatin interneurons during intrinsically generated hippocampal theta rhythm’, *Journal of Neuroscience*, 36(25), pp. 6605–6622. doi: 10.1523/JNEUROSCI.3951-13.2016.

Hussman, J. P. (2001) ‘Suppressed GABAergic inhibition as a common factor in suspected etiologies of autism’, *Journal of autism and developmental disorders*, 31(2), pp. 247–248. doi: 10.1023/A:1010715619091.

Jacobs, A. *et al.* (2006) ‘Verapamil decreases ventricular tachyarrhythmias in a patient with Timothy syndrome (LQT8)’, *Heart rhythm*, 3(8), pp. 967–970. doi: 10.1016/J.HRTHM.2006.04.024.

Jiang, M. and Swann, J. W. (2005) ‘A role for L-type calcium channels in the maturation of parvalbumin-containing hippocampal interneurons’, *Neuroscience*, 135(3), pp. 839–850. doi: 10.1016/j.neuroscience.2005.06.073.

Jiruska, P. *et al.* (2013) ‘Synchronization and desynchronization in epilepsy: controversies and hypotheses’, *The Journal of Physiology*, 591(4), pp. 787–797. doi: 10.1113/JPHYSIOL.2012.239590.

Kadivar, A. *et al.* (2023) ‘58. The Potential Use of Visual Contrast Sensitivity as a Biomarker in Early Psychosis Patients’, *Biological Psychiatry*, 93(9), p. S117. doi: 10.1016/j.biopsych.2023.02.298.

Kalaska, J. *et al.* (1995) ‘Synchronization of neuronal activity in hippocampus by individual GABAergic interneurons’, *Nature 1995 378:6552*, 378(6552), pp. 75–78. doi: 10.1038/378075a0.

Kallas, D. *et al.* (2018) ‘Dynamic Electrocardiographic Abnormalities Captured in Timothy Syndrome’, *JACC. Clinical electrophysiology*, 4(11), pp. 1486–1487. doi: 10.1016/J.JACEP.2018.06.019.

Kamijo, S. *et al.* (2018) ‘A Critical Neurodevelopmental Role for L-Type Voltage-Gated Calcium Channels in Neurite Extension and Radial Migration’, *The Journal of Neuroscience*, 38(24), p. 5551. doi: 10.1523/JNEUROSCI.2357-17.2018.

Kaplan, D. I., Isom, L. L. and Petrou, S. (2016) ‘Role of Sodium Channels in Epilepsy’, *Cold Spring Harbor Perspectives in Medicine*, 6(6). doi: 10.1101/CSHPERSPECT.A022814.

Kawaida, M. *et al.* (2016) ‘A case of Timothy syndrome with adrenal medullary dystrophy’, *Pathology International*, 66(10), pp. 587–592. doi: 10.1111/pin.12456.

Kéïta, L. *et al.* (2014) ‘An early origin for detailed perception in Autism Spectrum Disorder: Biased sensitivity for high-spatial frequency information’, *Scientific Reports*, 4(1), pp. 1–6. doi: 10.1038/srep05475.

Kikuchi, M. *et al.* (2011) ‘Frontal areas contribute to reduced global coordination of resting-state gamma activities in drug-naïve patients with schizophrenia’, *Schizophrenia Research*, 130(1–3), pp. 187–194. doi: 10.1016/j.schres.2011.06.003.

Kleiner, M. *et al.* (2007) ‘What’s new in psychtoolbox-3’, *Perception*, 36(14), pp. 1–16. Available at: https://nyuscholars.nyu.edu/en/publications/whats-new-in-psychtoolbox-3 (Accessed: 15 February 2024).

Knowles, J. K. *et al.* (2022) ‘Maladaptive myelination promotes generalized epilepsy progression’, *Nature Neuroscience*, 25(5), p. 596. doi: 10.1038/S41593-022-01052-2.

Kogan, C. S. *et al.* (2004) ‘Differential impact of the FMR1 gene on visual processing in fragile X syndrome’, *Brain : a journal of neurology*, 127(Pt 3), pp. 591–601. doi: 10.1093/BRAIN/AWH069.

Koh, H. C., Milne, E. and Dobkins, K. (2010) ‘Spatial contrast sensitivity in adolescents with autism spectrum disorders’, *Journal of Autism and Developmental Disorders*, 40(8), pp. 978–987. doi: 10.1007/S10803-010-0953-7/FIGURES/2.

Kopell, N. *et al.* (2010) ‘Gamma and Theta Rhythms in Biophysical Models of Hippocampal Circuits’, in *Hippocampal Microcircuits*. Springer New York, pp. 423–457. doi: 10.1007/978-1-4419-0996-1_15.

Korkosh, V. S. *et al.* (2019) ‘Atomic mechanisms of Timothy syndrome-associated mutations in calcium channel Cav1.2’, *Frontiers in Physiology*, 10(MAR), p. 402639. doi: 10.3389/FPHYS.2019.00335/BIBTEX.

Kosaki, R. *et al.* (2018) ‘Timothy syndrome-like condition with syndactyly but without prolongation of the QT interval’, *American Journal of Medical Genetics Part A*, 176(7), pp. 1657–1661. doi: 10.1002/AJMG.A.38833.

Kothe, C. (no date) *Fast serialize/deserialize - File Exchange - MATLAB Central*. Available at: https://www.mathworks.com/matlabcentral/fileexchange/34564-fast-serialize-deserialize (Accessed: 16 February 2024).

Kourdougli, N. *et al.* (2023) ‘Improvement of sensory deficits in fragile X mice by increasing cortical interneuron activity after the critical period’, *Neuron*, 111(18), pp. 2863-2880.e6. doi: 10.1016/J.NEURON.2023.06.009.

Kozono, N. *et al.* (2020) ‘Gamma power abnormalities in a Fmr1-targeted transgenic rat model of fragile X syndrome’, *Scientific reports*, 10(1). doi: 10.1038/S41598-020-75893-X.

Krause, U. *et al.* (2011) ‘A rare association of long QT syndrome and syndactyly: Timothy Syndrome (LQT 8)’, *Clinical Research in Cardiology*. Springer, pp. 1123–1127. doi: 10.1007/s00392-011-0358-4.

Krey, J. F. *et al.* (2013) ‘Timothy syndrome is associated with activity-dependent dendritic retraction in rodent and human neurons’, *Nature neuroscience*, 16(2), pp. 201–209. doi: 10.1038/NN.3307.

Kumar, D. *et al.* (2015) ‘ Cacna1c (Cav1.2) Modulates Electroencephalographic Rhythm and Rapid Eye Movement Sleep Recovery ’, *Sleep*, 38(9), pp. 1371–1380. doi: 10.5665/sleep.4972.

Kummer, S. *et al.* (2022) ‘Hyperinsulinemic Hypoglycemia Associated with a CaV1.2 Variant with Mixed Gain- and Loss-of-Function Effects’, *International Journal of Molecular Sciences*, 23(15), p. 8097. doi: 10.3390/IJMS23158097/S1.

Kwakye, L. D. *et al.* (2011) ‘Altered auditory and multisensory temporal processing in autism spectrum disorders’, *Frontiers in Integrative Neuroscience*, (JANUARFY 2011). doi: 10.3389/FNINT.2010.00129.

Lauber, E., Filice, F. and Schwaller, B. (2016) ‘Prenatal Valproate Exposure Differentially

Affects Parvalbumin-Expressing Neurons and Related Circuits in the Cortex and Striatum of Mice', *Frontiers in molecular neuroscience*, 9(DEC2016). doi: 10.3389/FNMOL.2016.00150.

Lawrence, Y. A. *et al.* (2010) 'Parvalbumin-, calbindin-, and calretinin-immunoreactive hippocampal interneuron density in autism', *Acta neurologica Scandinavica*, 121(2), pp. 99–108. doi: 10.1111/J.1600-0404.2009.01234.X.

Lee, F. H. F. *et al.* (2019) 'Altered cortical Cytoarchitecture in the Fmr1 knockout mouse', *Molecular Brain*, 12(1), pp. 1–12. doi: 10.1186/S13041-019-0478-8/FIGURES/5.

Leitch, B. *et al.* (2009) 'Subcellular distribution of L-type calcium channel subtypes in rat hippocampal neurons', *Neuroscience*, 164(2), pp. 641–657. doi: 10.1016/J.NEUROSCIENCE.2009.08.006.

Leopold, D. A. (2012) 'Primary visual cortex, awareness and blindsight', *Annual review of neuroscience*, 35, p. 91. doi: 10.1146/ANNUREV-NEURO-062111-150356.

Li, J. *et al.* (2015) 'Schizophrenia Related Variants in CACNA1C also Confer Risk of Autism', *PLOS ONE*. Edited by D. Zheng, 10(7), p. e0133247. doi: 10.1371/journal.pone.0133247.

Lingle, C. J. *et al.* (2018) 'Roles of Na+, Ca2+, and K+ channels in the generation of repetitive firing and rhythmic bursting in adrenal chromaffin cells', *Pflugers Archiv : European journal of physiology*, 470(1), p. 39. doi: 10.1007/S00424-017-2048-1.

Liu, Y. *et al.* (2011) 'Meta-analysis of genome-wide association data of bipolar disorder and major depressive disorder', *Molecular Psychiatry*, pp. 2–4. doi: 10.1038/mp.2009.107.

Liu, Z. *et al.* (2022) 'Sustained deep-tissue voltage recording using a fast indicator evolved for two-photon microscopy', *Cell*, 185(18), pp. 3408-3425.e29. doi: 10.1016/J.CELL.2022.07.013.

Lu, A. T.-H. *et al.* (2012) 'Support for calcium channel gene defects in autism spectrum disorders', *Molecular Autism*, 3(1), p. 18. doi: 10.1186/2040-2392-3-18.

Luque, M. A. *et al.* (2017) 'Excitability is increased in hippocampal CA1 pyramidal cells of Fmr1 knockout mice', *PLoS ONE*, 12(9). doi: 10.1371/JOURNAL.PONE.0185067.

Mably, A. J. and Colgin, L. L. (2018) 'Gamma oscillations in cognitive disorders', *Current Opinion in Neurobiology*, 52, pp. 182–187. doi: 10.1016/J.CONB.2018.07.009.

Magloire, V. *et al.* (2019) 'GABAergic Interneurons in Seizures: Investigating Causality WithOptogenetics', *The Neuroscientist*, 25(4), p. 344. doi: 10.1177/1073858418805002.

Mangiafico, S. (2023) 'Functions to Support Extension Education Program Evaluation [R package rcompanion version 2.4.34]'. Available at: https://cran.r-project.org/package=rcompanion (Accessed: 16 February 2024).

Marcantoni, A. *et al.* (2008) 'Calcium channels in chromaffin cells: focus on L and T types', *Acta Physiologica*, 192(2), pp. 233–246. doi: 10.1111/J.1748-1716.2007.01815.X.

Marco, E. J. *et al.* (2011) 'Sensory processing in autism: A review of neurophysiologic findings', *Pediatric Research*, 69(5 PART 2), pp. 48–54. doi: 10.1203/PDR.0b013e3182130c54.

Matsui, M. *et al.* (2023) 'Multiple beta cell-independent mechanisms drive hypoglycemia in Timothy syndrome', *bioRxiv*, p. 2023.06.16.544987. doi: 10.1101/2023.06.16.544987.

McCleery, J. P. *et al.* (2007) 'Abnormal magnocellular pathway visual processing in infants at risk for autism', *Biological psychiatry*, 62(9), pp. 1007–1014. doi: 10.1016/J.BIOPSYCH.2007.02.009.

McKendrick, A. M. *et al.* (2007) 'Contrast Sensitivity Changes Due to Glaucoma and Normal Aging: Low-Spatial-Frequency Losses in Both Magnocellular and Parvocellular Pathways', *Investigative Ophthalmology & Visual Science*, 48(5), pp. 2115–2122. doi: 10.1167/IOVS.06-1208.

Mesirca, P. *et al.* (2024) 'Selective blockade of Cav1.2 (α1C) versus Cav1.3 (α1D) L-type calcium channels by the black mamba toxin calciseptine', *Nature Communications 2024 15:1*, 15(1), pp. 1–12. doi: 10.1038/s41467-023-43502-w.

Metzner, C. *et al.* (2022) 'The effect of alterations of schizophrenia-associated genes on gamma band oscillations', *Schizophrenia 2022 8:1*, 8(1), pp. 1–10. doi: 10.1038/s41537-022-00255-7.

Milne, E. and Buckley, D. (2010) 'Contrast sensitivity thresholds in children with autistic spectrum disorder', *British and Irish Orthoptic Journal*, 7(0), p. 62. doi: 10.22599/BIOJ.29.

Minio-Paluello, I. *et al.* (2020) 'Face individual identity recognition: a potential endophenotype in autism', *Molecular Autism 2020 11:1*, 11(1), pp. 1–16. doi: 10.1186/S13229-020-00371-0.

Mio, C. *et al.* (2020) 'CACNA1C haploinsufficiency accounts for the common features of interstitial 12p13.33 deletion carriers', *European journal of medical genetics*, 63(4). doi: 10.1016/J.EJMG.2020.103843.

Moon, A. L. *et al.* (2018) 'CACNA1C: Association with psychiatric disorders, behavior, and neurogenesis', *Schizophrenia Bulletin*, 44(5), pp. 958–965. doi: 10.1093/schbul/sby096.

Moon, A. L. (2018) 'The impact of genetic variation in Cacna1c and prepubertal stress on hippocampal function'.

Moore, S. J. and Murphy, G. G. (2020) 'The Role of L-Type Calcium Channels in Neuronal Excitability and Aging', *Neurobiology of learning and memory*, 173, p. 107230. doi: 10.1016/J.NLM.2020.107230.

Mottron, L. *et al.* (2006) 'Enhanced perceptual functioning in autism: an update, and eight principles of autistic perception', *Journal of autism and developmental disorders*, 36(1), pp. 27–43. doi: 10.1007/S10803-005-0040-7.

Muller, C. L., Anacker, A. M. J. and Veenstra-VanderWeele, J. (2016) 'The serotonin system in autism spectrum disorder: from biomarker to animal models', *Neuroscience*, 321, p. 24. doi: 10.1016/J.NEUROSCIENCE.2015.11.010.

Nakagawa, S. and Schielzeth, H. (2013) ‘A general and simple method for obtaining R2 from generalized linear mixed-effects models’, *Methods in Ecology and Evolution*, 4(2), pp. 133–142. doi: 10.1111/J.2041-210X.2012.00261.X.

‘Neurodevelopmental Disorders’ (2013) in *Diagnostic and Statistical Manual of Mental Disorders*. American Psychiatric Association. doi: 10.1176/appi.books.9780890425596.dsm01.

Niemeyer, J. E. and Paradiso, M. A. (2017) ‘Sensory Processing: Contrast sensitivity, V1 neural activity, and natural vision’, *Journal of Neurophysiology*, 117(2), p. 492. doi: 10.1152/JN.00635.2016.

Overbeek, B. U. H. *et al.* (2018) ‘Are visual functions diagnostic signs of the minimally conscious state? an integrative review’, *Journal of Neurology*, 265(9), p. 1957. doi: 10.1007/S00415-018-8788-9.

Ozawa, J. *et al.* (2018) ‘A novel CACNA1C mutation identified in a patient with Timothy syndrome without syndactyly exerts both marked loss- and gain-of-function effects’, *HeartRhythm case reports*, 4(7), pp. 273–277. doi: 10.1016/J.HRCR.2018.03.003.

Ozawa, J. *et al.* (2022) ‘Increased CaV1.2 late current by a CACNA1C p.R412M variant causes an atypical Timothy syndrome without syndactyly’, *Scientific reports*, 12(1). doi: 10.1038/S41598-022-23512-2.

Pachitariu, M. *et al.* (2016) ‘Suite2p: beyond 10,000 neurons with standard two-photon microscopy’, *bioRxiv*, p. 061507. doi: 10.1101/061507.

Panagiotakos, G. *et al.* (2019) ‘Aberrant calcium channel splicing drives defects in cortical differentiation in timothy syndrome’, *eLife*, 8. doi: 10.7554/ELIFE.51037.

Pape, H. C. (1996) ‘Queer current and pacemaker: the hyperpolarization-activated cation current in neurons’, *Annual review of physiology*, 58, pp. 299–327. doi: 10.1146/ANNUREV.PH.58.030196.001503.

Parikshak, N. N. *et al.* (2016) ‘Genome-wide changes in lncRNA, splicing, and regional gene expression patterns in autism’, *Nature*, 540(7633), pp. 423–427. doi: 10.1038/NATURE20612.

Parton, L. E. *et al.* (2007) ‘Glucose sensing by POMC neurons regulates glucose homeostasis and is impaired in obesity’, *Nature*, 449(7159), pp. 228–232. doi: 10.1038/NATURE06098.

Pasca, A. M. *et al.* (2015) ‘Functional cortical neurons and astrocytes from human pluripotent stem cells in 3D culture’, *Nature Methods 2015 12:7*, 12(7), pp. 671–678. doi: 10.1038/nmeth.3415.

Paşca, S. P. *et al.* (2011) ‘Using iPSC-derived neurons to uncover cellular phenotypes associated with Timothy syndrome’, *Nature Medicine*, 17(12), pp. 1657–1662. doi: 10.1038/nm.2576.

Patel, D. C. *et al.* (2019) ‘Neuron–glia interactions in the pathophysiology of epilepsy’, *Nature Reviews Neuroscience 2019 20:5*, 20(5), pp. 282–297. doi: 10.1038/s41583-019-0126-4.

Paterno, R. *et al.* (2021) ‘Hippocampal gamma and sharp-wave ripple oscillations are altered in a Cntnap2 mouse model of autism spectrum disorder’, *Cell Reports*, 37(6), p. 109970. doi: 10.1016/j.celrep.2021.109970.

Paterno, R., Casalia, M. and Baraban, S. C. (2020) ‘Interneuron deficits in neurodevelopmental disorders: Implications for disease pathology and interneuron-based therapies’, *European journal of paediatric neurology : EJPN : official journal of the European Paediatric Neurology Society*, 24, p. 81. doi: 10.1016/J.EJPN.2019.12.015.

Pelphrey, K. A. *et al.* (2002) ‘Visual Scanning of Faces in Autism’, *Journal of Autism and Developmental Disorders*, 32(4), pp. 249–261. doi: 10.1023/A:1016374617369/METRICS.

Perche, O. *et al.* (2021) ‘Electroretinography and contrast sensitivity, complementary translational biomarkers of sensory deficits in the visual system of individuals with fragile X syndrome’, *Journal of Neurodevelopmental Disorders 2021 13:1*, 13(1), pp. 1–19. doi: 10.1186/S11689-021-09375-0.

Perneger, T. V. (1998) ‘What’s wrong with Bonferroni adjustments’, *BMJ : British Medical Journal*, 316(7139), p. 1236. doi: 10.1136/BMJ.316.7139.1236.

Petkov, G. V. (2009) ‘Ion Channels’, *Pharmacology*, pp. 387–427. doi: 10.1016/B978-0-12-369521-5.00016-6.

Philipp, L. R. and Rodriguez, F. H. (2016) ‘Cardiac Arrest Refractory to Standard Intervention in Atypical Timothy Syndrome (Lqt8 Type 2)’, *Baylor University Medical Center Proceedings*, 29(2), pp. 160–162. doi: 10.1080/08998280.2016.11929398.

Pitt, G. S. *et al.* (2001) ‘Molecular Basis of Calmodulin Tethering and Ca2+-dependent Inactivation of L-type Ca2+ Channels’, *Journal of Biological Chemistry*, 276(33), pp. 30794–30802. doi: 10.1074/jbc.M104959200.

Plumbly, W. *et al.* (2019) ‘L-type voltage-gated calcium channel regulation of in vitro human cortical neuronal networks’, *Scientific Reports*, 9(1), pp. 1–12. doi: 10.1038/s41598-019-50226-9.

Po’, C. *et al.* (2019) ‘Photosensitive epilepsy and long QT: expanding Timothy syndrome phenotype’, *Clinical neurophysiology : official journal of the International Federation of Clinical Neurophysiology*, 130(11), pp. 2134–2136. doi: 10.1016/J.CLINPH.2019.09.003.

Pollali, E., Hollnagel, J.-O. and Çalışkan, G. (2021) ‘Hippocampal gamma-band oscillopathy in a mouse model of Fragile X Syndrome’, *bioRxiv*, p. 2021.04.24.441239. doi: 10.1101/2021.04.24.441239.

Pologruto, T. A., Sabatini, B. L. and Svoboda, K. (2003) ‘ScanImage: Flexible software for operating laser scanning microscopes’, *BioMedical Engineering Online*, 2(1), p. 13. doi: 10.1186/1475-925X-2-13.

Powell, A. *et al.* (2020) ‘Stable Encoding of Visual Cues in the Mouse Retrosplenial Cortex’, *Cerebral Cortex*, 30, pp. 4424–4437. doi: 10.1093/cercor/bhaa030.

Powell, K. L. *et al.* (2014) 'Low threshold T-type calcium channels as targets for novel epilepsy treatments', *British Journal of Clinical Pharmacology*, 77(5), p. 729. doi: 10.1111/BCP.12205.

Prusky, G. T. *et al.* (2004) 'Rapid quantification of adult and developing mouse spatial vision using a virtual optomotor system', *Investigative Ophthalmology and Visual Science*, 45(12), pp. 4611–4616. doi: 10.1167/iovs.04-0541.

Prusky, G. T. and Douglas, R. M. (2004) 'Characterization of mouse cortical spatial vision', *Vision research*, 44(28), pp. 3411–3418. doi: 10.1016/J.VISRES.2004.09.001.

Ramachandran, K. V. *et al.* (2013) 'Calcium influx through L-type CaV1.2 Ca2+ channels regulates mandibular development', *The Journal of clinical investigation*, 123(4), pp. 1638–1646. doi: 10.1172/JCI66903.

Ranson, A. (2017) 'Stability and Plasticity of Contextual Modulation in the Mouse Visual Cortex', *Cell Reports*, 18(4), pp. 840–848. doi: 10.1016/j.celrep.2016.12.080.

Rendall, A. R. *et al.* (2017) 'Auditory Processing Enhancements in the TS2-Neo Mouse Model of Timothy Syndrome, a Rare Genetic Disorder Associated with Autism Spectrum Disorders', *Advances in Neurodevelopmental Disorders*, 1(3), pp. 176–189. doi: 10.1007/s41252-017-0029-1.

Righes Marafiga, J., Vendramin Pasquetti, M. and Calcagnotto, M. E. (2021) 'GABAergic interneurons in epilepsy: More than a simple change in inhibition', *Epilepsy & Behavior*, 121, p. 106935. doi: 10.1016/J.YEBEH.2020.106935.

Ripke, S. *et al.* (2014) 'Biological insights from 108 schizophrenia-associated genetic loci', *Nature*, 511(7510), pp. 421–427. doi: 10.1038/nature13595.

Riz, M., Braun, M. and Pedersen, M. G. (2014) 'Mathematical Modeling of Heterogeneous Electrophysiological Responses in Human β-Cells', *PLOS Computational Biology*, 10(1), p. e1003389. doi: 10.1371/JOURNAL.PCBI.1003389.

Robertson, C. E. and Baron-Cohen, S. (2017) 'Sensory perception in autism', *Nature Reviews Neuroscience*. Nature Publishing Group, pp. 671–684. doi: 10.1038/nrn.2017.112.

Rodan, L. H. *et al.* (2021) 'Phenotypic expansion of CACNA1C-associated disorders to include isolated neurological manifestations', *Genetics in medicine : official journal of the American College of Medical Genetics*, 23(10), pp. 1922–1932. doi: 10.1038/S41436-021-01232-8.

Rojas, D. C. and Wilson, L. B. (2014) 'Gamma-band abnormalities as markers of autism spectrum disorders', *Biomarkers in medicine*, 8(3), p. 353. doi: 10.2217/BMM.14.15.

Savalli, N. *et al.* (2016) 'The α2δ-1 subunit remodels CaV1.2 voltage sensors and allows Ca2+ influx at physiological membrane potentials', *The Journal of General Physiology*, 148(2), p. 147. doi: 10.1085/JGP.201611586.

Schaffler, M. D., Middleton, L. J. and Abdus-Saboor, I. (2019) 'Mechanisms of Tactile Sensory Phenotypes in Autism: Current Understanding and Future Directions for Research', *Current Psychiatry Reports*, 21(12), pp. 1–10. doi: 10.1007/S11920-019-

1122-0/FIGURES/2.

Schielzeth, H. *et al.* (2020) ‘Robustness of linear mixed-effects models to violations of distributional assumptions’, *Methods in Ecology and Evolution*, 11(9), pp. 1141–1152. doi: 10.1111/2041-210X.13434.

Schwede, M. *et al.* (2018) ‘Strong correlation of downregulated genes related to synaptic transmission and mitochondria in post-mortem autism cerebral cortex’, *Journal of Neurodevelopmental Disorders*, 10(1), pp. 1–9. doi: 10.1186/S11689-018-9237-X/FIGURES/3.

Searle, S. R., Speed, F. M. and Milliken, G. A. (2024) ‘Estimated Marginal Means, aka Least-Squares Means [R package emmeans version 1.10.0]’, *American Statistician*, 34(4), pp. 216–221. doi: 10.1080/00031305.1980.10483031.

Sepp, R. *et al.* (2017) ‘Timothy syndrome 1 genotype without syndactyly and major extracardiac manifestations’, *American journal of medical genetics. Part A*, 173(3), pp. 784–789. doi: 10.1002/AJMG.A.38084.

Serdar, C. C. *et al.* (2021) ‘Sample size, power and effect size revisited: simplified and practical approaches in pre-clinical, clinical and laboratory studies’, *Biochemia Medica*, 31(1), pp. 1–27. doi: 10.11613/BM.2021.010502.

Servili, E. *et al.* (2020) ‘Elevated basal transcription can underlie timothy channel association with autism related disorders’, *Progress in neurobiology*, 191. doi: 10.1016/J.PNEUROBIO.2020.101820.

Shah, A. and Frith, U. (1983) ‘AN ISLET OF ABILITY IN AUTISTIC CHILDREN: A RESEARCH NOTE’, *Journal of Child Psychology and Psychiatry*, 24(4), pp. 613–620. doi: 10.1111/J.1469-7610.1983.TB00137.X.

Shah, D. P. *et al.* (2012) ‘Ranolazine safely decreases ventricular and atrial fibrillation in Timothy syndrome (LQT8)’, *Pacing and clinical electrophysiology : PACE*, 35(3). doi: 10.1111/J.1540-8159.2010.02913.X.

Shah, K. *et al.* (2022) ‘Calcium Channels in the Heart: Disease States and Drugs’, *Cells*, 11(6). doi: 10.3390/CELLS11060943.

Shah, M. M. (2014) ‘Cortical HCN channels: function, trafficking and plasticity’, *The Journal of Physiology*, 592(Pt 13), p. 2711. doi: 10.1113/JPHYSIOL.2013.270058.

Shao, L. R. *et al.* (1999) ‘The role of BK-type Ca2+-dependent K+ channels in spike broadening during repetitive firing in rat hippocampal pyramidal cells’, *The Journal of physiology*, 521 Pt 1(Pt 1), pp. 135–146. doi: 10.1111/J.1469-7793.1999.00135.X.

Shu, J. *et al.* (2014) ‘Two types of T wave alternans in long-QT syndrome’, *Journal of cardiovascular electrophysiology*, 25(8), pp. 910–912. doi: 10.1111/JCE.12427.

Simms, B. A. and Zamponi, G. W. (2014) ‘Neuronal Voltage-Gated Calcium Channels: Structure, Function, and Dysfunction’, *Neuron*, 82(1), pp. 24–45. doi: 10.1016/J.NEURON.2014.03.016.

Skottun, B. C. and Skoyles, J. R. (2007) ‘Contrast sensitivity and magnocellular functioning in schizophrenia', *Vision research*, 47(23), pp. 2923–2933. doi: 10.1016/J.VISRES.2007.07.016.

Sloan, S. A. and Barres, B. A. (2014) 'Mechanisms of astrocyte development and their contributions to neurodevelopmental disorders', *Current opinion in neurobiology*, 27, p. 75. doi: 10.1016/J.CONB.2014.03.005.

Spencer, K. M. *et al.* (2003) 'Abnormal neural synchrony in schizophrenia', *Journal of Neuroscience*, 23(19), pp. 7407–7411. doi: 10.1523/jneurosci.23-19-07407.2003.

Spencer, K. M. (2012) 'Baseline gamma power during auditory steady-state stimulation in schizophrenia', *Frontiers in Human Neuroscience*, 5(JANUARY 2012), pp. 1–7. doi: 10.3389/fnhum.2011.00190.

Splawski, I. *et al.* (2004) 'CaV1.2 calcium channel dysfunction causes a multisystem disorder including arrhythmia and autism', *Cell*, 119(1), pp. 19–31. doi: 10.1016/j.cell.2004.09.011.

Splawski, I. *et al.* (2005) 'Severe arrhythmia disorder caused by cardiac L-type calcium channel mutations', *Proceedings of the National Academy of Sciences of the United States of America*, 102(23), pp. 8089–8096. doi: 10.1073/pnas.0502506102.

Spruston, N. (2008) 'Pyramidal neurons: dendritic structure and synaptic integration', *Nature reviews. Neuroscience*, 9(3), pp. 206–221. doi: 10.1038/NRN2286.

Stantić, M. *et al.* (2022) 'Face memory and face perception in autism', *Autism*, 26(1), p. 276. doi: 10.1177/13623613211027685.

Storm, J. F. (1987) 'Action potential repolarization and a fast after-hyperpolarization in rat hippocampal pyramidal cells', *The Journal of physiology*, 385(1), pp. 733–759. doi: 10.1113/JPHYSIOL.1987.SP016517.

Striessnig, J. *et al.* (2014) 'L-type Ca2+ channels in heart and brain', *Wiley Interdisciplinary Reviews. Membrane Transport and Signaling*, 3(2), p. 15. doi: 10.1002/WMTS.102.

Sunkin, S. M. *et al.* (2013) 'Allen Brain Atlas: an integrated spatio-temporal portal for exploring the central nervous system', *Nucleic Acids Research*, 41(D1), pp. D996–D1008. doi: 10.1093/NAR/GKS1042.

Swietek, B. *et al.* (2016) 'Immunostaining of Biocytin-filled and Processed Sections for Neurochemical Markers', *J. Vis. Exp*, (118), p. 54880. doi: 10.3791/54880.

Sykes, L. *et al.* (2019) 'Genetic Variation in the Psychiatric Risk Gene CACNA1C Modulates Reversal Learning Across Species', *Schizophrenia Bulletin*, 45(5), pp. 1024–1032. doi: 10.1093/schbul/sby146.

Takahashi, N. *et al.* (2016) 'Active cortical dendrites modulate perception', *Science*, 354(6319), pp. 1587–1590. doi: 10.1126/SCIENCE.AAH6066/SUPPL_FILE/TAKAHASHI-SM.PDF.

Tamagnini, F. *et al.* (2015) 'Altered intrinsic excitability of hippocampal CA1 pyramidal neurons in aged PDAPP mice', *Frontiers in Cellular Neuroscience*, 9(OCT), p. 372. doi:

10.3389/FNCEL.2015.00372.

Teufel, C. and Fletcher, P. C. (2016) ‘The promises and pitfalls of applying computational models to neurological and psychiatric disorders’, *Brain*, 139(10), p. 2600. doi: 10.1093/BRAIN/AWW209.

Thevenon, J. *et al.* (2013) ‘12p13.33 microdeletion including ELKS/ERC1, a new locus associated with childhood apraxia of speech’, *European Journal of Human Genetics*, 21(1), p. 82. doi: 10.1038/EJHG.2012.116.

Tian, Y. *et al.* (2014) ‘Alteration in basal and depolarization induced transcriptional network in iPSC derived neurons from Timothy syndrome’, *Genome Medicine*, 6(10), p. 75. doi: 10.1186/s13073-014-0075-5.

Tigaret, C. M. *et al.* (2021) ‘Neurotrophin receptor activation rescues cognitive and synaptic abnormalities caused by hemizygosity of the psychiatric risk gene Cacna1c’, *Molecular Psychiatry 2021 26:6*, 26(6), pp. 1748–1760. doi: 10.1038/s41380-020-01001-0.

Traub, R. D. and Miles, R. (1991) *Neuronal Networks of the Hippocampus*, *Neuronal Networks of the Hippocampus*. Cambridge University Press. doi: 10.1017/cbo9780511895401.

Tripathi, P. P. *et al.* (2009) ‘Increased susceptibility to kainic acid-induced seizures in Engrailed-2 knockout mice’, *Neuroscience*, 159(2), pp. 842–849. doi: 10.1016/J.NEUROSCIENCE.2009.01.007.

Tuluc, P. *et al.* (2021) ‘Role of High Voltage-Gated Ca2+ Channel Subunits in Pancreatic β-Cell Insulin Release. From Structure to Function’, *Cells*, 10(8). doi: 10.3390/CELLS10082004.

Tunca Sahin, G. and Ergul, Y. (2018) ‘A case report: Is mexiletine usage effective in the shortening of QTC interval and improving the T-wave alternans in Timothy syndrome?’, *Annals of noninvasive electrocardiology : the official journal of the International Society for Holter and Noninvasive Electrocardiology, Inc*, 23(3). doi: 10.1111/ANEC.12522.

Uhlén, M. *et al.* (2015) ‘Tissue-based map of the human proteome’, *Science*, 347(6220). doi: 10.1126/SCIENCE.1260419/SUPPL_FILE/1260419_UHLEN.SM.PDF.

Uhlhaas, P. J. and Singer, W. (2010) ‘Abnormal neural oscillations and synchrony in schizophrenia’, *Nature Reviews Neuroscience*. Nat Rev Neurosci, pp. 100–113. doi: 10.1038/nrn2774.

Umino, Y., Pasquale, R. and Solessio, E. (2018) ‘Visual Temporal Contrast Sensitivity in the Behaving Mouse Shares Fundamental Properties with Human Psychophysics’, *eNeuro*, 5(4). doi: 10.1523/ENEURO.0181-18.2018.

Vaughan, S. *et al.* (2020) ‘A Quantitative Sensory Testing Approach to Pain in Autism Spectrum Disorders’, *Journal of Autism and Developmental Disorders*, 50(5), pp. 1607–1620. doi: 10.1007/S10803-019-03918-0/TABLES/4.

Vlamings, P. H. J. M. *et al.* (2010) ‘Basic abnormalities in visual processing affect face processing at an early age in autism spectrum disorder’, *Biological Psychiatry*, 68(12), pp. 1107–1113. doi: 10.1016/j.biopsych.2010.06.024.

Walsh, M. A. *et al.* (2018) ‘A multicentre study of patients with Timothy syndrome’, *Europace*, 20(2), pp. 377–385. doi: 10.1093/europace/euw433.

Wang, J. *et al.* (2024) ‘Dentition Abnormalities in a Timothy Syndrome Patient With a Novel Genetic Mutation: A Case Report’, *Journal of Genetics and Genomics*, 51(2), pp. 197–207. doi: 10.1016/j.jgg.2023.04.013.

Wang, Q. *et al.* (2020) ‘The Allen Mouse Brain Common Coordinate Framework: A 3D Reference Atlas’, *Cell*, 181(4), pp. 936-953.e20. doi: 10.1016/J.CELL.2020.04.007.

Wang, X. J. and Buzsáki, G. (1996) ‘Gamma oscillation by synaptic inhibition in a hippocampal interneuronal network model’, *Journal of Neuroscience*, 16(20), pp. 6402–6413. doi: 10.1523/jneurosci.16-20-06402.1996.

Wickham, H. *et al.* (2019) ‘Welcome to the Tidyverse’, *Journal of Open Source Software*, 4(43), p. 1686. doi: 10.21105/JOSS.01686.

Wilson, E. B. (1927) ‘Probable Inference, the Law of Succession, and Statistical Inference’, *Journal of the American Statistical Association*, 22(158), pp. 209–212. doi: 10.1080/01621459.1927.10502953.

Xiao, J. *et al.* (2019) ‘Visual Contrast Sensitivity Correlates to the Retinal Degeneration in Rhodopsin Knockout Mice’, *Investigative Ophthalmology & Visual Science*, 60(13), p. 4196. doi: 10.1167/IOVS.19-26966.

Yang, K. *et al.* (2021) ‘SENP1 in the retrosplenial agranular cortex regulates core autistic-like symptoms in mice’, *Cell Reports*, 37(5), p. 109939. doi: 10.1016/J.CELREP.2021.109939.

Yoshimizu, T. *et al.* (2015) ‘Functional implications of a psychiatric risk variant within CACNA1C in induced human neurons’, *Molecular Psychiatry*, 20(2), pp. 162–169. doi: 10.1038/mp.2014.143.

Yucel, G. *et al.* (2013) ‘State-dependent signaling by Cav1.2 regulates hair follicle stem cell function’, *Genes & Development*, 27(11), pp. 1217–1222. doi: 10.1101/GAD.216556.113.

Zhang, X. *et al.* (2015) ‘The Topographical Arrangement of Cutoff Spatial Frequencies across Lower and Upper Visual Fields in Mouse V1’, *Scientific Reports 2015 5:1*, 5(1), pp. 1–9. doi: 10.1038/srep07734.

Zhang, Yujiao *et al.* (2021) ‘The Control of Rat Hippocampal Gamma Oscillation Strength by BK Channel Activity’, *Neuroscience*, 475, pp. 220–228. doi: 10.1016/J.NEUROSCIENCE.2021.09.002.

Zheng, E. E. *et al.* (2022) ‘Classic Timothy Syndrome Associated With Bilateral Border Digit Syndactyly: A Case Series’, *The Journal of hand surgery*. doi: 10.1016/J.JHSA.2022.09.003.

Zhou, R. *et al.* (2023) ‘Why do children with autism spectrum disorder have abnormal visual perception?’, *Frontiers in psychiatry*, 14. doi: 10.3389/FPSYT.2023.1087122.

Zou, X. *et al.* (2011) ‘Computational Study of Hippocampal-Septal Theta Rhythm Changes Due to Beta-Amyloid-Altered Ionic Channels’, *PLOS ONE*, 6(6), p. e21579. doi: 10.1371/JOURNAL.PONE.0021579.